# Heavy Resonance Hunting at the LHC

Dissertation
zur Erlangung des Grades

**"Doktor der Naturwissenschaften"**

im Promotionsfach Physik
am Fachbereich Physik, Mathematik und Informatik
der Johannes Gutenberg-Universität in Mainz

**Malte Seán Andreas Buschmann**
geb. in der Freien und Hansestadt Hamburg

Mainz, den 26. April 2017

Tag der mündlichen Prüfung: 21.8.2017

# Abstract

The need for new physics beyond the Standard Model is apparent given all the evidence collected in experiments throughout the last decades. Many new physics models, that try to explain the deviations from the Standard Model, predict heavy particles that are accessible at the Large Hadron Collider (LHC). Although there are different ways to discover new particles, resonance searches belong to one of the most powerful types of analyses. In this dissertation, we will present various aspects of resonance searches and how they can be used to constrain physics beyond the Standard Model.

By recasting an existing LHC search we determine limits on a lepton flavour violating two Higgs doublet model. For a quark flavour violating two Higgs doublet model we develop a new superior analysis for a top plus two Higgs final state and compare the results to existing and projected limits.

In some circumstances the pair production channel of a new heavy state provides a model-independent way to test the particle's existence, whereas the single resonance production mode would be model-dependent. This is the case for a massive coloured octet vector. We design a search dedicated to find such a pair produced resonance if neither a subsequent decay to top quarks nor to lighter quarks dominates.

Furthermore, we determine the prospects of spin discrimination for a heavy resonance decaying to two massive bosons. We study the implications of jet substructure techniques on angular correlations that are vital for such a discrimination. Using a fully hadronic final state we determine the projected reach at the LHC.

Occasionally, a resonance cannot be seen directly since the final state particles may be dark matter. We use a displaced and prompt lepton jet analysis to study how effects of a parton shower in the dark sector can yield information about the underlying physics. We also provide a semi-analytic description of such a dark shower.

# Contents

CHAPTER 1

# Introduction

The Standard Model of Particle Physics is commonly regarded as *the best model we ever had*. With a few basic building blocks of fundamental particles and their respective interactions, it can explain an incredibly vast variety of observations. It predicted the outcome of measurements with extraordinary precision and withstood many experimental tests.

But the current Standard Model cannot be the final answer. There are still some measurements and observations that are not explicable, like non-zero neutrino masses and the gravitational effects from dark matter. But even if we would not have those conflicting observations, the Standard Model itself has a few conceptual issues, *e.g.* the hierarchy problem. Most of those are somewhat philosophical in nature, but they nevertheless suggest that there must be more: new physics.

Plenty ideas of how to extend the Standard Model emerged throughout the last decades. Many of them tackling different problems, introducing new kinds of particles, and making different predictions. Most are well-motivated from a certain point of view, but of course, we do not know yet which of those extensions is, after all, an accurate description of Nature.

The Large Hadron Collider (LHC) with its four main detectors ATLAS, CMS, LHCb and ALICE is one of the most important high-energy experiments currently operating. The hopes for a discovery of new particles were high when this 27 km long circular collider was first switched on in 2009. And indeed, only a few years after on the 4th of July 2012, ATLAS and CMS announced the discovery of the Higgs particle [1, 2].

In the past few years, the LHC strengthened our understanding with many interesting measurements. But concerning the biggest problems of the Standard Model, that are briefly summarised in the next chapter, very little progress has been made in terms of discoveries. The data places strong limits on various Standard Model extensions, even ruling out some of them. While obtaining bounds on new physics models is important, a discovery of something new would surely be better. But so far this has not happened.

That does not necessarily mean that the new physics we are looking for is not accessible at the LHC. First, the LHC is still collecting data and accumulating more statistics will help to extend the reach. But secondly, we might just be looking in the wrong places. The data recorded by the LHC is incredibly rich and it is non-trivial to analyse it. A lot of effort has been spent on reinterpreting the data and improving common analysis techniques.

Particle physics is often divided into three frontiers of discovery: the energy, intensity, and cosmic frontier. They all try to address basic fundamental questions, but using distinct approaches to a particular open question. Intensity frontier experiments can constrain weakly coupled particles using intense sources and highly sensitive detectors. Energy frontier experiments like the LHC require larger couplings, but as they provide a lot of energy they can produce very massive particles.

Typically (although this is not the only possibility) heavy particles are resonantly produced at the LHC and decay to lighter particles. Thus the new state itself is not measured and only its decay products might be visible. Most analyses will try to identify these decay products and reconstruct the heavy particle from them. This is exactly how the Higgs boson has been found.

This dissertation will deal with various aspects of resonance searches. Motivated by various different new physics models we will reinterpret and optimise existing analyses, develop new search strategies, and determine projections for the future.

A summary of the main reasons we believe in the need for new physics in the first place is given in chapter 2. In Chapter 3 we will then elaborate on how new physics models can look like in general. This, of course, will not be a complete list but aims at briefly presenting the main ideas and introducing the Standard Model extensions used later on. The LHC will be described in chapter 4, including some of the common techniques used to reconstruct objects. As there is almost an infinite amount to say about the LHC we will restrict ourselves to some either non-trivial or technical aspects relevant for the rest of the dissertation.

In chapter 5 we will discuss basic and new searches looking for flavour violating couplings of the Higgs. The aim here is to find a heavy resonance and to determine

what a non-discovery means for the model parameter space. Similarly, Chapter 6 will present a new analysis dealing with a pair-produced resonance of a coloured octet vector, as this production channel provides a model-independent test. In Chapter 7 we will then assume that a diboson resonance has been found and show how additional information about the nature of the resonance can be drawn from data. In Chapter 8 we emphasise that even if the resonance itself is invisible for the detector, there are sometimes underlying effects that are accessible. This chapter is based on prompt and displaced lepton jet searches. We will conclude in chapter 9.

The chapters 5 and 7 are based on the publications in ref. [3] and [4], respectively. Chapter 6 contains preliminary results which are to be published very soon. Chapter 8 includes results from ref. [5] and a section of a 100 TeV collider report in ref. [6].

# CHAPTER 2

# The Need for New Physics

## 2.1 Experimental Hints

### 2.1.1 Dark Matter

The experimental evidence for dark matter is immense. As early as the 1930's people started to notice grand discrepancies when trying to understand the kinematics of large galaxy cluster. By using the virial theorem and measuring the velocity dispersion of the Coma cluster it was possible to determine the total mass of the cluster [7]. It was found that this mass was greatly larger than the mass obtained by looking at the luminous matter. To resolve this issue the existence of a new kind of matter, a *dark* matter, was first postulated in ref. [8].

More discrepancies became apparent in the 1970's when the rotational velocity of stars around the centre of the galaxy was measured as a function of its distance to the centre [9]. According to Kepler's Second Law, this galaxy rotation curve should decrease for large distances if the visible matter is all there is. Instead, it was found to be flat and asymptote to a constant non-zero value. The leading explanation for this is again dark matter, which extends as a halo outside the visible galaxy.

Since then more and more evidence has been collected throughout the decades. Gravitational lensing, where the light of distance objects is gravitationally bent around very massive foreground objects like galaxy clusters. The way the light is bent offers an independent measurement of the total mass of the lens, which again turns out to be far larger than that of the luminous matter (see for example ref. [10]).

Dark matter also affects the cosmic microwave background (CMB), radiation which was emitted shortly after the Big Bang during the time of recombination. Since dark matter does not interact with this radiation, but normal matter does, dark matter leaves a distinct imprint on the CMB spectrum (see eg. ref. [11]).

This is just to give a few examples, more measurements have been performed that all point towards the same conclusion: Some kind of *dark* matter has to exist.

### 2.1.2 Dark Energy

The nature of dark energy is less clear than that of dark matter. Nevertheless, strong evidence for its presence exists, although only indirectly.

It is an established fact that the universe expands at an accelerating pace by looking at so-called standard candles. As the intrinsic luminosity of a supernova is known its distance can therefore be deduced by looking at the observed luminosity. At the same time, the red-shift of the supernova can be measured and translated into a distance. The relation between both distance measurements indicates that the expansion of the Universe accelerates [12]. The cause of this acceleration is unknown but the energy necessary for it is denoted dark energy.

Additionally, the CMB spectrum does not only tell us something about dark matter but also that the shape of the Universe is flat. This is only possible if the total mass and energy in the Universe is equal to the so-called critical density $\rho_c = 3H^2/(8\pi G)$, where $H$ is the Hubble parameter and $G$ Newton's gravitational constant. However, all known matter and radiation, including dark matter, does not add up to the critical density, indicating that a significant part of the Universe is made up of dark energy [13].

Furthermore, large scale structure formation of for example galaxy clusters supports the existence of dark energy (see eg. ref. [14] for a review).

### 2.1.3 Neutrino Masses

Neutrinos are massless in the Standard Model, but for many years by now we know this is not a true assumption. In principle neutrino oscillations are observed as early as the 1960's [15], although it took decades to understand the measurement results thoroughly. These flavour oscillations are only possible if neutrinos have a non-zero mass term, as otherwise the (diagonalised) mass basis and flavour basis would align.

Adding a neutrino mass term to the Standard Model is in a sense straightforward[1]. But there are different ways to do so, especially when it comes to explaining the

[1] These extensions usually leave other effects than just neutrino masses.

smallness of the mass parameter. The correct way of treating neutrino masses is still to be determined.

### 2.1.4 Baryon Asymmetry

The problem of baryonic imbalance is easy to perceive but very puzzling nonetheless. The fact that there is obviously a lot more baryonic matter than anti-baryonic matter in the Universe is not explained by the Standard Model. The natural assumption is that the Universe is in a neutral state at the time of the Big Bang. As relevant charges are conserved in the Standard Model, such an asymmetry should not have appeared.

## 2.2 Theoretical Hints

### 2.2.1 Hierarchy Problem

The Hierarchy problem is a problem of naturalness. It is about the question why some values are either so large, so tiny or exactly the way they are. The best example is the mass of the Higgs boson, whose bare mass is naïvely of order the Plank mass. As it turns out though the quadratic radiative corrections to the Higgs mass are large as well, cancelling off the bare mass term to almost but not quite zero. Therefore the observed Higgs mass of $\sim$125 GeV is regarded as highly fine-tuned.

### 2.2.2 Grand Unification

Grand unification is technically not a problem, but rather a very appealing concept not realised in the current Standard Model. Throughout the history, physics knew about various different kind of forces. But in many cases, it turned out that two forces which were thought to have no relation could be described by just one. The most popular example is that of electromagnetism, the unification of the electric and magnetic force.

The Standard Model is based on the three fundamental forces, weak force, strong force, and the electromagnetic force, but not yet gravity. Since the coupling strength of a force depends on the energy, the three forces of the Standard Model could in principle merge to one single grand force at high energy. This is however not the case as the crossing points between the respective forces are slightly off.

### 2.2.3 Strong CP Problem

Experiments like the measurement of the electric dipole moment of the neutron [16] tell us that QCD is not CP violating, or at least very little. This is somewhat surprising from a theoretical point of view, as CP violating $\mathcal{O}(1)$ terms proportional $F_{\mu\nu}\tilde{F}^{\mu\nu}$ are allowed by the symmetries of the Standard Model. Here, $F_{\mu\nu}$ is the usual field strength tensor and $\tilde{F}^{\mu\nu}$ its dual.

As it is a consensus that all terms that are allowed by gauge symmetries should exist, this is surely a problem. Thus one has to explain why this term does not exist or why it appears to be so unnaturally small.

CHAPTER 3

# Popular Models Beyond the Standard Model

After the previous chapter described what the Standard Model is struggling with, this chapter aims at introducing some of the common concepts for extending the Standard Model. All of these extensions try to resolve one or several of the previously mentioned issues. The emphasis will be mainly on concepts relevant for the rest of this dissertation.

## 3.1 Supersymmetry

Supersymmetry is one of the – if not *the* – most popular models probed at the LHC. The basic idea of supersymmetry is rather simple: it introduces a new symmetry relating bosons and fermions. The implications and phenomenology of supersymmetry, on the other hand, are not so straightforward.

Such a new symmetry results in the existence of a superpartner to each Standard Model particle. Supersymmetry must be spontaneously broken, otherwise superpartners would share the same mass as their Standard Model equivalent. Depending on the exact details of the model, many of these heavy superpartners would be accessible at the LHC, although none has been detected yet. Nevertheless, supersymmetry is an appealing concept, as it addresses almost all previously mentioned issues of the Standard Model.

## 3.2 Extended Higgs Sector

Since the existence of the Higgs bosons was confirmed only a few years ago [1, 2] we do not understand this sector very well yet. As of now, the Higgs boson found at the LHC is in agreement with the Standard Model Higgs bosons, although some hints appeared in form of flavour changing couplings that this might not actually be the case [17]. These kind of couplings would be an immediate hint for a modified Higgs sector [18–32].

Nevertheless, understanding the Higgs boson will yield great information about physics beyond the Standard Model. Naturally, extensions of the Higgs sector were developed and throughout the next years we expect to learn more about the true nature of the Higgs sector. This section will introduce a popular extension, known as two Higgs doublet model (2HDM) [33] (see for example ref. [34, 35] and refs. [36, 37] for a review and work in the context of the Higgs discovery).

### 3.2.1 Two Higgs Doublet Model

The 2HDM introduces a second scalar $SU(2)_L$ doublet to the Standard Model which mixes with the original Higgs doublet. As both are $SU(2)_L$ doublets the basis can be freely chosen. For the rest of this dissertation, we will work in the so-called Georgi basis, where only one of the two doublets develops a vacuum expectation value (vev). They can therefore be written as [36]

$$\Phi_1 = \begin{pmatrix} G^+ \\ \frac{1}{\sqrt{2}}(v + h_1 + iG^0) \end{pmatrix}, \qquad \Phi_2 = \begin{pmatrix} H^+ \\ \frac{1}{\sqrt{2}}(h_2 + ih_3) \end{pmatrix}. \tag{1}$$

Here, $v = 246$ GeV is the Standard Model vev. The field content of this model comprises a charged and neutral Goldstone bosons, $G^+$ and $G^0$, a charged Higgs boson $H^+$ and three neutral Higgs bosons $h_1$, $h_2$, and $h_3$. The neutral Higgs bosons are not yet physical states as they still mass mix.

Let us consider the most general type of potential for this model, then known as a 2HDM of type-III. It reads [38]

$$\begin{aligned} V = {} & \mu_1^2 \Phi_1^\dagger \Phi_1 + \mu_2^2 \Phi_2^\dagger \Phi_2 + (\mu_3^2 \Phi_1^\dagger \Phi_2 + h.c.) \\ & + \lambda_1 (\Phi_1^\dagger \Phi_1)^2 + \lambda_2 (\Phi_2^\dagger \Phi_2)^2 + \lambda_3 (\Phi_1^\dagger \Phi_1)(\Phi_2^\dagger \Phi_2) + \lambda_4 (\Phi_1^\dagger \Phi_2)(\Phi_2^\dagger \Phi_1) \\ & + \left[ \left( \lambda_5 \Phi_1^\dagger \Phi_2 + \lambda_6 \Phi_1^\dagger \Phi_1 + \lambda_7 \Phi_2^\dagger \Phi_2 \right) (\Phi_1^\dagger \Phi_2) + h.c. \right], \end{aligned} \tag{2}$$

with real parameters $\mu_1^2$, $\mu_2^2$, $\lambda_1$, $\lambda_2$, $\lambda_3$, and $\lambda_4$ and complex parameters $\mu_3^2$, $\lambda_5$, $\lambda_6$, and $\lambda_7$.

If any of the above complex parameters exhibit indeed an imaginary contribution, the quantity $\mathrm{Im}[\Phi_1^\dagger \Phi_2]$ will violate the CP symmetry. We will, however, consider the CP-conserving case in which all parameters of the scalar potential are real.

A definite CP parity can be assigned to the physical states now. $h_3$ will be a CP-odd Higgs boson, relabelled as $A^0$. The other two Higgs bosons $h_1$ and $h_2$ instead mix to the Standard Model-like Higgs boson $h$ and a heavy neutral Higgs boson $H^0$, according to

$$\begin{pmatrix} h \\ H^0 \end{pmatrix} = \begin{pmatrix} \cos\alpha & \sin\alpha \\ -\sin\alpha & \cos\alpha \end{pmatrix} \begin{pmatrix} h_1 \\ h_2 \end{pmatrix} . \tag{3}$$

The mixing angle $\alpha$, which will be typically small, can be expressed as

$$\tan 2\alpha = \frac{-2\lambda_6 v^2}{m_{A^0}^2 + 2v^2(\lambda_5 - \lambda_1)} . \tag{4}$$

The mass of $A^0$ appearing in eq. 4 can be obtained by taking derivatives of the scalar potential $V$. The first derivative has to vanish in any field space direction at the minimum of $V$, $\Phi_1 = (0, v/\sqrt{2})$ and $\Phi_2 = (0, 0)$. This leads to the two relations

$$\mu_1^2 = -\lambda_1 v^2 \qquad \text{and} \qquad \mu_3^2 = -\lambda_6 \frac{v^2}{2} . \tag{5}$$

The second derivatives at this point give the masses of the charged Higgs field $H^\pm$ and $A^0$,

$$m_{H^\pm}^2 = \mu_2^2 + \lambda_3 \frac{v^2}{2} \qquad \text{and} \qquad m_{A^0}^2 = m_{H^\pm}^2 + v^2\left(\tfrac{1}{2}\lambda_4 - \lambda_5\right) . \tag{6}$$

The masses of the neutral CP even Higgs bosons can then be expressed as

$$m_{h,H^0}^2 = \frac{1}{2} m_{H^\pm}^2 + \frac{1}{2} v^2\left(2\lambda_1 + \tfrac{1}{2}\lambda_4 + \lambda_5\right) \pm \frac{1}{2}\sqrt{[m_A^2 + 2v^2(\lambda_5 - \lambda_1)]^2 + 4v^4\lambda_6^2} . \tag{7}$$

One interesting observation in the 2HDM type-III is that of flavour changing couplings [18, 21, 22, 27, 28, 39–50]. Those couplings do not appear in the Standard Model Higgs sector since the Yukawa matrix and fermion mass matrix align. Thus diagonalising the fermion mass matrix automatically implies a diagonal Yukawa interaction matrix, therefore all interactions are flavour conserving.

In a 2HDM, however, only one doublet $\Phi_1$ contributes in the Georgi basis, whereas both doublets contribute to the Yukawa matrix. Therefore, fermion mass matrix and Yukawa matrix can naturally misalign, *i.e.* flavour changing couplings are possible. Let us now consider the two possible cases, flavour violating couplings in the quark sector and in the lepton sector.

#### 3.2.1.1 Flavour Changing Couplings in the Quark Sector

For the quark sector, the Yukawa couplings for up-type quarks can be written as

$$\mathcal{L}_{\text{up}} = -\eta^{ij}_{u,1}\overline{Q^i_L}\tilde{\Phi}_1 u^j_R - \eta^{ij}_{u,2}\overline{Q^i_L}\tilde{\Phi}_2 u^j_R + h.c.\,, \tag{8}$$

where $\tilde{\Phi}_k \equiv i\sigma^2\Phi^\dagger_k$ with $\sigma^2$ as the second Pauli matrix. $Q^i_L$ and $u^j_R$ are the usual left-handed fermion doublets and right-handed fermion singlets. The indices $i, j$ denote the quark flavour, thus $i, j = 1, 2, 3$ or equivalently $i, j = u, c, t$. Wherever unambiguous we will omit the subscipt $u$ on the interaction parameter $\eta$, for example $\eta^{13}_{u,2} \equiv \eta^{ut}_2$. The Lagrangian for down-type quarks can be written analogously.

After electroweak symmetry breaking this becomes

$$\mathcal{L}_{\text{up}} = -m_i\overline{u^i_L}u^i_R - y^{ij}_{u,h}\overline{u^i_L}u^j_R h - y^{ij}_{u,H}\overline{u^i_L}u^j_R H^0 + h.c.\,, \tag{9}$$

where we are working in the mass basis with $\eta^{ij}_{u,1} \propto \delta^{ij}$ and $m_i = \eta^{ii}_{u,1}v/\sqrt{2}$. The Yukawa couplings can be expressed as

$$y^{ij}_{u,h} = \frac{m_i}{v}\delta^{ij}\cos\alpha + \frac{1}{\sqrt{2}}\eta^{ij}_{u,2}\sin\alpha \tag{10}$$

$$y^{ij}_{u,H^0} = -\frac{m_i}{v}\delta^{ij}\sin\alpha + \frac{1}{\sqrt{2}}\eta^{ij}_{u,2}\cos\alpha\,. \tag{11}$$

We will assume that all flavour violating Yukawa couplings are real to avoid CP violation. Now an interesting feature becomes apparent: For a very small mixing around $\alpha \approx 0$, $h$ remains Standard Model-like, whereas $H^0$ can exhibit large flavour violation couplings.

The corresponding flavour violating decay rates can be computed as

$$\Gamma_{h\to\bar{t}u} = \Gamma_{h\to\bar{u}t} = \frac{3}{32\pi}m_h\Big(1 - \frac{m^2_{H^0}}{m^2_h}\frac{x_t}{4}\Big)^2\sin^2\alpha\Big[\big|\eta^{ut}_2\big|^2 + \big|\eta^{tu}_2\big|^2\Big]\,, \tag{12}$$

$$\Gamma_{H^0\to\bar{t}u} = \Gamma_{H^0\to\bar{u}t} = \frac{3}{32\pi}m_{H^0}\Big(1 - \frac{x_t}{4}\Big)^2\cos^2\alpha\Big[\big|\eta^{ut}_2\big|^2 + \big|\eta^{tu}_2\big|^2\Big]\,, \tag{13}$$

with $x_t \equiv 4m_t^2/m_{H^0}^2$ and analogously for other quark combinations. In order to determine the branching ratios for the heavy Higgs $H^0$ we also need to determine the other dominant partial decays widths, which are

$$\Gamma_{H^0\to t\bar{t}} = \frac{3}{8\pi} m_{H^0} \left( -\sin\alpha \frac{m_t}{v} + \cos\alpha \frac{\eta_2^{tt}}{\sqrt{2}} \right)^2 (1-x_t)^{3/2}\,, \tag{14}$$

$$\Gamma_{H^0\to WW} = \frac{1}{64\pi} \frac{m_{H^0}^3}{v^2} \sin^2\alpha \sqrt{1-x_W}(4-4x_W+3x_W^2)\,, \tag{15}$$

$$\Gamma_{H^0\to ZZ} = \frac{1}{128\pi} \frac{m_{H^0}^3}{v^2} \sin^2\alpha \sqrt{1-x_Z}(4-4x_Z+3x_Z^2)\,, \tag{16}$$

$$\Gamma_{H^0\to hh} = \frac{1}{8\pi} \frac{g_{H^0hh}^2 v^2}{m_{H^0}} \sqrt{1-x_h}\,, \tag{17}$$

where again $x_a \equiv 4m_a^2/m_{H^0}^2$ with $a = t, W, Z, h$. Here we also introduced the coupling constant $g_{H^0hh}$, which is defined as

$$\mathcal{L}_{H^0hh} = g_{H^0hh}\, v\, H^0 hh\,. \tag{18}$$

Note that the decay widths of $H^0 \to WW,\ ZZ$ are the same as in the Standard Model with an additional suppression factor of $\sin^2\alpha$ due to the mixing between $h$ and $H^0$. This is true since in the Georgi basis $\Phi_2$ does not acquire a vev. If furthermore the diagonal couplings of $\Phi_2$ to up-type quarks vanish, $\eta_{u,2}^{ii} = 0$, the above statement holds also for $H^0 \to t\bar{t}$.

#### 3.2.1.2 Flavour Changing Couplings in the Lepton Sector

Similarly to the quark sector, one can write down flavour violating couplings in the lepton sector,

$$\mathcal{L}_\ell \supset -\eta_{\ell,1}^{ij} \overline{L_L^i} \Phi_1 e_R^j - \eta_{\ell,2}^{ij} \overline{L_L^i} \Phi_2 e_R^j + h.c.\,, \tag{19}$$

where $L_L^i$ and $e_R^j$ are the left-handed lepton doublets and right-handed charged lepton singlets. $i, j$ are here again the flavour indices, but now in the lepton sector. Thus $i, j = 1, 2, 3$ or $e, \mu, \tau$. Again we will omit the subscript $\ell$ whenever possible to enhance readability.

The above expression can be written after electroweak symmetry breaking as

$$\mathcal{L}_\ell = -\bar{e}_L^i e_R^j \left[ h\left( \frac{m_i}{v}\delta^{ij}\cos\alpha + \frac{\eta_{\ell,2}^{ij}}{\sqrt{2}}\sin\alpha \right) + H^0\left( -\frac{m_i}{v}\delta^{ij}\sin\alpha + \frac{\eta_{\ell,2}^{ij}}{\sqrt{2}}\cos\alpha \right) \right] + h.c. \tag{20}$$

$$\equiv -\bar{e}_L^i e_R^j \left[ y_{\ell,h}^{ij} h + y_{\ell,H}^{ij} H^0 \right] + h.c.\,. \tag{21}$$

The corresponding flavour violating partial decay widths for $H^0$ and $h$ can be expressed as

$$\Gamma(H^0 \to \tau^+\mu^-) = \Gamma(H^0 \to \tau^-\mu^+) = \frac{1}{32\pi} m_{H^0} \cos^2\alpha \left( |\eta_2^{\mu\tau}|^2 + |\eta_2^{\tau\mu}|^2 \right), \tag{22}$$

$$\Gamma(h \to \tau^+\mu^-) = \Gamma(h \to \tau^-\mu^+) = \frac{1}{32\pi} m_h \sin^2\alpha \left( |\eta_2^{\mu\tau}|^2 + |\eta_2^{\tau\mu}|^2 \right) \tag{23}$$

and analogously for other flavour combinations. Again note that $h$ develops Standard Model-like couplings for small mixing angles $\alpha$, whereas flavour changing couplings can be large for the heavy Higgs $H^0$.

## 3.3 Extended Colour Sector

There are many ways to extend the colour sector, but we want to focus on those in which a massive colour octet vector arises. Typically these involve either an extended colour gauge group or extra dimensions. Their respective details are described in the two subsections 3.3.1 and 3.3.2.

Heavy octet vectors $X_\mu^a$ can be naïvely seen as a massive version of the gluon. As such they interact with quarks and the most general interaction Lagrangian can be written as

$$\mathcal{L} \supset g_s \left( g_L^{ij} \bar{q}_i \gamma^\mu T^a X_\mu^a P_L q_j + g_R^{ij} \bar{q}_i \gamma^\mu T^a X_\mu^a P_R q_j \right). \tag{24}$$

Here, $i$ and $j$ are flavour indices, $T^a$ the $SU(3)$ generators and $P_{L/R}$ the usual projection operators $(1 \mp \gamma_5)/2$. Furthermore, the up-type and down-type quarks are separated in the flavour sum to conserve electric charge.

The coupling matrices $g_L$ and $g_R$ have to be symmetric due to $CPT$ symmetry, but are otherwise unrestricted from a theoretical point of view. But even though off-diagonal couplings are possible, they correspond to flavour changing neutral currents. These are strongly constraint by flavour experiments, most dominantly $\bar{K}$–$K$, $\bar{B}$–$B$, and $\bar{D}$–$D$ meson oscillations [51].

The partial width for $X$ decaying to quark pairs can be written as

$$\Gamma(X \to \bar{q}_i q_j) = \frac{\alpha_s m_X}{6}\left((1 - \frac{m_{q_i}^2 + m_{q_j}^2}{m_X^2})(g_L^{ij} g_R^{ij}) + 2\frac{m_i m_j}{m_X^2}((g_L^{ij})^2 + (g_R^{ij})^2)\right) * \\ * \left(1 - 2\frac{m_{q_i}^2 + m_{q_j}^2}{m_X^2} + \frac{(m_{q_i}^2 - m_{q_j}^2)^2}{m_X^4}\right)^{1/2}. \quad (25)$$

Since flavour changing couplings are so strongly constrained [51] we will focus on diagonal $g_L$ and $g_R$ matrices, in which case eq. 25 simplifies to

$$\Gamma(X \to \bar{q}q) = \frac{\alpha_s m_X}{6}\left((1 - \frac{2m_q^2}{m_X^2})g_L g_R + \frac{2m_q^2}{m_X^2}(g_L^2 + g_R^2)\right)\left(1 - \frac{4m_q^2}{m_X^2}\right)^{1/2}. \quad (26)$$

Note that we omit the trivial flavour indices to simplify the notation.

### 3.3.1 Extra Colour Gauge Group

Colour octet vectors arise in models with an extended colour symmetry $SU(3)_1 \times SU(3)_2$. Besides the colour group, a bifundamental complex scalar field $\Sigma$ is introduced, whose most general renormalisable potential [52–54] reads

$$V(\Sigma) = -m_\Sigma^2 \mathrm{Tr}(\Sigma\Sigma^\dagger) - \mu(\det\Sigma + \text{h.c.}) + \frac{\lambda}{2}\mathrm{Tr}^2(\Sigma\Sigma^\dagger) + \frac{\kappa}{2}\mathrm{Tr}(\Sigma\Sigma^\dagger\Sigma\Sigma^\dagger), \quad (27)$$

with $\mu, m_\Sigma^2 > 0$. This field acquires a vev,

$$\langle\Sigma\rangle = \frac{f_\Sigma}{\sqrt{6}}\mathbb{1}_3 = \frac{\sqrt{4(\kappa + 3\lambda)m_\Sigma^2 + \mu^2} + \mu}{2(\kappa + 3\lambda)}\mathbb{1}_3, \quad (28)$$

such that it brakes $SU(3)_1 \times SU(3)_2$ to its diagonal subgroup. This subgroup is identified as the Standard Model gauge group $SU(3)_c$. Expanding the $\Sigma$ around its vev yields

$$\Sigma = \frac{1}{\sqrt{6}}(f_\Sigma + \phi_R + i\phi_I)\mathbb{1}_3 + (G_H^a + iG_G^a)T^a, \quad (29)$$

where $\phi_R$ and $\phi_I$ are a real and pseudoreal colour singlet scalar, and $G_H^a$ and $G_G^a$ are real colour octet scalars. $G_G^a$ are the Nambu-Goldstone modes of the broken $SU(3)_1 \times SU(3)_2$ symmetry and can be identified as the longitudinal degrees of freedom of the heavy colour octed vector $X_\mu^a$. $\phi_R$, $\phi_I$ and $G_H^a$ are often assumed to be heavy enough to be of no phenomenological relevance.

The kinetic term of $\Sigma$ can be written as

$$\mathcal{L} \supset \mathrm{Tr}(D_\mu \Sigma^\dagger D^\mu \Sigma), \tag{30}$$

where the covariant derivative is given by

$$D^\mu = \partial^\mu - i h_1 G_1^{\mu a} T^a + i h_2 G_2^{\mu a} T^a. \tag{31}$$

$G_1^{\mu a}$ and $G_2^{\mu a}$ are the respective $SU(3)_1 \times SU(3)_2$ gauge fields with a gauge coupling of $h_1$ and $h_2$, respectively. In order to identify the diagonal subgroup of the broken $SU(3)_1 \times SU(3)_2$ symmetry with the Standard Model colour gauge group $SU(3)_c$ these gauge couplings have to fulfil the relation

$$\frac{1}{g_s^2} = \frac{1}{h_1^2} + \frac{1}{h_2^2}. \tag{32}$$

The kinetic term in eq. 30 yields a mass matrix for the gauge fields. Upon diagonalisation these two fields mix to the massless QCD gluon $g^{\mu a}$ and the colour octet vector $X^{\mu a}$, according to

$$g^{\mu a} = \cos\theta\, G_1^{\mu a} + \sin\theta\, G_2^{\mu a}, \tag{33}$$

$$X^{\mu a} = \sin\theta\, G_1^{\mu a} - \cos\theta\, G_2^{\mu a}. \tag{34}$$

$\theta$ is the mixing angle which can be expressed as $\theta = \tan^{-1}(h_1/h_2)$. The mass of the heavy octet vector is then given by [52, 54]

$$m_X = \sqrt{\frac{2}{3}} \frac{g_s}{\sin(2\theta)} f_\Sigma. \tag{35}$$

Different types of models arise depending on how the Standard Model quarks are charged under the parent $SU(3)_1 \times SU(3)_2$ gauge group. Universally coupled models, *i.e.* $X$ couples with the same strength to all quarks, charge all quark generations identically under the same gauge representation. In this case the gauge symmetry commutes with the Standard Model quark flavour symmetry.

One commonly considered model is the coloron model [52–57], where all quarks transform as $\square$[1] under one of the two $SU(3)$ groups and as a singlet under the respective other. In this case $g_L = g_R = \tan\theta \cdot \mathbb{1}_3$ holds, such that the interaction

[1] Here, $\square$ denotes that the field transforms in the fundamental representation under the respective gauge group, so in this particular case as a triplet.

Lagrangian is flavour universal and reads

$$\mathcal{L} \supset g_s \tan\theta \bar{q}\gamma^\mu T^a X^a_\mu q. \tag{36}$$

Thus the heavy octet vector exhibits only purely vector couplings in this model and is referred to as the *coloron*.

An axial component arises when left-handed and right-handed quark fields are charged differently under the two $SU(3)$ gauge groups. Such a model is known as the chiral colour model [58–67] and the heavy octet vector is dubbed *axigluon*. Consider for example the case in which left-handed quarks transform as $(\square, \mathbf{1})$ and right-handed quarks as $(\mathbf{1}, \square)$ under the parent $SU(3)_1 \times SU(3)_2$ gauge group. The interaction Lagrangian then reads

$$\mathcal{L} \supset g_s \bar{q}\gamma^\mu T^a X^a_\mu (\tan\theta P_L - \cot\theta P_R) q. \tag{37}$$

However, this charge assignment leads to anomalies, notably $SU(3)_1^2 \times U(1)_Y$ and $SU(3)_2^2 \times U(1)_Y$, that have to be cancelled by new fermions. But these new fermions can be very massive such that they are of no phenomenological relevance.

An example of a flavour non-universal model is the so-called topcolour model [53, 68–71]. Here, the third generation quarks have a different gauge charge under $SU(3)_1 \times SU(3)_2$ than the first two generations, for example $Q_L^{1,2} \sim (\square, \mathbf{1})$, $Q_L^3 \sim (\mathbf{1}, \square)$, $u_R^{1,2} \sim (\square, \mathbf{1})$, $u_R^3 \sim (\mathbf{1}, \square)$, $d_R^{1,2,3} \sim (\square, \mathbf{1})$, where the upper index refers to the quark generation. In this case the coupling structure can be expressed as

$$\mathcal{L} \supset g_s \cot\theta (\bar{t}\gamma^\mu T^a X^a_\mu t + \bar{b}_L \gamma^\mu T^a X^a_\mu b_L) + g_s \tan\theta (\bar{b}_R \gamma^\mu T^a X^a_\mu b_R + \sum_{i=1}^{4} \bar{q}_i \gamma^\mu T^a X^a_\mu q_i). \tag{38}$$

Here, the sum in the last term goes over the $u$, $d$, $c$ and $s$ quark flavours. Also in this case anomalies arise, which can be cancelled by two electroweak singlet quarks transforming as $(\mathbf{1}, \square)$ and $(\square, \mathbf{1})$, each with hypercharge $-2/3$. Typically, the branching ratio of the heavy octet vector to top pair in the topcolour model ranges from 80% to 97% [72].

### 3.3.2 Extra Dimensions

Models which introduce extra spatial dimensions typically feature heavy octet vectors as excitations in the Kaluza-Klein (KK) tower. The most prominent are models with a large extra dimension [73], universal extra dimension [74], and a warped extra

dimension in a Randall-Sundrum framework [75–78]. These kinds of models can be divided into two categories, featuring either a *flat* or a *warped* extra dimension.

An example for a flat extra dimension is known as a universal extra dimension [74]. This extra dimension is compactified to avoid direct observation, often on a circle with two endpoints, $S_1/Z_2$. The size of the extra dimension is then given by the Radius $R$ of the circle. The compactification quantises the momentum of any Standard Model particle as $n/R$, leading to a so-called tower of KK excitations for every particle. These KK excitations are massive, as the momentum components proportional to $n/R$ can be interpreted as a mass. Every particle on the $n$-th KK level is naïvely degenerate in mass, but receives for example strong radiative corrections, lifting the degeneracy.

The heavy colour octet vector is given by the level-2 KK excitation of the gluon, where the gluon corresponds to level-0. The level-1 KK excitation does not decay to Standard Model particles as usually KK parity is assumed, defined as $(-1)^n$ with $n$ as the level number. The lightest level-1 KK excitation is therefore absolutely stable as it would otherwise violate KK parity. However, the level-2 KK gluon couples to quarks through a loop of level-1 KK excitation of the gluon. The relevant coupling is given by [79]

$$\mathcal{L} \supset g_s \frac{1}{\sqrt{2}} \frac{1}{16\pi^2} \log\left(\frac{\Lambda}{\mu}\right)^2 \bar{q}_i \gamma^\mu T^a X^a_\mu \left[ P_L(\frac{1}{8}g_1^2 + \frac{27}{8}g_2^2 - \frac{11}{2}g_s^2) + P_R(2g_1^2 - \frac{11}{2}g_s^2) \right] q_i \tag{39}$$

for up-type quarks and

$$\mathcal{L} \supset g_s \frac{1}{\sqrt{2}} \frac{1}{16\pi^2} \log\left(\frac{\Lambda}{\mu}\right)^2 \bar{q}_i \gamma^\mu T^a X^a_\mu \left[ P_L(\frac{1}{8}g_1^2 + \frac{27}{8}g_2^2 - \frac{11}{2}g_s^2) + P_R(\frac{1}{2}g_1^2 - \frac{11}{2}g_s^2) \right] q_i \tag{40}$$

for down-type quarks. $\Lambda$ is the ultraviolet scale larger than $1/R$ and $\mu$ is the renormalisation scale at which the coupling is evaluated. $g_1$ and $g_2$ are the hypercharge gauge coupling and weak gauge coupling, respectively.

A Randall-Sundrum model [75–78] assumes a warped extra dimension and is based on a slice of a 5-dimensional anti-de Sitter space ($\mathrm{AdS}_5$). The non-factorisable background metric is given by

$$ds^2 = e^{-2k|y|} n_{\mu\nu} dx^\mu dx^\nu - dy^2 \,, \tag{41}$$

where $k$ is the curvature of the $\mathrm{AdS}_5$, $e^{-2k|y|}$ is known as the warp factor, and $y$

denotes the fifth dimension. In a typical scenario the extra dimension is finite this space in bounded by two branes at each end. The ultraviolet brane is located at the Planck scale with $y = 0$ and the infrared brane at the TeV scale with $y = \pi R$.

The Standard Model fields are free to propagate the bulk between both branes. Typically, the Higgs and the top quark are close to the infrared brane, whereas all other quarks are near the ultraviolet brane. Thus the wavefunction overlap of the Higgs and top is significant, explaining the much larger coupling of the Higgs to the top than to other quarks. This localisation of the fields in the bulk is described by the bulk mass parameter $c$.

More explicitly, the 5-dimensional fermion fields can be decomposed as (see e.g. [80])

$$\Psi(x^\mu, y) = \frac{1}{\sqrt{2\pi R}} \sum_{n=0}^{\infty} \Psi^{(n)}(x^\mu) f_n(y). \tag{42}$$

$\Psi^{(n)}$ is the tower of KK excitations, where $n$ is again the level number. $R$ is the length of the extra dimension and $f_n$ is the corresponding wave function to the $n$th excitation. Note that even though the background metric is non-factorisable, the wave function solutions very well are. $f_n$ only depends on the 5th dimension and thereofore implicitly on the bulk mass parameter, whereas the KK tower only depends on the usual 4-dimensional space.

The actual mass spectrum and the couplings of the KK modes depends strongly on the bulk mass parameter, but also on the boundary conditions imposed on the two branes. The KK modes are typically close to the infrared brane, thus having a large wavefunction overlap with the top quark. $X_\mu$, which can be identified as the first KK excitation of the gluon as KK parity is absent in a Randall-Sundrum scenario, therefore decays preferentially to top quarks. The branching ratio is typically between 80% and 97%. The coupling of $X_\mu$ to quarks is given by [72]

$$g_L^{ij} \approx \frac{m_X}{\sqrt{2} M_{\mathrm{KK}}} \left( \frac{1}{\sqrt{2L}} \delta_{ij} - \sqrt{2R} F(c_{Q_i}) F(c_{Q_j}) \right) \tag{43}$$

for left-handed quark fields and

$$g_R^{ij} \approx \frac{m_X}{\sqrt{2} M_{\mathrm{KK}}} \left( \frac{1}{\sqrt{2L}} \delta_{ij} - \sqrt{2R} F(c_{q_i}) F(c_{q_j}) \right) \tag{44}$$

for right-handed quark fields. The ratio $m_X \approx 2.4 M_{\mathrm{KK}}$ is fixed by the aforementioned boundary conditions, and $c_{Q_i}$ ($c_{q_i}$) is the bulk mass parameter for left-handed (right-handed) quark fields of flavour $i$. The function $F(c)$ is known as the *profile function*

and derives from the wave functions $f_n$ in eq. 42. It can be expressed as [72]

$$F(c) = \mathrm{sgn}(\cos(\pi c))\sqrt{\frac{1+2c}{1-\epsilon^{1+2c}}}, \tag{45}$$

where $\epsilon$ is the ratio between the electroweak and Planck scale, $\epsilon = \Lambda_{\mathrm{Weak}}/\Lambda_{\mathrm{Pl}}$, and sgn is the signum function.

## 3.4 Extended Electroweak Sector

### 3.4.1 $Z'$

As most Standard Model extensions deal with larger gauge groups than the usual $SU(3) \times SU(2) \times U(1)$ of the Standard Model, the typical question is how this group is then broken down. In grand unified theories based on $SO(10)$ or $E_6$ it is possible to obtain the Standard Model gauge group with an additional $U(1)'$ symmetry. This leads to a $Z'$ boson in analogy to the Standard Model $Z$ boson.

But $Z'$ bosons cannot only be generated in grand unified theories. Models with extra dimensions like the Kaluza-Klein theory [81, 82] are also able to include $Z'$ bosons.

### 3.4.2 $W'$

$W'$ gauge bosons appear when the electroweak $SU(2)$ symmetry is accompanied by an additional $SU(2)$ gauge group. The $SU(2) \times SU(2)$ symmetry is then spontaneously broken to the diagonal subgroup $SU(2)_{\mathrm{EW}}$. This leads to an additional gauge boson, which is commonly called $W'$ in analogy to the Standard Model $W$ due to its similarity in origin and properties. As no new bosons are not discovered yet they are often assumed to have a mass of $\mathcal{O}(\mathrm{TeV})$.

As for the $Z'$, also $W'$ bosons can arise in other kind of models, for example in models with extra dimensions like the Kaluza-Klein theory [81, 82].

## 3.5 Gravitons

A graviton is introduced for example in models that assume the existence of extra dimensions. It can arise as a Kaluza-Klein excitation [81, 82], similar to a $W'$ or $Z'$, in a Randall-Sundrum model [75, 76]. Here, the graviton is the result of a variation

around the warped background metric, which can be written as

$$ds^2 = e^{-2k|y|} n_{\mu\nu} dx^\mu dx^\nu - dy^2 \,. \tag{46}$$

Here, $e^{-2k|y|}$ is a warp factor and $y$ denotes the additional 5th dimension. This extra dimension is a slice of an anti-de Sitter spacetime with strong curvature and is compactified. In the original Randall-Sundrum model the extra dimension is of finite length with two branes at each end, the infrared brane and the ultraviolet brane. The Standard Model fields are localised on the infrared brane, whereas the graviton exist in the bulk between both. The graviton is a spin-2 particle and couples to the Standard Model through the energy-momentum tensor of the matter fields.

## 3.6 Dark Matter Models

Looking at all the evidence, the need for a dark matter model becomes apparent. Some extensions like supersymmetry naturally provide dark matter candidates. But there are various different approaches to this issue and some of these concepts are briefly summarised in the following section.

### 3.6.1 WIMPs

WIMP is an acronym for Weakly Interactive Massive Particle and they are exactly that. They define a class of dark matter models, meaning that WIMP-like particles can be realised in various different kinds of Standard Model extensions, *e.g.* supersymmetry.

WIMP dark matter is especially attractive due to the so-called *WIMP miracle*. In order to be a viable dark matter candidate, today's relic abundance in the Universe needs to be matched. Although this depends strongly on the dark matter production mechanism, dark matter created after the Big Bang often needs to annihilate to deplete its number density. It turns out that particles at the weak scale have naturally the correct annihilation rate in order to match observations.

Specifically, their comoving number density can be regarded as constant today due to the so-called freeze-out mechanism. Put crudely, the freeze-out mechanism describes the process where at a certain point in time due to advanced annihilation but also the expansion of the Universe, dark matter particles will be so spread out that they cannot annihilate with each other anymore.

### 3.6.2 MACHOs

MACHOs are Massive Astrophysical Compact Halo Objects. Possible candidates are black holes, neutron stars, brown, white, or red dwarfs, and rogue planets, so all massive bound baryonic objects that do not emit any or only very little light. The idea is that they have a much larger abundance than initially thought and therefore account for the missing mass in various observations.

### 3.6.3 Axions

Axions were first introduced to address the strong CP problem [83, 84]. But furthermore, axions are a viable dark matter candidate.

The idea is to introduce a global U(1) symmetry, known as Peccei-Quinn symmetry [83, 84]. The symmetry is spontaneously broken by a complex scalar field and the associated Goldstone boson is the axion. This procedure effectively promotes the prefactor $\theta$ of the CP violating term $F_{\mu\nu}\tilde{F}^{\mu\nu}$ to a dynamical field, rendering it naturally small.

### 3.6.4 Asymmetric Dark Matter

Asymmetric dark matter denotes a class of models inspired by the baryon asymmetry puzzle (see for example ref. [85]). Motivated by the observation that the mass densities of visible matter and dark matter are similar, it assumes that both sectors are connected in some way. Since the visible sector shows an excess in particles over antiparticles, such an asymmetry could be connected to similar asymmetry in the dark matter sector.

This implies for dark matter candidates that the bulge of dark matter is made up of particles, whereas all antiparticles annihilated already. Thus the relic density can be naturally explained by the asymmetry between particles and antiparticles.

## 3.7 Hidden Sectors

Hidden sectors appear in a variety of Standard Model extensions and include particles that are somewhat decoupled from the Standard Model. Both, Standard Model and extension, are typically not charged under each others symmetries. Common examples are so-called dark photons and axion-like particles, the latter previously introduced for example in section 3.6.3.

### 3.7.1 Dark Photons

The dark photon $A'$ is associated with a new U(1) symmetry [86]. The relevant Lagrangian reads

$$\mathcal{L}_{A'} = \frac{1}{4} F'_{\mu\nu} F'^{\mu\nu} + \frac{1}{2} m_{A'} A'_{\mu} A'^{\mu}, \tag{47}$$

where $F'_{\mu\nu}$ is defined analogously to the field strength tensor $F_{\mu\nu}$ of the photon. The mass of the dark photon can range from completely massless to $\mathcal{O}(\text{GeV})$ and could, for example, be generated via a dark sector Higgs mechanism or the Stückelberg mechanism.

The Standard Model is not charged under this new symmetry but interacts with the dark photon via kinetic mixing,

$$\mathcal{L}_{\text{int}} = -\frac{\epsilon}{2} F'_{\mu\nu} F^{\mu\nu}. \tag{48}$$

In principle, there is also a kinetic mixing with the $Z$ boson, but this effect is suppressed by $m^2_{A'}/m^2_Z$. The latter is therefore of little phenomenological interest.

The kinetic mixing with the photon is particularly interesting, as it makes a massive dark photon unstable. Through the photon, a dark photon will decay to Standard Model particles. The dimensionless mixing parameter $\epsilon$ defines how fast this decay will happen and thus determines the lifetime of $A'$, whereas the $A'$ branching ratios are set by its mass.

We computed the branching ratios of the dark photon as a function of its mass. Here, one has to distinguish between two different regimes, above and below $m_{A'} \approx 2$ GeV. The boundary between these two regimes is related to the QCD hadronisation scale, as below approximately 2 GeV one has to describe the process as a decay to hadrons, whereas for above 2 GeV the decay is more conveniently described by quarks in the final state.

Below 2 GeV, the main decay channels are electrons and muons, the decay to taus being not kinematically allowed. Furthermore, several hadronic resonances appear, most dominantly those of the $\rho$, $\omega$, and $\phi$ meson.

The partial decay width to a pair of leptons of flavour $\ell$ is calculated straightforwardly as

$$\Gamma(A' \to \ell^+ \ell^-) = \frac{1}{3} \alpha \epsilon^2 m_{A'} \sqrt{1 - 4\frac{m^2_\ell}{m^2_{A'}}} \left(1 + 2\frac{m^2_\ell}{m^2_{A'}}\right). \tag{49}$$

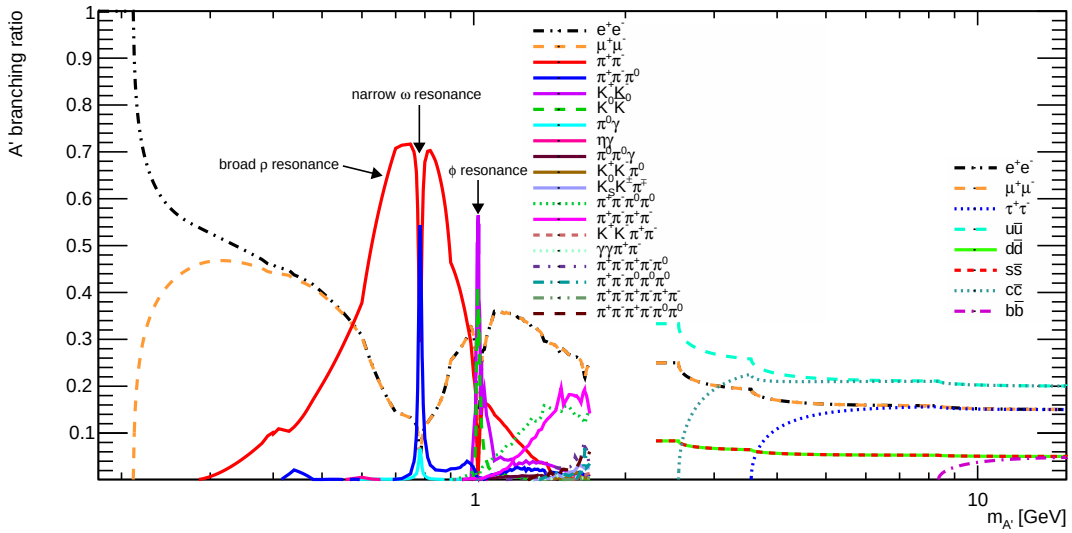


Figure 1: Branching ratios of the dark photon as a function of its mass. We included the 19 most dominant channels.

Determining the partial widths to hadrons is slightly more cumbersome, but can be done using a simple trick. The $A'$ decay is mediated by a photon, whose off-shellness corresponds to the mass of the dark photon. At an $e^+e^-$ collider off-shell s-channel photons are created, which subsequently decay. Their off-shellness is very well known, as it is the center-of-mass energy $\sqrt{s}$ of the collider. Thus by measuring the ratio $R(s)$ of $\sigma(e^+e^- \to \text{hadrons})$ to $\sigma(e^+e^- \to \mu^+\mu^-)$ at a given energy $\sqrt{s}$, one can unfold this measurement to obtain the dark photon decay widths,

$$\Gamma(A' \to \text{hadrons}) = \Gamma(A' \to \mu^+\mu^-)R(\sqrt{s} = m'_A). \tag{50}$$

We use the result of [87, 88] to calculate the hadronic partial widths and branching ratios accordingly. However, when extracting the hadronic cross sections care has to be taken to not double count hadronic degrees of freedom. This is due to heavier mesons with subsequent decays. Consider for example the $\omega$ meson which dominantly decays to $\pi^+\pi^-\pi^0$. If the $\omega$ mesons is produced via the decay $A' \to \omega\pi^0$ it subsequently contributes to the direct pion production channel $A' \to \pi^+\pi^-\pi^0\pi^0$.

To avoid this issue we treat decay channels on the level of pions and kaons instead of including heavier intermediate mesons. Exceptions are heavy mesons where no double counting occurs. We do, however, neglect decays of kaons to pions, as the corresponding branching ratio is very small.

For dark photon masses above 2 GeV it is possible to compute partial widths

completely analytical in terms of QCD language. For the partial width to quarks of flavour $q_f$ one can rescale the leptonic partial width by their electric charge $Q_{q_f}$ and the colour factor $N_c = 3$,

$$\Gamma(A' \to q_f \bar{q}_f) = N_c Q_{q_f}^2 \Gamma(A' \to \ell^+ \ell^-). \tag{51}$$

We present our results of dark photon branching ratios in fig. 1. Only for masses around the boundary, $m_{A'} \approx 2$ GeV, a large number of hadronic resonances appear. None of both regimes give an adequate description, thus we decided to leave an open gap.

Furthermore, it is possible to obtain the $A'$ lifetime $\tau$ from the partial widths shown above. From eq. 49 it is immediately obvious that it scales with $1/(\epsilon^2 m_{A'})$.

CHAPTER 4

# The Large Hadron Collider

The LHC is (most of the time) a circular proton-proton collider with design center-of-mass energy of 14 TeV. There are four main collision points, each surrounded by a different detector. Each of those detectors has its own science objective. The two detectors relevant for this dissertation are ATLAS and CMS.

This chapter will briefly introduce both detectors. We will, however, focus on phenomenological aspects, as they are crucial for this dissertation. Even though the technical details differ greatly between ATLAS and CMS, these are from a phenomenological point of view very similar. Therefore, even though with different technology, they are essentially measuring the same observables. Thus, instead of explaining *how* they measure it, I will focus on *what* they measure.

## 4.1 Detector Design

Both detectors, ATLAS and CMS, can be naïvely split into three distinct parts: inner detector, calorimeters and muon detector. ATLAS has a larger inner detector and calorimeters, whereas CMS is more compact. Instead, CMS has a slightly more precise muon spectrometer. Each of these components measures different properties of the majority of particles created in a collision.

### 4.1.1 Inner Detector

The main purpose of the inner detector is to track charged particles. Each particle with electric charge will leave a track, which will be curved due to an external magnetic

field. This provides information on the electric charge and energy of the particle.

Furthermore, the origin of these particles can be determined. Since at the LHC protons come in bunches, at each bunch crossing much more than just a single collision will take place. As all collision products are measured at the same time, it is important to assign each particle to a specific interaction vertex, called primary vertex. Thus the tracking chamber has a crucial role in disentangling the individual collisions.

### 4.1.2 Calorimeters

There are two different types of calorimeters present in ATLAS and CMS. The first, *i.e.* closest to the interaction point, is an electromagnetic calorimeter. All particles that can undergo a strong electromagnetic interactions will be detected, as they usually completely deposit their energy in this part of the detector. This concerns mainly electrons and photons. Muons, as well as charged hadrons, interact only weakly electromagnetically, thus will leave a trace in the electromagnetic calorimeter. However, their radiation length is large enough to transverse the complete calorimeter almost undisturbed.

The second kind of calorimeter follows immediately after the electromagnetic calorimeter. It is a hadronic calorimeter, targeting hadrons interacting via the strong nuclear force. All hadrons, whether charged or neutral, will be absorbed in the material and their energy can be accurately measured. Muons will also leave a slight trace in this part, but again traverse basically undisturbed.

### 4.1.3 Muon Spectrometer

The outermost part of the ATLAS and CMS detector is the muon spectrometer. All particles of the Standard Model are usually absorbed in the calorimeter, with the exception of muons and neutrinos. The latter, however, interact so weakly that they will not be detectable at all and leave the detector without any trace. The muon spectrometer instead measures the energy of only muons, but with very high precision.

## 4.2 Object Reconstruction

Each component described in the last section yields information on the majority of particles. But in order to analyse the events, all information has to be pieced together. Therefore, objects are identified and reconstructed from the underlying data using different techniques, which will be briefly summarised in the following.

Great emphasis is on introducing jet substructure techniques for boosted objects, as their understanding will be crucial for some parts of this dissertation.

### 4.2.1 Leptons and Photons

Photons, $e^+$ and $e^-$ are disentangled by using combined information from the inner detector and the electromagnetic calorimeter. Muons are straightforwardly reconstructed in the muon spectrometer. Taus, on the other hand, decay so fast that only their decay products can be measured. Neutrinos interact too weakly to be detected and are only visible as so-called missing (transverse) energy[1].

### 4.2.2 Jets

The final state particles of a hard process in a LHC collision are often quarks and gluons. But those are not measured directly as they hadronise quickly. The result is a directed jet of particles, dominated by charged pions, photons from $\pi^0$ decays and protons. For most analyses it is important to have access to the original quark, thus an algorithm is necessary to group the measured final state particles together. The result is called a jet, which serves as a good proxy for the original quark.

There are several algorithms in use, the most common ones are called $k_T$ [89], anti-$k_T$ [90] and Cambridge/Aachen [91]. These algorithms group together particles according to their transverse boost and respective angular separation. They differ by how they weight the different geometrical characteristics. The only input parameter to those algorithms is the cone size $R$, which defines the angular size of the jet.

### 4.2.3 Jet Substructure

Jet substructure techniques [92–96] are used if a heavy object like a $W$, $Z$, $h$, or $t$ decays into quarks. If the parent particles are boosted, their decay products will be close in space, typically with an angular separation of $\Delta R \approx 2m_X/p_T$, where $m_X$ is the parent mass and $p_T$ its transverse momentum. If those quarks hadronise, their respective jets start to overlap, thus making it difficult for a normal jet reconstruction algorithm to disentangle them.

This is *per se* not an issue if one is interested only in the transverse momentum of the parent particle. In this case, it is sufficient to just sum up all jets and one has not to worry about the overlap. Typically though one would like to know more about the origin, especially whether the jet just reconstructed is indeed coming from the decay of a boosted $W$, $Z$, $h$, ..., or just a normal quark or gluon. The latter two are

[1] Even though it is often referred to as *missing energy*, what is actually meant is *missing momentum*.

dominating the LHC, whereas the heavy objects are usually occurring in searches for new physics. Thus a discrimination is crucial.

The goal of jet substructure techniques is to resolve this issue. Most start with reconstructing a normal jet with very large angular size, called a *fat jet*. The jet radius $R$ is chosen such that all final state particles from the decay and subsequent hadronisation of the parent particle are included. Then one or several algorithms are applied.

On one hand, they try to clean the fat jet from soft radiation to enhance the resolution of the invariant mass of the jet. This mass peak should be around the mass of the parent particle but is in practice very broad and slightly shifted due to detector and reconstruction effects. On the other hand, these algorithms try to determine whether the fat jet has a two-prong structure, *i.e.* has two overlapping subjets, or not. Both helps to discriminate the jet against QCD background.

Several techniques were developed in the past, optimised towards a good tagging efficiency of two-prong jets while simultaneously minimising the mistagging rate of QCD jets[2]. They are also used to discard pile-up contamination from secondary interactions [97, 98]. In the following, we will summarise some of the most important techniques used later on.

#### 4.2.3.1 Mass-Drop Filter

The input to the mass-drop filter technique [92] is a fat jet reconstructed with the Cambridge/Aachen [91] algorithm. The idea is to *uncluster* the jet in reverse order, which means that a jet is split into two subjets at each step. Those two subjets are then verified to fulfil two conditions, explained below, in which case the algorithm is stopped. If they do not fulfil the criteria the softer subjet is discarded from the event and the unclustering continues on the harder jet, if possible.

The first condition is the so-called mass-drop, which requires both subjets to fulfil $\mu_i \equiv m_i/m_0 \leq \mu_f$. $\mu_f$ is a given input parameter, $m_i$ the subjet mass and $m_0$ the mass of the original fat jet.

The second criteria is a momentum balance condition. It is critical for jet substructure techniques as it helps discarding QCD jets. If a jet has a proper two-prong structure, one expects to find two subjets which are reasonably well balanced in their transverse momentum. There should not be a strong hierarchy between both sub-

[2] Jets originating from a quark or gluon.

jets, although some models favour this kinematical feature. A QCD jet, however, is expected to have only a single subjet and all other subjets that the algorithm might pick up are just a relic of soft radiation. Therefore, one expects a large imbalance in transverse momentum for QCD jets.

Basically all jet substructure techniques use this particular feature in one way or the other, although it is sometimes hidden in the structure of the algorithm.

The mass-drop filter imposes

$$\sqrt{y} = \min(p_{T_1},\ p_{T_2})\frac{\Delta R}{m_0} \geq \sqrt{y_{\min}}\ , \tag{52}$$

where $\Delta R$ is the angular distance between both subjets and $y_{\min}$ a free parameter. In order to see that this is indeed a requirement on the subjet momentum balance we have to rewrite the above equation using the relation

$$m_0^2 = 2p_{T_1}p_{T_2}\left(\cosh(\Delta\eta) - \cos(\Delta\phi)\right) \approx p_{T_1}p_{T_2}(\Delta R)^2\ . \tag{53}$$

$\Delta\eta$ and $\Delta\phi$ are the pseudo-rapidity and azimuthal separation with $\Delta R = \sqrt{(\Delta\phi)^2 + (\Delta\eta)^2}$. We additionally used the approximation that the angular separation is small. This yields

$$y \approx \frac{\{\ \min(p_{T_1},\ p_{T_2})\}^2}{p_{T_1}p_{T_2}} = \frac{p_{T,\,\min}}{p_{T,\,\max}} \geq y_{\min}\ , \tag{54}$$

thus the parameter $y$ is indeed a measure for the momentum imbalance.

#### 4.2.3.2 Jet Pruning

While the mass-drop filter reverses the clustering procedure of original fat jet recursively, the jet pruning method [99, 100] does the opposite. It reclusters the fat jet using the Cambridge/Aachen technique, thus starts at the other end of the jet clustering algorithm. At each step, two criteria are applied on the two subjets in question. Only if both criteria are fulfilled the softer subjet is not discarded. Thus the fat jet is *pruned* by discarding soft constituents from the event. The algorithm continues until all constituents of the original fat jet are either included or discarded.

The first condition is a requirement on the the *hardness* $z$ of the softer subjet. It is defined as

$$z = \min\left(\frac{p_{T_i}}{p_{T_p}}, \frac{p_{T_j}}{p_{T_p}}\right)\ , \tag{55}$$

where $p_{T_p}$ is the sum of transverse momentum of the two subjets $i$ and $j$. $z$ has to be larger than some minimum value $z_{\min}$.

This requirement is again a condition on the subjet momentum balance discussed earlier. This can easily be seen by relating $z$ and $y$ via

$$y \approx \frac{p_{T,\,\min}}{p_{T,\,\max}} = \frac{z}{1-z} \ . \tag{56}$$

As before, this relation is only approximate since we assume the angular separation between the subjets to be small.

In addition to the momentum balance criteria the two subjets have to be close in angular distance. This is parameterised by the $D_{\text{cut}}$ parameter, given by

$$\Delta R < D_{\text{cut}} \equiv \frac{m_{\text{orig}}}{p_{T,\,\text{orig}}} \ . \tag{57}$$

$m_{\text{orig}}$ and $p_{T,\,\text{orig}}$ are the mass and transverse momentum of the original fat jet.

#### 4.2.3.3 Jet Trimming

The trimming procedure [101] differs slightly from the previous algorithms as it does not consider pairs of subjets. Instead, it reclusters the fat jet with the $k_T$ algorithm and a very small cone radius of $R = 0.2$. All subjets $j$ are kept which satisfy

$$\frac{p_{T_j}}{p_{T_J}} > z_{\min} \ , \tag{58}$$

all others are discarded. Here, $J$ denotes the fat jet. This is again an equivalent to a requirement on a subjet momentum balance if an idealised fat jet with exactly two subjets is considered, according to

$$y \approx \frac{p_{T,\,\min}}{p_{T,\,\max}} \geq y_{\min} = \frac{z_{\min}}{1-z_{\min}} \ . \tag{59}$$

#### 4.2.3.4 $N$-Subjettiness

$N$-subjettiness [102, 103] is a set of variables that are designed to measure the number of *prongs* of a fat jet. $N$-subjettiness itself works on the level of jet constituents and is defined as

$$\tau_N = \frac{1}{d_0} \sum_k p_{T_k} \, \min(\Delta R_{1,k}, \ldots, \Delta R_{N,k}) \ . \tag{60}$$

$p_{T_k}$ is the transverse momentum of the $k$th constituent and $d_0 \equiv \Sigma_k p_{T,k} R_0$ a normalisation factor with $R_0$ as the cone size of the fat jet. $\Delta R_{n,k}$ is the angular distance to the $n$th subjet axis. The parameter $N$ defines the number of subjets taken into account. Subjets are determined by reclustering the fat jet with the $k_T$ algorithm and halting the reclustering when $N$ distinguishable subjets are formed.

To test a fat jet for a two-prong structure the ratio $\tau_{21} = \tau_2/\tau_1$ is computed. This ratio is typically high for 1-prong jets, but low for those with a 2-prong structure.

#### 4.2.3.5 Energy Correlation Function

An alternative to the $N$-subjettiness variable are energy correlation functions [104–106]. They do not require the reconstruction of any subjet, thus are independent of any jet clustering algorithm. The three relevant 1-point, 2-point and 3-point correlation functions are

$$\begin{aligned} e_1^{(\beta)} &= \sum_{1 \le i \le n_J} p_{T_i} \ , \\ e_2^{(\beta)} &= \sum_{1 \le i < j \le n_J} p_{T_i} p_{T_j} \Delta R_{ij}^{\beta} \ , \\ e_3^{(\beta)} &= \sum_{1 \le i < j < k \le n_J} p_{T_i} p_{T_j} p_{T_k} \Delta R_{ij}^{\beta} \Delta R_{ik}^{\beta} \Delta R_{jk}^{\beta} \ , \end{aligned} \tag{61}$$

where the sum is over fat jet constituents. The free parameter $\beta$ defines how much emphasis is given to the angular separation of constituents over their respective hardness. Those correlation functions are then combined to the ratio function

$$D_2^{(\beta)} = \frac{e_3^{(\beta)} \left(e_1^{(\beta)}\right)^3}{\left(e_2^{(\beta)}\right)^3} \ , \tag{62}$$

which yields typically small values for a jet with 2-prong structure and large values for QCD jets with a 1-prong topology.

CHAPTER 5

# Flavour Violating Couplings of the Higgs

## 5.1 Motivation

As we have seen previously in section 3.2.1, the Higgs boson can develop flavour violating couplings only if its vev is not the only source of electroweak symmetry breaking. The discovery of such a coupling would therefore be an immediate hint for new physics and a dedicated search is subsequently very compelling.

So far we used a 2HDM to demonstrate the possible existence of flavour changing couplings and will continue to do so in this chapter. But note that this is not the only possible Standard Model extension that leads to such kind of coupling. They have been studied also in context of warped extra dimensions [107–111], supersymmetric models [21, 42, 112–114], models aiming to explain the flavour structure of the Standard Model [115–120], and neutrino masses [21, 121–123], models with vector-like fermions [124], leptoquark models [125, 126], flavoured dark matter models [127], and composite Higgs models [42, 128].

Flavour changing couplings have also been studied in connection with a possible new source of CP violation [39]. Various search strategies have been proposed for the quark sector [129–133] and lepton sector [29, 30]. In a more model independent way flavour changing Higgs couplings can also be generated using dimension-6 operators

like

$$\mathcal{Q}_d^{ij} \equiv \overline{Q_L^i} H d_R^j (H^\dagger H)\,, \tag{63}$$

$$\mathcal{Q}_u^{ij} \equiv \overline{Q_L^i} \tilde{H} u_R^j (H^\dagger H)\,, \tag{64}$$

$$\mathcal{Q}_\ell^{ij} \equiv \overline{L_L^i} H e_R^j (H^\dagger H)\,. \tag{65}$$

As before $Q_L^i$ and $L_L^i$ are the left-handed fermion doublets, $d_R^j$, $u_R^j$, $e_R^j$ the right-handed fermion singlets, and $H$ the Higgs doublet with $H \equiv i\sigma^2 H^\dagger$.

Possible sources of flavour violating Higgs couplings are thus plenty, but the obvious question is how could we measure them. Of course there have been plenty of existing studies, constraining both couplings in the lepton and quark sector.

In the quark sector, measurements of anomalous rare meson decays and anomalous contributions to neutral meson mixing [134, 135] are sensitive to couplings which do not involve the top quark. The bounds are strong enough that couplings other than $htu$ and $htc$ are not considered accessible at the LHC anymore.

In the lepton sector, flavour violating decays like $\tau \to \mu\gamma$ and $\tau \to 3\mu$ would point towards the existence of the couplings $h\tau\mu$ or $h\tau e$ [26, 29]. Similarly, the non-existence of the low-energy decays $\mu \to e\gamma$ and $\mu \to 3e$, as well as $\mu \to e$ conversion in nuclei, constrain the couplings $h\mu e$. Although none of these measurements were able to confirm the existence of such couplings, the interactions $h\tau\mu$ and $h\tau e$ are still considered viable at the LHC.

In summary, the only couplings that are not already tightly constrained are those involving the top or $\tau$. In addition the simultaneous presence of $h\tau\mu$ and $h\tau e$, as well as $htu$ and $htc$ is also ruled out by precision measurements [29]. We can therefore focus on these two types of couplings.

The above constraints are all based on indirect measurements where the coupling in question is attached to a loop. At the LHC, however, more direct measurements are possible. By looking at single Higgs production with a subsequent decay to a $\tau\mu$ pair. By measuring the invariant mass of this pair one could reconstruct the Higgs mass peak. This kind of search has been carried out by ATLAS [136] and CMS [17]. The CMS analysis reports a $2\sigma$ excess, which is a first hint that such a coupling could really exists. The subsequent ATLAS analysis does not show an excess but is consistent with both, the CMS measurement and the null hypothesis.

All constraints so far mentioned are based on couplings involving the Higgs. But as we have seen in chapter 3.2.1 the Higgs particle is not the only possibly relevant particle if flavour changing couplings are generated in a 2HDM. Specifically, the heavy

neutral Higgs boson $H^0$ is of interest for small mixing parameters $\alpha$. As we have seen the Standard Model like Higgs bosons $h$ has in this case naturally small but non-zero flavour changing couplings, in good agreement with observation. Instead, the heavy $H^0$ exhibits very large flavour changing couplings.

The idea of this chapter is that instead of focusing on searches based on couplings to $h$, it might be beneficial to look for a flavour changing coupling of $H^0$. This, of course, is not as model-independent as other searches, but as we will see yields much stronger limits on a 2HDM.

In addition, it is often much easier to look for flavour changing couplings of a $H^0$ boson instead of searching for a $H^0$ resonance in other decay channels. This is due to the fact that the Standard Model background is usually lower. Thus looking for a flavour changing coupling of a $H^0$ boson might very well offer the first sign of a 2HDM at the LHC.

The chapter is split into two parts. In the first section, we will focus on the lepton sector, looking for a $H^0 \to \tau\mu$ decay. The second section will consider the quark sector. Here, the flavour changing coupling will be in the production mode of a $H^0$ rather than its decay.

## 5.2 Lepton Sector: $H^0 \to \tau\mu$ Decay

A search for $H^0 \to \tau\mu$ is highly motivated by the CMS $2\sigma$ excess for $h \to \tau\mu$ [17]. The CMS search is in a way the simplest resonances search one can do. The resonance is produced and decays to well-known particles. Data is collected having these particles in the final state and their invariant mass is plotted. Using a statistical analysis one can look for a resonance peak in the typically smoothly falling background spectrum.

Collecting data with the correct final state particles is to first order independent of the resonance mass you are aiming for. Thus we can simply reuse the CMS analysis. It was designed to look for a resonance peak at $m_h = 126$ GeV, but CMS presents data far above this mass, especially where one would expect a $H^0$ resonance peak. In their data sample no particular feature is present at higher masses, but the non-existence can be translated into constraints on the 2HDM parameter space.

In order to determine bounds we first have to calculate the $H^0$ production rate and branching fractions. In addition, we will discuss indirect constraints on this type of model in order to put our bounds into a global context.

### 5.2.1 Reducing the Parameter Space

Before we can compute production cross sections and decay rates, we have to point out that the 2HDM type-III has with $\lambda_1,\ldots,\lambda_7$ and $\mu_1,\ldots,\mu_3$ a large number of parameters, see section 3.2.1. Assuming that all parameters are real, *i.e.* no CP violation, this spans a 10-dimensional space. Fortunately, there are a couple of constraints and simplifications one can do in order to reduce the number of parameters and subsequently to enhance the accessibility of this model.

First of all, we know that the potential must be bounded from below. This leads to the constraints

$$\lambda_1 > 0\,, \qquad \lambda_2 > 0\,, \qquad \lambda_3 > -2\sqrt{\lambda_1\lambda_2}\,, \qquad \lambda_3+\lambda_4-2\lambda_5 > -2\sqrt{\lambda_1\lambda_2}\,, \tag{66}$$

where $\lambda_5$ should be replaced by $|\lambda_5|$ if $\lambda_6 = \lambda_7 = 0$. Furthermore, we know that $|\lambda_j| \ll 4\pi$ for all $j = 1\ldots7$ must hold in order to have a perturbative theory. In addition, we obtain constraints by requiring tree level unitarity using 2HDMC [137].

By minimising the potential we already obtained two constraints, eliminating $\mu_1$ and $\mu_2$. Note that $\lambda_2$ is only relevant for the quartic coupling. Since we are not interested in Higgs self-interactions we can safely neglect this parameter. Another parameter can be eliminated by assuming $m_{A^0} = m_{H^\pm}$, which is preferred by custodial symmetry. This leads to the relation $\lambda_5 = \lambda_4/2$. Thus we are left with $\lambda_1$, $\lambda_3$, $\lambda_4$, $\lambda_6$, $\lambda_7$, and $\mu_2$.

A subset of these remaining parameters can be now expressed in term of physical quantities, giving

$$\lambda_1^{\pm} = \frac{m_{H^0}^2 + m_h^2 \pm \cos 2\alpha\,(m_{H^0}^2 - m_h^2)}{4v^2}\,, \tag{67}$$

$$\lambda_4^{\pm} = \frac{m_{H^0}^2 + m_h^2 - 2m_{H^\pm}^2 \mp \cos 2\alpha\,(m_{H^0}^2 - m_h^2)}{2v^2}\,, \tag{68}$$

$$\lambda_6 = -\sin 2\alpha\,\frac{m_{H^0}^2 - m_h^2}{2v^2}\,. \tag{69}$$

Note that $\lambda_1$ and $\lambda_4$ have two solutions. The $+$ $(-)$ solution is valid for $\cos\alpha < 0$ $(> 0)$. Since we require $\alpha$ to be small we will work with the $-$ solution. We illustrate the above relations in fig. 2.

From the left panel of fig. 2 we can see that for a reasonable choice of $\alpha$, the parameter $\lambda_4$ is only a function of $m_{H^0}$ and $m_{H^\pm}$. But more importantly, $\lambda_4$ typically yields $m_{H^0} \approx m_{H^\pm}$ if one requires $\lambda_4$ to be in the perturbative regime. Thus we assume $m_{H^0} = m_{H^\pm}$ as an approximation.

From the right panel of fig. 2 we can read of that $\lambda_1$ is well within the perturbative

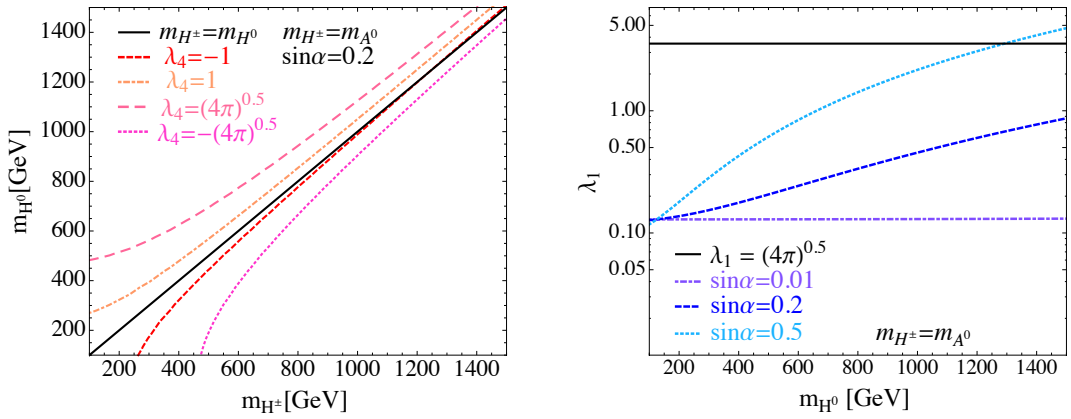


(a) (b)

Figure 2: *Left panel:* Contours of the mixed quartic coupling $\lambda_4$ as a function of the charged Higgs boson mass $m_{H^\pm}$ and the mass of the heavy CP-even neutral Higgs boson $m_{H^0}$. *Right panel:* The $\Phi_1$ quartic coupling $\lambda_1$ as a function the heavy Higgs boson masses, assuming $m_{H^0} = m_{H^\pm} = m_{A^0}$, for different values of the Higgs mixing $\sin\alpha$.

regime for reasonable choices of $\sin\alpha$ and a large range of possible $H^0$ masses.

In summary, all ten parameters can be reduced by using common constraints and some approximations to effectively four: $\sin\alpha$, $m_{H^0}$, $\lambda_3$, and $\lambda_7$. We additionally find that the $H^0hh$ coupling, defined in eq. 70, can be now expressed as

$$\begin{aligned} g_{H^0hh} &= 3\sin\alpha\cos\alpha\left(\frac{\lambda_7}{2}\sin\alpha - \lambda_1\cos\alpha\right) + \tfrac{1}{2}\left(\lambda_3+\lambda_4+2\lambda_5\right)\sin\alpha\left(3\cos^2\alpha - 1\right) \\ &\qquad + \tfrac{3}{2}\lambda_6\cos\alpha\left(1-3\sin^2\alpha\right) \\ &\simeq \sin\alpha\left(\lambda_3 - \frac{3m_{H^0}^2}{2v^2}\right) + \tfrac{3}{2}\lambda_7\sin^2\alpha + \mathcal{O}(\sin^3\alpha)\,. \end{aligned} \tag{70}$$

This is the only place where the parameters $\lambda_3$ and $\lambda_7$ appear. As we are not particularly interested in the $H^0hh$ couplings for now we can safely assume $\lambda_3 = \lambda_7 = 0$ for simplicity.

In terms of couplings we assume $\eta^{\mu\tau}_{\ell,2}$ and $\eta^{\tau\mu}_{\ell,2}$ to be the only non-zero elements of $\eta_{\ell,2}$. For simplicity, we additionally require them to be real and identical. As the $H^0$ boson will be – just like the Standard Model $h$ – dominantly produced through gluon fusion, the parameter $\eta^{tt}_{u,2}$ will be crucial and we, therefore, allow also this coupling to be non-zero. This assumes that $H^0$ has a similar coupling hierarchy to quarks as the Standard Model Higgs.

### 5.2.2 Indirect Constraints

The strongest indirect constraint comes from the rare decay $\tau \to \mu\gamma$ [26, 29, 138]. This kind of decay is mediated by loop-diagrams involving $h$, $H^0$, $A^0$, and $H^\pm$. When calculating these kind of diagrams one has to include 2-loop contributions as well, since 1-loop terms are suppressed by the small $\tau$ Yukawa coupling.

We quantify this constraint by working with the effective operators

$$\mathcal{L}_{\text{eff},\,\tau\to\mu\gamma} = c_L Q_{L\gamma} + c_R Q_{R\gamma}\,, \tag{71}$$

where we are following the notation of ref. [29, 39]. $c_L$ and $c_R$ are Wilson coefficients and the dimension-5 operators $Q_L$ and $Q_R$ are given by

$$Q_{L\gamma,R\gamma} = \frac{e}{8\pi^2} m_\tau \big(\bar{\mu}\sigma^{\alpha\beta} P_{L,R}\tau\big) F_{\alpha\beta}\,. \tag{72}$$

We take the loop diagrams involving only $h$ or $H^0$ from ref. [29] (adopted from [139]), whereas diagrams involving both $h$ and $H^0$ typically cancel out. This is due to the fact that each diagram contains one flavour violating and one flavour conserving Yukawa coupling. As we can see in eq. 20 those two components differ by a minus sign[1].

We identify the Yukawa matrices in the reference above with $y_{\ell,h}$ and $y_{\ell,H}$ from eq. 21 for leptons and with $y^{tt}_{u,h}$ and $y^{tt}_{u,H}$ from eq. 10 and 11. By replacing the up quark Yukawa couplings in the expression from ref. [29] by $-i\eta^{ij}_{u,2}/\sqrt{2}$ and the lepton Yukawa coupling by $i\eta^{ij}_{\ell,2}/\sqrt{2}$, we can calculate the $A^0$ contribution [43]. The only relevant diagram here is the 2-loop Barr-Zee diagram with a top-quark loop, as the $A^0$ does not mix with any other neutral Higgs boson. This is due to our assumption that all Yukawa couplings of $\Phi_2$ vanish except $\eta_2^{\mu\tau}$, $\eta_2^{\tau\mu}$, and $\eta_2^{tt}$.

Furthermore, we estimate the contribution of $H^\pm$ diagrams by using the crude assumption that these are of the same order as diagrams involving only $H^0$ or only $A^0$. We will, however, include the uncertainty of this assumption in our plots.

### 5.2.3 LHC Constraints

One constraint on the model parameter space comes from the direct CMS search for $h \to \tau^\pm\mu^\mp$ [17]. The combined branching ratio has to be smaller than 1.51% at 95% confidence level (CL), which translates into $\sqrt{|\eta_2^{\mu\tau}|^2 + |\eta_2^{\tau\mu}|^2}\sin\alpha < 0.0050$ according to eq. 23. The best fit value due to the excess is $\text{BR}(h \to \tau\mu) = (0.84^{+0.39}_{-0.37})\%$.

This constraint is given as a bound on the branching ratio $\text{BR}(h \to \tau\mu)$, but what CMS technically determines is a bound on $\sigma(pp \to h) \times \text{BR}(h \to \tau\mu) \times A_h$. Since the

[1] The only exception being diagrams with $h$ or $H^0$ coupled to a top quark loop when $(m_t/v)\sin\alpha < \eta_2^{tt}/\sqrt{2}$.

Higgs production cross section $\sigma(pp \to h)$ and the detector and analysis acceptance $A_h$ is known this can easily be unfolded.

Since our goal is to reuse the existing CMS analysis by replacing $h$ by $H^0$, we need to subsequently know $\sigma(pp \to H^0)$, $\mathrm{BR}(H^0 \to \tau\mu)$, and $A_{H^0}$. The latter is to be determined by a recast of the CMS analysis, whereas the others are to be calculated analytically. Only then we can determine the bound on $\sigma(pp \to H^0) \times \mathrm{BR}(H^0 \to \tau\mu) \times A_{H^0}$ and translate it into a constraints on the model parameter space.

Since the only relevant coupling in our setup of $H^0$ to quarks is given by $\eta_2^{tt}$, the dominant production mode is gluon fusion. As the relevant diagram is very similar to the Standard Model gluon fusion process, we can obtain the production cross section via the relation

$$\sigma(pp \to H^0) \simeq \left(\sin\alpha - \eta_2^{tt} \cos\alpha \frac{v}{\sqrt{2} m_t}\right)^2 \times \sigma(gg \to h)\big|^{\mathrm{SM}}_{m_h = m_{H^0}} . \tag{73}$$

The first term proportional to $\sin\alpha$ is due to the mixing of the two CP even states $h_1$ and $h_2$. The term proportional to $\cos\alpha$ is cause by the direct coupling of $h_2$ to the top quark, thus weighted by $\eta_2^{tt}$. $\sigma(gg \to h)\big|^{\mathrm{SM}}_{m_h = m_{H^0}}$ is the production cross section of the Standard Model Higgs, rescaled by $m_h = m_{H^0}$ [140]. We provide the $H^0$ production cross section in fig. 3 and the dominant branching fractions in fig. 4 for different choices of model parameters.

The above relation of the production cross sections is of course only true if $H^0$ couples only to the top. This is a very good approximation for the Standard Model Higgs, but might not be entirely accurate for the heavy Higgs. In this case, other quarks will contribute too and add the extra term

$$-\eta_2^{qq} \cos\alpha \frac{v}{\sqrt{2} m_t} \times \frac{f(4m_q^2/m_{H^0}^2)}{f(4m_t^2/m_{H^0}^2)} \tag{74}$$

in the squared parentheses of eq. 73. Here, $\eta_2^{qq}$ is the Yukawa coupling of the extra quark $q$ to the second Higgs doublet $\Phi_2$. $f(x) = x[1 + (1-x)F(x)]$ is a loop function [141–143], where $F(x)$ is given by

$$F(x) = \begin{cases} \arcsin^2(1/\sqrt{x}) & \text{for } x \geq 1 \\ \frac{1}{2}\left[\log\left(\frac{1+\sqrt{1-x}}{1-\sqrt{1-x}}\right) - i\pi\right]^2 & \text{for } x < 1 \end{cases} . \tag{75}$$

However, we will not consider the possibility of an extra contribution for simplicity.

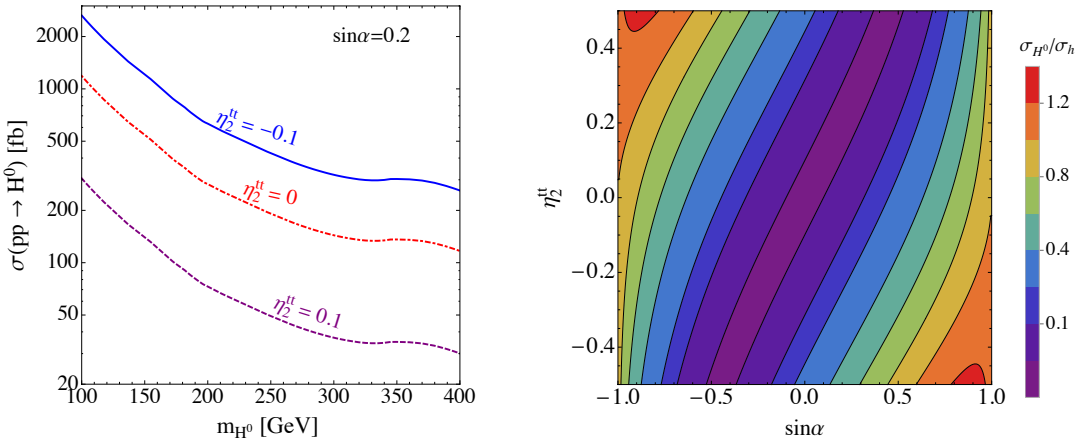


(a) (b)

Figure 3: (a) The production cross section of the heavy neutral Higgs boson $H^0$ via gluon fusion (see eq. (73)) as a function of $m_{H^0}$ and for different choices of Yukawa couplings. The shape of the curves follows that of the SM Higgs production cross section as given in [140]. (b) Ratio of the $H^0$ production cross section to the production cross section of the Standard Model Higgs at the same mass as a function of the neutral Higgs boson mixing angle $\sin\alpha$ and the Yukawa coupling of the second Higgs doublet to top quarks, $\eta_2^{tt}$. This ratio is independent of $m_{H^0}$.

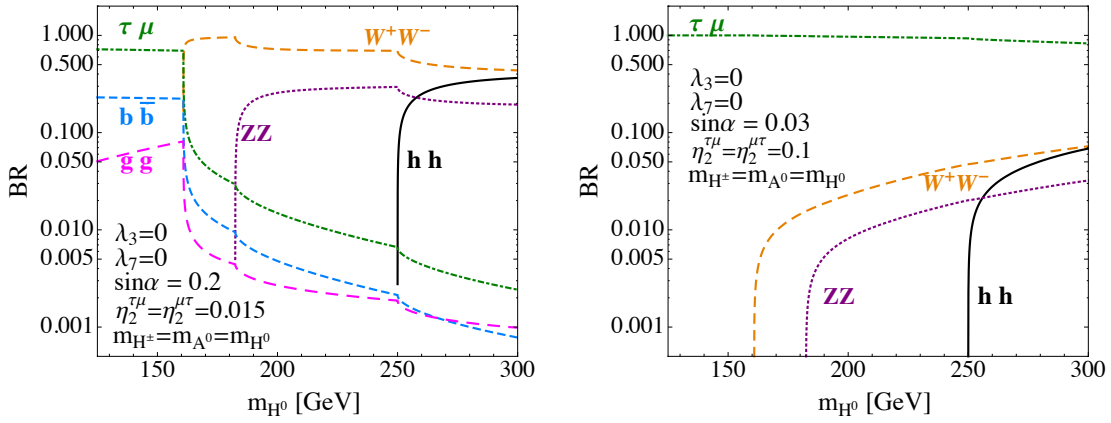


(a) (b)

Figure 4: Branching ratios of the heavy neutral CP-even Higgs boson $H^0$ as a function of its mass $m_{H^0}$ for two different parameter points of the lepton flavour violating 2HDM. We assume here a scenario with large lepton flavour violation in the $\mu$–$\tau$ sector, as expressed by the Yukawa couplings $\eta_2^{\mu\tau}$, $\eta_2^{\tau\mu}$ of the second Higgs doublet.

Next, we need to determine the efficiency $A_{H^0}$ by recasting the CMS analysis [17] and comparing the event yield with the respective background. For this, we simulate parton level signal events with proper leading order cross section using MadGraph 5 v2.3 [144]. As the CMS search includes categories with several jets in the final state we are generating inclusive samples. Parton shower, MLM jet matching and hadronisation are then implemented by Pythia 6.4 [145] with a jet matching scale of $q = 30$ GeV. To properly account for detector effects we pass the events to Delphes 3.1.2 [146]. We will keep on using this simulation setup for the rest of the chapter.

We apply the CMS analysis cuts on these events and carefully reconstruct the collinear resonance mass $m_{\mu\tau}^{\text{coll}}$. CMS presents its results in six different channels. They consider two decay channels of the tau, $\tau \to e\nu_\tau\bar{\nu}_e$ and $\tau \to$ hadrons. A decay to muons suffers from large backgrounds from for example $Z \to \mu\mu$ production, as the flavour violation is transferred onto the invisible neutrinos. For both channels, they divide the sample into subcategories depending on the number of extra jets in the final state.

CMS considers up to two additional jets, however, we will restrict ourselves to only up to one additional jet. First, properly simulating additional jets is a difficult task for technical reasons and second, the category with two additional jets provides only little statistical power.

The resonance mass $m_{\mu\tau}^{\text{coll}}$ is denoted *collinear* as it is determined using approximations. A leptonic $\tau$ decay yields two neutrinos of which only their combined transverse momentum is measured. The invariant mass is then obtained assuming that both neutrinos are collinear to the electron, which is a fair approximation due to the large Lorentz boost of the $\tau$ [147].

In case of a hadronic $\tau$ decay the difficulty is in distinguishing the resulting jets from a quark or gluon initiated jets. This is done using sophisticated algorithms that identify typical decay products of a hadronic $\tau$ decay by combining information from the calorimeters and the tracker in the inner detector [148]. These decay products are usually one or three charged hadrons and zero or more short lived neutral hadrons, together with a neutrino.

As we use the CMS search unmodified we can refer to their background estimation. The hadronic channel with $\tau \to$ hadrons, denoted by $\tau_h$, is dominated by background events coming from fake leptons. The leptonic channel with $\tau \to e\nu_\tau\bar{\nu}_e$, denoted by $\tau_e$, suffers from backgrounds coming from $Z \to \tau\tau$, diboson production, and fake leptons. In those channels with multiple additional jets in the final state the $t\bar{t}$ backgrounds contributes too.

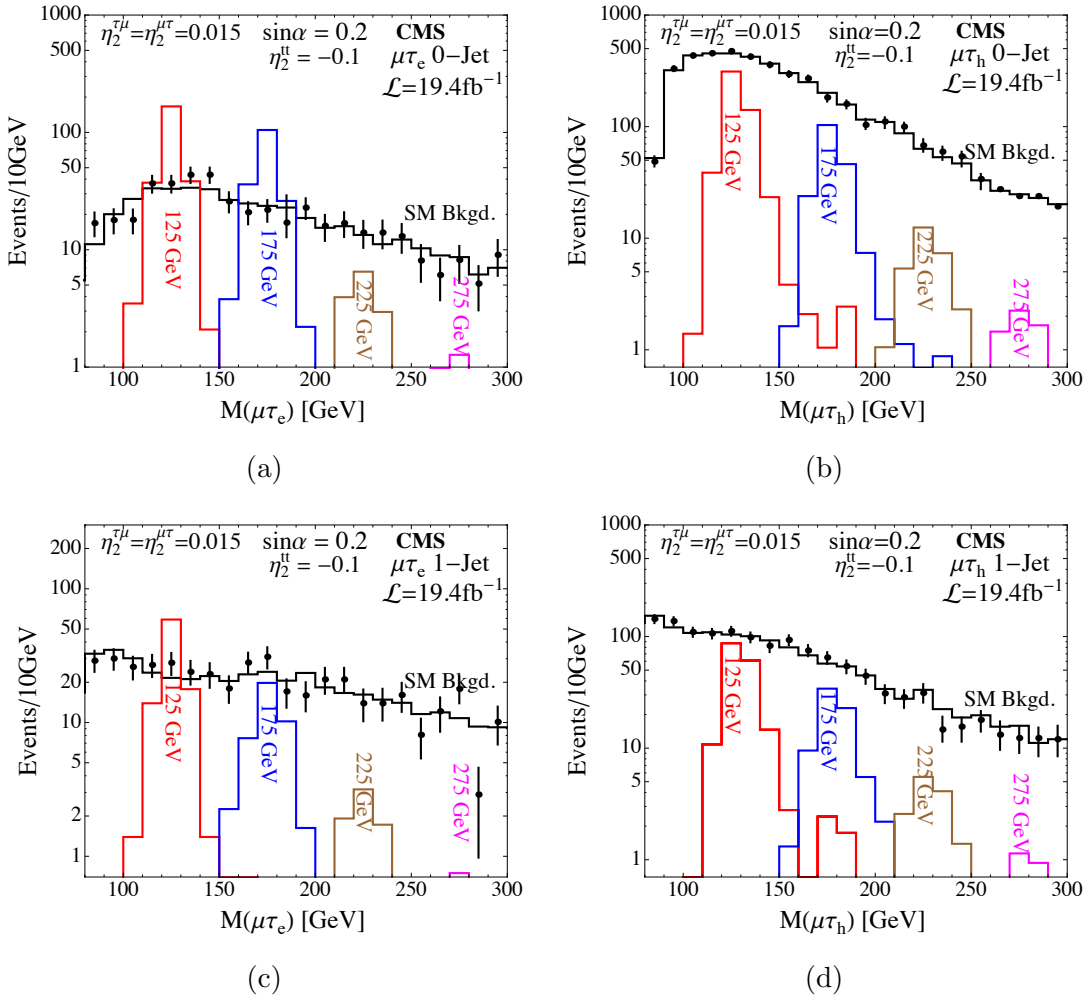


Figure 5: Distribution of the collinear mass $m_{\mu\tau}^{\text{coll}}$ after cuts for the SM background from the CMS analysis in [17] for various values of $m_{H^0}$ of our signal. The panels on the left are for events with leptonic $\tau$ decays $\tau \to e\nu\nu$, denoted here as $\tau_e$, while the panels on the right include only events with $\tau \to$ hadrons, denoted as $\tau_h$. In the upper row we show events with no additional jets with $p_T > 30$ GeV, $|\eta| < 4.7$, while in the bottom row we require exactly one such jet.

We compare our obtained signal events for various $m_{H^0}$ masses with the CMS background contribution [17] in fig. 5. We can immediately read off that we can obtain competitive limits for about $m_{H^0} \lesssim 250$ GeV, whereas for larger masses $\sigma \times \text{BR}$ is simply too small. To obtain proper limits on $\sigma \times \text{BR}$ we run a 95% confidence level test [149]. We verify our setup by using $m_{H^0} = 125$ GeV and $\sin\alpha = 1$, which is equivalent to the Standard Model-like Higgs used in the CMS analysis. The limit we obtain is about 15% weaker than that of CMS, which is due to our negligence of the 2-jet category.

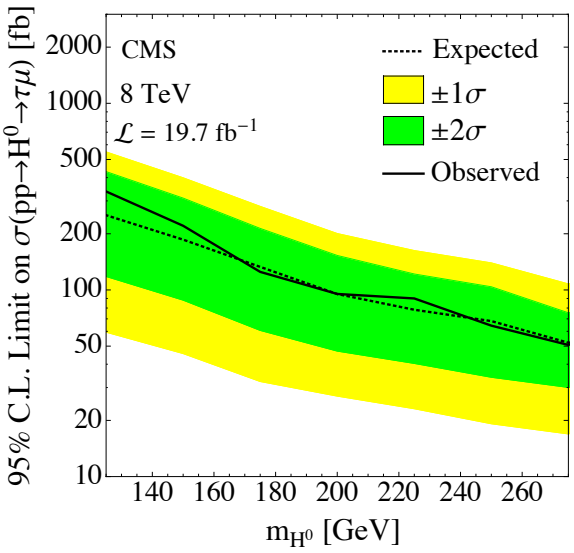


Figure 6: 95% CL limit on $\sigma(pp \to H^0) \times \mathrm{BR}(H^0 \to \tau\mu)$ signal as a function of $m_{H^0}$, obtained by recasting the results from the CMS search in [17]. We also include the $\pm1\sigma$ and $\pm2\sigma$ bands.

We present our expected and observed bounds on $\sigma \times$ BR in fig. 6. These bounds are translated into constraints on the model parameter space of the 2HDM in fig. 7. We present the result as a function of two parameters while keeping the others fixed. Additionally, the results with the indirect constraints from the $\tau \to \mu\gamma$ search and the direct CMS results for the bound on $h \to \tau\mu$, as well as the respective best fit point due to their excess in events, are overlaid.

One can see that our limits are stronger than direct or indirect constraints for very low masses of $H^0$. Especially, it excludes the CMS best fit point in this regime, which means that if this excess would be true, it cannot be explained by the 2HDM using our setup. For higher masses our recast is not competitive anymore, as the branching fraction for $H^0 \to \tau\mu$ drops rapidly as soon as a decay to a pair of $W$'s is kinematically allowed at $m_{H^0} > 2m_W$.

The strongest limits are obtained if either $\sin\alpha$ is small, as $\mathrm{BR}(h \to \tau\mu)$ and $\mathrm{BR}(\tau \to \gamma\mu)$ are suppressed; or if $\eta_2^{tt}$ is negative, as it adds to the $\sin\alpha$ contribution with the same sign in eq. 73 instead of canceling it off.

## 5.3 Quark Sector: $H^0tq$ Coupling

In the previous section, we have seen how we can obtain new information about a possible 2HDM with lepton flavour violating couplings by simply looking for a

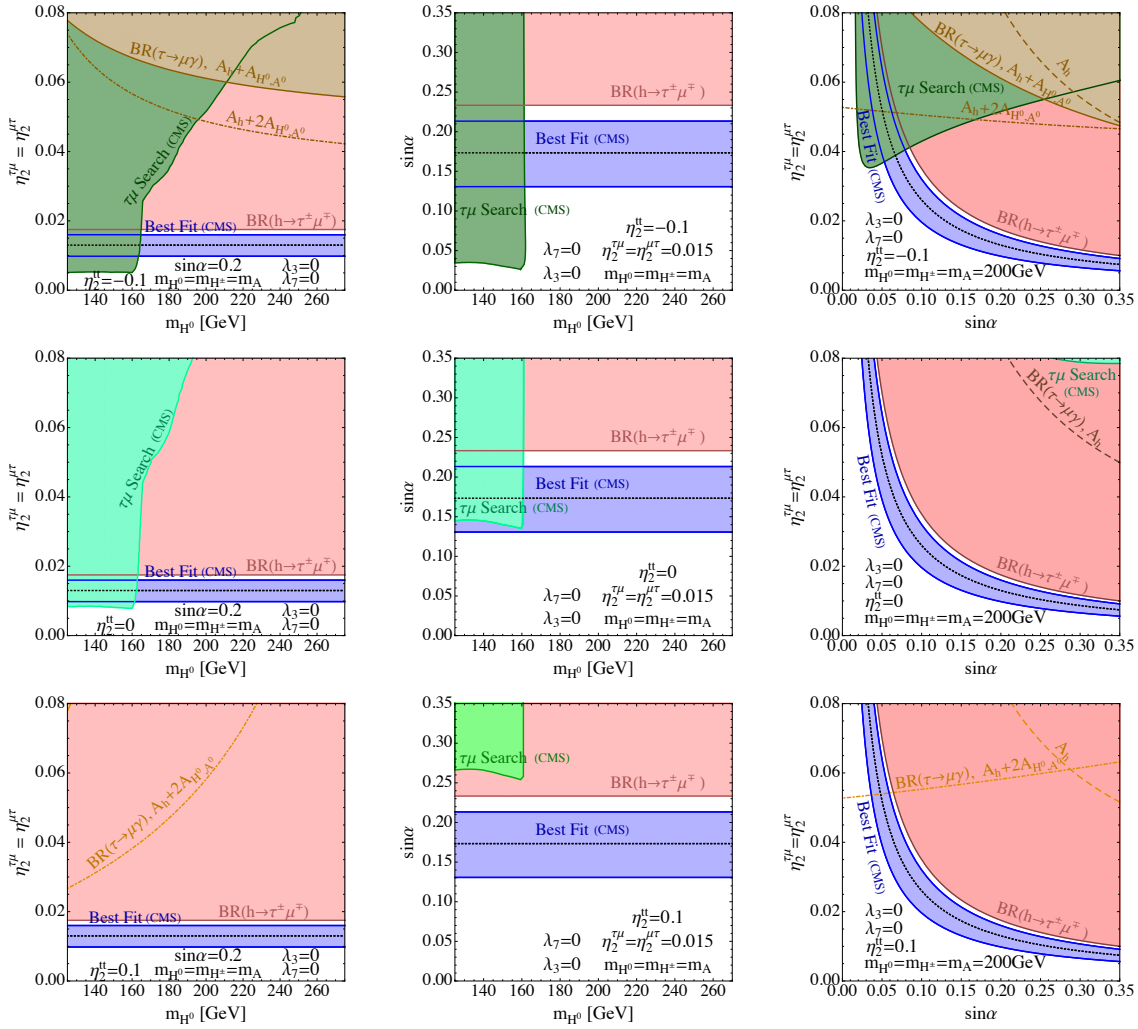


Figure 7: 95% CL constraints on the parameter space of the 2HDM. We show results from our search for $H^0 \to \tau\mu$ based on recasting and reinterpretation of the CMS analysis in [17] (green contours), from the same CMS search for $h \to \tau\mu$ (red exclusion regions and blue $1\sigma$ preferred regions) [17], and from $\tau \to \mu\gamma$ limits (brown/orange). For the $\tau \to \mu\gamma$ amplitude, we estimate that the contribution $A_{H^\pm}$ of diagrams involving $H^\pm$ is of the same order as the contribution $A_{H^0,A^0}$ of diagrams involving $H^0$ or $A^0$ (solid curves, shaded regions). The uncertainty of this rough approximation is estimated by also showing the constraint in case the $H^\pm$ contribution is twice as large (dot-dashed curves) or cancels $A_{H^0,A^0}$ exactly (dashed curves). Note that typically not all of these curves are visible within the chosen plot ranges. The panels on the left show constraints on the heavy Higgs mass $m_{H^0}$ and the flavour violating Yukawa coupling $\eta_2^{\mu\tau} = \eta_2^{\tau\mu}$, the panels in the middle column show $m_{H^0}$ vs. the neutral Higgs mixing $\sin\alpha$, and the panels on the right display $\sin\alpha$ vs. $\eta_2^{\mu\tau} = \eta_2^{\tau\mu}$. The three rows of plots correspond to different values of the top quark Yukawa coupling $\eta_2^{tt}$ to the second Higgs doublet $\Phi_2$. This coupling affects $H^0$ production through gluon fusion and the two-loop contributions to $\tau \to \mu\gamma$.

resonance peak in the $\tau\mu$ collinear mass spectrum measured by CMS.

This section will use the same 2HDM setup but instead employs flavour changing couplings in the quark sector. This means we enable couplings of the kind $htu$, $htc$, $H^0tu$, and/or $H^0tc$. However, a simple search like $h/H^0 \to \tau\mu$ is not possible.

First of all, the Higgs bosons $h$ is lighter than the top, thus we actually need to look for the rare top decay $t \to hu$. This search has already been done.

But as in the lepton sector, our goal is to look for flavour changing couplings of the $H^0$ boson as they are naturally larger than those of $h$. The decay $H^0 \to tu$ is in principle possible, depending on the mass of $H^0$. But a top-up final state is difficult to identify due to large backgrounds from single-top and $t\bar{t}$ production. Also flavour tagging of quarks is not very efficient and in any case only possible for heavy quarks.

Thus incorporating the flavour changing coupling in the decay of $H^0$ is not viable. But instead we can use it in the production mode. The parton distribution function (PDF) of the top is basically zero, thus the only viable production mode including the flavour changing coupling is $gu \to tH^0$. In principle, we can replace $u$ by $c$, but this process will be suppressed by the $c$ quark PDF. We will, therefore, focus on the couplings $htu$ and $H^0tu$.

This process will have a reasonable cross section and is. depending on the subsequent decays of $H^0$ and $t$, relatively easy to identify.

### 5.3.1 Existing Constraints

Before we can define benchmark points for our new search, we need to be aware of current constraints on the quark flavour violating 2HDM.

The most stringent constraint comes from the search for the rare decay $t \to qh$. The relevant 95% CL limits determined by ATLAS [150, 151] are

$$\mathrm{BR}(t \to ch) < 0.0046 \qquad \text{and} \qquad \mathrm{BR}(t \to uh) < 0.0045. \tag{76}$$

One can translate above limits into

$$\sqrt{|y^{ct}|^2 + |y^{tc}|^2} < 0.13 \qquad \text{and} \qquad \sqrt{|y^{ut}|^2 + |y^{tu}|^2} < 0.12 \tag{77}$$

using the leading order branching ratio [132] together with the next-to-leading order (NLO) QCD correction factor $\eta_{QCD} \simeq 1 + 0.97\alpha_s = 1.10$ [132, 152] according to

$$\mathrm{BR}(t \to hq) = \frac{|y^{tq}|^2 + |y^{qt}|^2}{2\sqrt{2}G_F} \frac{(m_t^2 - m_h^2)^2}{(m_t^2 - m_W^2)^2(m_t^2 + 2m_W^2)} \eta_{QCD} \simeq 0.29\big(|y^{tq}|^2 + |y^{qt}|^2\big)\,. \tag{78}$$

Using the relations from the previous section this can be related to $\eta_2^{tq}$, $\eta_2^{qt}$, and $\sin\alpha$. The above bound could be improved by incorporating the $pp \to th$ channel. This is only relevant for the $thu$ coupling again due to the $c$ quark PDF suppression and would yield roughly $\sqrt{|y^{ut}|^2 + |y^{tu}|^2} < 0.08$ [132].

CMS obtains very similar but slightly weaker limits than ATLAS. Their limit at 95% CL reads $\mathrm{BR}(t \to hq) < 0.0056$ for $q = u, c$, which translates into $\sqrt{|y^{qt}|^2 + |y^{tq}|^2} < 0.14$ [153–155].

Same-sign top production through a $t$-channel Higgs exchange is another way of testing these couplings. By recasting the CMS same-sign dilepton+$b$-jet search [156], ref. [157] was able to derive limits on $\sqrt{|y^{qt}|^2 + |y^{tq}|^2}$. They are, however, weaker than those from rare top decays.

In addition, anomalous di-Higgs production, mediated by a t-channel top, constrains in principle flavour changing couplings of the Higgs. But since this production mode scales with four powers of the already small couplings $y^{tq}$ and $y^{qt}$, the cross section is small: $\sim 4$ fb at $\sqrt{s} = 8$ TeV and $\sim 7.4$ fb at $\sqrt{s} = 13$ TeV. This production mode is, therefore, irrelevant for all practical purposes.

All limits mentioned so far involve only the $h$ boson, thus are independent of the mechanism which induces flavour violating couplings. Since we are working in a 2HDM the additional field content leads to further constraints.

Low energy flavour experiments impose strong limits, but mainly on those processes involving lighter quarks. Neutral meson mixing and radiative $b$ quark decays, however, are still relevant. $B_d - \bar{B}_d$ mixing involves a $t - H^\pm - W$ loop and limits of $|\eta_2^{tu}| \lesssim \mathcal{O}(1)$ and $|\eta_2^{ut}| \lesssim \mathcal{O}(0.01)$ can be derived [134, 135]. Due to the strong limit on $\eta_2^{ut}$ we will set this coupling to zero. With only $\eta_2^{tu}$ turned on, the only remaining bounds are coming from LHC searches.

Flavour changing couplings of the heavy $H^0$ boson contribute to a few channels inducing same-sign lepton final states. This includes of course the $pp \to tH^0$ production mode as discussed before. But also $h$ and $H^0$ t-channel exchange in the same-sign top production process $pp \to tt$ is possible. Note that both processes only involve $t$, but not $\bar{t}$ as the latter would need to involve sea quarks, whereas the first comes from the more likely valence quarks. Furthermore, a process $pp \to th$ is irrelevant as it is suppressed by $\sin^4\alpha$, but also because $h$ cannot decay to on-shell gauge bosons.

We recast the relevant di-lepton+$b$-jet searches of CMS [156] and ATLAS [158]. The limits are presented as a function a few model parameters in fig. 8. The CMS search yields better limits than the ATLAS search, even though it uses with 10.5/fb less integrated luminosity than ATLAS with 14.3/fb. The reason is that CMS splits

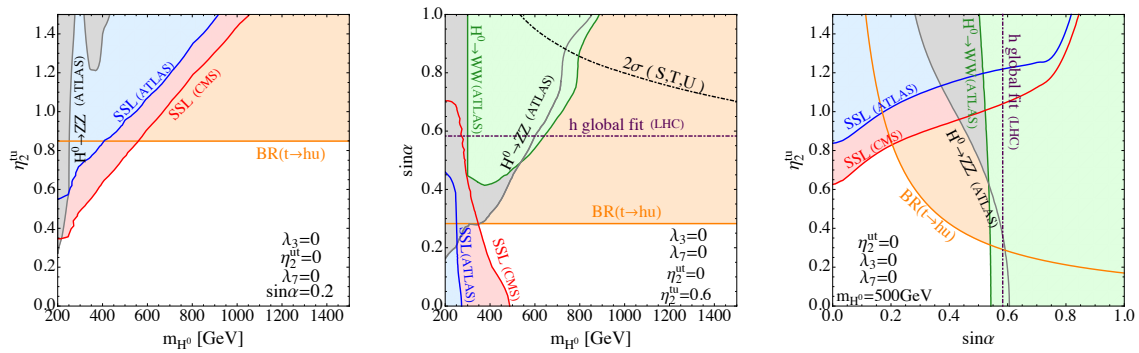


(a) (b) (c)

Figure 8: 95% CL constraints on the 2HDM parameter space as a function of the heavy Higgs mass $m_{H^0}$, the flavour violating Yukawa coupling $\eta_2^{tu}$ of the second Higgs doublet $\Phi_2$, and the mixing angle $\sin\alpha$. We show results from recasting the same-sign di-lepton (SSL) + $b$-jet searches in ATLAS [158] (blue) and CMS [156] (red), from ATLAS searches for heavy Higgs bosons in the $H^0 \to WW, ZZ$ final states [159, 160] (green, grey), from the ATLAS search for $t \to hq$ [151] (orange), from a global fit to the data on the Standard Model-like Higgs boson (purple dot-dashed line in panels (b) and (c)) [161], and from electroweak precision data (black dot-dashed curve in panel (b)) [137].

its event sample into two signal regions with either two positive or two negative leptons. Our signal contributes only to one of these two signal regions, thus by combining them as ATLAS harms the overall efficiency.

Furthermore, we expect constraints coming from direct searches for $H^0$ decays to $WW$ and $ZZ$ [159, 160, 162, 163]. We will focus on recasting the respective ATLAS searches [159, 160], as they employ 20/fb of integrated luminosity of 8 TeV data, whereas CMS searches [163] are older and therefore based on less data: 5.1/fb at 7 TeV and 5.3/fb at 8 TeV.

These searches target not only flavour violating production modes such as $pp \to tH^0, \bar{t}H^0$ but also the gluon fusion process. As the latter is still possible even if $\eta_2^{tu}$ is zero, non-trivial limits are expected.

The $H^0 \to ZZ$ search [160] is separated into different signal regions optimised towards the gluon fusion and vector boson fusion (VBF) production mode, respectively. ATLAS also distinguishes between the different $WW$ decay channels $4\ell$, $2\ell 2\nu$, and $2q2\ell + 2q2\nu$.

The most sensitive category is the VBF category with four leptons in the final state. As our dominant production mode is often $pp \to tH^0$, except at very small flavour violating couplings, we naturally find a lot of extra jets in the final state. The gluon

fusion channel, however, requires a low jet multiplicity, thus the loose cuts in the VBF $4\ell$ channel boost the sensitivity.

In the ATLAS $H^0 \to WW$ search [159] the event samples are again split into different production modes. The gluon fusion channel requires $N_j = 0$ or 1, whereas VBF requires $N_j \geq 2$. Here, ATLAS purifies the VBF event sample by imposing strong cuts on the invariant jet mass $m_{jj} > 500$ GeV in addition to their pseudo-rapidity difference $|\Delta\eta_{jj}| > 2.8$. The majority of our signal events would not pass these cuts, therefore we restrict ourselves to a recast of the gluon fusion channel.

In addition, we checked that constraints from non-resonant di-Higgs production via $u\bar{u} \to hh$ can be neglected. ATLAS [164] determines a 95% CL limit on its production cross section of 0.69 pb, which translates into $\eta_2^{tu} \sin\alpha < 1.09$. This is much weaker than the limit derived from the $t \to hq$ decay.

The mixing angle $\sin\alpha$ is furthermore constraint by Higgs global fit data. The mixing angle suppresses the decay rates of $h \to WW$ and $h \to ZZ$ by $\cos^2\alpha$, thus upper bounds can be derived from the measured branching fractions. A global analysis yields $\sin^2\alpha < 0.34$ at 95% CL [161].

Similarly, the modified Higgs sector influences electroweak precision data. By using the oblique parameters $S$, $T$, and $U$ [165–167] and employing the program 2HDMC [137] we find that those constraints are very weak. This is mainly due to the fact that our 2HDM setup assumes $m_{H^0} = m_{A^0} = m_{H^\pm}$ and therefore does not violate custodial symmetry.

We present all bounds described in this section superimposed in fig. 8.

### 5.3.2 Benchmarks

To illustrate the behaviour of our search in the following section, it is of advantage to define two different benchmark points and describe how the limits are changing once we depart from these points. Based on current exclusion limits shown in fig. 8 we decide to use $\sin\alpha = 0.2$ for both benchmarks.

The two parameters $\lambda_3$ and $\lambda_7$ affect only the $g_{H^0hh}$ coupling, see eq. 70. Since $\lambda_7$ enters only at $\mathcal{O}(\sin^2\alpha)$ we will ignore this parameter for simplicity. The dominant parameter in this expression is $\lambda_3$ as it contributes already at $\mathcal{O}(\sin\alpha)$.

Please note that both, $\lambda_3$ and $\lambda_7$, control only the $H^0 \to hh$ decay width, but keep other decay rates untouched, as well as the $H^0$ production rate. We find that for positive values of $\lambda_3$ the respective branching ratio of $H^0 \to hh$ is suppressed due to a partial cancellation between the term proportional to $\sin\alpha$ and the $\sin^2\alpha$ term. Accordingly, for negative values of $\lambda_3$ this branching ratio is enhanced. For our

| | Benchmark 1 | Benchmark 2 | Comments |
|---|---|---|---|
| $\sin\alpha$ | 0.2 | 0.2 | see fig. 8 |
| $\eta_2^{ut}$ | 0 | 0 | $b \to d\gamma$ constraint |
| $\eta_2^{tu}$ | 0.6 | 0.6 | see fig. 8 |
| $\lambda_7$ | 0 | 0 | enters $g_{H^0hh}$ only at $\mathcal{O}(\sin^2\alpha)$ |
| $\lambda_3$ | 0 | $-3$ | influences $g_{H^0hh}$ |
| $m_{A^0}$ | $m_{H^\pm}$ | $m_{H^\pm}$ | preferred by custodial symmetry |
| $m_{H^\pm}$ | $m_{H^0}$ | $m_{H^0}$ | preferred by perturbativity (see fig. 2 (b)) |

Table 1: Benchmark points for the quark flavour violating 2HDM.

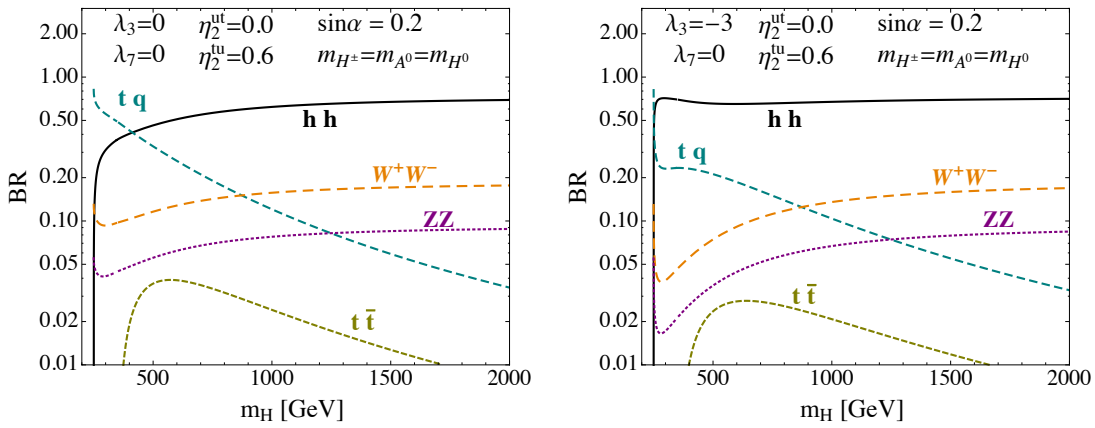


Figure 9: The branching ratios of the different $H^0$ decay modes for two different parameter points of the 2HDM as described in the text.

benchmarks, we assume the two values $\lambda_3 = 0$ and $\lambda_3 = -3$.

As mentioned before, we use $\eta_2^{ut} = 0$ due to the strong constraints from meson mixing. $\eta_2^{tu}$ instead is set to 0.6, which is close to the current upper limits, see again fig. 8.

We summarise our two benchmark points in tab. 1. We additionally derive the branching fraction of $H^0$ for both benchmark points, presented in fig. 9. We can clearly see that a flavour changing decay $H^0 \to tq$ dominates only at small $H^0$ masses, whereas the decay to heavy gauge bosons takes over quickly as soon as it is kinematically allowed. The decays $H \to WW,\ ZZ,\ hh$ rise so quickly since their rates scale with the third power of $m_{H^0}$, namely $m_{H^0}^3/v^2$.

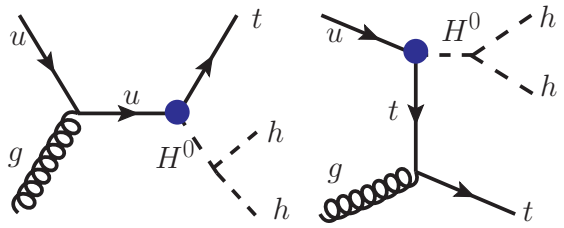


Figure 10: The Feynman diagrams for the process $pp \to t + (H^0 \to hh)$ in the 2HDM. The blue dot indicates the flavour violating Yukawa coupling proportional to $\eta_2^{tu}$.

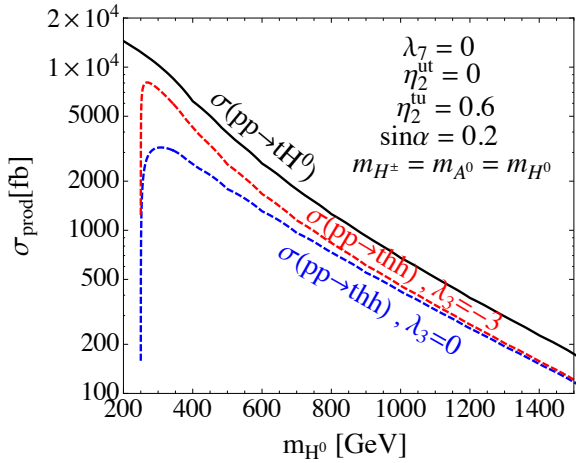


Figure 11: The production cross section of $H^0$ associated with a top (black solid curve), and the cross sections for the production + decay process $pp \to t + (H^0 \to hh)$ (red dashed and blue dashed curves). Production of $H^0$ is here dominantly mediated by the flavour violating Yukawa coupling $\eta_2^{tu}$.

### 5.3.3 *thh* Search

We previously discussed our goal to directly look for flavour changing couplings by using them in the $ug \to tH^0$ production mode. As seen in section 5.3.1 this production mode contributes already to various different LHC searches, but given our benchmark points a dedicated search can yield superior limits.

As shown in fig. 9 for a broad range of $H^0$ masses the subsequent decay $H^0 \to hh$ is dominant. Thus we are effectively facing a $thh$ final state, where the two Higgs bosons $h$ reassemble a $H^0$ resonance. The Feynman diagrams of this process can be found in fig. 10. We present the corresponding production cross section at $\sqrt{s} = 13$ TeV for both benchmark points in fig. 11.

The final state particles $t$ and $h$ will decay further. As we need to avoid the otherwise overwhelming QCD background we have to require at least one lepton at the end of the decay chain. As the Higgs bosons $h$ has only very small Yukawa couplings to

leptons, we consider only leptonic decays of the top, $t \to b\ell\nu$. For $h$ it is less obvious which decay will be favourable. We considered the dominant decays and respective combinations for both Higgs bosons. We found only the most dominant, $h \to b\bar{b}$, to be feasible. Other decays suffer from small branching ratios and the relative softness of the decay products. Thus the effective final state is $\ell + 5b + \not{E}_T$. Due to the large amount of $b$-jets the only relevant Standard Model background is $t\bar{t}$+jets.

We use the same simulation setup as in section 5.2. The $t\bar{t}$+jets background is additionally generated by SHERPA+OPENLOOPS [168–171] with zero or one extra jet at NLO and matrix elements with two or three additional jets at LO. Here, we treat $c$ and $b$ quarks as massive in the parton shower. To confirm that other background sources are negligible we simulate events of $V$ + jets, $VV'$ + jets, $t\bar{t} + V$, $t\bar{t} + h$ and single-top production, with $V, V' = W, Z$, using SHERPA + BLACKHAT [172]. The first of these processes is treated at NLO accuracy, while the others are generated at LO. The results confirmed that the only relevant background is $t\bar{t}$+jets.

First, we need to preselect objects. We require exactly one isolated and positively charged lepton with transverse momentum $p_T \geq 10$ GeV and pseudo-rapidity $|\eta| \leq 2.5$. We reconstruct jets using the anti-$k_T$ algorithm with a standard cone radius of $R = 0.5$. We require in total 5 jets with $p_T \geq 20$ GeV and $|\eta| < 2.5$. To account for the kinematics of our signal and to reduce the background further we apply cuts on the jets. Sorting jets by their transverse momentum we require $p_{T,j_1} > 140$ GeV, $p_{T,j_2} > 100$ GeV, and $p_{T,j_3} > 60$ GeV.

A good part of this analysis focuses on $b$-jets. Jets are b-tagged with a tagging efficiency of 70% and a light quark and gluon mistag rate of 1% [173, 174]. Although the final state includes five $b$-quarks, we require only four due to the limited tagging efficiency.

As the neutrino is the only source of missing energy, it can be reconstructed using the lepton and the on-shell condition for the $W$, $m^2_{\ell\nu} = m^2_W$, according to

$$p^z_\nu = \frac{1}{2p^2_{T\ell}}\left[(m^2_W + 2\vec{p}_{T\ell}\cdot\vec{\not{p}}_T)p^z_\ell \pm E_\ell\sqrt{(m^2_W + 2\vec{p}_{T\ell}\cdot\vec{\not{p}}_T)^2 - 4p^2_{T\ell}\not{p}^2_T}\right]. \tag{79}$$

$m_{\ell\nu}$ denotes the invariant mass of the reconstructed charged lepton and the neutrino, $E_\ell$ and $\vec{p}_{T\ell}$ the energy and transverse momentum of the charged lepton and $\vec{\not{p}}_T$ the missing transverse momentum.

The above equation has two solutions, which in general may be complex. We break this ambiguity when we assign each jet to a parent particle. This assignment is in any case necessary to reconstruct resonance peaks for the two $h$ bosons, the $H^0$ bosons and

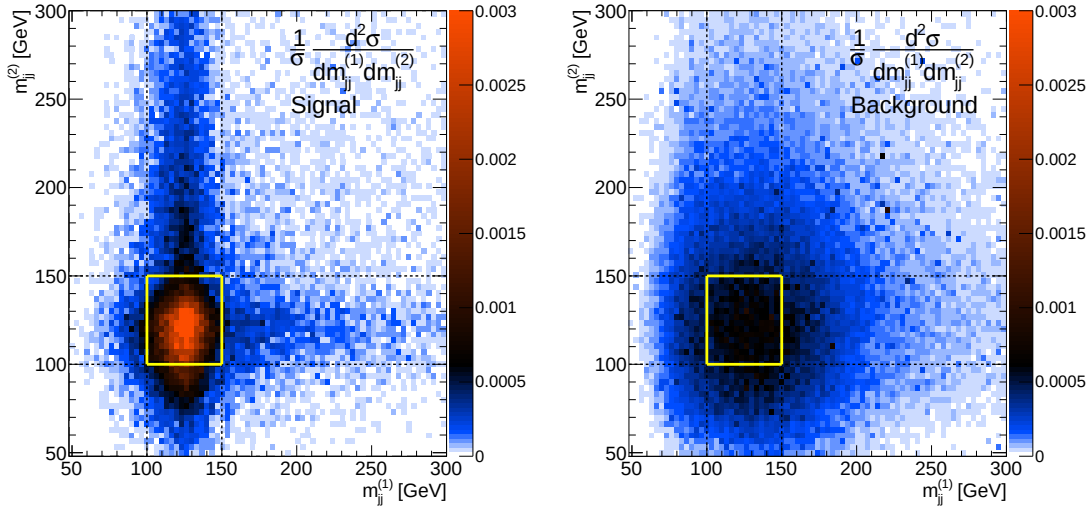


(a) (b)

Figure 12: Distribution of the reconstructed Higgs masses $m_{jj}^{(1,2)}$ for (a) $thh$ signal events simulated after integrating out $H^0$, and (b) $t\bar{t}$ background events. The yellow square indicates the invariant mass cuts imposed in our analysis.

the top in order to suppress background. Due to large combinatorics, this association is not trivial. We use a $\chi^2$ method by minimising the quantity

$$\chi^2 \equiv \frac{(m_{jj}^{(1)} - m_h)^2}{(\Delta m_h)^2} + \frac{(m_{jj}^{(2)} - m_h)^2}{(\Delta m_h)^2} + \frac{(m_{j\ell\nu} - m_t)^2}{(\Delta m_t)^2} \tag{80}$$

over all possible jet combinations and solutions for the neutrino momentum. As we expect only $b$-tagged jets in our signal, even though at reconstruction level this is not the case anymore, we do not differentiate anymore between $b$-tagged and non-$b$-tagged jets at this stage. For the uncertainties in eq. 80 we take $\Delta m_h = 12$ GeV (the mass resolution for $h \to b\bar{b}$ in CMS [1, 175]) and $\Delta m_t = 1.35$ GeV (the width of the top quark [167]). Varying these two parameters by $\mathcal{O}(1)$ changes the outcome only marginally.

To ensure a proper reconstruction of the two $h$ bosons and the top we apply cuts on their respective invariant masses, 150 GeV $< m_{j\ell\nu} <$ 200 GeV and 100 GeV $< m_{jj}^{(1,2)} <$ 150 GeV.

We illustrate the efficiency of this method in fig. 12. As the outcome depends to some extent on the kinematics of the system, thus on the mass $m_{H^0}$, we show this result with the heavy $H^0$ boson integrated out and normalised differential cross sections. This is equivalent to an effective theory approach. We show the differential

| cut | signal ($thh$) | background ($t\bar{t}$) |
|---|---|---|
| $\sigma_{\text{prod}}$ [fb] | 273.6 | $5.9 \times 10^5$ |
| preselection | 28.5% | 2.20% |
| $b$-tagging | 18.4% | 0.55% |
| $p_T^{j_1} > 140$ GeV | 90.6% | 31.1% |
| $p_T^{j_2} > 100$ GeV | 93.9% | 66.3% |
| $p_T^{j_3} > 60$ GeV | 97.3% | 84.6% |
| Higgs, top mass window | 14.3% | 8.6% |
| $p_T^{h_2} > 150$ GeV | 71.9% | 35.3% |
| $p_T^{h_1} > 200$ GeV | 94.4% | 90.3% |
| $0.9 \leq \Delta R_{b\bar{b}}^{\text{max}} < 2.1$ | 89.8% | 67.8% |
| $m_{H^0}$ mass window | 69.9% | 31.1% |
| $\sigma_{\text{final}}$ [fb] | 0.72 | 0.071 |

Table 2: Cut flow table for the $thh$ signal in the 2HDM with benchmark 1 as defined in tab. 1 and $m_{H^0} = 500$ GeV. If we use benchmark 2 instead, we find a signal cross section before cuts of $\sigma_{\text{prod}} = 192.9$ fb, and a signal cross section after cuts of $\sigma_{\text{final}} = 0.51$ fb. The cut efficiencies remain unchanged.

cross section after the $\chi^2$ method as a function of $m_{jj}^{(1)}$ and $m_{jj}^{(2)}$. We also integrated out the dependence on $m_{j\ell\nu}$ as both, signal and background, are containing top quarks, thus should trivially fulfil this requirement.

We can see how a clear resonance peak forms in the left-hand panel around the Higgs mass. The bands where only one invariant mass is near the resonance peak occurs when only one of the two $h$ bosons could be reconstructed properly. Due to large combinatorics, the background tends to be around the resonance peak, but is spread out.

After identifying the two $h$ bosons and the top we are applying further cuts. We found requiring $p_{T,h_1} > 200$ GeV and $p_{T,h_2} > 150$ GeV to be useful concerning background discrimination. Here, $h_1$ and $h_2$ are the two Higgs bosons ordered by transverse momentum. In addition, both $h$ bosons are originating from the same parent particle, thus are expected to be close in angular distance. No such correlation is expected for the background. Thus we impose $0.9 \leq \Delta R_{bb}^{\text{max}} = \max(\Delta R_{bb}^{h_1}, \Delta R_{bb}^{h_2}) < 2.1$. The lower bound is to avoid contamination from final state radiation.

Lastly, we make use of the $H^0$ resonance peak by combining both $h$ bosons, $|m_{hh} - m_{H^0}^{\text{test}}| < 0.1 m_{H^0}^{\text{test}}$, where $m_{H^0}^{\text{test}}$ is the $H^0$ mass to be tested.

We present the cutflow to this analysis in tab. 2. For this particular resonance mass $m_{H^0}$ the signal rate is about a factor of 10 larger than the $t\bar{t}$ background rate. Using this result we perform a statistical test using the $CL_s$ method [149] and assuming

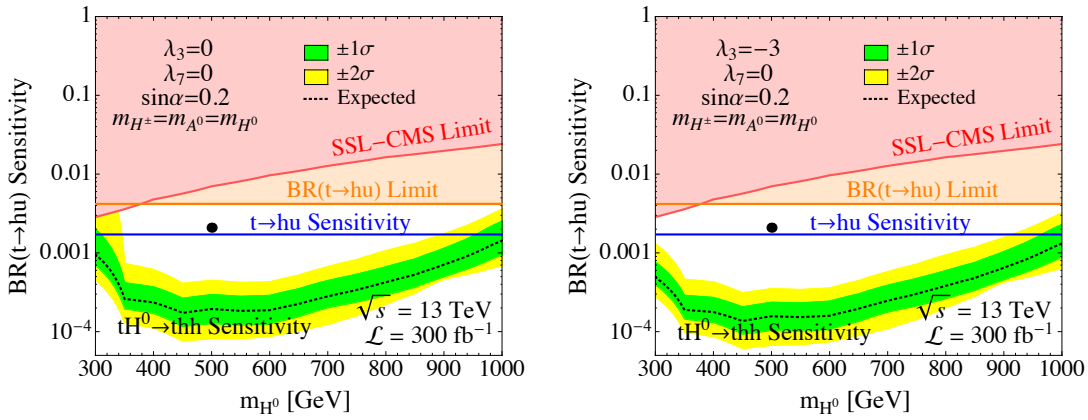


(a) (b)

Figure 13: In the context of the 2HDM, we show the 95% CL sensitivity of our proposed search for the $thh$ final state, expressed here in terms of the branching ratio of the decay $t \to hu$ (Brazilian bands). Comparing to the projected sensitivity of a direct search for the rare decay $t \to hu$ from [132] (horizontal blue lines), we find that the $thh$ search is more sensitive in a wide range of heavy Higgs masses $m_{H^0}$. For comparison, we also show the current limit on BR($t \to hu$) from ref. [151] (horizontal orange lines) and the current limits on $pp \to tH^0$ from a recasting of the CMS search for same-sign di-leptons (SSL) + $b$ jets [156] (red shaded regions). The black dots are the two benchmark points in table 1.

30% systematic uncertainty on the background and signal event samples. We consider 300/fb of integrated luminosity.

We scan over various masses of $H^0$ and show our result in fig. 13. We translated the upper bounds on the production cross section of $thh$ with appropriate branching ratios into an upper limit on BR($t \to hu$). To compare our result with existing searches we superimpose it with the current strongest limit from the rare top decay $t \to hu$, as well as its expected reach at same luminosity and $\sqrt{s}$ energy. For smaller masses the same-sign lepton search of CMS becomes comparable.

Our proposed search is sensitive to a large range of $H^0$ masses for both benchmark points. At low masses, it looses sensitivity as the branching ratio $H^0 \to hh$ becomes small. Here, a direct search for $H^0 \to tu$ might be interesting. For large masses above 1 TeV, the search is limited by the production cross section. The rare top decay search, of course, does not suffer from this problem. For a large range of $H^0$ masses our search is superior to any currently existing search, improving the result by about one order of magnitude.

## 5.4 Discussion

In this chapter, we discussed how flavour violating couplings to the Higgs appear when extending the Higgs sector. We discuss current constraints in both, the Higgs-lepton sector and the Higgs-quark sector. Basically, all of these constraints were limited to searches involving the Standard Model-like Higgs boson $h$.

Using a 2HDM type-III framework we have seen how flavour violating couplings are induced and that small couplings for $h$ typically imply large couplings for $H^0$. Since we know that they have to be small for $h$, this motivated a series of searches where we directly looked for flavour changing couplings involving $H^0$ rather than $h$.

In the lepton sector, we discussed a simple resonance search for $H^0 \to \tau\mu$. We were able to reinterpret the CMS search for $h \to \tau\mu$ [17] and obtain limits on the 2HDM model parameter space. We showed that these limits extend the reach of the direct $h \to \tau\mu$ search. This is of particular interest, as the CMS search showed an $2\sigma$ excess, indicating the existence of such a coupling. We were able to show that the best fit point of this excess can not be realised by some sets of 2HDM parameters.

In the quark sector, we developed a new search based on a $thh$ final state, where the two $h$ bosons are the product of a $H^0$ resonance. By reconstructing all intermediate invariant masses we are able to achieve a large signal to background ratio. Subsequently, the upper bounds on the branching ratio $\mathrm{BR}(t \to hu)$ are superior to direct search for the rare top decay $t \to hu$.

CHAPTER 6

# Pair Production of a Coloured Resonance

## 6.1 Motivation

We presented in the previous chapter a few examples of simple resonance searches. The invariant mass peak of a $H^0 \to \tau\mu$ resonance from a $\tau\mu$ final state was reconstructed, as well as several intermediate mass peaks in the more complex process $pp \to tH^0 \to thh$. These searches were motivated by a 2HDM framework, but we now want to move on to a different kind of Standard Model extension. We introduced in section 3.3 a massive colour octet vector $X_\mu$ and described in which scenarios such a particle appears. Concerning resonance searches the colour octet vector has very peculiar features.

The single production of $X_\mu$ is $q\bar{q}$ initiated, as no tree-level $ggX$ coupling exists[1]. The relevant Feynman diagram is shown in fig. 14. But as it involves the coupling between quarks and $X_\mu$ the process depends strongly on the gauge couplings, thus on the details of the model. Explicitly, for the coloron model the partonic production cross section can be approximated as

$$\sigma(q\bar{q} \to X) \approx \frac{8\pi^2 \alpha_s \tan^2\theta}{9 m_X} \delta\left(\sqrt{\hat{s}} - m_X\right), \tag{81}$$

[1] This would require higher-dimensional operators, which we can neglect.

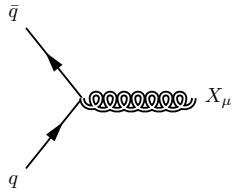


Figure 14: Feynman diagram for the single $X$ resonance production channel via a $q\bar{q}$ initial state. A $gg$ initiated production mode does not exist due to the absence of a $ggX$ coupling. Double curly lines represent the heavy octet vector.

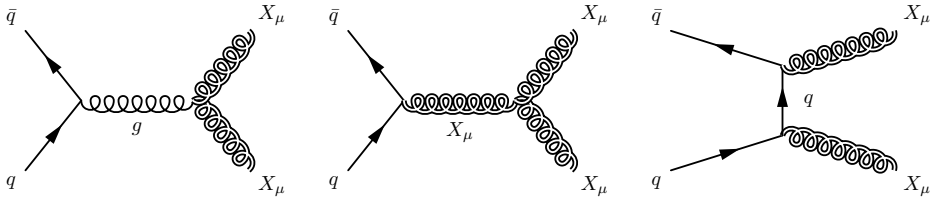


Figure 15: $s$- and $t$-channel Feynman diagrams for $XX$ pair production via a $q\bar{q}$ initial state. We do not show $u$-channel diagrams. Double curly lines represent the heavy octet vector.

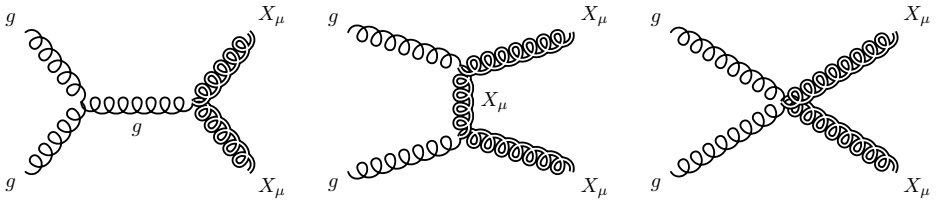


Figure 16: $s$- and $t$-channel Feynman diagrams for $XX$ pair production via a $gg$ initial state. We do not show $u$-channel diagrams. Double curly lines represent the heavy octet vector.

where $\hat{s}$ is the partonic center-of-mass energy. Eq. 81 is derived using the narrow width approximation. This cross section scales with $\tan^2\theta = h_1^2/h_2^2$, where $h_1$ and $h_2$ are the gauge couplings of the respective $SU(3)_1 \times SU(3)_2$ gauge fields. If the quark fields are charged differently under the parent $SU(3)_1 \times SU(3)_2$ gauge symmetry that strongly affects the $pp \to X$ production cross section.

The pair production process of $X_\mu$ behaves differently. Here, besides the $q\bar{q}$ initiated production channels depicted in fig. 15, the heavy octet vector pair can also be produced through a $gg$ initial state, see fig. 16. The process through a $q\bar{q}$ initial state still relies on the coupling of $X_\mu$ to quarks, but the $gg$ initiated process does not. This makes the $gg \to XX$ process independent of the details of the model, since its production cross section will depend only on the mass of $X_\mu$ and not on the details

of how quarks are charged under the new gauge symmetry. The relevant $gg$ initiated partonic production cross section can be expressed as [176]

$$\sigma(gg \to XX) = \frac{9\pi\alpha_s^2}{16\hat{s}^3}\left[\beta\hat{s}\left(\frac{8\hat{s}}{m_X^2} + 13\hat{s} + 34m_X^2\right) - 8\left(\hat{s}^2 + 3m_X^2\hat{s} - 3m_X^4\right)\ln\left(\frac{1+\beta}{1-\beta}\right)\right]. \tag{82}$$

Here, $\beta = (1 - 4m_X^2/\hat{s})^{1/2}$ denotes the boost of $X_\mu$.

Since the $q\bar{q}$ initiated process is PDF suppressed at the LHC, the $gg \to XX$ production channel will be dominant. Therefore, in contrast to the single $X$ production mode, the pair production process is almost completely model-independent. Thus a search for a pair produced heavy octet vector will yield very solid bounds, whereas limits from a single $X_\mu$ resonance search may be discussed away in a specific model context.

As a heavy octet vector decays to pairs of quarks, the final state for a pair produced resonance will be $(q\bar{q})(q'\bar{q}')$, where $q$,$q'$ can be any of the Standard Model quarks. ATLAS and CMS performed searches for pair produced resonances in a four jet final state, where the jet can originate from all quarks but the top. In addition, they searched in a $t\bar{t}t\bar{t}$ final state for heavy octet vectors. The overall relevant cross section $\sigma \times \mathrm{BR}$ in the first search scales as $(1 - \mathrm{BR}(X \to t\bar{t}))^2$, whereas the second search scales as $\mathrm{BR}(X \to t\bar{t})^2$. Thus, the searches are sensitive if $\mathrm{BR}(X \to t\bar{t})$ is either very large or very small. For intermediate values of $\mathrm{BR}(X \to t\bar{t})$ however, none of the searches will be optimal.

This motivates an analysis for a mixed final state $(t\bar{t})(JJ)$, where $J$ is a container for all quarks but the top. In the following we will present such a search and obtain limits on the branching ratios of $X_\mu$ as a function of its mass. We discuss existing limits on the heavy octet vector in section 6.2, which we can compare to our search. The $(t\bar{t})(JJ)$ analysis itself is described in section 6.3 and 6.4 for a semi-leptonic and fully leptonic decay of the $t\bar{t}$ pair, respectively. We present our results in section 6.5 and summarise this chapter in section 6.6.

## 6.2 Collider Limits

A flavour-conserving heavy octet vector $X$ can be probed at the LHC via single resonance production and pair production. As the pair production cross section is model-independent, the process depends only on the decay branching ratios. Therefore, we want to focus purely on limits on the branching ratio $\mathrm{BR}(X \to JJ) = 1 - \mathrm{BR}(X \to t\bar{t})$. Here, $J$ denotes all light quarks including $b$-quarks, assuming them to be universally

coupled. Later on we will loosen the latter requirement by also allowing the $b$-quark branching ratio to be alterable. We will refer to all light quarks excluding the $b$-quark as $j$.

Bounds on the branching ratio $\mathrm{BR}(X \to JJ)$ from the single $X$ production channel involves resonance searches in dijet and ditop final states. These searches will yield an upper and lower limit on $\mathrm{BR}(X \to JJ)$, respectively. As these bounds are model dependent they can in principle be evaded by a proper choice of parameters. To illustrate which $X$ mass regime they constrain we will nevertheless show representative limits.

Dijet searches have been performed at $\sqrt{s} = 13$ TeV by ATLAS [177] with 37/fb of integrated luminosity and by CMS [178] with 36/fb of integrated luminosity. Note that they place limits on $JJ$ rather than $jj$ as they do not $b$-tag jets. The limits are shown for a specific choice of $\Gamma/m_X$, where $\Gamma$ is the total decay width of $X$. This is done using the relation

$$\sigma_{\mathrm{excl}}(pp \to (JJ)_{\mathrm{res}}) = \sigma_0(pp \to X) \times \frac{\Gamma^0_{JJ}}{\Gamma} \tag{83}$$

$$= \sigma_0(pp \to X) \times \frac{\Gamma^0_{JJ}}{\Gamma^{\mathrm{excl}}_{JJ}} \frac{\Gamma^{\mathrm{excl}}_{JJ}}{\Gamma} \tag{84}$$

$$= \sigma_0(pp \to X) \times \frac{g_0^2}{g_{\mathrm{excl}}^2} \mathrm{BR}(X \to JJ)_{\mathrm{excl}}. \tag{85}$$

Here, $\sigma_{\mathrm{excl}}(pp \to (JJ)_{\mathrm{res}})$ is the experimentally determined limit on $\sigma \times \mathrm{BR}$ at a given mass $m_X$. $g_0$ is the reference coupling with which the production cross section $\sigma_0(pp \to X)$ and partial decay width to jets, $\Gamma^0_{JJ}$, is calculated. $g_{\mathrm{excl}}$ corresponds to the coupling with which the excluded branching ratio $\mathrm{BR}(X \to JJ)_{\mathrm{excl}}$ is determined. This branching ratio is taken in reference to the previously fixed total width $\Gamma$, hence the model-dependence. For a mass range of $m_X = 1200$ GeV to 2200 GeV this search yields an upper limit of about $\mathrm{BR}(X \to JJ) \sim 70\%$ for $\Gamma/m_X = 3 \cdot 10^{-4}$.

The limits from the ATLAS [179] and CMS [180] resonance searches in the $t\bar{t}$ final state are calculated analogously. These searches were performed at $\sqrt{s} = 8$ TeV with 20.3/fb and 19.7/fb of integrated luminosity, respectively. The lower limit on $\mathrm{BR}(X \to JJ)$ becomes negligible for masses above 1700 GeV and $\Gamma/m_X = 3 \cdot 10^{-4}$.

In addition CMS performed a resonance search in the $b\bar{b}$ channel [181], but given that this search is based on 8 TeV data it cannot compete with the 13 TeV dijet searches [177, 178], if the fraction $\mathrm{BR}(X \to b\bar{b})/\mathrm{BR}(X \to jj) = 1/5$ is fixed.

We furthermore include limits from searches for pair-produced resonance in the $t\bar{t}t\bar{t}$ and $JJJJ$ final state. The $t\bar{t}t\bar{t}$ searches are performed by ATLAS [182] at $\sqrt{s}$ =13 TeV

with 3.2/fb of integrated luminosity and CMS [183] at $\sqrt{s}$ =8 TeV with 19.6/fb of integrated luminosity. The $JJJJ$ searches utilise $\sqrt{s}$ =13 TeV ATLAS data [184] and $\sqrt{s}$ =8 TeV CMS data [185] with 15.4/fb and 19.4/fb of integrated luminosity, respectively. As both CMS searches are based on older data we found their limits to be weaker.

ATLAS does not unfold their signal tagging efficiencies in the results of their $JJJJ$ search. We therefore assume a flat signal tagging efficiency of 60%. These limits are strongly constraining for masses below ∼1400 GeV, but vanish quickly for higher masses. The steep fall of the bound is mainly due to the squared dependence of the limits on the branching ratio to jets and tops, respectively.

Meson mixing and rare meson decays constrain flavour changing coupling of $X_\mu$ to quarks [51, 186], but also in the flavour conserving case the heavy octet vector contributes. In meson mixing, however, the lowest order diagram involving $X_\mu$ is only at 2-loop, can thus safely be neglected. The contribution to meson decays is via Penguin diagrams, *i.e.* at 1-loop. But given that the heavy octet vector couples not to leptons, it does not contribute to any rare decays. In fact, it is always possible to write down an equivalent Standard Model tree-level charged current diagram. Thus there are no relevant limits expected from meson decays either.

To obtain limits from our search for the mixed final state $t\bar{t}JJ$ we simulate signal events using MadGraph5 v.2.4.3 [144] + Pythia8 [145, 187]. We do not apply a NLO $K$-factor to the signal, as its calculation is a work in progress. As we want to avoid the overwhelming QCD background we focus on the semi-leptonic and fully leptonic decay modes of the top pair. The dominant background to this final states are $t\bar{t}$+jets events. Having certain analysis cuts in mind we simulate $t\bar{t}j$ events with up to two additional jets at leading order using Sherpa v.2.1.0 [168]. We apply a flat NLO $K$-factor of 1.5, as determined by Sherpa+BlackHat [172]. Detector effects are simulated and final state objects are reconstructed using Delphes v3.1.2 [146].

## 6.3 Semi-Leptonic Final State

The semi-leptonic search will generally yield better limits than the fully leptonic search, as it is less suppressed by branching ratios while still having a reasonably clean signature. The aim in this search is to reconstruct the resonance peaks. But the $t\bar{t}$ resonance is challenging to reconstruct due to its subsequent decays. The resolution is poor, hence the dijet resonance peak will be the leading discriminator. The $t\bar{t}$ decay products will merely be an effective way to diminish various other possible

background sources.

The overall process is $pp \to XX \to (b\ell\nu)(\bar{b}jj)(JJ)$ where $JJ = b\bar{b}/jj$. We therefore select jets with $p_T > 50$ GeV and $|\eta| < 4.9$, which are clustered using the anti-$k_T$ algorithm with a cone radius of $R = 0.5$. Jets are b-tagged with a $p_T$ and $\eta$ dependent tagging efficiency of about 70%, a $c$-misidentification rate of about 15%, and a light quark mistagging rate of 0.1%. We require at least five jets where two or more are $b$-tagged. At least one of these jets must not be $b$-tagged, the one that originates from the hadronically decaying top if $JJ = b\bar{b}$. We tighten the $p_T$ cuts for the leading jets: The leading $b$-tagged and non-$b$-tagged jets must fulfil $p_T > 250$ GeV, and the subleading non-$b$-tagged jet $p_T > 80$ GeV.

In addition, the event must contain exactly one isolated charged lepton with $p_T > 20$ GeV and $\eta < 2.5$. Missing energy is required to exceed a certain level, addressing the neutrino from the leptonically decaying top: $\not{E}_T > 80$ GeV. We also apply a cut on $H_T = \Sigma_{\text{jets}}|p_T| \geq 4/3 m_X$ to enhance signal-to-background discrimination without significantly skewing the resonance peak.

The dijet resonance peak in the $thh$ search from last chapter is not easily identified due to jet combinatorics. The situation here is very similar due to the extra jets from the ditop resonance. The nuisance jets from the top decay are dominantly $b$-jets, whereas our $JJ$ resonance can be either, $b\bar{b}$ or $jj$. We therefore split our event samples into two signal regions, one targeting $JJ = b\bar{b}$, the other $JJ = jj$. The first requires more than two $b$-tagged jets, whereas the latter signal region exactly two.

For the $JJ = b\bar{b}$ signal region we assume that the leading $b$-jet is part of the $JJ$ system. As the nuisance $b$-jets are decay products from top quarks we expect them to be slightly softer. Either the leading light jet or subleading $b$-tagged jet is chose as the second jet for the $JJ$ resonance, whichever is harder in $p_T$. This takes the possibility into account that one of the two resonance jets is mistagged as a light jet.

In case of $JJ = jj$ we assume that the hardest light jet $j_1$ belongs to the system. The second jet $j_2$ is then the hardest light jet satisfying $\Delta R_{j_1 j_2} \leq \pi$. Furthermore, we found that whenever possible, adding the next hardest light jet $j_3$ with $\Delta R_{j_1 j_3} \leq \pi$ to the system improves the resonance peak resolution, if the two jets $j_1$ and $j_2$ are not balanced in transverse momentum, $y = p_{T,j_2}/p_{T,j_1} \leq 0.15$. In this case final state radiation caused one of the jets to split when applying the jet clustering algorithm.

We will use the $JJ$ invariant mass peak as a discriminant between signal and background. We show tagging efficiencies in tab. 3 for an exemplary mass point of $m_X = 1400$ GeV. The cutflow for other masses is very similar. In addition we present

| | Signal $m_X = 1400$ GeV | background $t\bar{t}$+jets |
|---|---|---|
| event selection | 0.93 fb | 5.8 fb |
| $\not{E}_T > 80$ GeV | 85% | 64% |
| $H_T \geq 4/3 m_X$ | 81% | 25% |
| remaining cross section | 0.64 fb | 0.94 fb |

Table 3: Cutflow for a resonance mass of $m_X = 1400$ GeV and dominant background $t\bar{t}$+jets for the semi-leptonic search at 13 TeV. All branching ratios are applied to signal and background when quoting cross sections. For the signal we assume $\mathrm{BR}(X \to t\bar{t}) = \mathrm{BR}(X \to JJ) = 50\%$. The acceptance rate for other signal masses is not shown as they are all very similar.

kinematic distributions in fig. 17. In order to compare different signal masses we omit the mass-dependent $H_T$ cut.

## 6.4 Leptonic Final State

The search for the leptonic final state is very similar to the semi-leptonic channel. We define and select jets and leptons as in the last section. However, we require one jet less but instead exactly two charged leptons of opposite charge rather than just one. As there is now an additional neutrino we reduce the cut on $\not{E}_T$ to 50 GeV, as their transverse momentum can partially cancel. We leave the cut on $H_T$ unchanged.

The dominant background is still $t\bar{t}$+jets, but a leptonic $Z$+jets also contributes slightly. To eradicate this additional background we veto events with $m_{\ell\ell} \leq 115$ GeV. As before we focus on reconstructing the $JJ$ resonance by using the same algorithm.

We present the cutflow in tab. 4 for an exemplary mass point of $m_X = 1400$ GeV. The cutflow for other masses is very similar. Nevertheless, we have to note that due to the branching ratio suppression the limits obtained in the fully leptonic final state are not as good as in the semi-leptonic final state. The contribution upon combination with the semi-leptonic channel is only marginally.

## 6.5 Results

We use the $JJ$ invariant mass spectra as a discriminant and obtain limits on the $X_\mu$ branching ratios using the $CL_s$ method [149], assuming a 20% systematic uncertainty on signal and background. We consider two scenarios: one where the couplings of $X_\mu$ to all quarks but the top are universal, the other where also the coupling to the bottom quark is altered. In both scenarios we combine the semi-leptonic and fully leptonic channels. In the first scenario we additionally know the branching fraction

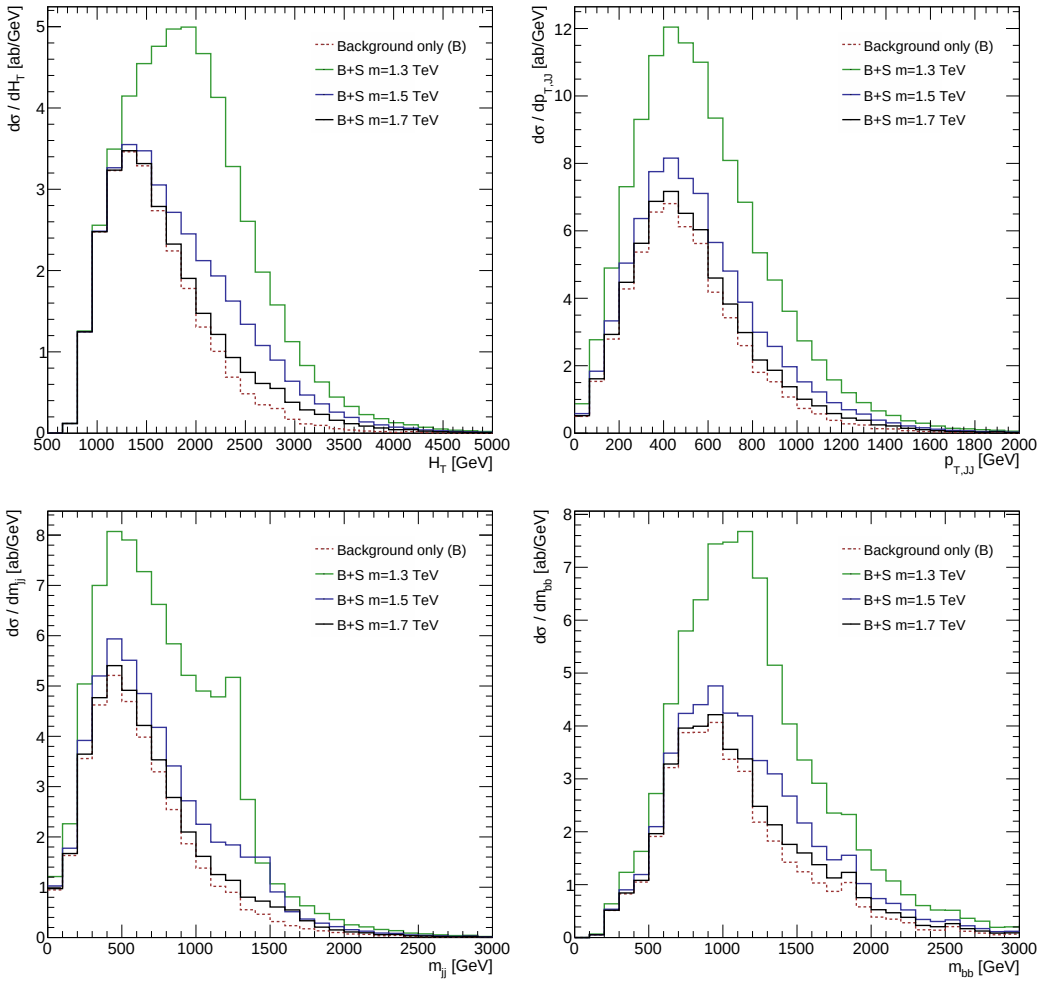


Figure 17: Different kinematic distributions for the resonance masses $m_X$=1300 GeV, 1500 GeV and 1700 GeV. We omit the mass-dependent cut on $H_T$ in order to have a fair comparison between different signal masses.

$\mathrm{BR}(X \to b\bar{b})/\mathrm{BR}(X \to jj) = 1/5$, thus we are able to combine the two signal regions $JJ = b\bar{b}$ and $JJ = jj$. In the second scenario both signal regions are evaluated independently.

We show the results for the first scenario in fig. 18. The limits are placed on the branching ratio $\mathrm{BR}(X \to JJ) = 1 - \mathrm{BR}(X \to t\bar{t})$, where the branching fraction $\mathrm{BR}(X \to b\bar{b})/\mathrm{BR}(X \to jj) = 1/5$ is fixed. We show our results for 3.2/fb, 15.4/fb, 37/fb, and 100/fb of integrated luminosity to directly compare them to existing limits and estimate future sensitivity.

We see that our limits cannot compete when either the branching ratio to top quarks

| | Signal $m_X = 1400$ GeV | background $t\bar{t}$+jets |
|---|---|---|
| event selection | 0.073 fb | 0.75 fb |
| $\not{E}_T > 80$ GeV | 96% | 91% |
| $m_{\ell\ell} \leq 115$ GeV | 69% | 37% |
| $H_T \geq 4/3 m_X$ | 60% | 15% |
| remaining cross section | 0.029 fb | 0.038 fb |

Table 4: Cut flow for a resonance mass of $m_X = 1400$ GeV and dominant background $t\bar{t}$+jets for the fully leptonic search at 13 TeV. All branching ratios are applied to signal and background when quoting cross sections. For the signal we assume $\text{BR}(X \to t\bar{t}) = \text{BR}(X \to JJ) = 50\%$. The acceptance rate for other signal masses is not shown as they are all very similar.

or light jets $J$ becomes small. But in the intermediate regime for $\text{BR}(X \to JJ) > 30\%$ and $\text{BR}(X \to JJ) < 60\%$ our mixed $t\bar{t}JJ$ search has a significant edge over existing searches.

In the second scenario, we show our results in fig. 19. Here, we present them in form of a unitarity triangle diagram, where each axis corresponds to the branching ratios $\text{BR}(X \to t\bar{t})$, $\text{BR}(X \to b\bar{b})$, or $\text{BR}(X \to jj)$. In the hand plot the colour shading represents the strongest lower bounds on the heavy octet vector mass $m_X$. The right plot illustrates which particular search yields the respective strongest limit. We omit the single resonance production searches as they are too model-dependent and, as mentioned before, can in principle be avoided.

We see that for either large $\text{BR}(X \to JJ)$ branching or very large $\text{BR}(X \to t\bar{t})$ the existing $JJJJ$ and $t\bar{t}t\bar{t}$ searches yield the strongest limits. But as soon as we are in the mixed regime, either our $t\bar{t}b\bar{b}$ or $t\bar{t}jj$ search take over.

## 6.6 Discussion

We discussed in this chapter the phenomenology of heavy octet vectors. Given that the pair production mode of an octet vector $X_\mu$ is model-independent, in contrast to the single resonance production mode, a dedicated search offers a robust way of testing the existence of such a vector.

Searches for pair produced resonances decaying to quarks were already performed in the four jet and four top final states. But this assumes either a very large or very small branching ratio of $X_\mu$ to $t\bar{t}$. We therefore motivated an analysis for a mixed $t\bar{t}JJ$ final state in order to cover the gap left by the existing searches.

We designed a search for a double resonance in the $t\bar{t}JJ$ final state with a fully

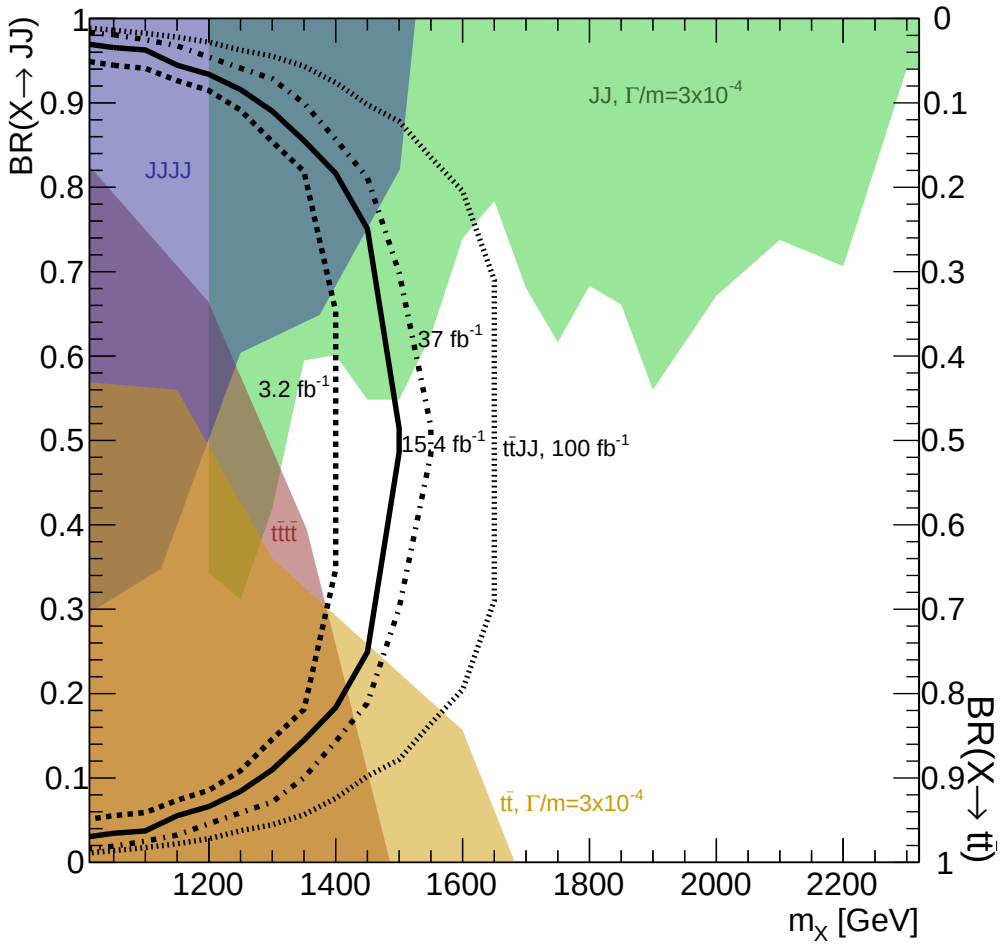


Figure 18: Exclusion limits for different resonance masses as a function of $\mathrm{Br}(X \to JJ) = 1 - \mathrm{Br}(X \to t\bar{t})$. We show our limit in black for 3.2/fb (dotted), 15.4/fb (solid), 37/fb (dash-dotted) and 100/fb (small dashes) of integrated luminosity. We also show current limits from $4t$ (red) and $4J$ (blue) searches by ATLAS [182, 184] at 13 TeV using 3.2/fb and 15.4/fb of integrated luminosity, respectively. The dijet limits are determined using the ATLAS search [177] at 13 TeV and 37/fb of integrated luminosity and the $t\bar{t}$ limits are based on the ATLAS search [179] at 8 TeV and 20.3/fb. The dijet and ditop limits assume $\Gamma/m_X = 3 \cdot 10^{-4}$. The respective limits obtained by CMS [178, 180, 183, 185] are either very similar or weaker due to older/less data, thus we omit them for readability.

leptonic or semi-leptonic decay of the $t\bar{t}$ pair. In each $t\bar{t}$ decay mode we defined two signal regions, where $JJ$ is either $b\bar{b}$ or light quark jets excluding $b$-quarks. We focused on reconstructing the $JJ$ invariant mass peak and obtained limits on the branching ratios. Here, we left either $\mathrm{BR}(X \to JJ)$ and $\mathrm{BR}(X \to t\bar{t})$ as a free parameter or $\mathrm{BR}(X \to jj)$, $\mathrm{BR}(X \to b\bar{b})$, and $\mathrm{BR}(X \to t\bar{t})$.

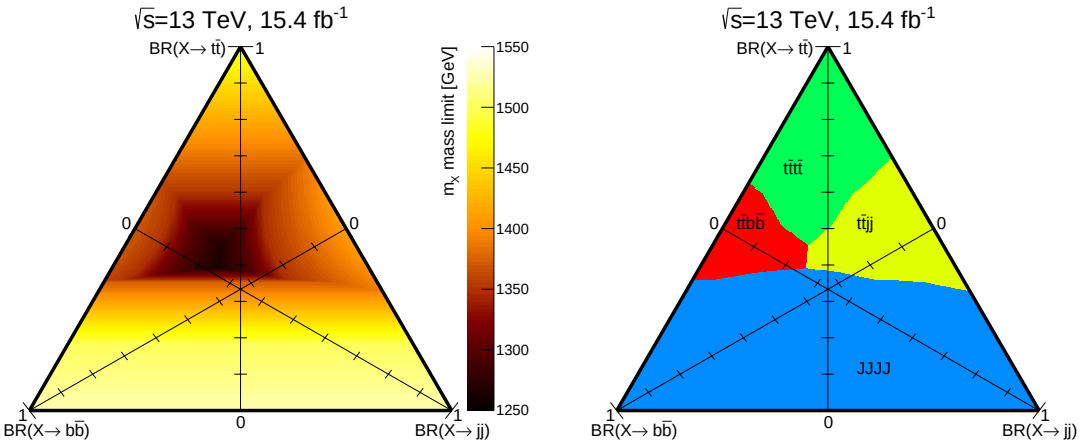


Figure 19: *Left:* Lower bound (colour shading) on the heavy octet vector mass $m_X$ as a function of the branching ratios $\mathrm{BR}(X \to t\bar{t})$, $\mathrm{BR}(X \to b\bar{b})$, and $\mathrm{BR}(X \to jj)$. *Right:* This plot indicates which particular search is responsible for the best limit in the plot on the left-hand side. We include our $t\bar{t}b\bar{b}$ and $t\bar{t}jj$ search assuming 15.4/fb at 13 TeV, as well as $4t$ and $4J$ searches by ATLAS [182, 184] at 13 TeV using 3.2/fb and 15.4/fb of integrated luminosity, respectively. The limits obtained by CMS [183, 185] are either very similar or weaker due to older/less data, thus we omit them for readability. Due to the strong model-dependence we also omit dijet and ditop searches.

We found that this search is able to access the so far unconstrained intermediate $\mathrm{BR}(X \to t\bar{t})$ regime, roughly between 30% and 60%.

CHAPTER 7

# Spin Discrimination in Boosted Diboson Final States

## 7.1 Motivation

In the last two chapters we saw a few examples of simple resonance searches. We reconstructed an invariant mass peak of a $H^0 \to \tau\mu$ resonance from a $\tau\mu$ final state, as well as several intermediate mass peaks in the more complex process $pp \to tH^0 \to thh$. In addition, we presented a search for a pair produced coloured resonance.

This chapter will be not so much about finding a heavy resonance in the first place, but rather on what other information can be drawn from data once a resonance is identified. Specifically, we will look at diboson resonances, which are processes where an intermediate heavy particle decays to $W^+W^-$, $W^\pm Z$ and/or $ZZ$.

Once such a resonance is found in the invariant mass spectrum $m_{VV'}$, where $V, V' = W, Z$, one can read off some information directly from the mass peak. From the integrated number of events over the background contribution, it is possible to determine $\sigma \times \mathrm{BR}$ of the underlying process. From the width of the peak, depending on how accurately it is measured, it is possible to deduce the overall decay width of the resonance. If $W$ and $Z$ bosons can be distinguished, it is furthermore possible to determine the electric charge of the resonance and the relative coupling strength to both bosons.

One of the most important properties of the resonance remains unknown though: the spin of the particle. To determine the nature of the underlying physics Lagrangian, this information is indispensable. The spin cannot be extracted directly from the mass

peak but is still encoded in the overall kinematics of the process.

How to extract spin information from data is already known and there is one famous example: the Higgs boson. The Higgs was first discovered in three different channels, $h \to ZZ \to 4\ell$, $h \to W^+W^- \to 2\ell 2\nu$, and $h \to \gamma\gamma$. The latter is technically a diboson resonance too but is often not referred to as such. Angular correlations between the final state particles were used and we will therefore define those in more detail in the following section. It was observed that the differential cross section as a function of some angles between the decay particles yield very different shapes based on the spin of the original resonance [188–193]. Those were used to discriminate between different spin hypotheses of the Higgs boson [194–197].

For any other heavy new resonance the same idea can be used. But unlike for the Higgs a few complications typically arise. First of all, a search for a diboson resonance depends strongly on the daughter particles of the two intermediate bosons.

Usually one distinguishes between a fully leptonic or hadronic decay, $4\ell$, $2\ell 2\nu$, and $4j$ and the semi-leptonic channels $2\nu jj$, $2\ell jj$, and $\ell\nu jj$. $j$ is here a place holder for a quark. Due to branching ratios the hadronic channel has a higher rate than the leptonic channel, with semi-leptonic decays somewhere in between. Very naïvely, one expects channels with higher rate to dominate the overall sensitivity. But this is only true for a background-free environment, which the LHC usually is not.

For the Higgs, this meant that the fully hadronic channel is, despite his higher rate, weaker than a fully leptonic channel. This is due to the overwhelming QCD background, which is steeply falling with energy, but still hard to come by even at a Higgs mass of $m_h = 126$ GeV. A fully leptonic final state, however, is basically background-free, which is also why $h \to ZZ \to 4\ell$ was called the *golden channel*. This makes the $4\ell$ in terms of discovery much more powerful than the $4j$. The same argument holds for $h \to W^+W^-$.

When we talk about a new heavy resonance in the diboson channel that typically implies resonance masses of $\mathcal{O}$(TeV). At these high energies, background rates are very different than for masses around $m_h$. Naturally, the fully leptonic channel is still basically background free and the main background for the fully hadronic channel remains QCD. But the QCD background rate is so much lower at resonance masses of $\mathcal{O}$(TeV) that it becomes manageable.

This has been impressively shown by ATLAS [198] and CMS [199], who both published searches tackling the fully hadronic channel. In fact, ATLAS discovered a peak in their invariant mass spectrum at about 2 TeV mass with $2.5\sigma$ global significance in $\sqrt{8}$ TeV data. This excess sparked a lot of excitement in the physics community and

several possible explanations emerged. Spin-0 explanations are discussed in context of a Higgs singlet [200], a two Higgs doublet model [201–204], sparticles [205, 206] or composite scalars [207, 208]. Spin-1 proposals include composite vector resonances [209–216], generic and effective field theory (EFT) models [217–220] as well as heavy $W'$ resonances [221–237], $Z'$ resonances [238–245] or both [246–252]. Other new physics scenarios include glueballs [253], excited composite objects [254], and in generic and EFT models [255–260].

Unfortunately, the excess was not confirmed in more recent 13 TeV data [261, 262] and, therefore, must have been a statistical fluctuation. But nevertheless, the resulting studies showed impressively how the discovery channel of a diboson resonance can be the fully hadronic channel, while still being consistent with the non-observation at 8 TeV in semi-leptonic [263–265] and fully leptonic diboson searches [266, 267], and other possible model-dependent searches [268, 269].

The latter are mainly self-consistency requirements as the new resonance has often a $jj$ and $Vh$ decay channel [222, 223, 225, 233, 240]. Thus extra constraints arise from the respective ATLAS [270–273] and CMS [274–278] searches.

Concerning spin discrimination the final state is important. It requires good reconstruction of the final state to determine angular correlations accurately [279–281]. For the Higgs those where leptons and photons, both of which can be measured with very high precision. For a fully hadronic final state those are jets, which are slightly harder to reconstruct.

But there is one bigger issue with the fully hadronic final state. The mass of the resonance is now at the TeV scale, which means a lot of energy will be transferred onto the two bosons. The decay products of the intermediate bosons are then separated by $\Delta R \approx 2m_V/p_T \approx 4m_V/m_X$, where $m_V$ is the boson mass and $m_X$ the mass of the heavy resonance. For a 2 TeV resonance (like the statistical fluctuation above) this yields $\Delta R \approx 0.15 - 0.2$, which is much smaller than the typical jet radius of $R = \mathcal{O}(0.5)$.

This implies that both jets merge and jet substructure techniques are necessary to disentangle them, see section 4.2.3. In fact, this is exactly what ATLAS and CMS do in their analyses. But at the same times, it makes the reconstruction of angular correlations a lot more complex. It is *per se* not clear what an effect jet substructure algorithms have on those observables. They employ cuts which might skew angular correlations in a non-trivial way, especially given that they are optimised towards signal-background discrimination and not spin discrimination.

This chapter will try to answer how well spin discrimination still works in the boosted regime, where final state particles are merged jets. We will use the 2 TeV

excess of the 8 TeV ATLAS analysis as a case study, as it is the best-understood mass point with plenty of viable models. Besides the fully hadronic channel, we will also consider semi-leptonic decays, where only one decay branch is reconstructed via jet substructure techniques.

We will introduce in section 7.2 the angular observables used for spin discrimination. The relevant ATLAS and CMS searches are briefly summarised in section 7.3. Based on our recast we will describe the influence of jet substructure algorithms on the angular observables for the fully hadronic $4j$ channel in section 7.4. The semi-leptonic channel is discussed in section 7.5. Once we understood the influence of jet substructure techniques we determine projections for spin discrimination in section 7.6. We will discuss the results in section 7.7.

## 7.2 Angular Observables

The angular observables in this study are defined analogously to those used for the spin discrimination of the Higgs. For a general process of the kind $pp \to X \to V_1V_2 \to (p_1p_2)(p_3p_4)$, in total the four four-momenta of the particles $p_1, \ldots, p_4$ are measured, provided the final state jets were disentangled using jet substructure algorithms. This makes sixteen parameters.

Since we can neglect the masses of the final state quarks this reduces the amount of parameters to twelve. Additionally, we know that four-momentum conservation holds, thus we are left with eight parameters. As the system is symmetrical for a rotation around the beam axis $\hat{z}$, the final number of independent parameters reduces to seven. Those can be parameterised as five angles and two intermediate vector boson masses. If the resonance mass is not known either it counts as an independent parameter too.

The five angles are known as Cabibbo–Maksymowicz–Dell'Aquila–Nelson angles [188–191] and carry all information about the kinematics of the system. They are defined as

$$\begin{aligned} \cos\theta_{p_1} &= -\hat{p}_{p_1} \cdot \hat{p}_{V_2} \ , & \Phi_{V_1} &= \frac{\vec{p}_{V_1} \cdot (\hat{n}_1 \times \hat{n}_{\text{sc}})}{|\vec{p}_{V_1} \cdot (\hat{n}_1 \times \hat{n}_{\text{sc}})|} \arccos(\hat{n}_1 \cdot \hat{n}_{\text{sc}}) \ , \\ \cos\theta_{p_3} &= -\hat{p}_{p_3} \cdot \hat{p}_{V_1} \ , & \Phi &= \frac{\vec{p}_{V_1} \cdot (\hat{n}_1 \times \hat{n}_2)}{|\vec{p}_{V_1} \cdot (\hat{n}_1 \times \hat{n}_2)|} \arccos(-\hat{n}_1 \cdot \hat{n}_2) \ , \\ \cos\theta^* &= \hat{p}_{V_1} \cdot \hat{z}_{\text{beam}} \ , \end{aligned} \tag{86}$$

where $V_1$ and $V_2$ are the two bosons, $X$ is the resonance, $\hat{z}_{\text{beam}}$ is the direction of the

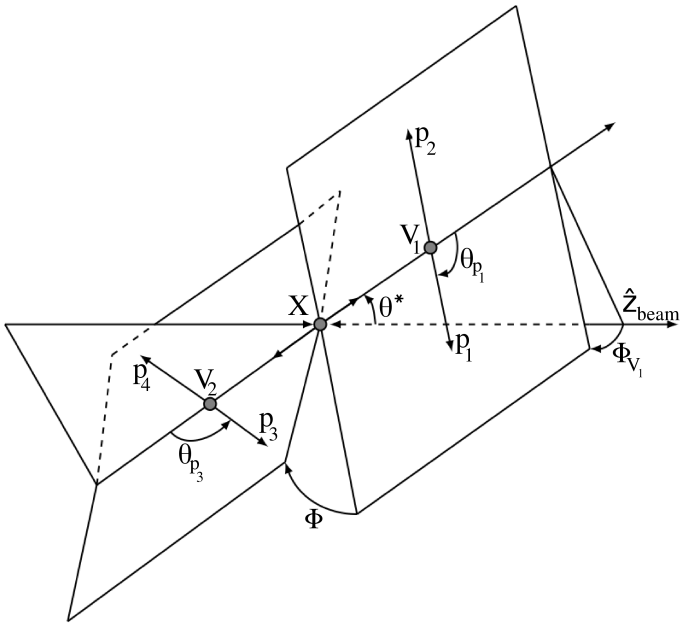


Figure 20: Representation of the Cabibbo–Maksymowicz–Dell'Aquila–Nelson angles defined in eq. 86.

beam axis and

$$\hat{n}_1 = \frac{\vec{p}_{p_1} \times \vec{p}_{p_2}}{|\vec{p}_{p_1} \times \vec{p}_{p_2}|} \ , \quad \hat{n}_2 = \frac{\vec{p}_{p_3} \times \vec{p}_{p_4}}{|\vec{p}_{p_3} \times \vec{p}_{p_4}|} \ , \text{ and } \hat{n}_{\text{sc}} = \frac{\hat{z}_{\text{beam}} \times \vec{p}_{p_1}}{|\hat{z}_{\text{beam}} \times \vec{p}_{p_1}|} \ . \tag{87}$$

We show their definition graphically in fig. 20.

The four-momenta of the intermediate vectors $V_1$ and $V_2$ are calculated as $p_{V_1} = p_{p_1} + p_{p_2}$, $p_{V_2} = p_{p_3} + p_{p_4}$, respectively, and for the heavy resonance $X$ subsequently $p_X = p_{V_1} + p_{V_2}$. Note that the two angles $\cos\theta_{p_1}$ and $\cos\theta_{p_3}$ are calculated in the rest frame of $V_1$ and $V_2$, respectively, whereas all other angles are boosted into the rest frame of $X$. In the rest of this chapter we will additionally consider the reparameterised angle $\Psi = \Phi_{V_1} + \Phi/2$ instead of $\Phi_{V_1}$. $\Psi$ can be interpreted as the average azimuthal angle of the two decay planes spanned by $p_1/p_2$ and $p_3/p_4$, respectively.

Analytic expressions for the differential cross section based on these angular observables are given in ref. [193]. These expressions, of course, depend on the spin of $X$, thus their usefulness for spin discrimination.

## 7.3 Diboson Searches

In order to analyse the angular distributions we need to recast the existing searches and define signal benchmarks. Since substructure techniques affect observables we need to know some of the details of the respective analysis. The substructure techniques themselves are already described previously in section 4.2.3.

In this section, we will briefly introduce the fully hadronic and semi-leptonic searches of ATLAS and CMS at both, 8 TeV and 13 TeV. Additionally, we will describe our simulation setup and the signal samples we generate.

### 7.3.1 ATLAS and CMS Fully Hadronic Analyses

#### 7.3.1.1 $4q$ Final State at 8 TeV by ATLAS

The ATLAS analysis of 8 TeV data for the $4q$ final state [198] is the analysis that initially found the 2 TeV excess. They start by reconstructing fat jets with the Cambridge/Aachen algorithm and cone radius of $R = 1.2$. They select events with exactly two of these jets with $p_T > 20$ GeV and $|\eta| < 2.0$. They require no leptonic activity, *i.e.* no electrons with $E_T > 20$ GeV and $|\eta| < 1.37$ or $1.52 < |\eta| < 2.47$, or muons with $p_T < 20$ GeV and $|\eta| < 2.5$. Missing energy is supposed to be small, thus $\not{E}_T < 350$ GeV.

The mass-drop filter technique is then applied to these fat jets with $\mu_f = 1$, *i.e.* no mass-drop, and $y_{\min} = 0.04$. See section 4.2.3.1 for further details. The original jets are denoted as *ungroomed* and those after the mass-drop filter *groomed*. The constituents from the two subjets of the groomed jet are reclustered a second time using the Cambridge/Aachen algorithm and smaller cone size of $R = 0.3$. The first three jets highest in $p_T$ are kept and denoted *filtered* jets. Those are used to reconstruct the $W$ and/or $Z$ candidates. Further cuts are applied on the two ungroomed jets. Their rapidity difference is required to be small, $|y_{J_1} - y_{J_2}| < 1.2$, as well as their $p_T$ asymmetry, $(p_{T,J_1} - p_{T,J_2}) / (p_{T,J_1} + p_{T,J_2}) < 0.15$.

The sum of filtered jets are tagged as a $W$ or $Z$ boson if they fulfil three requirements:

- The two subjets of the groomed jet satisfy a higher momentum balance criteria as in the original mass-drop filter, $y > y_{\min} = 0.2025$.

- The ungroomed jet is associated with less than 30 charged tracks with $p_T \geq 500$ MeV.

- The $W$ and $Z$ candidates need to fulfil $|m_J - m_V| < 13$ GeV, where $m_V$ is either 82.4 GeV for a $W$ boson or 92.8 GeV for a $Z$ boson. These values differ slightly from the actual $Z$ and $W$ masses, as detector and reconstruction effects alter the shape of the resonance peak such that the complete distribution is shifted. Note that both invariant mass windows overlap, which means a $V$ candidate can be tagged as both, a $W$ and $Z$ boson.

Finally, ATLAS requires a minimum invariant mass of the resonance by imposing $m_{JJ} > 1.05$ TeV.

#### 7.3.1.2 $4q$ Final State at 8 TeV by CMS

CMS [199] starts by requiring at least two Cambridge/Aachen fat jets with a slightly smaller cone radius of $R = 0.8$. They impose $p_T > 30$ GeV and $|\eta| < 2.5$. In addition the two leading jets have to fulfil $|\Delta\eta| < 1.3$ and $m_{JJ} > 890$ GeV.

Fat jets are then pruned with $z_{min} = 0.1$, which is equivalent to $y_{\min} \approx 0.11$. See section 4.2.3.2 for more details. The pruned fat jets are then denoted a $W/Z$ candidate if they fulfil 70 GeV $< m_J <$ 100 GeV. They are furthermore divided by purity, which is determined by calculating their $N$-subjettiness ratio $\tau_{21}$, see section 4.2.3.4. They are of high purity if $\tau_{21} < 0.5$ and of low purity if $0.5 < \tau_{21} < 0.75$. For other values of $\tau_{21}$ they are not considered anymore. The resonance is then reconstructed from the two leading $W/Z$ candidates, of which at least one must be of high purity.

#### 7.3.1.3 $4q$ Final State at 13 TeV by ATLAS

The ATLAS 13 TeV [261] analysis differs greatly from their 8 TeV search. Fat jets are reconstructed using the anti-$k_T$ algorithm with $R = 1.0$, $p_T > 200$ GeV, $|\eta| < 2.0$, and $m_J > 50$ GeV. They require exactly two jets with an invariant mass between 1 TeV and 2.5 TeV, a rapidity difference of $|y_{J_1} - y_{J_2}| < 1.2$, and a $p_T$ asymmetry of $(p_{T,J_1} - p_{T,J_2}) / (p_{T,J_1} + p_{T,J_2}) < 0.15$. Additionally, the leading fat jet must have a transverse momentum of $p_T > 450$ GeV and events with leptons with $p_T > 25$ GeV and $|\eta| < 2.5$ are vetoed. Furthermore, missing energy has to be small, $\not{E}_T < 250$ GeV.

ATLAS does not use the mass-drop filter anymore, but employs the trimming algorithm with the $k_T$ algorithm, cone radius of $R = 0.2$, and $z_{\min} = 0.05$, see section 4.2.3.3. In order to distinguish between QCD and $V$ jets they require that a maximum value of the energy correlation function $D_2^{(\beta=1)}$ is not exceeded. See section 4.2.3.5 for further details. The exact maximum value depends on the transverse momentum of the trimmed jet and whether it is a $W$ or $Z$ candidate. We linearly interpolate between the two values quoted in their analysis, $D_2 = 1.0$ at $p_T = 250$ GeV and $D_2 = 1.8$ at $p_T = 1500$ GeV.

Trimmed jets have to fulfil a set of final criteria: First, less than 30 charged tracks are associated with the original fat jet, and second, $|m_J - m_V| < 15$ GeV, where $m_V = 84$ GeV for a $W$ boson and $m_V = 96$ GeV for a $Z$ boson.

#### 7.3.1.4 $4q$ Final State at 13 TeV by CMS

The 13 TeV CMS search [262] is very similar to their 8 TeV analysis. Thus we restrict ourself to mentioning the few changes.

The two fat jets must now lie within $|\eta| < 2.4$ and their rapidity difference is required to be $|\Delta\eta| < 1.3$. Their minimum invariant mass is raised to $m_{JJ} > 1$ TeV. The mass window for $W/Z$ candidates is slightly widened to 65 GeV$< m_{W/Z} <$ 105 GeV and the purity criteria tightened by requiring $\tau_{21} \leq 0.45$ and $0.45 < \tau_{21} < 0.75$, respectively.

### 7.3.2 ATLAS and CMS Semi-Leptonic Analyses

#### 7.3.2.1 $\ell\ell qq$ Final State at 8 TeV by ATLAS

ATLAS [263] selects exactly two muons or electrons of opposite charge. Muons are required to have $p_T > 25$ GeV and $|\eta| < 2.4$. Electrons must satisfy $p_T > 25$ GeV and $|\eta| < 2.47$, excluding $1.37 < |\eta| < 1.52$. All leptons must pass a track isolation (calorimeter isolation) requirement (see ref. [263] for details). The lepton pair has to fulfil 66 GeV$< m_{\ell\ell} <$ 116 GeV and $p_T^{\ell\ell} > 400$ GeV.

To reconstruct the hadronic decay they cluster fat jets with the Cambridge/Aachen algorithm and R=1.2. These must have $p_T > 100$ GeV and $|\eta| < 1.2$. Exactly one jet has to pass the mass-drop filter technique with $\mu_f = 1$ and $y_{\min} = 0.2025$. The requirements on the jet are then tightened by imposing $p_T > 400$ GeV and 70 GeV$< m <$110 GeV.

#### 7.3.2.2 $\ell\ell qq$ Final State at 8 TeV by CMS

CMS [265] selects electrons with $p_T > 40$ GeV and $|\eta| < 2.5$, excluding $1.44 < |\eta| < 1.56$. Muons are required to satisfy $p_T > 20$ GeV and $|\eta| < 2.1$. All leptons must be isolated from other tracks as well as in the calorimeter. A pair of leptons of same flavour and opposite charge is selected, which has to satisfy 70 GeV $< m_{\ell\ell} <$ 110 GeV. For a muon pair $p_T > 40$ GeV is imposed in addition.

Using the Cambridge/Aachen algorithm and $R = 0.8$ fat jets with $p_T > 30$ GeV and $|\eta| < 2.4$ are reconstructed. They are then pruned with $z_{\min} = 0.1$ and assigned a purity using the $N$-subjettiness variable $\tau_{21}$ analogously to the CMS $4q$ 8 TeV search. 65 GeV $< m_J <$ 110 GeV is applied to selected $W/Z$ candidates.

Leptonic and hadronic $V$ candidates have to satisfy $p_T^V > 80$ GeV and the pair $m_{VV} > 500$ GeV. If there are multiple hadronic $V$ candidates, the hardest $p_T$ candidate in the higher purity category is used.

#### 7.3.2.3 $\ell\ell qq$ Final State at 13 TeV by ATLAS

Leptons are selected similar to the respective 8 TeV analysis [282]. The lepton pair has to fulfil 66 GeV $< m_{\mu^+\mu^-} <$ 116 GeV or 83 GeV$< m_{e^+e^-} <$ 99 GeV, respectively.

Fat jets are reconstructed using the anti-$k_T$ algorithm with $R = 1.0$, $p_T > 200$ GeV and $|\eta| < 2.0$. They undergo the trimming procedure with $z_{\min} = 0.05$, and must satisfy $p_T^J > 0.4\, m_{\ell\ell J}$ and 68.2 GeV $< m_J <$ 108.4 GeV. The same cut on the energy correlator function $D_2^{(\beta)}$ as in the $4q$ analysis is applied. The lepton pair must furthermore fulfil $p_T^{\ell\ell} > 0.4\, m_{\ell\ell J}$.

#### 7.3.2.4 $\ell\nu qq$ Final State at 8 TeV by ATLAS

Leptons are selected with the same criteria as in the 8 TeV $llqq$ search by ATLAS [264]. Missing transverse energy must exceed 30 GeV. The neutrino momentum is reconstructed as in eq. 79. To break the ambiguity in solutions they use the real part of a complex momentum, otherwise the smaller in absolute value. $p_T^{\ell\nu} > 400$ GeV must hold.

Jets are selected and groomed as in the 8 TeV $llqq$ search but with the modified cuts $|\eta| < 2.0$ and 65 GeV $< m_J <$ 105 GeV. In addition, $\Delta\phi$ between this jet and the missing transverse energy vector must exceed 1. Events with $b$-tagged jets are vetoed (see ref. [264] for details).

#### 7.3.2.5 $\ell\nu qq$ Final State at 8 TeV by CMS

CMS [262] selects isolated electrons with $p_T > 90$ GeV and $|\eta| < 2.5$, excluding $1.44 < |\eta| < 1.56$, and isolated muons with $p_T > 50$ GeV and $|\eta| < 2.1$. For events with an electron (muon) missing transverse energy must exceed 80 GeV (40 GeV). After reconstructing the neutrino $p_T^{\ell\nu} > 200$ GeV is imposed.

Jets are selected as in the $\ell\ell qq$ search by CMS with the altered requirement of $p_T^J > 200$ GeV. Furthermore, $\Delta R_{J,(\ell\nu)} > \pi/2$, $\Delta\phi_{J,\not{E}_T} > 2.0$, $\Delta\phi_{J,(\ell\nu)} > 2.0$ and $m_{J\ell\nu} > 700$ GeV must hold and events with $b$-tagged jets are vetoed.

#### 7.3.2.6 $\ell\nu qq$ Final State at 13 TeV by ATLAS

The lepton and jet selection is identical to the $\ell\nu qq$ search [283]. Missing transverse energy must exceed 100 GeV and the jet invariant mass window is altered to

70.2 GeV $< m_J <$ 106.4 GeV. $p_T^J > 0.4\, m_{\ell\nu J}$, $p_T^{\ell\nu} > 0.4\, m_{\ell\nu J}$ and $p_T^{\ell\nu} > 200$ GeV is imposed, and events with $b$-tagged jets are vetoed.

#### 7.3.2.7 $\ell\nu qq$ Final State at 13 TeV by CMS

Isolated electrons are selected with $p_T > 120$ GeV and $|\eta| < 2.5$, excluding $1.44 < |\eta| < 1.56$, and isolated muon candidates must fulfil $p_T > 53$ GeV and $|\eta| < 2.1$ [262]. Missing transverse energy must exceed 80 GeV (40 GeV) in case of a single electron (muon). $p_T^{\ell\nu} > 200$ GeV is imposed. Jets are reconstructed as in the respective 8 TeV search with an altered mass window of 65 GeV $< m_J <$ 105 GeV. Furthermore, $\Delta R_{J,(\ell\nu)} > \pi/2$, $\Delta\phi_{J,\not{E}_T} > 2.0$, $\Delta\phi_{J,(\ell\nu)} > 2.0$, and $m_{J\ell\nu} > 700$ GeV is imposed and events with $b$-tagged jets are vetoed.

### 7.3.3 Signal Benchmarks and Simulation Setup

To test the potential of spin discrimination by using angular correlations we need various signal samples with different resonance spins. We consider a spin-0 model, three spin-1 resonances and one spin-2 case. All cases are shown to match the 2 TeV excess we are using as a case study.

The spin-0 case is an ad-hoc real scalar with $0^+$ spin built from the Universal FeynRules Output [284] implementation. It is based on Standard Model Higgs effective couplings to gluons in MadGraph v.1.5.14 [285] and is included purely to demonstrate a heavy real scalar coupled dominantly to longitudinal vector bosons.

The spin-1 resonance include a $Z'$ and $W'$ based on the Heavy Vector Triplet model [211, 286], which was described in context of the 2 TeV excess in ref. [211]. We furthermore consider a $W_R$ spin-1 resonance, which we generate using UFO model files from ref. [233]. See also section 3.4 for further brief details on the respective models.

The spin-2 resonance is based on a heavy graviton implemented in a Randall-Sundrum scenario [75, 76]. See ref. [287] for the MadGraph model file implementation and section 3.5 for further brief information about the model.

Parton level events are generated in MadGraph with an on-shell resonance. The subsequent decays to vector bosons and final state fermions are also included at parton level to ensure proper treatment of spin correlations. We cross-checked the parton level angular distributions with the analytic expectation from ref. [193].

The dominant QCD dijet background is simulated at parton level using Pythia v.8.2 [288].

The results are then showered and hadronised by Pythia v.8.2 [288]. We use Delphes v.3.1 [146] for the reconstruction of leptons and $b$-tagging including de-

tector effects. Since DELPHES has no jet substructure algorithms implemented we reconstruct fat jets and apply the various jet substructure techniques using FASTJET v.3.1.0 [289]. To account for detector effects we smear the $p_T$, $\phi$ and $\eta$ of the jet constituents according to their respective energy fraction in respect to the full jet. We checked that the resulting $W$ and $Z$ mass resolution matches those of the $4q$ ATLAS analysis.

## 7.4 Analysis Effects in the Hadronic Final State

We recast the hadronic $4q$ searches by ATLAS and CMS at 8 TeV and 13 TeV using the simulation setup described in the previous section. Using the subjets determined by the different jet substructure techniques we reconstruct the angular correlations. Due to the poor mass resolution of the $W$ and $Z$ peaks a discrimination between both is poor. Thus we treat both as equivalent and therefore merge the two observables $\cos\theta_{p1}$ and $\cos\theta_{p3}$ to $\cos\theta_q$.

Furthermore, it is not possible to distinguish between quarks and anti-quarks, thus we assign the label $p_1$ and $p_2$, and $p_3$ and $p_4$ randomly. This renders the sign of $\cos\theta_q$ ambiguous. As for any differential observable a higher rate is important we do not distinguish between high- and low-purity vector bosons in case of the CMS analysis either.

From all angles defined in section 7.2 we find that $\cos\theta^*$, $\cos\theta_q$ and $\Psi$ yield significant discrimination power between different spin hypotheses. The following section will go through them one by one and we will explain how the analysis skews the respective differential shape. In order to do so each set of figures will include the original differential shapes at parton level, *i.e.* without any analysis cuts at Monte Carlo truth level, and those after proper reconstruction using jet substructure techniques.

### 7.4.1 $\cos\theta^*$

$\cos\theta^*$ is the angle between one of the vector bosons and the beam axis in the rest frame of $X$. Under the assumption that the threshold approximation holds the rest frame of $X$ can be identified with the lab frame. We present the results for the $\cos\theta^*$ angle in fig. 21. Each panel corresponds to one analysis, ATLAS at 8 TeV (upper left), CMS at 8 TeV (upper right), ATLAS at 13 TeV (lower left), and CMS at 13 TeV (lower right), respectively. Thin lines correspond to parton level results and thick lines to those after the analysis is applied.

We see that at parton level this angle provides very good discrimination power between a spin-1 resonance and a spin-0/2 model. Also, a spin-0 and spin-2 model

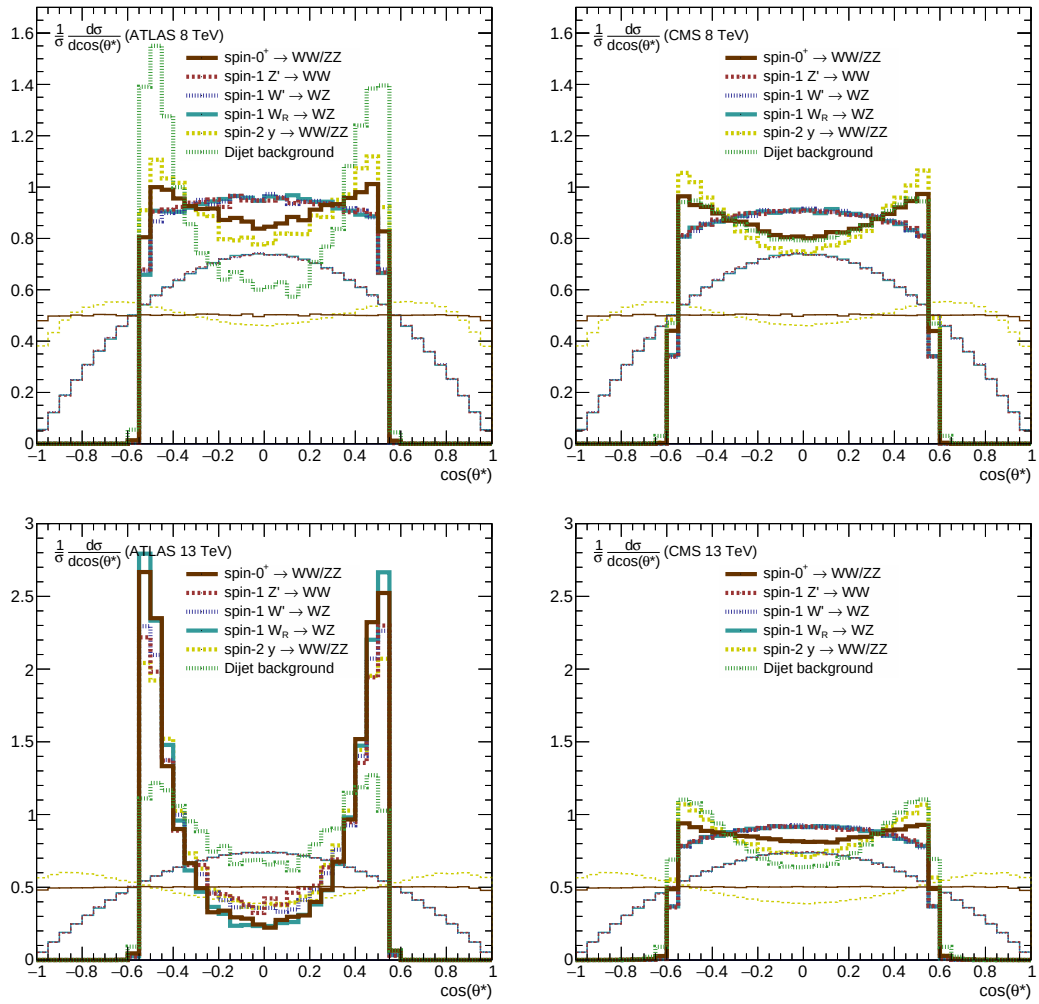


Figure 21: Comparison of the $\cos\theta^*$ angle between parton level results (thin lines) and reconstruction of showered events via jet substructure algorithms (thick lines) for the ATLAS (left) and CMS (right) hadronic diboson search at 8 TeV (top) and 13 TeV (bottom). Each differential distribution is unit-normalized.

can be discriminated due to extra oscillations for a spin-2 resonance.

After applying the analysis cuts some of this discrimination power is lost, especially for the spin-0 versus spin-2 case. Only a spin-1 resonance shows significant difference to the other model hypothesis.

In total we can note two major differences between parton level results and those after analysis effects are taken into account. First, we see a very pronounced sharp cut at around $|\cos\theta^*| \lesssim 0.55$ for ATLAS and $|\cos\theta^*| \lesssim 0.6$ for CMS. And second, there is a slight deficit of events around $\cos\theta^* \approx 0$ in each analysis. This can most

easily be seen by looking at the spin-0 hypothesis, which yields a perfectly flat distribution at parton level but develops a concavity after reconstruction on top of the just mentioned sharp cut. The effect is most prominent in the ATLAS 13 TeV analysis.

The sharp edge can simply be explained by the cut on the rapidity difference $|\Delta\eta|$ between the two fat jets, which is employed in every analysis. Since $\cos\theta^*$ measures the angle with respect to the beam axis, it is of course related to the pseudorapidity $\eta = -\log\tan(\theta/2)$. In the rest frame of the $X$ resonance this gives the relation

$$|\cos\theta^*| = \cos\left(2\arctan e^{-\frac{|\Delta\eta|}{2}}\right) = \tanh\frac{|\Delta\eta|}{2} \leq \tanh\frac{|\Delta\eta_{\max}|}{2} \ . \tag{88}$$

The analysis cuts of ATLAS and CMS are $|\Delta y_{\max}| = 1.2$ and $|\Delta y_{\max}| = 1.3$, which subsequently results in a sharp cut at $|\cos\theta^*| \approx 0.54$ and 0.57, respectively. The slope is, however, slightly affected by the net transverse momentum of the $X$ resonance in the lab frame, in which case the direct relation to the pseudorapidity becomes only approximate.

The cause for the deficit at $\cos\theta^* \approx 0$ is a little bit more subtle and is related to the angular scale chosen in each jet substructure technique. We know from eq. 88 that $\cos\theta^*$ is connected to the pseudorapidity difference of the two fat jets $|\Delta\eta|$. But furthermore, we found that this pseudorapidity difference is also correlated with the angular separation of their subjets $\Delta R$. We present this correlation in fig. 22 at parton level.

This figure shows two distinct bands which correspond to a $W$ and $Z$ boson due to their difference in mass, respectively. As we can see the bulk follows the approximation $\Delta R \approx 4m_V/m_X$ with $m_X = 2$ TeV. We use a $W'$ event sample to illustrate this behaviour, but the basic shape of the differential distribution holds also for other signal hypotheses. The only difference is the relative weight between the $W$ and $Z$ band.

Note that for less central jets the angular separation $\Delta R$ of their subjets is typically larger than for central jets. This is an important information, as a larger separation between the subjets means they are easier to disentangle by the substructure algorithm. This explains the slightly higher selection efficiency for large $|\Delta\eta|$, *i.e.* large $|\cos\theta^*|$.

This effect is most prominent in the ATLAS 13 TeV analysis, as they recluster the constituents of the fat jet with a cone radius of $R = 0.2$. Such a large angular scale will cause most subjets with $\Delta R < 0.2$ to merge together, thus almost no events with $\cos\theta^* \approx 0$ can pass our event selection. But note that the latter is only true when one

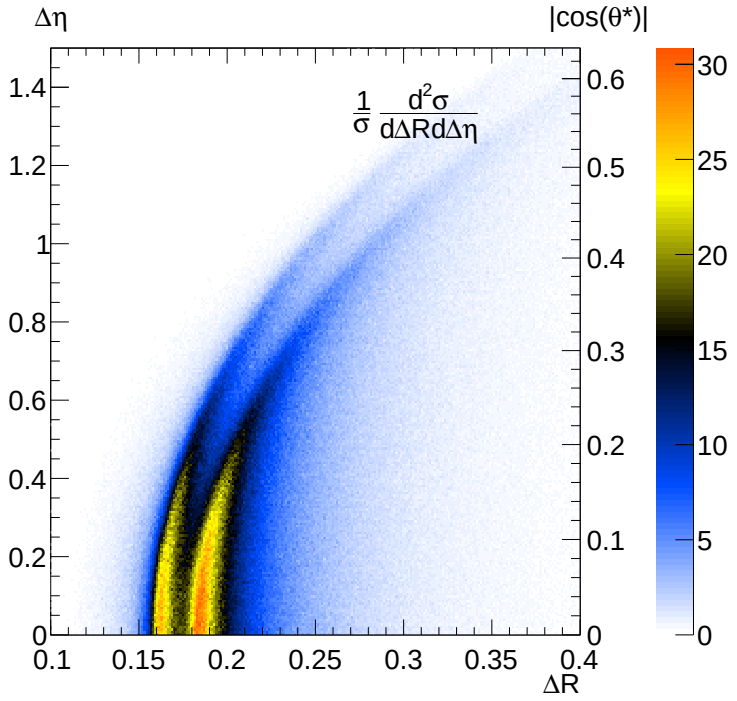


Figure 22: Spin-1 $W'$ parton level correlation of the angular separation $\Delta R$ between the $V$ decay products and the pseudorapidity difference $\Delta\eta$ of the two fat jets. The left band shows the $W$ decay products and the right band shows the $Z$ decay products, and the shading shows the relative event weight. This correlation holds also for other spin scenarios. The $\Delta\eta$ axis is translated to a $|\cos\theta^*|$ axis according to eq. 88.

tries to reconstruct angular correlations. ATLAS does not attempt this, thus they do not actually require the identification of two distinct subjets as we have to do it. Instead, they employ the energy correlator function $D_2^{(\beta)}$ on top of their reclustering to test the two-prong structure of the fat jet. As they are not interested in the subjets anyways, their analysis is still fine by not reconstruction the four-momenta of the subjets explicitly. Nevertheless, that means that the ATLAS analysis at 13 TeV is not particularly suitable for spin discrimination.

### 7.4.2 $\cos\theta_q$

The $\cos\theta_q$ angle measures the angular distance between one subjet in the rest frame of the parent $V$ boson and the boost vector of the parent. As there are two $V$ bosons, each event contributes twice. We present the differential shapes in fig. 23.

It is easy to see by looking at the parton level results, that the only spin hypothesis

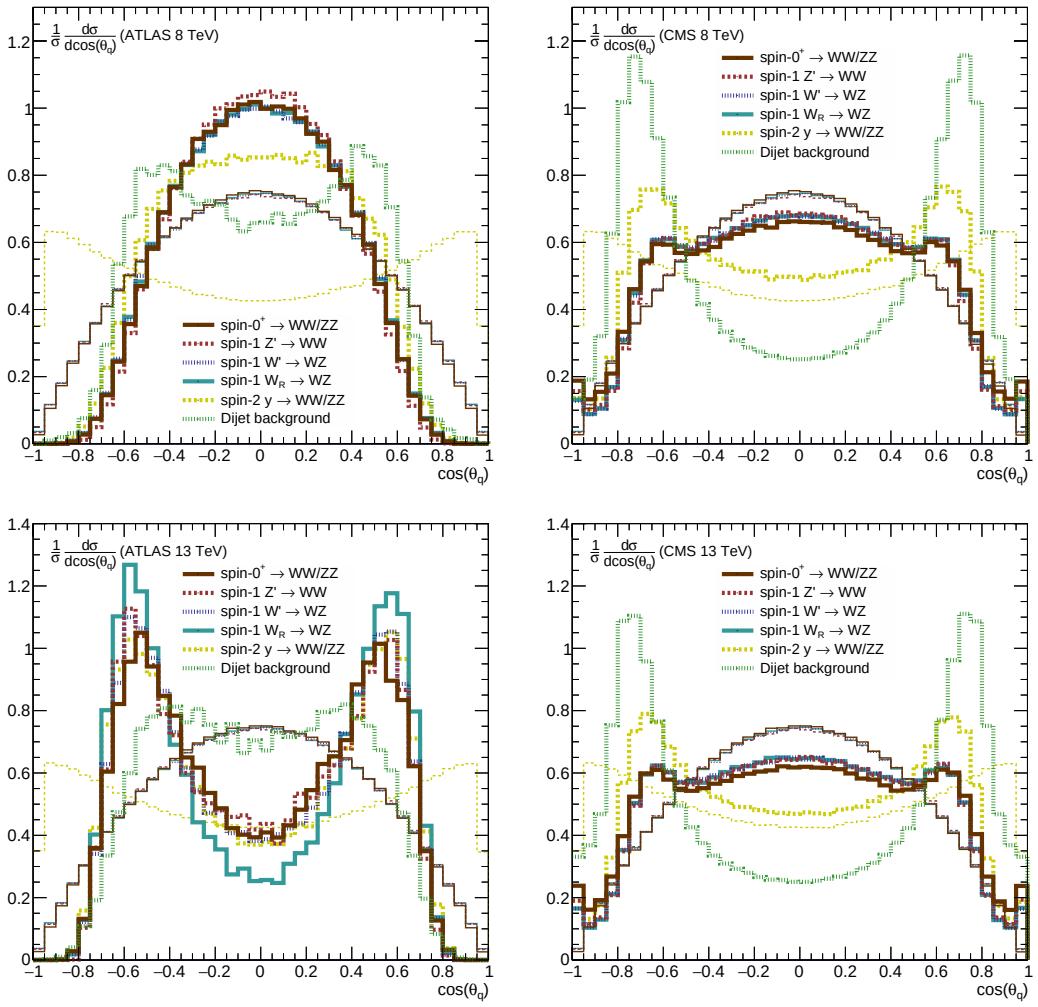


Figure 23: Comparison of the $\cos\theta_q$ angle between parton level results (thin lines) and reconstruction of showered events via jet substructure algorithms (thick lines) for the ATLAS (left) and CMS (right) $4q$ searches at 8 TeV (top) and 13 TeV (bottom).

that differs from others is that of a spin-2 resonance. This is interesting, as the spin-2 resonance couples dominantly to transversely polarised vector bosons, whereas the other scenarios are coupled preferably to longitudinally polarised bosons. Thus, the $\cos\theta_q$ angle is a realistic proxy for studying the sensitivity of jet substructure techniques to the electroweak boson polarisation.

More specifically, the analytic expression for a purely longitudinally polarised boson is $3/4\left(1-\cos^2\theta_q\right)$, while it is $3/8\left(1+\cos^2\theta_q\right)$ for transversely polarised bosons [193]. Hence, sensitivity towards the edges of $\cos\theta_q$ will play an important role. This also agrees with an earlier CMS study [290], but we carry the analysis further by studying various different state-of-the-art jet substructure algorithms to understand the impact

of vector boson polarisation on the selection efficiency.

Regarding the differences between parton level and reconstruction level the differential shape of the $\cos\theta_q$ shows very similar features as the $\cos\theta^*$ angle. There is a cliff, although not as pronounced, around $\cos\theta_q \approx \pm 0.6$ and $\cos\theta_q \approx \pm 0.8$ for ATLAS and CMS, respectively. Furthermore, we observe again a deficit of events at around $\cos\theta_q \approx 0$, which is again most prominent in the ATLAS 13 TeV analysis. These effects, however, are of different origin than those of the $\cos\theta^*$ angle.

To understand the soft cliff it is helpful to derive an approximate relation between $\cos\theta_q$ and the subjet momentum balance $y$, as defined earlier. For this we need to go back to the definition of the angle in terms of momentum, $\cos\theta_q \equiv \hat{p}_{p_1} \cdot \hat{p}_{V_2}$, where we identified $\cos\theta_q$ with $\cos\theta_{p_1}$ without loss of generality. Here, both momenta are boosted into the rest frame of $V_1$. Assuming threshold production the rest frame of $X$ coincides with the lab frame, thus $V_1$ and $V_2$ are back-to-back. Then $\hat{p}_{V_2}$ can be replaced by $-\hat{p}_{V_1}$ going from the lab frame to the $V_1$ rest frame.

Hence, $\cos\theta_q$ is a function of eight momentum parameters, or in the limiting case of absent longitudinal momentum of $V_1$ and $V_2$ only six. $-\hat{p}_{V_1}$ can be replaced by $p_2$ using four-momentum conservation. In addition we have four constraints on the system, reducing the amount of free parameters to two: $(p_1+p_2)^2 = m_{V_1}^2$, $p_1^2 = p_2^2 = 0$, and $y = p_{T_2}/p_{T_1}$. We chose those two parameters to be the transverse momentum of $V_1$, $p_{T,V_1}$, and the angle $\Theta$ between the decay plane spanned by its decay products $p_1$ and $p_2$ relative to the transverse plane. However, this can only reproduce the absolute value of $\cos\theta_q$, as we order both subjets in $p_T$ when defining $y$. But since we cannot distinguish $p_1$ and $p_2$ at the LHC anyway this is not an issue.

Note that the angle $\Theta$ can be chosen almost arbitrarily. Thus by aligning it with either the transverse plane or the plane that is spanned by the beam axis and the $V_1$ boson, a lower and upper bound on $|\cos\theta_q|$ can be determined. These are after proper reparameterisation given by

$$\frac{p_{T,V}}{\sqrt{m_V^2 + p_{T,V}^2}} \frac{1-y}{1+y} \leq |\cos\theta_q| \leq \frac{\sqrt{m_V^2 + p_{T,V}^2}}{p_{T,V}} \frac{1-y}{1+y} \,. \tag{89}$$

In order to derive these bounds we performed an azimuthal rotation to align $V_1$ with $\hat{y}$ without loss of generality.

The upper bound in eq. 89 can in principle exceed 1 for some phase space regime, which is because of restrictions on the choice of $\Theta$. Aligning the decay plane with the beam axis may become unphysical and a slight rotation is needed. In this case, the upper bound simply saturates at 1.

In the limit of boosted bosons with $p_{T,V} \gg m_V$, which is certainly the case in this

study, this yields

$$|\cos\theta_q| \approx \frac{1-y}{1+y} \leq \frac{1-y_{\min}}{1+y_{\min}} \ . \tag{90}$$

Hence, $\cos\theta_q$ is directly related to the momentum asymmetry of the two subjets. As every jet substructure algorithms requires a certain amount of balance in one way or the other, this skews the angular observable accordingly. Using the respective limits of $y_{\min} = 0.20$, 0.11, or 0.05 for the ATLAS 8 TeV, CMS, and ATLAS 13 TeV analyses, we expect a cliff to appear at $|\cos\theta_q| = 0.66$, 0.80, or 0.90, respectively.

Note that eq. 90 is only an approximate relation, as we ignored during the derivation any longitudinal boost of the parent particle $V$. Including this boost $\cos\theta_q$ will receive corrections, effectively smearing out the cliff. This effect can be observed in fig. 23.

The expected position of the cliffs in the $\cos\theta_q$ distribution matches well the observation in fig. 23, except for ATLAS at 13 TeV. There, the imposed cut is $y_{\min} = 0.05$ and therefore one expects $|\cos\theta_q| \leq 0.9$. The cliff, however, seems to be closer to 0.7.

The reason for the discrepancy is the energy correlator function $D_2^{(\beta)}$. This observable inhibits a correlation with the momentum balance $y$, as shown in fig. 24. ATLAS places an upper limit on $D_2^{(\beta)}$, which varies between $D_2 = 1.0$ for a fat jet of $p_T = 250$ GeV to $D_2 = 1.8$ for $p_T = 1500$ GeV. According to fig. 24 this corresponds to a cut parameter of $y_{\min} \approx 0.1$–$0.2$. This cut is tighter than before, which is now in agreement with the position of the cliff.

The deficit of events for $\cos\theta_q \approx 0$ is – like the deficit $\cos\theta^* \approx 0$ – caused by a cross-relation between $\Delta R$ and another variable. This other variable is the transverse momentum balance $y$, as this is the parameter $\cos\theta_q$ depends on primarily. We show the relevant relation in fig. 25. Also, this figure is based on the spin-1 $W'$ hypothesis but holds also in a similar fashion for the other scenarios. Hence, a bias towards larger $\cos\theta_q$ is induced by using a large angular scale in the jet substructure algorithm. As this scale is with $R = 0.2$ in the ATLAS 13 TeV analysis the largest one compared to the other analyses, the effect is most prominent in this search.

### 7.4.3 $\Psi$

The angle $\Psi$ is the average angle between the two decay planes spanned by the decay products of the each $V$ boson. We present the differential distribution for this angle in fig 26. The differential shape is completely flat for all spin hypotheses except for the spin-2 scenario. For this model, we expect terms proportional to 1 and $\cos(4\Psi)$ [192,

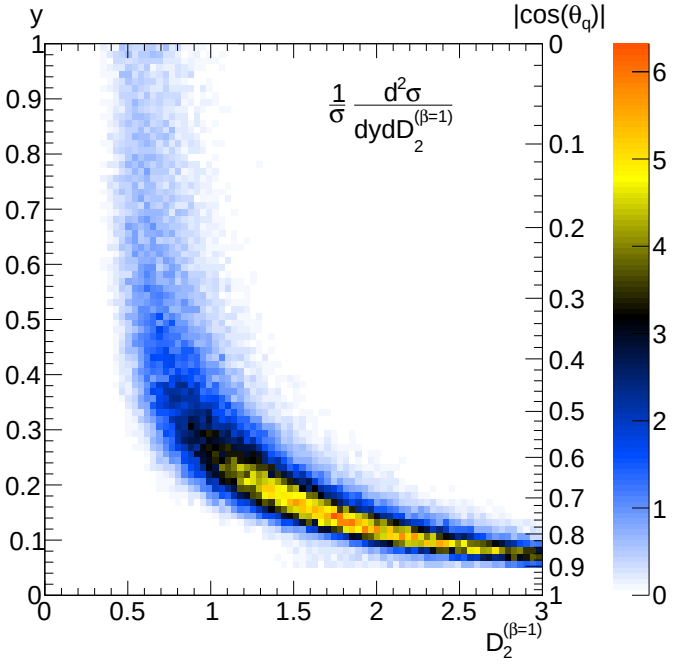


Figure 24: Correlation between the energy correlation function $D_2^{(\beta=1)}$ and the transverse momentum balance $y$ of the two leading subjets. All analysis cuts of the ATLAS 13 TeV analysis are applied, except the cut on $D_2^{(\beta=1)}$ itself. This particular plot is based on the spin-1 $W'$ model, but the correlation seen holds also for other spin scenarios. The $y$ axis is translated to a $|\cos\theta_q|$ axis according to eq. 90.

193]. The relative amplitude of both components depends at parton level on the helicity states of the vector bosons and the initial state partons, thus are model-dependent. A third contribution proportional to $\cos(2\Psi)$ could appear if particles and anti-particles of the $V$ decay products could be distinguished.

Curiously, after applying the complete analysis, the amplitude of the $\cos(4\Psi)$ oscillation grows compared to the initial parton level result. Thus the discrimination power between the different signal scenarios actually increases. This effect can be explained by the same two cuts that already affected the two other angular observables $\cos\theta^*$ and $\cos\theta_q$, namely $\Delta\eta_{\max}$ and $y_{\min}$.

This can be seen by using the analytic fully differential result of ref. [192, 193]. By carefully integrating out all angles except $\Psi$ with the respective integration bounds given by eq. 88 and eq. 90 and using a unit-normalisation, we obtain

$$\frac{1}{\sigma^{(\text{spin-2})}}\frac{d\sigma^{(\text{spin-2})}}{d\Psi} = \frac{1}{2\pi} - \mathcal{A}(y_{\min}, \Delta\eta_{\max})\cos(4\Psi)\ . \tag{91}$$

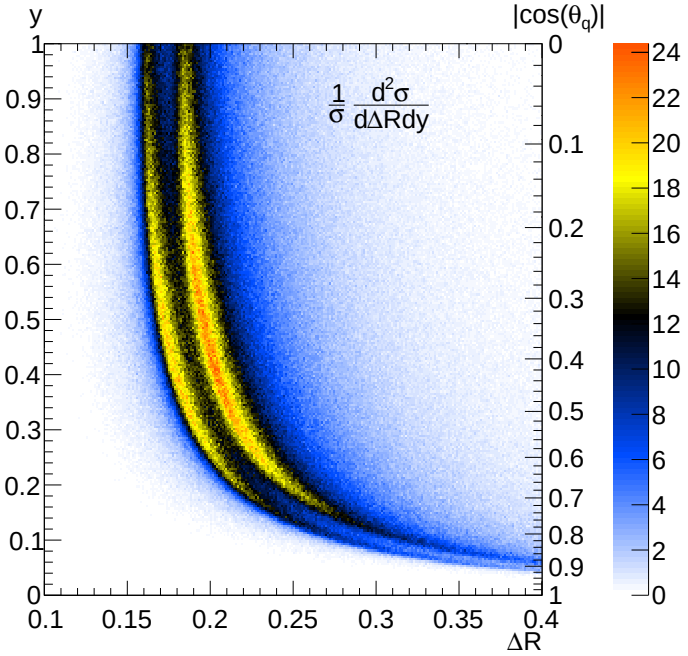


Figure 25: Spin-1 $W'$ parton level correlations of the angular separation $\Delta R$ between the $W/Z$ decay products and their ratio in transverse momentum $y$, where the shading shows the relative event rate. This basic correlation holds also for other spin scenarios. The $y$ axis is translated to an approximate $|\cos\theta_q|$ axis according to eq. 90.

The $\cos(4\Psi)$ amplitude is a function of the two cut parameters and given by

$$\mathcal{A} = \frac{1}{24\pi} F_{+-} \left(1 + 4y_{\min} + y_{\min}^2\right)^2 (5f_{q\bar{q}} - 1)(8 + 6\cosh\Delta\eta_{\max} + \cosh 2\Delta\eta_{\max}) \Big/ \tag{92}$$

$$\left[ F_{+-} \left(1 + y_{\min} + y_{\min}^2\right)^2 \Big( (5f_{q\bar{q}} + 1)(1 + 2\cosh\Delta\eta_{\max}) + 2\cosh 2\Delta\eta_{\max} \Big) + \right.$$

$$\left. F_{00} \left(1 + 4y_{\min} + y_{\min}^2\right)^2 (-15f_{q\bar{q}} + 8 + 6\cosh\Delta\eta_{\max} + \cosh 2\Delta\eta_{\max}) \right] .$$

Here, beside the cut parameters, a few model-dependent parameters enter. $F_{\lambda_1\lambda_2}$ is the fraction of events with two gauge bosons in helicity state $\lambda_1$ and $\lambda_2$. $f_{q\bar{q}}$ is the production fraction of $q\bar{q}$ initial state quarks, compared to a gluon initiated resonance.

For our choice of model the respective values are $F_{+-} = F_{-+} = 45.8\%$, $F_{00} = 7.8\%$ and 0.6% others. We neglect subleading helicity states as they are suppressed by powers of $m_V/m_X$. The production fractions are energy dependent and $f_{q\bar{q}} \approx 65.5\%$ at 8 TeV and $f_{q\bar{q}} \approx 45.0\%$ at 13 TeV. We show the scaling behaviour of the amplitude

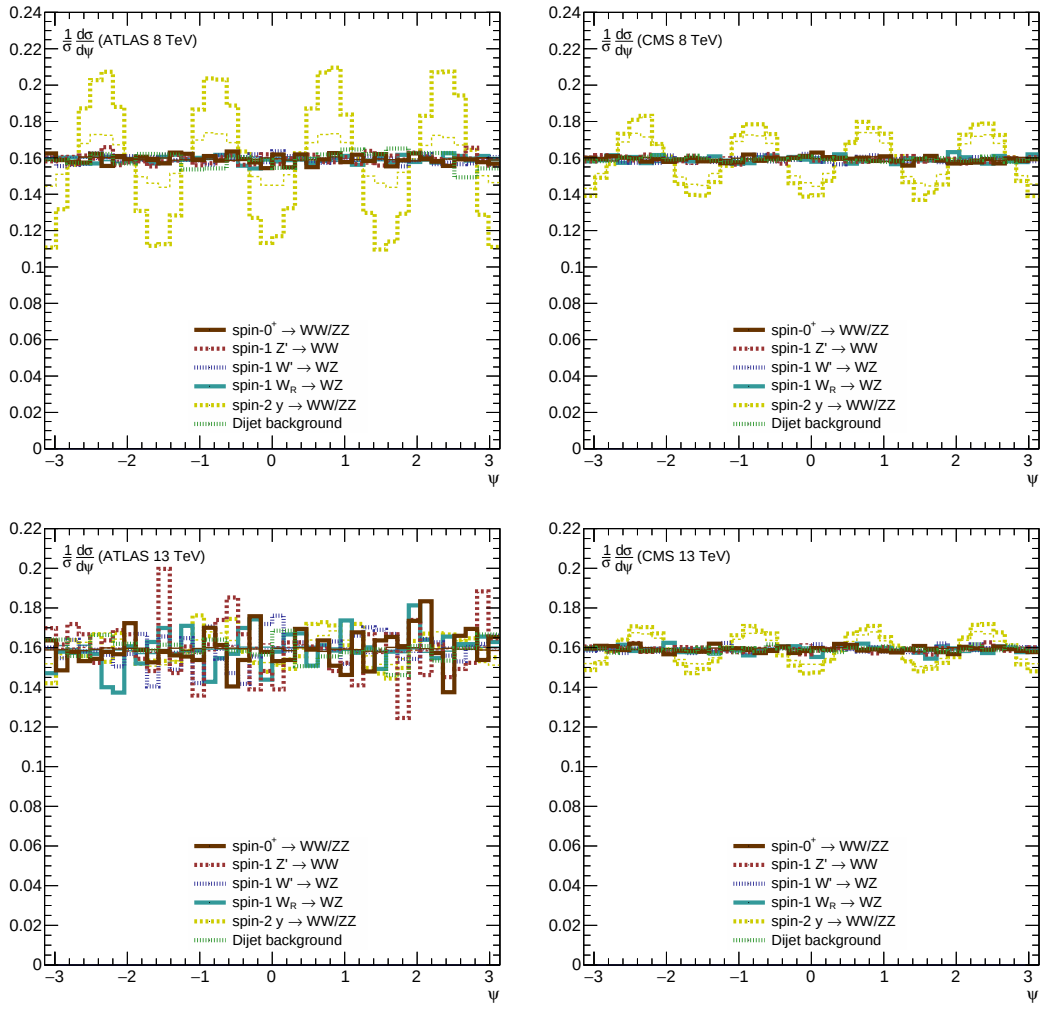


Figure 26: Comparison of the $\Psi$ angle between parton level results (thin lines) and reconstruction of showered events via jet substructure (thick lines) for the ATLAS (left) and CMS (right) hadronic diboson search at 8 TeV (top) and 13 TeV (bottom). Note that the ATLAS 13 TeV analysis suffers from large statistical fluctuations due to its low subjet reconstruction efficiency.

$\mathcal{A}$ in fig. 27 at 8 TeV and 13 TeV with the respective working points of ATLAS and CMS.

Fig. 27 directly allows us to read off the expected $\cos(4\Psi)$ amplitude, which is relevant for spin discrimination. For the limits $y_{\min} \to 0$ and $\Delta\eta_{\max} \to \infty$ we are able to recover the parton level results without any cuts: $\mathcal{A} \approx 0.014$ at 8 TeV and $\mathcal{A} \approx 0.0077$ at 13 TeV. For the working points of both experiments we determine $\mathcal{A} \approx 0.045$ and $\mathcal{A} \approx 0.034$ for ATLAS and CMS at 8 TeV, respectively, and $\mathcal{A} \approx 0.021$ for CMS at 13 TeV. The latter is slightly higher than that seen in fig. 26. This is due to

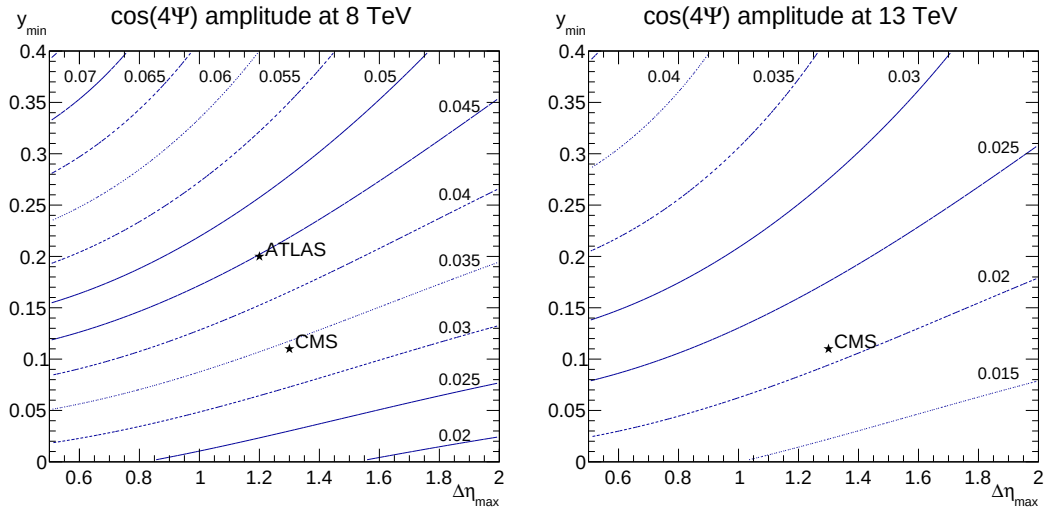


Figure 27: Expected cos(4Ψ) amplitude $\mathcal{A}$ (contours) for a spin-2 resonance at 8 TeV (left) and 13 TeV (right) as function of the cut parameter $y_{\min}$ and $\Delta\eta_{\max}$, as shown in eq. 92. We superimpose the respective working points of ATLAS and CMS, except for ATLAS at 13 TeV, where the effective $y_{\min}$ is not a fixed parameter.

the approximation used when determining the integration bounds, most dominantly for $\cos\theta_q$.

## 7.5 Analysis Effects in the Semi-Leptonic Final State

The semi-leptonic analyses have a couple of advantages over the fully hadronic channel [291, 292]. They are easier to reconstruct as the leptonic side is cleaner and easier to measure in the detector. They also help in disentangling the different $X$ decay channels, as the charge of one of the two $V$ branches is known.

But even though they will typically have a higher signal efficiency due to different sources of backgrounds, the overall rate is still suppressed by the smaller branching fractions of $V$ to leptons. The relevant penalty is about $\mathrm{Br}(W^{\pm}Z \to \ell\ell qq)$ / $\mathrm{Br}(W^{\pm}Z \to 4q) \approx 0.094$, for $\ell = e, \mu$. As we have seen by the 2 TeV excess it is not unlikely that a resonance will show up first in the fully hadronic channel. But for any other mass point and underlying physics, it is not clear which of those channels will actually win over the others. Most definitely the semi-leptonic channel plays an important complementary role. As this channel also contains a hadronic branch, studying the influence of jet substructure techniques is still crucial.

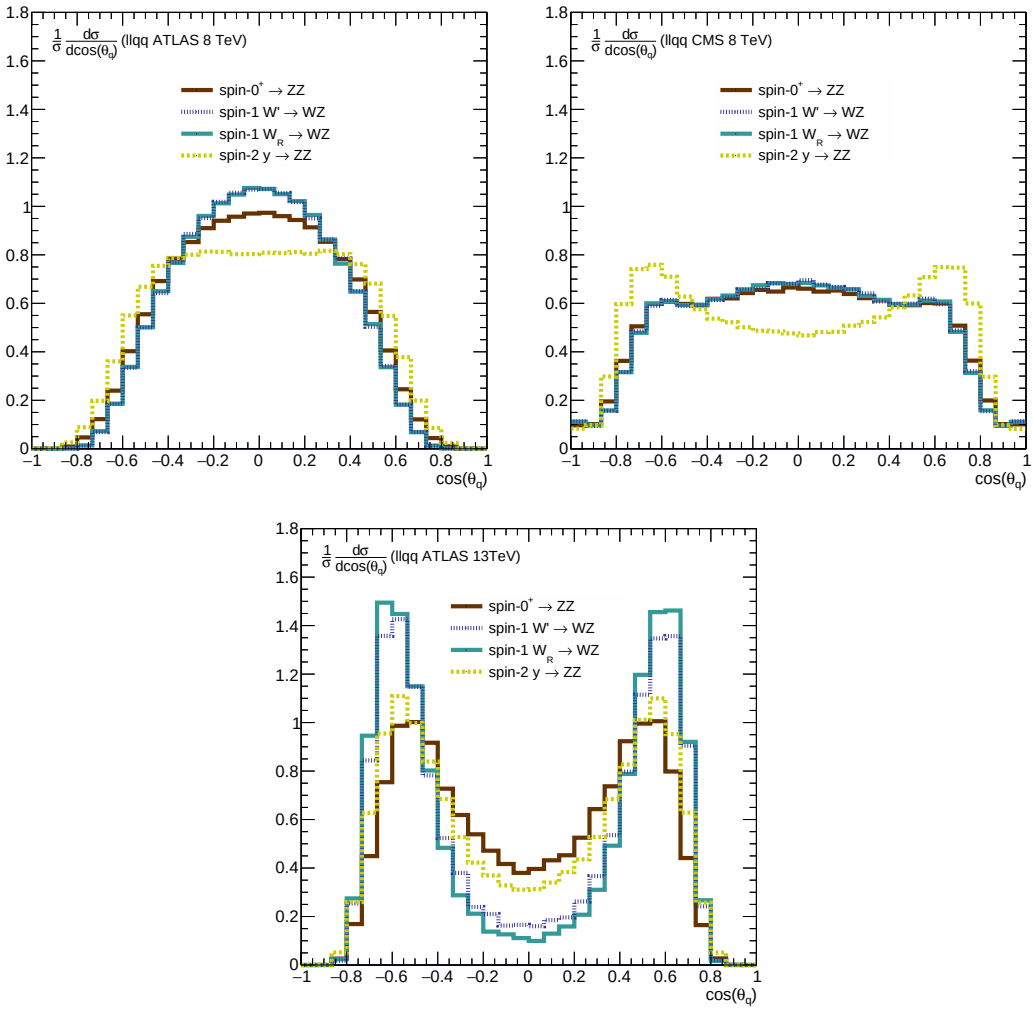


Figure 28: Normalized differential distributions for $\cos\theta_q$ in the semi-leptonic final state $\ell\ell qq$, after imposing the ATLAS 8 TeV (top left), CMS 8 TeV (top right), and ATLAS 13 TeV (bottom) analysis cuts.

We recast the respective ATLAS and CMS $\ell\ell qq$ and $\ell\nu qq$ searches at 8 TeV and 13 TeV, as summarised in section 7.3.2. The angular observables are defined analogously to the fully hadronic case, with the difference that each $V$ boson now contributes to either $\cos\theta_q$ or $\cos\theta_\ell$.

Let us first focus on the $\ell\ell qq$ final state. We present the results for the observables $\cos\theta_q$, $\cos\theta_l$, $\cos\theta^*$ and $\Psi$ in fig. 28, 29, 30, and 31, respectively. For all shown figures we use the same signal samples as before, but for simplicity ignore the different sources of backgrounds.

Many of the shown results mimic the behaviour of the $4q$ analysis with sculpting

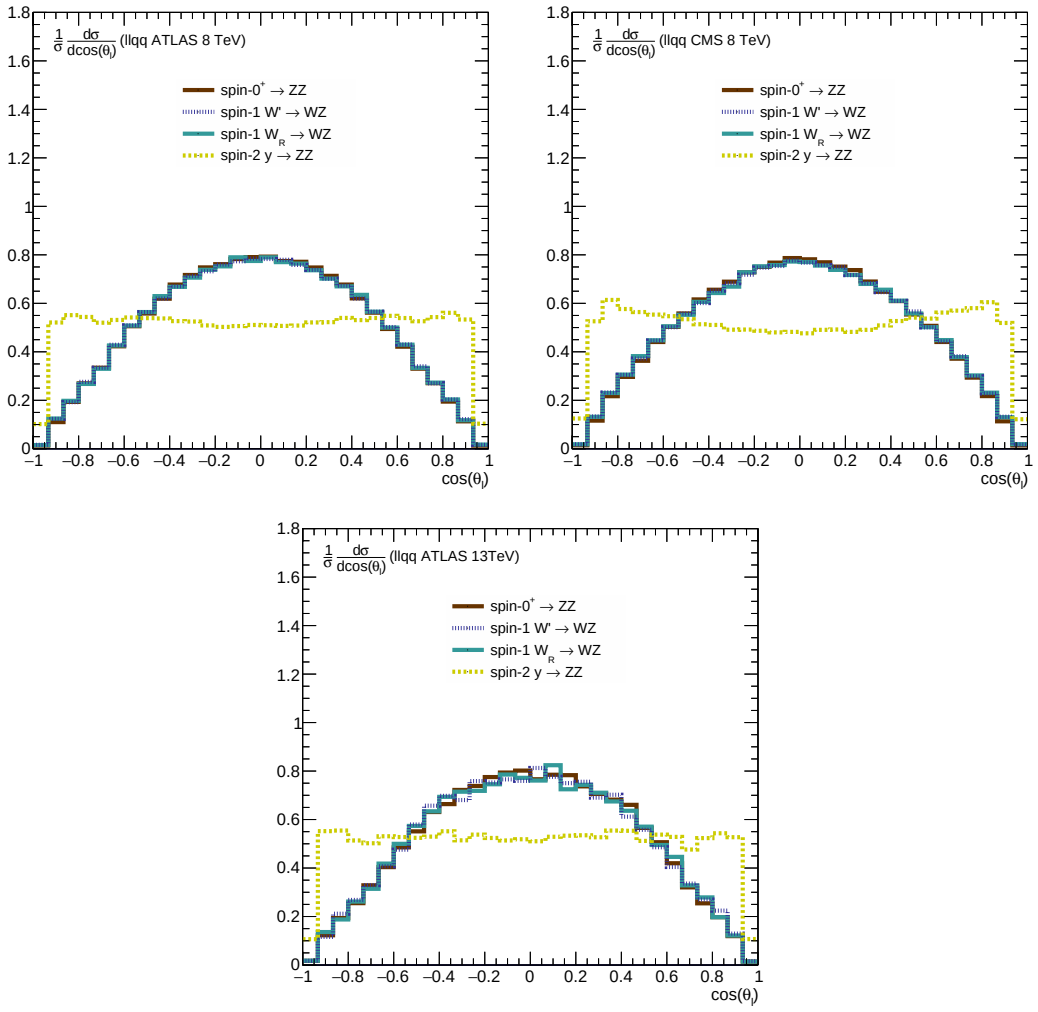


Figure 29: Normalized differential distributions for $\cos\theta_l$ in the semi-leptonic final state $\ell\ell qq$, after imposing the ATLAS 8 TeV (top left), CMS 8 TeV (top right), and ATLAS 13 TeV (bottom) analysis cuts.

effects especially in $\cos\theta_q$. But note that the $\cos\theta_\ell$ angle does not struggle with the same issues $\cos\theta_q$ does. Most of its phase space is preserved, as there is no direct requirement on the momentum balance of the leptons. Nevertheless, the hard cut on the lepton $p_T$ effectively flattens the shape of the spin-2 resonance in this angle compared to $\cos\theta_q$. This is due to the fact that for a large lepton $p_T$ imbalance near $\cos\theta_\ell = \pm 1$ the analysis tends to miss one of the leptons.

The $\cos\theta^*$ observable in fig. 30 preserves generally a very large part of phase space, as no cut on the rapidity difference between the combined leptons and the fat jet is applied. Nevertheless, we see a sharp cut in the ATLAS 13 TeV analysis. Even

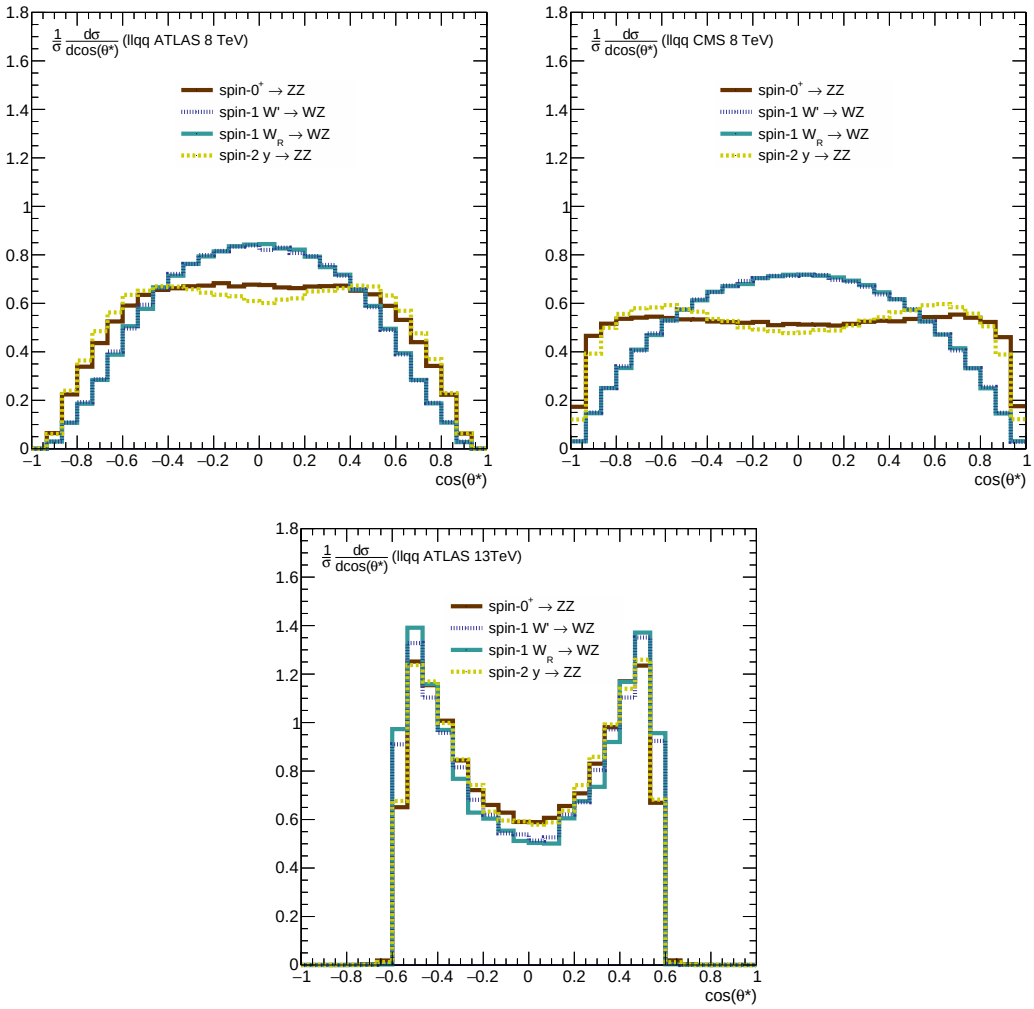


Figure 30: Normalized differential distributions for $\cos\theta^*$ in the semi-leptonic final state $\ell\ell qq$, after imposing the ATLAS 8 TeV (top left), CMS 8 TeV (top right), and ATLAS 13 TeV (bottom) analysis cuts.

though they do not impose a rapidity difference criterion directly, they employ the cuts $p_T^{\ell\ell} > 0.4\, m_{\ell\ell J}$ and $p_T^J > 0.4\, m_{\ell\ell J}$. Using eq. 53 this can be translated into a criterion on the rapidity difference of $\Delta\eta_{\max} \sim 2.1$. This corresponds to $|\cos\theta^*| \lesssim 0.6$ and matches what we observe in the bottom panel of fig. 30.

The same effect, although much weaker, can be observed in the 8 TeV ATLAS analysis, induced by the loose cuts $p_T^{\ell\ell} > 400$ GeV and $p_T^J > 400$ GeV. This corresponds to a cliff at $|\cos(\theta^*)| = 0.92$. In this regard the CMS analysis provides a much better spin discrimination than the ATLAS analyses.

The observable $\Psi$, shown in fig. 31, behaves very similar to the fully hadronic channel.

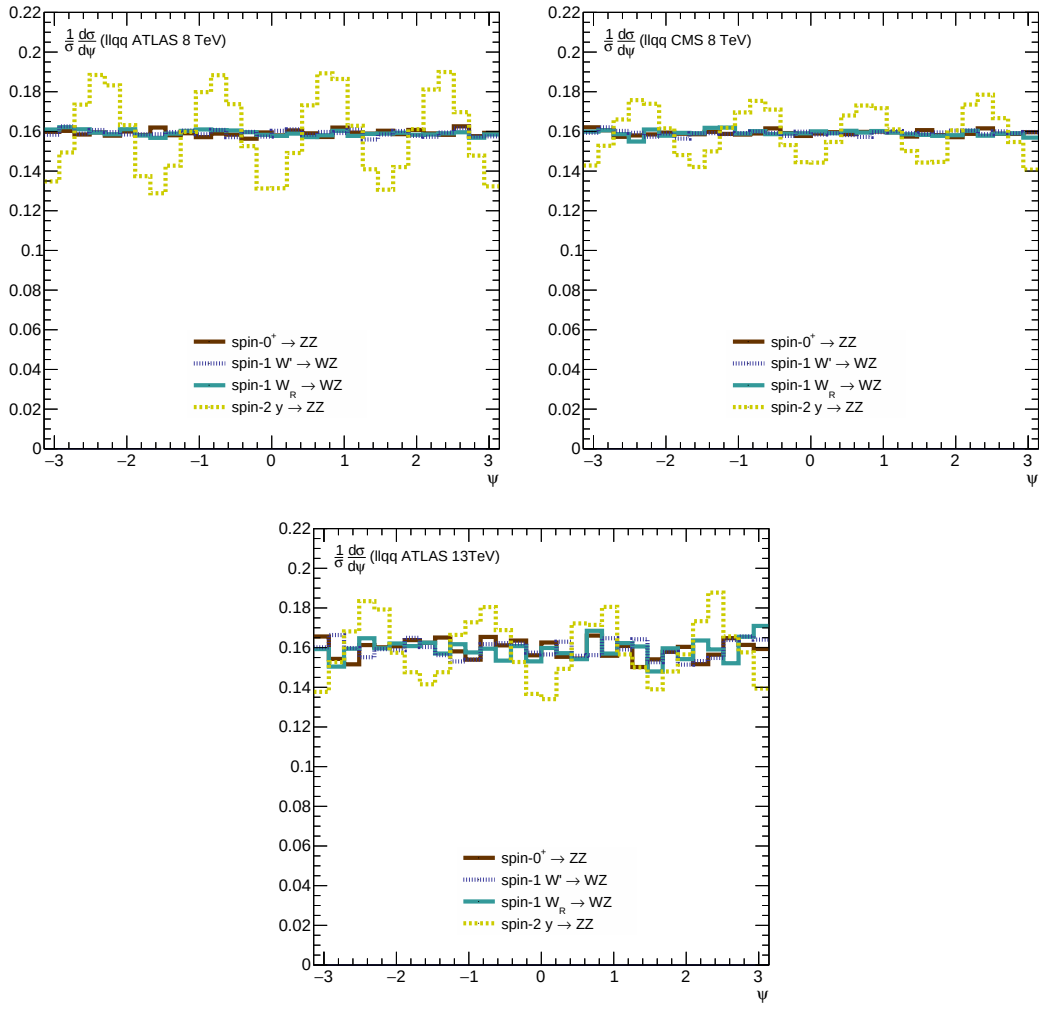


Figure 31: Normalized differential distributions for $\Psi$ in the semi-leptonic final state $\ell\ell qq$, after imposing the ATLAS 8 TeV (top left), CMS 8 TeV (top right), and ATLAS 13 TeV (bottom) analysis cuts.

Coming now to the $\ell\nu qq$ final state, we show the results for the $\ell\nu qq$ searches for $\cos\theta^*$, $\cos\theta_q$, $\cos\theta_l$ in fig. 32, 33, and 34. We omit the observable $\Psi$ for this final state as it does not show any significant discrimination power between different spin hypotheses.

Again we see a very similar picture, the most dominant change though is visible in the $\cos\theta_\ell$ distribution. This distribution is asymmetric, which is caused by a contamination of $\tau$ leptons. The extra neutrino in the decays $\tau \to e\bar{\nu}\nu$ and $\tau \to \mu\bar{\nu}\nu$ leads to a false reconstruction of the $W^\pm$ rest frame.

This effect is not visible in the $\ell\ell qq$ final state with $\ell = \tau$, as here both neutrino

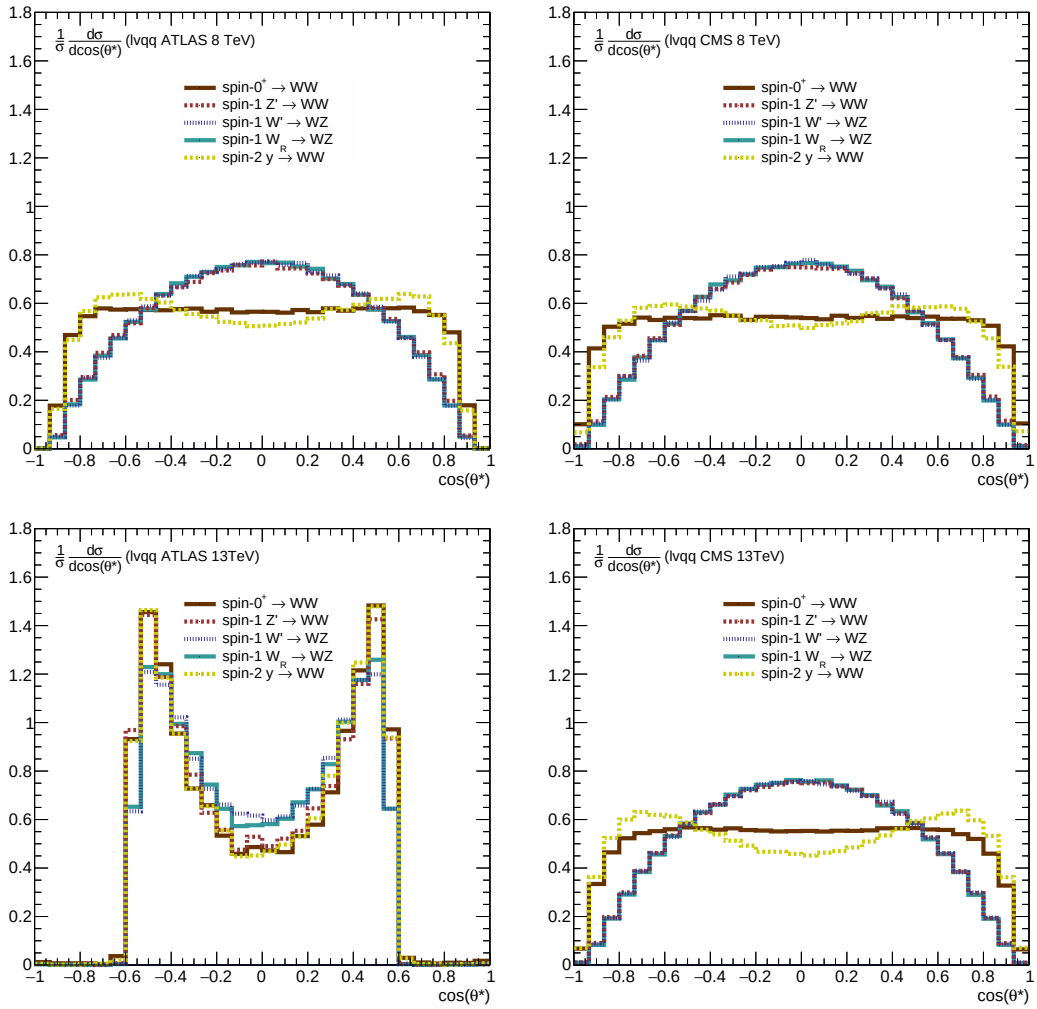


Figure 32: Normalized differential distributions for $\cos\theta^*$ for the semi-leptonic final state $\ell\nu qq$, after imposing the ATLAS 8 TeV (top left), CMS 8 TeV (top right), ATLAS 13 TeV (bottom left), and CMS 13 TeV (bottom right) analysis cuts.

components tend to cancel out. It still skews the overall distribution but in a symmetric way. For the $\ell\nu qq$ final state, however, only one $\tau$ appears. The incorrect rest frame determination causes the charged lepton to typically appear closer to the $W^{\pm}$ rest frame boost vector, as it actually is. Thus the distribution is skewed towards one side in the $\cos\theta_\ell$ distribution.

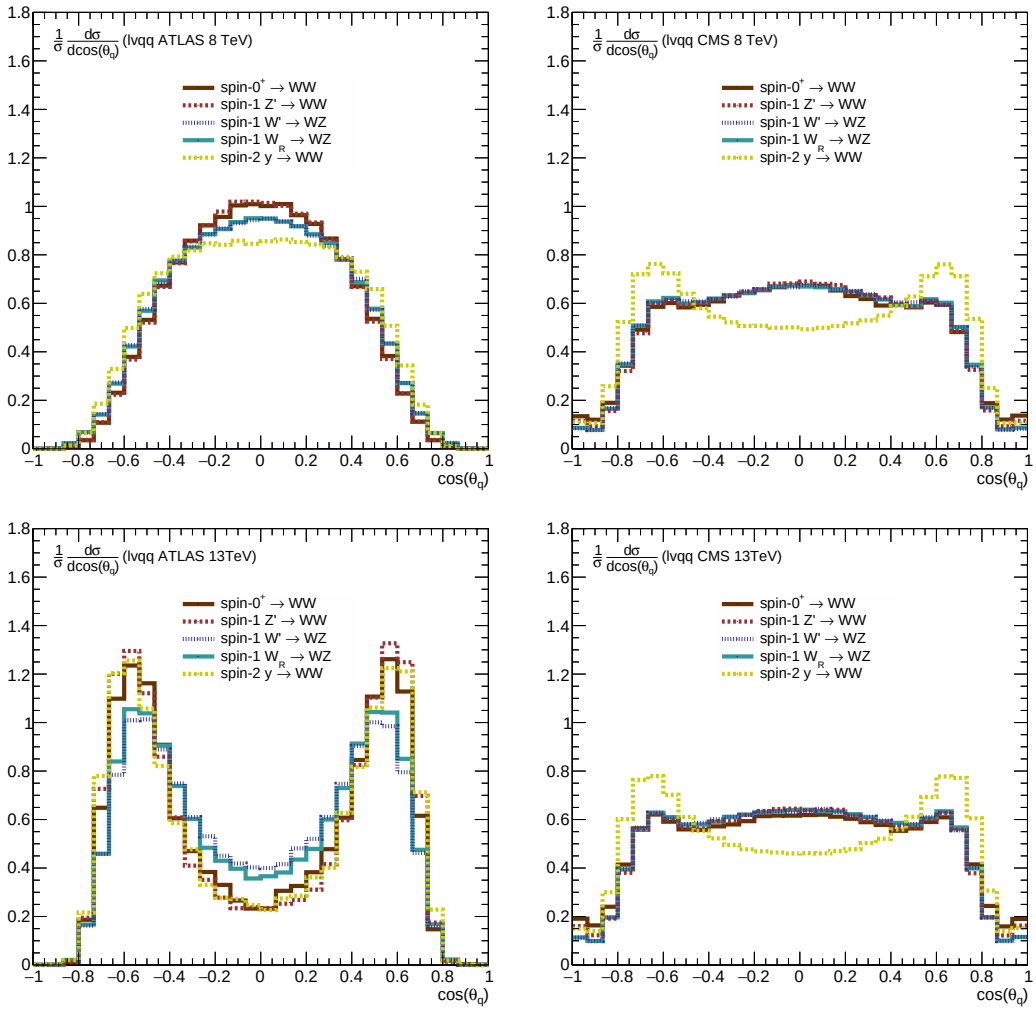


Figure 33: Normalized differential distributions for $\cos\theta_q$ for the semi-leptonic final state $\ell\nu qq$, after imposing the ATLAS 8 TeV (top left), CMS 8 TeV (top right), ATLAS 13 TeV (bottom left), and CMS 13 TeV (bottom right) analysis cuts.

## 7.6 Projection for Model Discrimination

After we have thoroughly discussed how the different analysis cuts and jet substructure techniques alter the differential shapes of angular observables, this examination was only a qualitative test of spin discrimination power. Hence, a quantitative examination using the $CL_s$ method [149] is necessary, where one signal hypothesis is tested against others.

We include all three angular observables which have proven to show discrimination power: $|\cos\theta^*|$, $|\cos\theta_q|$, and $|\Psi|$. We will focus on the fully hadronic channel $4q$, thus final state particles and intermediate vector bosons are not distinguishable, or

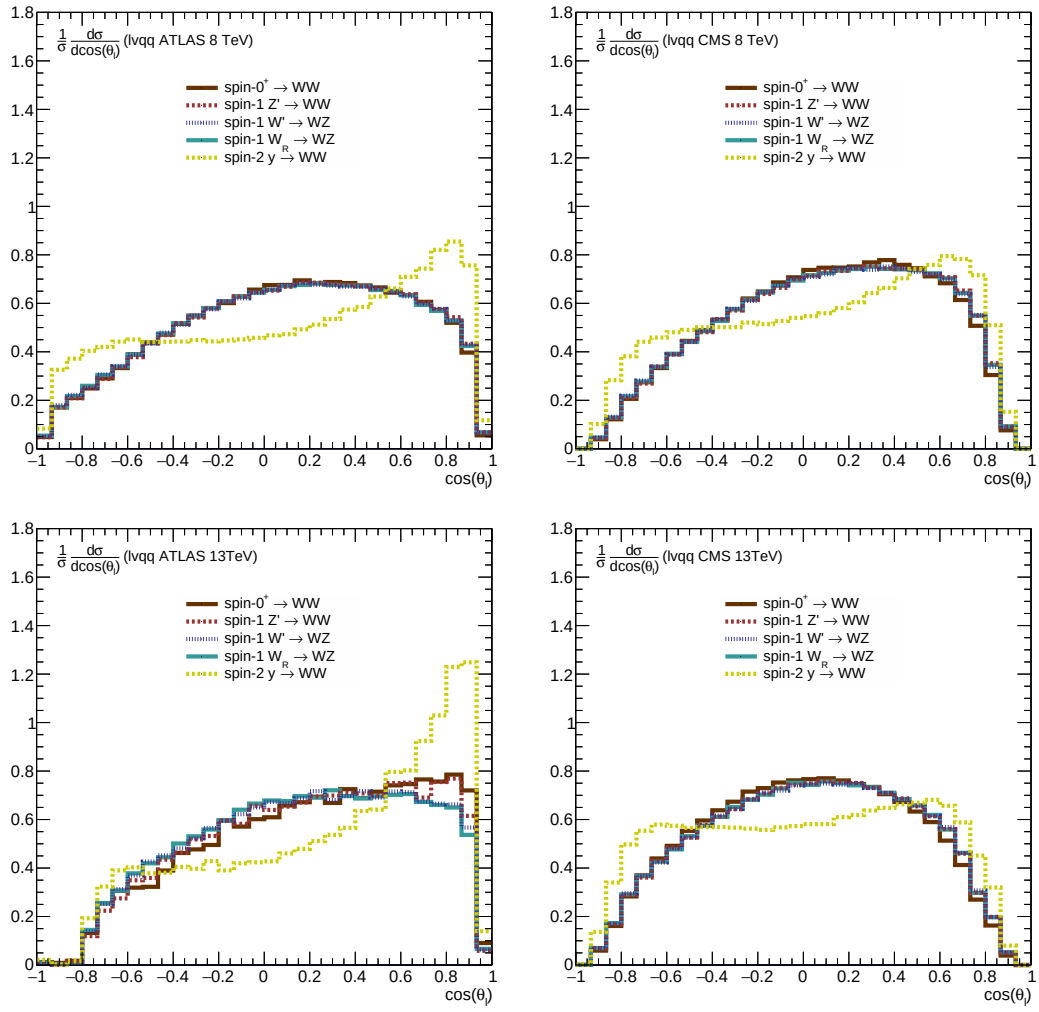


Figure 34: Normalized differential distributions for $\cos\theta_l$ for the semi-leptonic final state $\ell\nu qq$, after imposing the ATLAS 8 TeV (top left), CMS 8 TeV (top right), ATLAS 13 TeV (bottom left), and CMS 13 TeV (bottom right) analysis cuts.

only very poorly. The observables are thus expected to be symmetric around 0. We therefore take the absolute value in order to enhance their statistical power. In addition, will we use a combination of all three observables, which will naturally yield the highest significance.

We perform pairwise tests of a signal A+background versus a signal B+background. Each of those tests is performed twice using a different setup each.

We are using the ATLAS 2 TeV excess [198] as a case study, which was seen at $\sqrt{s} = 8$ TeV. Our statistical test, however, will be based on $\sqrt{s} = 13$ TeV, as this is where a new resonance could still be detected. Thus an appropriate scaling factor on

the production cross sections has to be included to move from $\sqrt{s} = 8$ TeV to 13 TeV. This scaling is dominated by PDF effects and as the various signal hypotheses are produced via different initial states the scaling will be different for each signal model.

Our spin-0 signal is produced via gluon fusion and will therefore have the highest increase in production rate. The spin-1 resonances will have the smallest increase, as they are based on a $qq'/q\bar{q}$ initial state. The spin-2 resonance is produced by a mix of both. Hence, if the 2 TeV excess would have been real, every signal model would have the same fiducial cross section at $\sqrt{s} = 8$ TeV, but not at $\sqrt{s} = 13$ TeV. In our first statistical test at $\sqrt{s} = 13$ TeV we take this difference in cross section into account.

For the second $CL_s$ test, however, we rescale the cross section of the signal model of the test hypothesis to the cross section of the signal of the null hypothesis. Hence, this test is based only on the differential shape of the angular observables, whereas the first test is based on rate and shape information. This second test is a better proxy for when a new resonance is found at a different mass, as all signal hypotheses have to match the measured fiducial cross section.

The overall signal normalisation is based on the ATLAS analysis at 8 TeV, where they reported 8 excess events over the expected 8.94 background events inside a mass window of 300 GeV width around a resonance mass of 2 TeV [198]. We assume that the complete resonance peak is enclosed in this window. Together with the PDF scaling factor, which we determined by simulation, and the respective signal efficiencies of each analysis, we use this information to normalise the signal.

The overall background normalisation is also taken from the respective experimental analysis, albeit based on slightly different mass windows. Specifically, those are $[1850, 2150]$ GeV for ATLAS at 8 TeV, $[1800, 2200]$ GeV for ATLAS at 13 TeV, and $[1852.3, 2136.4]$ GeV for CMS at 13 TeV.

One further complication for the ATLAS analysis at $\sqrt{s} = 13$ TeV arises. As we do not distinguish between $W$ and $Z$ bosons to keep the overall rate high, we need to know the inclusive diboson rate. This information is not provided by ATLAS at 13 TeV, as it only presents values for the $WW$, $WZ$, and $ZZ$ categories. Since the respective $W$ and $Z$ mass windows overlap, a single event can contribute to several of these categories. Thus we need to disentangle these channels first to avoid double counting.

Fortunately, ATLAS mentions that in the mass range 1 TeV$< m_{JJ} <$2.5 TeV in total 38 events lie in the overlap region such that they contribute to all three categories. We can use this information to estimate the inclusive rate. For this we assign $p \approx \sqrt{38/N}$ as the flat probability that a boson is tagged as both, a $W$ and a $Z$. $N$ is here the number of inclusive events, *i.e.* our value of interest. We can

express $N$ as $N = N^0_{WZ} + N^0_{WW} + N^0_{ZZ}$, where $N^0_{VV'}$ is the exclusive category with an intermediate $V$ and $V'$ boson, so *without* any overlap.

Similarly, we can rewrite $N$ as a sum of $N_{VV'}$, which are the respective categories *with* overlap, but subtracting double- and triple-counted events,

$$\begin{aligned} N = {} & N_{WZ} + N_{WW} + N_{ZZ} \\ & - N^0_{WZ} \cdot [\mathcal{P}(Z \text{ in overlap region}) + \mathcal{P}(W \text{ in overlap region}) + \\ & \qquad 2\mathcal{P}(W \text{ and } Z \text{ in overlap region})] \\ & - N^0_{WW} \cdot [\mathcal{P}(\text{one } W \text{ in overlap region}) + 2\mathcal{P}(\text{both } W \text{ in overlap region})] \\ & - N^0_{ZZ} \cdot [\mathcal{P}(\text{one } Z \text{ in overlap region}) + 2\mathcal{P}(\text{both } Z \text{ in overlap region})] \ . \end{aligned} \tag{93}$$

The occasional factors of 2 arise due to the fact that in this case, the event contributes to all three categories, thus two events have to be subtracted from the sum. ATLAS claims to have $N_{WZ} + N_{WW} + N_{ZZ} = 300$, thus

$$\begin{aligned} N &= 300 - N^0_{WZ} \left[p(1-p) + p(1-p) + 2p^2\right] \\ &\quad - N^0_{WW} \left[2p(1-p) + 2p^2\right] \\ &\quad - N^0_{ZZ} \left[2p(1-p) + 2p^2\right] \\ &= 300 - 2Np \ . \end{aligned} \tag{94}$$

Together with $p \approx \sqrt{38/N}$ we can solve the above equation for $N$, which yields $N \approx 149$. Broken up into the different categories that means 75 events were double-counted and 38 events triple-counted. This fraction of double- and triple-counted events is very similar to the one presented in the ATLAS 8 TeV analysis. We use this result to estimate the expected number of background events.

We show the result of our pairwise $CL_s$ tests in fig. 35 for ATLAS and fig. 36 for CMS at 30/fb of integrated luminosity. We assume a systematic uncertainty of 25% on the signal and 30% on the QCD dijet background. Each row shows the test of one signal model as the null hypothesis and another signal as the test hypothesis based on one angular observable or their combination. The solid black line corresponds to the obtained $CL_s$ value purely based on the shape differences of the differential cross section. The dotted line is the equivalent when including rate information as discussed before. The shape based test also includes the 95% and 68% error bands in green and yellow. The long dashed line represents the 95% C.L. limit.

Note that the results are not symmetric under exchange of null and test hypothesis, for both test methods. Including rate information, the Poisson error is not equal under this exchange, whereas for the test based on shapes only, the signal cross section

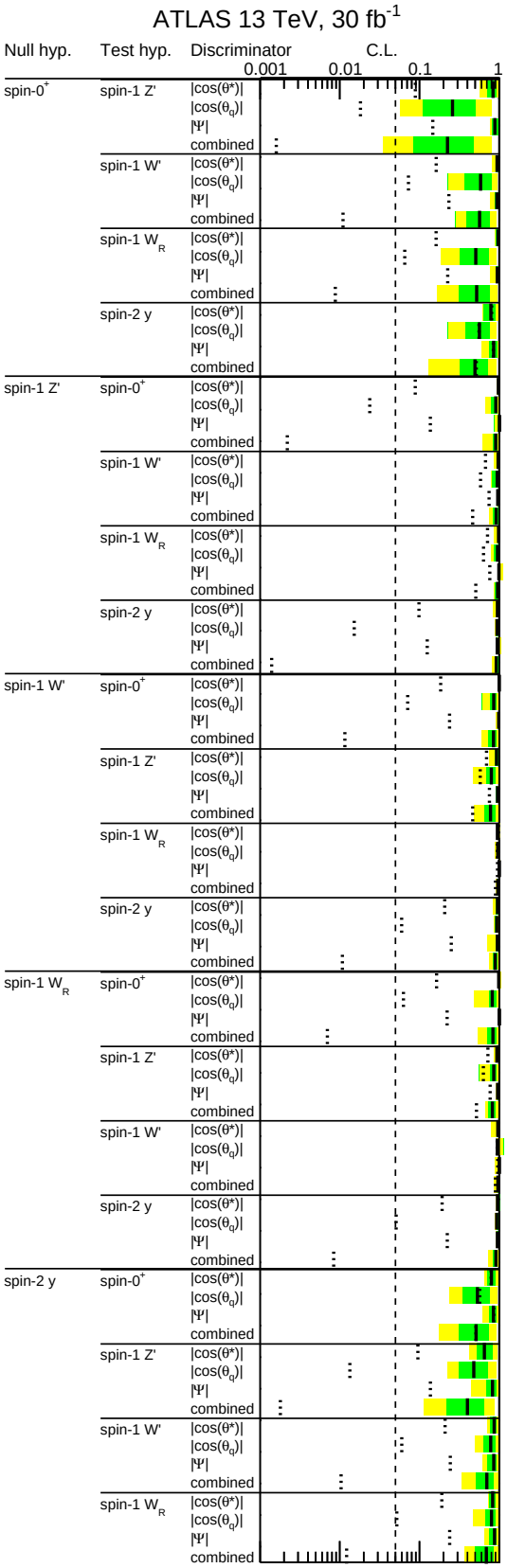


Figure 35: Projected spin sensitivity for the 13 TeV ATLAS analysis with 30 $fb^{-1}$ integrated luminosity. The long vertical dashed line indicates the 95% exclusion C.L. Within each row, the solid black line and the green and yellow shaded areas denote the central expected exclusion and the 68% and 95% likelihood expected exclusion intervals, using only shape information. The dotted black line in each row shows the central expected exclusion limit including rate information, using the 2 TeV excess as the normalization of the respective signal hypotheses.

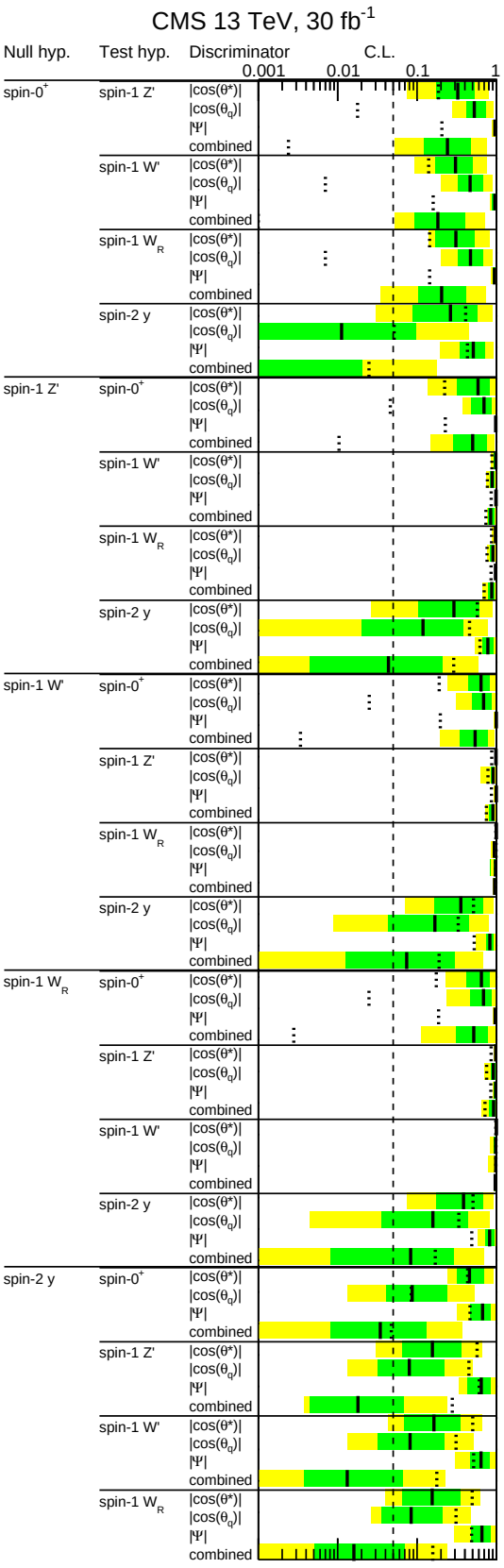


Figure 36: Projected spin sensitivity for the 13 TeV CMS analysis with 30 $fb^{-1}$ integrated luminosity. The long vertical dashed line indicates the 95% exclusion C.L. Within each row, the solid black line and the green and yellow shaded areas denote the central expected exclusion and the 68% and 95% likelihood expected exclusion intervals, using only shape information. The dotted black line in each row shows the central expected exclusion limit including rate information, using the 2 TeV excess as the normalization of the respective signal hypotheses.

of the test hypothesis is always scaled to the cross section of the null hypothesis. Also this is not equal under exchange of test and null hypothesis.

First of all, we can see that the CMS analysis yields a much better discriminative power than the ATLAS analysis. This is mainly due to the previously discussed angular scale with which the in ATLAS employed jet substructure technique works. As ATLAS reclusters jets with $R = 0.2$, which is larger than the average subjet separation of $\Delta R = 0.15 - 0.2$, this analysis fails often at reconstructing the four-momentum of the subjets. Thus, the angular observables of many signal events cannot be reconstructed.

CMS instead shows good discrimination power between spin-0, spin-1, and spin-2. Especially the $\cos\theta_q$ observable provides useful information to separate a spin-2 hypothesis, as this signal hypothesis has a very distinct shape in this observable compared to a spin-0 or spin-1 mode. In addition, this observable benefits from the fact that every event contributes twice, thus has twice the statistical power.

A spin-0 hypothesis can in principle be distinguished from a spin-1 resonance using $\cos\theta^*$, but yields better limits once combined with $\cos\theta_q$. Nevertheless, to reach an exclusion at 95% C.L. more integrated luminosity would be needed for the case study presented here. Including rate information, however, the discrimination to all other hypotheses is superb due to the significant PDF scaling for the $gg$ initiated resonance.

Note that the different spin-1 hypotheses are basically not distinguishable as their kinematics are expected to be very similar once $V$ bosons and their decay products cannot be differentiated. Here, a semi-leptonic analysis would yield an improvement, as the charge of the resonance can be identified much easier. The small relic sensitivity between the different spin-1 hypotheses comes from the slightly different PDF scalings due to the $qq'$ versus $q\bar{q}$ initial state.

Curiously, the sensitivity decreases when including extra rate information in some few cases. This is because each differential shape consists of two components, the signal and the background shape. When rate information is added, only the signal component is rescaled. This effectively changes the overall differential shape. This additional shape difference can be a disadvantage, in fact sometimes so much that it completely compensates the extra sensitivity due to additional rate information. This affects mainly observables where the discrimination power is already good based on the differential shapes only.

## 7.7 Discussion

In this chapter, we introduced a diboson resonance and discussed how – once found – further information can be drawn from data. Using various different signal samples and jet substructure techniques we illustrated how spin discrimination can be achieved using angular observables.

We found that those observables are heavily skewed by the different analysis techniques used to identify the resonance, limiting the statistical power. Most dominantly they are affected by the required maximum rapidity difference $\Delta\eta_{\text{max}}$ on the fat jets and the criterion on the subjet transverse momentum balance $y_{\text{min}}$. Both are indispensable for each analysis and the cut values are tuned towards the discovery of the resonance.

As soon as the resonance is discovered, however, it is of advantage to loosen those cuts. That will decrease the signal-over-background rate, but allows to test more phase space. Especially for a spin-2 resonance it would be possible to access more of the second oscillatory mode in the different angular observables, thus making a discrimination easier. In addition, since the statistical test is based on differential shapes, an overall higher rate will be beneficial.

Nevertheless, even with the current analyses, spin discrimination can be achieved between some different hypotheses, using just 30/fb of integrated luminosity for a 2 TeV excess. We expect a similar outcome for other mass points.

CHAPTER 8

# Lepton Jets from Radiating Dark Matter

## 8.1 Motivation

In the previous chapter, we dealt with various aspects of resonance searches. We developed new searches for a single or pair produced resonances and discussed how spin information about the resonance itself can be extracted from data. All these different searches were possible because the final state products are visible in the detector. Exceptions were neutrinos, but as long as they are either collimated or there is just a single neutrino, they can still be reconstructed.

One of the hot topics nowadays is dark matter. Unfortunately, dark matter is invisible for the detector. So even though it might be resonantly produced at the LHC through some kind of portal, it is incredibly difficult to search for it. One relies on additional effects accompanying the process.

The easiest of them is significant initial state radiation, as it is a pure Standard Model effect. The resonance that produces the dark matter pair receives from the initial state radiation a transverse momentum boost, which is measurable as missing transverse energy. The initial state radiation will show up as a monojet.

Monojet searches are relatively straightforward as the process does not involve many particles that need to be reconstructed. But that also implies there is not much room for improvements, especially concerning potential background suppression. Hence,

this kind of search is quickly dominated by systematic uncertainties.

This chapter will try a different approach. Instead of initial state radiation, it will consider final state radiation accompanying the dark matter pair production. While this step seems to be rather obvious, in practice it is not so trivial. Final state radiation, in contrast to initial state radiation, requires physics beyond the Standard Model, as it must be emitted from the dark matter particles. Thus a new gauge interaction in the dark sector is necessary.

Such gauge interactions have been discussed in various different contexts already. They typically induce dark matter self-interactions [293, 294], which has a series of implications. Self-interactions lead for example to Sommerfeld enhancements of the dark matter annihilation cross section [295–297], which is important for predicting the dark matter relic density in our Universe. Another effect can be the creation of dark matter bound states [298, 299]. Additionally, they might actually explain differences between the observation and theory of small scale structures such as dwarf galaxies. Those discrepancies exist for a long time already and proposed solutions were *e.g.* baryonic feedback [300, 301] and the very dark matter self-interactions [293, 294]. Furthermore, there are hints from the observations of the Abell 3827 galaxy cluster that self-interactions could exist [302] (see, however, [303]).

To study the effects of final state radiation from dark matter, which we will dub *radiating dark matter* in the following, we will work in a simplified model framework. Using a toy model, the following results will serve as a proxy for more complicated scenarios. The dark matter will be pair produced through a $Z'$ resonance. Final state radiation will then be achieved by an interaction between dark matter $\chi$ and a dark photon $A'$ [297, 304, 305]. When the $Z'$ boson has a mass of $\mathcal{O}(\text{TeV})$, whereas $\chi$ and $A'$ are of $\mathcal{O}(\text{GeV})$, significant radiation of dark photons can be expected in the collinear direction. This is very similar to the mechanism in QED or in a QCD parton shower.

We introduced the dark photon in section 3.7.1 already, where we discussed possible decays through its kinetic mixing with the Standard Model photon. Those decays are mass dependent and typically electrons, muons or light mesons. As in a such a dark parton shower, several dark photons can be produced, the resulting signature is a collimated jet of $A'$ decay products. This kind of jet is known as an exotic type of jet, a *lepton jet*.

ATLAS performed two type of lepton jet searches already [306, 307], where they search for prompt and displaced lepton jet signatures. Their motivation, however, was slightly different, as lepton jets can emerge in various different contexts [308–

320]. Nevertheless, their searches are suitable for our purposes, thus in this chapter we will recast the above ATLAS searches and reinterpret the results for radiating dark matter. Depending on the strength of the kinetic mixing between the dark photon and the Standard Model photon either the displaced lepton jet search or the prompt lepton jet search will be sensitive. Note that the term *lepton jet* has to be taken with a grain of salt. ATLAS defines a lepton jet category based on purely hadronic activity. Such a category targets the dark photon decays to mesons. A few other papers have studied similar signatures for such a hadronic jet [321–324].

In section 8.2 we will introduce in more detail our toy model for radiating dark matter. We will define benchmark points after going through various constraints on such a scenario. Section 8.3 aims at advancing the understanding of dark parton showers. Even though there are very strong similarities to a QED shower, the dark photon is massive and therefore alters the kinematics compared to the radiation of a photon. We will develop a semi-analytic description of such a dark parton shower. Section 8.4 will then introduce the prompt and displaced lepton jet search by ATLAS. We will present and discuss the results of our recast in the context of our model. Finally, section 8.5 will give a brief excursion away from the LHC to a future 100 TeV collider. As the dynamics of the dark parton shower depends immensely on the energy of the system, we briefly discuss possible search strategies. We summarise the results in section 8.6.

## 8.2 Radiating Dark Matter Model

### 8.2.1 The Toy Model

Our toy model can be split into two part, the production mechanism for a dark matter pair, and the implementation of final state radiation. For the latter, we assume that a fermionic dark matter $\chi$ couples to a massive $U(1)'$ gauge bosons, $A'$. Their respective interaction and kinematic terms are described by the Lagrangian

$$\mathcal{L}_{\text{dark}} \equiv \bar{\chi}(i\partial\!\!\!/ - m_\chi + ig_{A'}A\!\!\!/')\chi - \frac{1}{4}F'_{\mu\nu}F'^{\mu\nu} + \frac{1}{2}m^2_{A'}A'_\mu A'^\mu - \frac{\epsilon}{2}F'_{\mu\nu}F^{\mu\nu}\,. \tag{95}$$

The coupling strength between the dark photon and $\chi$ is given by $g_{A'}$, which is defined via the dark fine structure constant $\alpha_{A'} \equiv g^2_{A'}/(4\pi)$. This coupling is crucial as it determines the number of dark photons radiated from a dark matter particle. In addition, dark photons are allowed to decay via kinetic mixing with the photon, as described in detail in section 3.7.1. The mixing parameter $\epsilon$ defines the lifetime of $A'$. In order to achieve significant radiation in an LHC environment we assume both

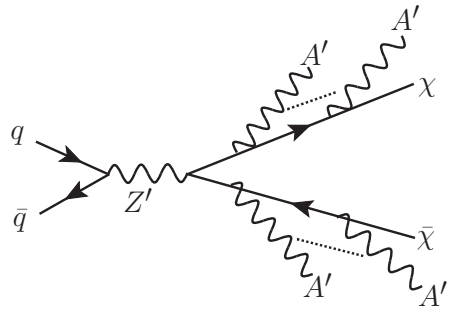


Figure 37: Relevant Feynman diagram for pair production of dark matter through a heavy $s$-channel $Z'$ resonance, followed by *dark radiation*, *i.e.* the emission of several dark photons. The dark photons will decay to Standard Model particles and result in a lepton jet signature.

particles have masses of $\mathcal{O}(\text{GeV})$.

The dark photon–photon mixing already serves as a portal between the Standard Model and the dark sector, thus it in principle contributes also to the production of the dark matter pair. But the mixing parameter is too small to yield a significant rate, thus a second interaction is needed to produce dark matter. The exact production mechanism is actually not critical, as long as the production rate is high enough. It merely defines the boost of the $\chi$ pair, thus modifies the energy spectrum of $\chi$ and $A'$, but it does not affect the phenomenology otherwise.

We chose to produce the dark matter pair through a heavy s-channel $Z'$ boson. Other options would be contact interaction, Higgs portals, or $t$-channel mediators. The $Z'$ is coupled to quarks and dark matter according to

$$\mathcal{L}_{Z'} \equiv g_q \sum_f \bar{q}_f \not{Z}' q_f + g_\chi \bar{\chi} \not{Z}' \chi \,, \tag{96}$$

where $q_f$ is the quark field of flavour $f$. $g_q$ and $g_\chi$ are the $Z'$ couplings to quarks and dark matter particles, respectively. We assume universal couplings to quarks for simplicity. In principle the dark photon and the $Z'$ mix just like the $A'$ and the $Z$, but this is highly suppressed by $m^2_{A'}/m^2_{Z'}$.

We present in fig. 37 the relevant Feynman diagram. It shows how the dark matter pair radiates several dark photons due to the small mass of $A'$ and $\chi$. The radiation probability is enhanced in the collinear direction and is significant for a moderate fine structure constant of $\alpha_{A'} \sim \mathcal{O}(0.1)$. The subsequent decay of the $A'$ particles is not depicted.

| Model Parameters | $m_{Z'}$ [TeV] | $g_q$ | $g_\chi$ | $m_\chi$ [GeV] | $m_{A'}$ [GeV] | $\alpha_{A'}$ | $c\tau$ [mm] |
|---|---|---|---|---|---|---|---|
| A | 1 | 0.1 | 1 | 4 | 1.5 | 0.2 | 10 |
| B | 1 | 0.03 | 0.3 | 0.4 | 0.4 | 0.2 | 1 |

| Derived Quantities | $\epsilon$ [$10^{-6}$] | $\sigma_7(Z')$ [pb] | $\sigma_8(Z')$ [pb] | $\sigma_{13}(Z')$ [pb] | $\Gamma_{Z'}$ [GeV] | BR($Z' \to \chi\bar{\chi}$) | $2\langle n_{A'}\rangle_8$ | $2\langle n_{A'}\rangle_{13}$ |
|---|---|---|---|---|---|---|---|---|
| A | 2.8 | 0.58 | 0.85 | 2.7 | 31.3 | 84.8% | 3.50 | 3.51 |
| B | 24 | 0.052 | 0.076 | 0.244 | 2.82 | 84.8% | 5.15 | 5.17 |

Table 5: Values of the model parameters (upper table) $m_{Z'}$ (heavy mediator mass), $g_q$, $g_\chi$ (heavy mediator couplings to quarks and dark matter), $m_\chi$ (dark matter mass), $m_{A'}$ (dark photon mass), $\alpha_{A'}$ (dark fine structure constant) and $c\tau$ (dark photon decay length) at our two benchmark points A and B. We also show the resulting values for several derived quantities (lower panel), in particular the kinetic mixing $\epsilon$ corresponding to the given $c\tau$ and $m_{A'}$, the resonance cross sections $\sigma_7(Z')$, $\sigma_8(Z')$ and $\sigma_{13}(Z')$ for $Z'$ production $pp \to Z'$ at the 7 TeV, 8 TeV and 13 TeV LHC, respectively, the total decay width $\Gamma_{Z'}$ of the heavy mediator $Z'$, its branching ratio to dark matter pairs, and the average numbers $2\,\langle n_{A'}\rangle_8$ ($2\,\langle n_{A'}\rangle_{13}$) of radiated dark photons in each dark matter pair production event at the 8 TeV (13 TeV) LHC. For the latter the number of two is due to the fact that each event contains two dark matter particles.

### 8.2.2 Benchmark Points

In order to discuss constraints on such a model and make the collider analysis more transparent, we define two different benchmark points in tab. 5. The table lists the explicit values for the model parameters, as well as a set of important derived quantities. We will demonstrate in the following that both benchmarks are consistent with current constraints. In addition, we will, later on, illustrate how collider limits from lepton jet searches change when one of the fundamental model parameters are varied, while others a kept fixed.

We assume a heavy mediator mass of $m_{Z'} = 1$ TeV, and the masses of $\chi$ and $A'$ of order GeV. The respective $Z'$ couplings to quark and dark matter, $g_q$ and $g_\chi$, are chosen such that the resonance production rate is just below 1 pb at $\sqrt{s} = 8$ TeV for benchmark point A, and at about 0.1 pb for B. As the ratio between $g_q$ and $g_\chi$ is kept fix for both benchmarks the branching ratio BR($Z' \to \chi\chi$) $= 1 -$ BR($Z' \to q\bar{q}$) $= 84.8\%$ is equal. To illustrate how significant the effects of dark radiation can be we chose a dark fine structure constant of $\alpha_{A'} = 0.2$.

We also list the average number of dark photons expected as final state radiation. The difference between both benchmark points is mainly due to the different masses of $A'$ and $\chi$. Note, that there is almost no increase in radiation between a center-of-mass energy of 13 TeV compared to 8 TeV. This is because the boost of $\chi$, relevant for

significant $A'$ radiation, is dictated by the mass of the heavy mediator, not by $\sqrt{s}$. A larger center-of-mass energy, of course, increases the reach towards higher resonance masses, which are subsequently much easier to detect.

We treat the dark photon decay length $c\tau$, where $\tau$ is its lifetime, as a fundamental parameter rather than the mixing parameter $\epsilon$. The only reason for this is that the influence of the decay length parameter is easier to grasp in a phenomenological study than the mixing parameter itself. If all other model parameters are fixed, $c\tau$ and $\epsilon$ have a one-to-one correspondence anyway. The size of $c\tau$ is chosen such that for benchmark point B the prompt lepton jet search will be most sensitive, whereas for benchmark point A the decay length is large enough that a significant amount of dark photon decays will be displaced from the interaction vertex. In this case, the displaced lepton jet search will be most sensitive.

### 8.2.3 Existing Constraints

We will demonstrate that both of our benchmark points are not excluded by any existing constraint on such a model.

As our model includes a dark matter candidate, we have to review a few cosmological constraints, probably the most important of which is the thermal relic abundance. For this the dark matter annihilation cross section to dark photons $\langle\sigma v\rangle_{\bar{\chi}\chi\to(q\bar{q},A'A')}$ must be similar to the thermal relic cross section being a few $\times\, 10^{-26}\mathrm{cm}^3/\mathrm{sec}$. In our case the annihilation rate to dark photons is given by [325]

$$\langle\sigma v\rangle_{\bar{\chi}\chi\to A'A'} \simeq \frac{\pi\alpha_{A'}^2}{m_\chi^2}\frac{(1-m_{A'}^2/m_\chi^2)^{3/2}}{(1-\frac{1}{2}m_{A'}^2/m_\chi^2)^2}\,, \tag{97}$$

which is in fact already larger than that required to match the thermal relic value. Reducing $\langle\sigma v\rangle_{\bar{\chi}\chi\to A'A'}$ would either require a smaller dark fine structure constant, in which case we would not expect any large final state radiation at the LHC anymore, or a much larger $A'$ mass with $m_{A'} > m_\chi$. In this case the annihilation channel to dark photons would be kinematically forbidden, leaving only a decay to quarks according to [326, 327]

$$\langle\sigma v\rangle_{\bar{\chi}\chi\to\bar{q}q} \simeq \frac{3N_f g_q^2 g_\chi^2}{2\pi}\frac{2m_\chi^2+m_q^2}{(4m_\chi^2-m_{Z'}^2)^2}\sqrt{1-\frac{m_q^2}{m_\chi^2}}\,. \tag{98}$$

Here, $N_f$ is the number of kinematically allowed quark flavours. This, however, is much smaller than the needed value, since $\langle\sigma v\rangle_{\bar{\chi}\chi\to\bar{q}q}$ scales as $g_q^2 g_\chi^2 m_\chi^2/m_{Z'}^4$. Thus instead of an underclosure of the Universe, it would lead to an overclosure. Only a

small range of parameters between both regimes would result in the correct thermal relic [328].

This observation implies one of two things. One, it could mean that what we call $\chi$ is not the only dark matter component. Especially with self-interacting dark matter this is not so uncommon. Given that the LHC relies on relatively large couplings to New Physics it is not surprising that it would discover subdominant components (in terms of abundance) of dark matter first.

Another possibility is that of asymmetric dark matter, see section 3.6.4, in which case the existence of dark photons is actually a feature. It this case they would explain the efficient annihilation rate needed to deplete the asymmetric component. Nevertheless, another opposite charge particle is needed to ensure gauge invariance for such small $A'$ masses [329].

But in any case, we will for simplicity call the $\chi$ particle dark matter for the rest of this chapter, even if it might just be a subdominant component.

Constraints also arise from direct and indirect dark matter searches. Both are trivially fulfilled if $\chi$ is a subdominant dark matter component and thus has a low relic abundance. Here, the dominant component is expected to be seen first. For models with primordial $\chi$–$\bar{\chi}$ asymmetry, direct detection constraints are also not a problem do to missing dark matter annihilation in today's Universe. And even indirect detection experiments are limited, as we consider light dark matter. Especially benchmark B is well below any detection threshold. Only low-threshold experiments like CDMSlite impose upper limits on the spin-independent $\chi$-nucleon scattering cross section $\sigma_{\chi N}$ of $1.5 \times 10^{-40}$ cm$^2$ on at $\chi$ mass of 4 GeV [330]. The equivalent rate is $\sigma_{\chi N} \simeq 6.5 \times 10^{-42}$ cm$^2$ for our benchmark point A, thus is not in disagreement with the measurement.

Constraints on the heavy mediator arise due to its decay to quarks, having a branching ratio at our benchmark points of 15.2%. Dijet searches with competitive limits on $\sigma(Z') \times \mathrm{BR}(Z' \to qq) \times A$ are performed by ATLAS [270], CMS [274], and CDF [331]. Here, $A$ is the respective detector efficiency.

ATLAS [270] obtains an upper limit using 8 TeV data with 20.3/fb of integrated luminosity of $\sigma(Z') \times \mathrm{BR}(Z' \to qq) \times A \lesssim 1$ pb at 95% confidence level (CL). This assumes an acceptance factor of $A \sim 0.6$. The respective limit from CMS [274] is not directly given in their publication for a mass of $m_{Z'} = 1$ TeV. But assuming that no feature is observed at this mass point their limit can be estimated by extrapolating their results for other resonance masses. This yields a limit that is about a factor of two stronger than that of ATLAS with a similar detector acceptance.

CDF [331] at the Tevatron quotes a limit of $\sigma(Z') \times \mathrm{BR}(Z' \to qq) \times A \lesssim 0.11$ pb.

The detector acceptance of CDF is not public, but given that they restrict their search to jets with rapidity $|y| < 1$, it is unlikely to be smaller than that of ATLAS and CMS. As a conservative estimate we, therefore, assume $A \sim 0.6$.

Those upper limits have to be compared to the $\sigma(Z') \times \mathrm{BR}(Z' \to qq) \times A$ of our benchmark points. These are 0.08 pb at the 8 TeV LHC and 0.001 pb at Tevatron for benchmark A, and even smaller for benchmark B. Thus none of them is excluded by dijet searches, even if the exact bounds are only approximately known in the case of CMS and CDF.

Besides dijet searches, monojet analyses are also sensitive to our model [332, 333]. Here, a dark matter pair is produced through a $Z'$ resonance, but instead of final state radiation, initial state radiation leaves a visible trace of this process. The strongest limits are from ATLAS [332] and quoted as $m_{Z'}/\sqrt{g_q g_\chi} \gtrsim 2$ TeV. Our benchmark points yield $m_{Z'}/\sqrt{g_q g_\chi} \sim 3.2$ TeV and $m_{Z'}/\sqrt{g_q g_\chi} \sim 10$ TeV, respectively, thus our two benchmark points are not expected to be seen in monojet searches either.

Furthermore, constraints arise from the dark matter self-interactions induced by the dark photon. They are coming mainly from its influence on colliding galaxy clusters like the Bullet Cluster [334], and on the ellipticity of dark matter halos of groups of galaxies [335]. The current upper limit on the self-scattering cross section is

$$\sigma_{\chi\chi}/m_\chi \lesssim 1 \text{ cm}^2/\text{g} = 1.78 \times 10^{-24} \text{ cm}^2/\text{GeV}\,. \tag{99}$$

Again, such a limit is only relevant if $\chi$ is the dominant dark matter component, as it is the case for the asymmetric model. The self-scattering cross section can be expressed as [294]

$$\sigma_{\chi\chi}/m_\chi \simeq 5 \times 10^{-31} \text{ cm}^2/\text{GeV} \times \left(\frac{\alpha_{A'}}{0.1}\right)^2 \left(\frac{m_\chi}{\text{GeV}}\right) \left(\frac{\text{GeV}}{m_{A'}}\right)^4, \tag{100}$$

where we assumed the perturbative regime with $\alpha_{A'} m_\chi / m_{A'} \lesssim 1$. Eq. 100 yields $10^{-30}$ cm$^2$/GeV and $10^{-29}$ cm$^2$/GeV for our two benchmark points, respectively, which is in agreement with the current limits.

Further strong constraints come from direct searches for dark photons. These are typically excluding paramter space with $\epsilon \lesssim 10^{-10}$ for $m_{A'} \lesssim 10$ MeV. For slightly larger masses however, the current bounds are with $\epsilon \lesssim 10^{-3}$ for 10 MeV $\lesssim m_{A'} \lesssim$ 10 GeV weaker. Thus both of our benchmark points are not excluded by these searches, but we will nevertheless describe these bounds in more detail in section 8.4.

## 8.3 Dark Parton Shower

The following section is aimed at providing additional information about a dark parton shower. Part of the discussion is similar to the one presented in ref. [336, 337]. When studying such a shower at the LHC we are looking at decay products of dark photons. Thus there are a few parameters linked to this process which are of interest. The two most important questions we try to answer are how many dark photons are radiated in the first place and how energetic they are.

A QED shower is very similar, thus we know that there will be a soft and collinear enhancement. As a result, a large number of radiated dark photons will be soft and their decay products below the tagging threshold. Nevertheless, a dark parton shower is slightly different as the dark photons are massive. They are therefore expected to regularise the divergence by providing a natural infrared cut-off. In this section we want to provide analytic expressions which can – once numerically evaluated – provide the average number of emitted dark photons and their respective energy spectrum.

First, we want to stress that just like in QED, the hard process (short range) and the parton shower (long range) can be separated [338]. This is known as the factorisation theorem. Thus we can describe the dark shower independent of the dark matter pair production mechanism and we only need to describe a single radiating dark matter particle.

The are in principle two different kinds of splittings in such a shower, $\chi \to \chi + A'$ and $A' \to \bar{\chi}\chi$. The probability for the latter is not divergent in the soft limit due to the structure of the splitting kernel. The $\chi \to \chi + A'$ process is therefore dominant. Furthermore, under the assumption of strongly ordered emission, where the virtuality of the incoming particle is much larger than the virtuality of the outgoing particles, the secondary splitting $A' \to \bar{\chi}\chi$ is just a small perturbation of the first splitting. We can therefore safely neglect the $A' \to \bar{\chi}\chi$ process. We consider each $\chi \to \chi + A'$ splitting as an isolated process and due to the energy threshold at the LHC, we are more interested in the collinear regime than the soft emissions.

The $\chi \to \chi + A'$ process is shown in fig. 38 and its differential collinear splitting probability can be written as

$$d\mathcal{P} = \frac{\alpha_{A'}}{2\pi} dx \, \frac{dt}{t} P_{\chi\to\chi}(x,t)\,. \tag{101}$$

Here, $x$ is the energy fraction that is transferred from the incoming dark matter particle to the outgoing dark matter particle. $t$ is the virtuality of the incoming $\chi$ particle. As we are working with strongly ordered emission the outgoing particles are

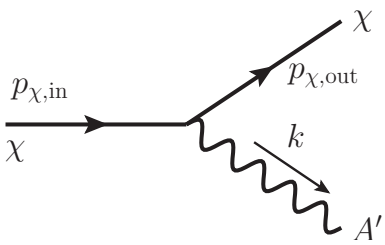


Figure 38: Radiation of a single dark photon $A'$ from a dark matter particle $\chi$.

considered on-shell. $P_{\chi\to\chi}(x,t)$ describes the actual splitting probability and contains the collinear and soft enhancement. It is in general model-dependent.

Eq. 101 corresponds to the matrix element squared of the $\chi \to \chi + A'$ process, multiplied by the propagator of the incoming particle and integrated over the phase space of the outgoing particles. Note that the propagator comes with a factor of $1/t$. This corresponds to the collinear divergence for $t \to 0$ but is regularised by the non-zero dark photon mass, as we will see later.

Furthermore, we neglect any renormalisation group running in order to treat $\alpha_{A'}$ independent of $t$. Such a logarithmic running is not only expected to have little effect on the dark parton shower, but would also be highly model-dependent and therefore require writing down the full particle content of our toy model.

### 8.3.1 Kinematics

In order to describe the parton shower properly we have to analyse the kinematics of the process first. For an incoming dark matter particle with energy $E$ moving in $\hat{z}$ direction its off-shell four-momentum can be written as

$$p_{\chi,\text{in}} = (E, 0, 0, p)\,. \tag{102}$$

In principle $E$ is not equal to $\sqrt{\hat{s}}/2$ due to the non-zero masses of the involved particles. Consider for example the second dark matter particle, which we will refer to as the spectator. Its three-momentum is $(0, 0, -p)$ in case it does not split, because of energy momentum conservation. The energy of the spectator is subsequently fixed to $E_s^2 = p^2 + m_\chi^2$, and hence $E \geq E_s + m_{A'}$ in case at least one $A'$ is radiated from the non-spectator. We will, however, work with the collinear approximation $E = E_s = \sqrt{\hat{s}}/2$, which is valid if $E \gg m_{A'} + m_\chi$ and for small opening angles between the outgoing particles. The first criterion is trivially fulfilled for $\mathcal{O}(\text{GeV})$ masses. If the latter is not fulfilled the dark photons are usually soft and thus of no phenomenological interest anyway.

The outgoing momenta of $\chi$ and $A'$ can then be expressed as

$$p_{\chi,\text{out}} = \left(xE,\ -k_t,\ 0,\ \sqrt{x^2E^2 - k_t^2 - m_\chi^2}\right), \tag{103}$$

and

$$k = \left((1-x)E,\ k_t,\ 0,\ \sqrt{(1-x)^2E^2 - k_t^2 - m_{A'}^2}\right), \tag{104}$$

respectively, where $x$ is again the energy fraction. For consistency

$$m_\chi/E < x < 1 - m_{A'}/E\,, \qquad x^2E^2 - m_\chi^2 \geq k_t^2\,, \text{ and } \quad (1-x)^2E^2 - m_{A'}^2 \geq k_t^2 \tag{105}$$

has to be invoked in order to ensure positive energy and momenta. Note that the first requirement on $x$ depends on the exact energy of the dark matter particle, and thus on every previous splitting. Unfortunately, this implies that these splittings are too correlated and an analytic description is not possible. Nevertheless, the energy of the incoming particle is much larger than the energy transfer and the particle masses, thus we can approximate the limits on $x$ according to

$$x_\text{min} \equiv m_\chi/E_0\,, \qquad x_\text{max} \equiv 1 - m_{A'}/E_0\,. \tag{106}$$

Here, $E_0$ is the energy of the initial $\chi$ particle before any splitting. We will discuss this approximation further when we compare our analytic results with Monte Carlo simulations.

Using the above notation we can express the virtuality as

$$t \equiv (p_{\chi,\text{out}} + k)^2 - m_\chi^2 = m_{A'}^2 + 2p_{\chi,\text{out}} \cdot k\,, \tag{107}$$

and the splitting kernel as [339]

$$P_{\chi\to\chi}(x,t) = \frac{1+x^2}{1-x} - \frac{2(m_\chi^2 + m_{A'}^2)}{t}\,. \tag{108}$$

The splitting kernel depends on both, $t$ and $x$ and (like the exact limits on $x$) it correlates the individual splittings with each other. Thus we need to drop the mass dependent term in the splitting kernel, which is valid due to the smallness of $m_{A'}$ and $m_\chi$. The result, which we denote simply as $P_{\chi\to\chi}(x)$, is divergent for $x = 1$. But note that this collinear divergence is never actually reached, due to eq. 106. The divergence is regularised by the $A'$ mass, although a large enhancement in the collinear regime

is still present.

Similarly, also the $t$ divergence of the collinear splitting probability is regularised for $t \to 0$. To see this, we need to determine the exact upper and lower bounds on $t$. We find

$$\begin{aligned} t_{\min}(x) &= m_{A'}^2 + 2p_{\chi,\text{out}} \cdot k\big|_{k_t \to 0} \\ &= m_{A'}^2 + 2\Big(E^2 x(1-x) - \sqrt{x^2E^2 - m_\chi^2}\sqrt{(1-x)^2E^2 - m_{A'}^2}\Big)\,, \end{aligned} \tag{109}$$

and

$$t_{\max}(x) = m_{A'}^2 + 2p_{\chi,\text{out}} \cdot k\big|_{k_{t,\max}}\,, \tag{110}$$

with

$$k_{t,\max}^2(x) = \min\left\{(1-x)^2E^2 - m_{A'}^2\,,\; x^2E^2 - m_\chi^2\right\}. \tag{111}$$

The lower bound is reached when $k_t \to 0$, whereas the upper bound is determined by the maximum of $k_t$. $k_{t,\max}$ is given by the constraints in eq. 105. As before we will assume $E = E_0$.

Note that the bounds on $x$ and $t$ are correlated. As a result, if $x$ takes its maximum or minimum value, the virtuality is fixed to $t = t_{\min} = t_{\max}$. Thus the splitting probability actually approaches zero when integrating out $t$, despite the large collinear enhancement in the splitting kernel.

### 8.3.2 Number of Emitted Dark Photons

The first quantity we are interested in is the average number of dark photons emitted by a dark matter particle with energy $E$. Given the maximum value for the virtuality $t_{\max}$ a dark matter particle will emit dark photons until its virtuality is reduced to the infrared cutoff $t_{\min}$. Thus we need to integrate the splitting kernel over the full allowed phase space given by $x$ and $t$,

$$\langle n_{A'}\rangle \simeq \frac{\alpha_{A'}}{2\pi}\int_{x_{\min}}^{x_{\max}} dx \int_{t_{\min}}^{t_{\max}} \frac{dt}{t} P_{\chi\to\chi}(x)\,. \tag{112}$$

Note that this is only an approximation as we ignored the $t$ dependence of the splitting kernel, as discussed previously.

The probability that no splitting occurs between $t_{\max}$ and $t_{\min}$ is given by the

Sudakov factor,

$$\Delta(t_{\min}, t_{\max}) \equiv e^{-\langle n_{A'} \rangle} \,, \tag{113}$$

Then the probability for exactly one splitting can be written as

$$\begin{aligned} p_1 &= \frac{\alpha_{A'}}{2\pi} \int_{x_{\min}}^{x_{\max}} dx \int_{t_{\min}}^{t_{\max}} \frac{dt}{t} \Delta(t_{\min}, t) P_{\chi\to\chi}(x) \Delta(t, t_{\max}) \\ &= e^{-\langle n_{A'} \rangle} \langle n_{A'} \rangle \,, \end{aligned} \tag{114}$$

where $\Delta(t_{\min}, t)$ and $\Delta(t, t_{\max})$ give the probabilities for no splittings to happen in the intervals $[t_{\min}, t)$ and $(t, t_{\max}]$, respectively. Thus $\Delta(t_{\min}, t) P_{\chi\to\chi}(x) \Delta(t, t_{\max})$ describes the probability that a single splitting happens with the exact energy fraction $x$ and virtuality $t$.

Analogously we can define the probability for exactly two splittings, which yields

$$\begin{aligned} p_2 &= \left(\frac{\alpha_{A'}}{2\pi}\right)^2 \int_{x_{\min}}^{x_{\max}} dx \int_{t_{\min}}^{t_{\max}} \frac{dt}{t} \int_{x_{\min}}^{x_{\max}} dx' \int_{t_{\min}}^{t} \frac{dt'}{t'} * \\ &\qquad * \Delta(t_{\min}, t) P_{\chi\to\chi}(x) \Delta(t, t') P_{\chi\to\chi}(x') \Delta(t', t_{\max}) \\ &\simeq e^{-\langle n_{A'} \rangle} \frac{1}{2!} \left(\frac{\alpha_{A'}}{2\pi}\right)^2 \int_{x_{\min}}^{x_{\max}} dx \int_{t_{\min}}^{t_{\max}} \frac{dt}{t} \int_{x_{\min}}^{x_{\max}} dx' \int_{t_{\min}}^{t_{\max}} \frac{dt'}{t'} P_{\chi\to\chi}(x) P_{\chi\to\chi}(x') \\ &= e^{-\langle n_{A'} \rangle} \frac{\langle n_{A'} \rangle^2}{2!} \,. \end{aligned} \tag{115}$$

Note that we extended the integration range of the first $dt'$ integral to $[t_{\min}, t_{\max}]$ in the second equality. This is based on the previously discussed assumption that we can treat both splittings as independent. As both dark photons are now indistinguishable we have to include an extra factor of $1/2!$ to avoid double-counting.

The results from eq. 113–115 can easily be generalised for more splittings [336]. This yields a Poisson distribution given by

$$p_m = \frac{e^{-\langle n_{A'} \rangle} \langle n_{A'} \rangle^m}{m!} \,. \tag{116}$$

### 8.3.3 Recursion Formalism

The average number of dark photons alone is not yet able to tell the full story. We know from the structure of the splitting kernel that most dark photons will be rather soft and therefore their decay products will escape detection. Thus on top of knowing their multiplicity, we also need to determine their energy spectrum. Fortunately, with

the approximations used before we can calculate it recursively.

Let us first compute the energy spectrum for the dark matter particle $\chi$ with initial energy $E_0$ and final energy $E_\chi$ after all splittings. The total fraction of transferred energy will be $X \equiv E_\chi/E_0$. Here, we use the convention that capital letters denote energy fractions relative to the initial dark matter energy $E_0$ and lower case letters for energy fractions relative to the dark matter energy just before a specific splitting.

The dark matter energy distribution can then be expressed as

$$f_\chi(X) = \sum_{m=0}^{\infty} p_m \, f_{\chi,m}(X) \,, \tag{117}$$

where $f_{\chi,m}(X)$ is the energy distribution of $\chi$ when exactly $m$ dark photons are emitted. These partial energy distributions can be obtained recursively [340] as

$$f_{\chi,m+1}(X) = \int_{x_{\min}}^{x_{\max}} dx_m \, f_{\chi,1}(x_m) \, \frac{f_{\chi,m}(X/x_m)}{x_m} \, \Theta(x_{\min} \leq X \leq x_{\max}) \,, \tag{118}$$

where

$$f_{\chi,1}(X) \equiv \frac{1}{\langle n_{A'} \rangle} \frac{\alpha_{A'}}{2\pi} \int_{t_{\min}}^{t_{\max}} \frac{dt}{t} P_{\chi\to\chi}(X) \, \Theta(x_{\min} \leq X \leq x_{\max}) \,. \tag{119}$$

$f_{\chi,1}(X)$ is the dark matter energy distribution after exactly one splitting and therefore seeds the recursive formalism. $\Theta(\,\cdot\,)$ denotes the Heaviside step function. For consistency we define the energy distribution for no splitting as a $\delta$-function, $f_{\chi,0}(X) \equiv \delta(1-X)$. Note that energy distributions are unit-normalised according to

$$\int dX \, f_{\chi,m}(X) = 1 \,. \tag{120}$$

The energy spectrum of the emitted dark photons can be obtained analogously by using the equivalent $Z = E_{A'}/E_0$. More specifically,

$$f_{A'}(Z) = \frac{1}{\langle n_{A'} \rangle} \sum_{m=1}^{\infty} \sum_{k=1}^{m} p_m f_{A',k}(Z) \,, \tag{121}$$

holds, where $f_{A',k}(Z)$ is the energy distribution of the $k$-th emitted $A'$ boson given recursively by

$$f_{A',k+1}(Z) = \int_{x_{\min}}^{x_{\max}} dx_k \, f_{\chi,1}(x_k) \frac{f_{A',k}(Z/x_k)}{x_k} \, \Theta(1 - x_{\max} \leq Z \leq 1 - x_{\min}) \,. \tag{122}$$

Also the $f_{A',k}(Z)$ are unit-normalised and independent of $m$ as each splitting can be regarded as independent from other dark photon emissions. When computing the energy spectra explicitly, it is of course not possible to compute all terms in $\Sigma_{m=0}^{\infty}$. Fortunately, each partial energy spectrum is weighted by the Poisson factor $p_m$, thus higher order terms do not contribute significantly. It is, therefore, safe to truncate the series at usually $m = \mathcal{O}(10)$.

### 8.3.4 Inverse Mellin Transformation

The just introduced recursive formalism offers an intuitive description of the energy spectra of $\chi$ and $A'$. Nevertheless, it has a practical disadvantage. Each integral has to be evaluated numerically and since the formalism is based on recursion one has to very quickly solve an enormous amount of integrals. Typically, as the series over $m$ is truncated, this can still be done in a reasonable time. But fortunately, there is a more elegant way of computing the energy distributions by using an inverse Mellin transformation.

The idea is to first compute the moments $\langle X^s \rangle$ and $\langle Z^s \rangle$ of the respective energy distribution in Mellin space, and then recover the actual energy spectrum through an inverse transformation.

The Mellin transformation of a function $f(X)$ is [341]

$$\mathcal{M}[f](s) \equiv \varphi(s) \equiv \int_0^\infty dX\, X^{s-1} f(X)\,, \tag{123}$$

and the inverse transform is given by

$$f(X) = \frac{1}{2\pi i} \int_{c-i\infty}^{c+i\infty} ds\, X^{-s}\, \varphi(s)\,. \tag{124}$$

The integral in eq. 124 is a line integral taken over a vertical line in the complex plane. There are direct relations between a Mellin transformation and a Fourier transform, in particular [341]

$$\mathcal{M}[f](s) \equiv \mathcal{F}[f(e^{-x})](-is)\,. \tag{125}$$

Thus, this formalism can be efficiently evaluated by rewriting the Mellin transform in terms of a Fourier transformation and using the FFT (Fast Fourier Transform) algorithm [342].

Using this framework, we can give the first moment for the dark matter particle

after a single $A'$ is emitted by

$$p_1 \langle X^s \rangle_{1A'} = e^{-\langle n_{A'} \rangle} \frac{\alpha_{A'}}{2\pi} \int_{x_{\min}}^{x_{\max}} dx\, x^s \int_{t_{\min}}^{t_{\max}} \frac{dt}{t} P_{\chi\to\chi}(x)$$
$$\equiv e^{-\langle n_{A'} \rangle} \langle n_{A'} \rangle \overline{X^s}\,. \tag{126}$$

Here, the moment is already weighted by its occurrence probability $p_1$ and we make the usual approximations. To make the expressions more compact we absorb the $dx$ and $dt$ integrals into the quantity

$$\overline{X^s} \equiv \frac{1}{\langle n_{A'} \rangle} \frac{\alpha_{A'}}{2\pi} \int_{x_{\min}}^{x_{\max}} dx\, x^s \int_{t_{\min}}^{t_{\max}} \frac{dt}{t} P_{\chi\to\chi}(x)\,. \tag{127}$$

Note that $\overline{X^s}$ is defined in Mellin space. Similarly we obtain the moment for the dark matter spectrum with exactly two emitted dark photons,

$$\begin{aligned} p_2 \langle X^s \rangle_{2A'} &= e^{-\langle n_{A'} \rangle} \left( \frac{\alpha_{A'}}{2\pi} \right)^2 \int_{x_{\min}}^{x_{\max}} dx\, x^s \int_{t_{\min}}^{t_{\max}} \frac{dt}{t} \int_{x_{\min}}^{x_{\max}} dx'\, x'^s \int_{t_{\min}}^{t} \frac{dt'}{t'} * \\ &\qquad * P_{\chi\to\chi}(x) P_{\chi\to\chi}(x') \\ &\simeq e^{-\langle n_{A'} \rangle} \frac{1}{2!} \left( \frac{\alpha_{A'}}{2\pi} \right)^2 \int_{x_{\min}}^{x_{\max}} dx\, x^s \int_{t_{\min}}^{t_{\max}} \frac{dt}{t} \int_{x_{\min}}^{x_{\max}} dx'\, x'^s \int_{t_{\min}}^{t_{\max}} \frac{dt'}{t'} * \\ &\qquad * P_{\chi\to\chi}(x) P_{\chi\to\chi}(x') \\ &= e^{-\langle n_{A'} \rangle} \frac{\langle n_{A'} \rangle^2}{2!} \overline{X^s}^2\,. \end{aligned} \tag{128}$$

Here the strength of the Mellin transform becomes apparent. Instead of referring recursively back to lower dark photon multiplicities, the higher moment can be expressed via a different power of the same quantity, $\overline{X^s}$. Thus the moments are easy to generalise for exactly $m$ emitted dark photons,

$$p_m \langle X^s \rangle_{mA'} = e^{-\langle n_{A'} \rangle} \frac{\langle n_{A'} \rangle^m}{m!} \overline{X^s}^m\,. \tag{129}$$

As a result also their sum over $m$ can be expressed in a closed form in Mellin space,

$$\varphi(s+1) \equiv \langle X^s \rangle = \sum_{m=0}^{\infty} p_m \langle X^s \rangle_{mA'} = e^{-\langle n_{A'} \rangle (1 - \overline{X^s})}\,. \tag{130}$$

$\varphi(s)$ is the dark matter energy spectrum in Mellin space, thus in the end the inverse Mellin transform has to be applied according to eq. 124 to obtain $f_\chi(X)$. This requires evaluating $\varphi(s)$ at complex values of s, which can be done in a numerically stable fashion by the FFT algorithm.

The dark photon energy spectrum can be computed analogously. The weighted moment for the $m$-th dark photon is

$$p_m \langle Z^s \rangle_{mA'} = \frac{1}{\langle n_{A'} \rangle} e^{-\langle n_{A'} \rangle} \frac{\langle n_{A'} \rangle^m}{m!} \overline{Z^s} \sum_{k=1}^{m} \overline{X^s}^{k-1} , \tag{131}$$

with

$$\overline{Z^s} \equiv \frac{1}{\langle n_{A'} \rangle} \frac{\alpha_{A'}}{2\pi} \int_{x_{\min}}^{x_{\max}} dx \, (1-x)^s \int_{t_{\min}}^{t_{\max}} \frac{dt}{t} P_{\chi \to \chi}(x) . \tag{132}$$

Note that $p_m \langle Z^s \rangle_{mA'}$ includes only one power of $\overline{Z^s}$, but up to $m-1$ powers of $\overline{X^s}$. This is because the $m$-th dark photon knows nothing about the previous dark photons in terms of their energy distribution. It interacts only with the dark matter particle after $m-1$ splittings, thus it depends on the previous dark matter moments and not on the respective dark photon moments.

Finally, the sum over all emissions in Mellin space yields

$$\langle Z^s \rangle = \frac{\overline{Z^s}}{\langle n_{A'} \rangle} \frac{1 - e^{-\langle n_{A'} \rangle (1 - \overline{X^s})}}{1 - \overline{X^s}} . \tag{133}$$

The inverse Mellin transform of $\langle Z^s \rangle$ is the $A'$ energy spectrum $f_{A'}(Z)$.

### 8.3.5 Comparison to Monte Carlo Simulation

In order to test how well our analytic approach[1] works we compare it with a fully numerical simulation using Monte Carlo techniques. For this, we use the *hidden valley* implementation within Pythia 8 [288, 343, 344]. Just like in our analytic approach Pythia only include the processes $\chi \to \chi A'$ and $\bar{\chi} \to \bar{\chi} A'$ and neglects the second order splitting $A' \to \bar{\chi}\chi$.

The energy of $\chi$ is dictated by the resonance mass the pair is created by. For our two benchmark points defined in section 8.2.2 with $m_{Z'} = 1$ TeV this means $E_0 \approx 500$ GeV. In Pythia this is achieved by simulating the process $e^+e^- \to Z' \to \bar{\chi}\chi$ with subsequent dark parton shower at a center-of-mass energy of $\sqrt{s} = 1$ TeV.

We compare a few relevant parameters between our analytic approach and Monte Carlo simulation in tab. 6 for various different $\chi$ and $A'$ masses. We compare the average number of dark photons, and the average energy fraction $\langle X \rangle$ and $\langle Z \rangle$. The

[1] As either integrals are solved numerically or a numeric FFT algorithm is used, the approach is technically *semi-analytic*.

| | $m_\chi$ [GeV] | $m_{A'}$ [GeV] | $2\langle n_{A'}\rangle$ | $2\langle n_{A'}\rangle_{\text{Pythia}}$ | $\langle X\rangle$ | $\langle X\rangle_{\text{Pythia}}$ | $\langle Z\rangle$ | $\langle Z\rangle_{\text{Pythia}}$ |
|---|---|---|---|---|---|---|---|---|
| | 50 | 1.5 | 2.130 | 2.340 | 0.873 | 0.837 | 0.119 | 0.140 |
| | 50 | 0.4 | 2.848 | 3.084 | 0.871 | 0.835 | 0.091 | 0.107 |
| A | 4 | 1.5 | 3.476 | 3.540 | 0.729 | 0.697 | 0.156 | 0.171 |
| | 4 | 0.4 | 4.990 | 4.825 | 0.712 | 0.681 | 0.116 | 0.132 |
| B | 0.4 | 0.4 | 5.691 | 5.215 | 0.626 | 0.608 | 0.132 | 0.150 |

Table 6: Characteristics of the dark photon shower for various choices of $m_\chi$ and $m_{A'}$. The rows labeled "A" and "B" correspond to the two benchmark points from table 5. In all cases, we assume $\chi$ pair production at a center of mass energy $\sqrt{\hat{s}} = 1$ TeV and we take $\alpha_{A'} = 0.2$. We show the predicted number $2\langle n_{A'}\rangle$ of dark photons per event (with the factor of 2 coming from the fact that we consider dark matter pair production), and the average energy fraction $\langle X\rangle$ and $\langle Z\rangle$. As expected, the results satisfy the energy conservation law $\langle X\rangle + \langle n_{A'}\rangle\langle Z\rangle = 1$.

values for our analytic approach are obtained using eq. (112), eq. (130) (with $s = 1$) and eq. (133) (with $s = 1$). There are small difference visible between Monte Carlo and our analytic formalism, which can be attributed to the approximation that we treat every dark photon splitting as independent. The agreement is nevertheless very good.

We performed a more thorough comparison in fig. 39 and fig.40. In the first figure, we compare the distribution of the number of dark photons. The distribution obtained using Monte Carlo simulation is not quite Poissonian as one would expect when each splitting process is treated independently. Nevertheless, the overall shape is very similar.

The second figure compares the dark matter and dark photon energy spectra for both our benchmark points. The comparison is between our recursion formalism, the Mellin transformation approach, Monte Carlo simulation and a simple leading order calculation of the first splitting using the full mass-dependent splitting kernel. The latter is performed in CalcHEP [345], which simulates the two processes $e^+e^- \to Z' \to \bar{\chi}\chi$ and $e^+e^- \to Z' \to \bar{\chi}\chi A'$.

Comparing our two analytic approaches they yield basically the same result as expected. The recursive approach, however, is less numerically stable, as errors on the numerical integration accumulate due to the recursive nature of the formalism.

Both analytic approaches match very well the leading-order CalcHEP calculation. Since CalcHEP is based on the complete splitting kernel it confirms that our approximation to drop mass-dependent terms in $P_{\chi\to\chi}(x,t)$ is justified.

Comparing the Monte Carlo simulation of Pythia with our analytic approaches,

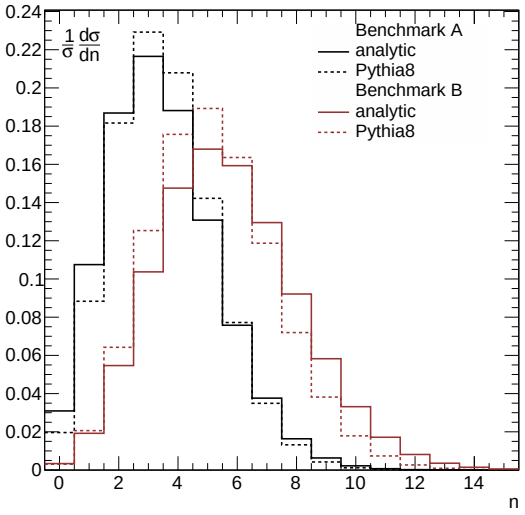


Figure 39: The distribution of the number of dark photons emitted in each $\bar{\chi}\chi$ pair production event at a center of mass energy of $\sqrt{\hat{s}} = 1$ TeV. The model parameters are given in tab. 5. The solid curves labeled "analytic" show the Poisson probability $e^{-2\langle n_{A'}\rangle}[2\langle n_{A'}\rangle]^n/n!$, with $\langle n_{A'}\rangle$ given by eq. (112). The factors of 2 arise from the fact that two DM particles are produced in each event. The dotted curves show the distribution obtained from a Monte Carlo simulation in Pythia.

we see a very good match over a large range. Only in the tails of the distributions, where rates are low, there is a disagreement. In this case, energy transfer is so large that any following splitting cannot be regarded as independent anymore. Thus our approximation breakes down in this regime. In the collinear regime, however, the agreement is excellent.

For illustrational purposes we also superimpose fig. 40 with the individual contributions of $p_m f_{\chi,m}(X)$ and $(1/\langle n_{A'}\rangle)\sum_{k=1}^{m} p_m f_{A',k}(Z)$. These describe events with a fixed number of dark photons.

Fig. 40 illustrates well the collinear enhancement for small $Z$ and large $X$. The pole responsible for it, however, has a large tail, which means that even boosted dark photons are being produced with a significant rate. Since the energy threshold will be at $\mathcal{O}$(few$\times$10 GeV) we expect that several of the $A'$ decay products produced in the dark parton shower will be visible at the LHC.

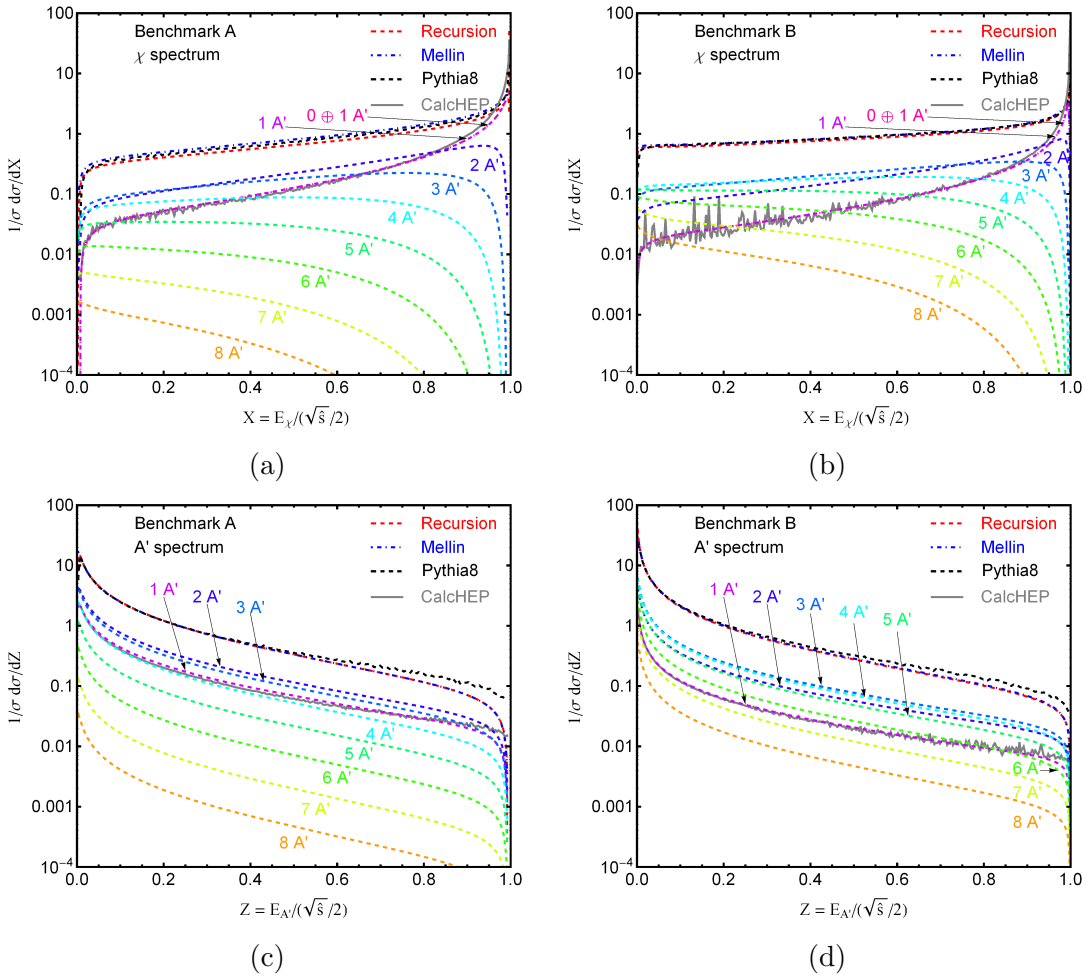


Figure 40: (a), (b) Energy spectrum $f_\chi(X)$ of dark matter particles $\chi$ after final state radiation of dark photons; (c), (d) energy spectrum $f_{A'}(Z)$ of dark photons $A'$ emitted as final state radiation. The panels on the left (right) are for benchmark point A (B) from table 5. In all cases, we assume $\chi$ pair production at a center of mass energy $\sqrt{\hat{s}} = 1$ TeV. We compare the results from the recursion formulism, the Mellin transform method, the dark photon shower simulation in Pythia, and a simple leading order simulation of $e^+e^- \to Z' \to \bar{\chi}\chi A'$ in CalcHEP. For the Mellin transform method, we also show the result separated according to the number of $A'$ bosons emitted in each $\bar{\chi}\chi$ pair production event.

## 8.4 Collider Searches

In order to constrain our radiating dark matter model we recast the ATLAS prompt [306] and displaced [307] lepton jet search. We simulate $pp \to Z' \to \chi\bar{\chi}$ with subsequent dark parton shower using the *hidden valley model* within Pythia 8. Events are simulated according to our two benchmark points tab. 5. In addition, we perform scans

over some model parameters while keeping others fixed in order to illustrate how the obtained limits will change with this parameter. The two ATLAS searches are based on 7 and 8 TeV data, respectively, but we will also simulate Monte Carlo events at $\sqrt{s} = 13$ TeV to estimate future sensitivity.

### 8.4.1 Prompt Lepton Jets

The prompt lepton jet search by ATLAS [306] defines two different kinds of lepton jets, electron jets and muon jets. The first category requires extensive knowledge about the detector response in the electromagnetic calorimeters. As they do not provide relevant tagging efficiencies it is difficult to reproduce their results. Thus we refrain from using electron jets and focus on muon jets.

For muon jets, ATLAS selects events that contain at trigger level either three muons with transverse momentum $p_T > 6$ GeV, or one muon with $p_T > 18$ GeV. Their pseudorapidity has to be less than $|\eta| < 2.5$. In addition, a track in the inner detector has to be associated with the muon, to ensure that it originates from a prompt decay. For our model that implies that the dark photon has to decay to muons before reaching the last layer of the silicon pixel detector at a radial distance of 122.5 mm from the interaction point. To match the muon with a specific interaction point the transverse impact parameter $|d_0|$ has to be less than 1 mm from the primary vertex.

A muonic lepton jet is then defined as a selection of collimated muons. For this, the muon with the largest $p_T$ is selected and all muons within an angular distance of $\Delta R < 0.1$ are collected. This step is repeated with the next subleading muon which is not yet part of a lepton jet until all muons are assigned.

ATLAS defines two different signal regions depending on the amount and quality of muonic lepton jets. The double muon jet event criterion requires two muon jets each containing at least two muons with $p_T > 11$ GeV. If the event was triggered by the single muon trigger the leading muon of the event has to satisfy additionally $p_T > 23$ GeV. To suppress background coming from $J/\Psi$ decays the two muons closest in $p_T$ need to fulfil $m_{\mu\mu} < 2$ GeV. This limits the reach effectively to dark photon masses below 2 GeV. Furthermore, ATLAS requires the lepton jets to be isolated by demanding

$$\rho \equiv \frac{\sum_i E_{T,i}}{p_{T,\mathrm{LJ}}} < 0.3\,. \tag{134}$$

The sum in eq. 134 runs over all calorimeter deposit within $\Delta R = 0.3$ of the lepton jet, but excluding contributions within $\Delta R < 0.05$ from any muon. $p_{T,\mathrm{LJ}}$ denotes the

transverse momentum of the lepton jet (LJ).

The single muon jet event criteria requires a single muon jet with at least four muons. Their respective transverse momentum has to fulfil $p_T > 19$ GeV, 16 GeV, 14 GeV for the three leading muons and $p_T > 4$ GeV for all other muons.

We found the latter signal region with just a single muon jet containing four muons within to be much less sensitive than double muon jet events. We will, therefore, focus only on events with two muon jets with at least two muons each.

The dominant background to this analysis are misidentified QCD multijet events. The expected rate is $0.5 \pm 0.3$ events at 5/fb of 7 TeV data according to ATLAS. In order to estimate the background contribution at 13 TeV, we rescale the background rate of the respective increase in QCD multijet production. This is about a factor of 3 [346]. We assume that the relative error remains the same. This estimate is of course only valid if we do not optimise any of the analysis cuts. Thus our limits will be conservative.

### 8.4.2 Displaced Lepton Jets

The displaced lepton jet search [307] is more complex than the prompt search, due to the exotic signatures that can arise when particles are in a part of the detector where they usual are not. This implies that we have to pay more attention to the detector response and various detector effects.

As there is no public detector simulation that properly simulates effects of displaced vertices, we simulate them on our own at particle level. The decay vertex of the dark photon and the momenta of its decay products are smeared using a Gaussian distribution with widths proportional to $1/L_{xy}$. $L_{xy}$ denotes here the transverse distance of the dark photon decay vertex to the beam axis. As dark photons themselves do not interact with the detector – unlike their decay products – heavily displaced vertices are affected less by the above smearing.

We tune the exact parameters of our smearing to match the lepton jet reconstruction efficiencies presented by ATLAS in figure 6 of ref. [307]. These efficiencies are based on a toy Monte Carlo simulation, where dark photon decays with flat transverse momentum and rapidity are generated, according to $p_T \in [10, 100]$ GeV and $\eta \in [-2.5, 2.5]$. We reproduce the same setup and to further improve the agreement we apply a fudge factor in each $L_{xy}$ bin.

Displaced muons are selected by ATLAS by employing only loose requirements on $p_T$ and $|\eta|$. They are just above the trigger threshold: $p_T > 6$ GeV and $|\eta| < 2.5$.

To ensure displacement ATLAS requires that the muons are not matched to a track in the inner detector. Thus the decay must happen after the dark photon travelled at least 122.5 mm, which corresponds to the last pixel detector layer. Those muons are often referred to as *stand-alone*. Nevertheless, the $A'$ decay must happen in the active detector volume so that the muon can be detected at all, *i.e.* $L_{xy} \lesssim 7$ m.

To suppress background from cosmic rays, the muon still has to be matched to a primary interaction vertex. Due to the lack of a track in the inner detector, the trajectory is extrapolated from the muon spectrometer. The requirements on the longitudinal and transverse impact parameters are therefore rather loose, $|z_0| < 270$ mm and $|d_0| < 200$ mm.

Furthermore, ATLAS reconstructs normal jets based on electromagnetic and hadronic calorimeter deposit. To avoid confusion with lepton jets we will refer to them as *calorimeter jets*. They are clustered using the anti-$k_T$ algorithm [90] as implemented in FastJet [289] with a cone radius $R = 0.4$. They have to fulfil $p_T > 20$ GeV and $|\eta| < 2.5$.

ATLAS distinguishes between three different types of lepton jets, to which they refer to as type-0, type-1, and type-2. An event has to contain exactly two lepton jets, regardless of type, with an azimuthal difference $|\Delta\phi| > 1.0$ between them. This yields the 6 different signal regions, 0–0, 0–1, 0–2, 1–1, 1–2, and 2–2 where e.g. 0–1 corresponds to an event reconstructed with one type-0 and one type-1 lepton jet.

A type-0 lepton jet is the equivalent of the muonic lepton jet in the prompt lepton jet search. A muonic type-0 lepton jet consists of at least two collimated displaced muons and is reconstructed as in the prompt search. Seeded by the highest-$p_T$ muon, other muons are collected within a distance of $\Delta R < 0.5$. If no other muon is found within this angular distance the muon is discarded.

If such a type-0 lepton jet is additionally accompanied by a single calorimeter jet, the combination of both are referred to as a type-1 mixed lepton jet instead of a type-0 lepton jet. If more calorimeter jets are found within $\Delta R < 0.5$ around the leading muon the lepton jet is discarded altogether.

Type-2 lepton jets are purely hadronic jets. Every calorimeter jet not yet associated with a type-1 lepton jet is referred to as a type-2 lepton jet if their electromagnetic fraction is lower than 0.1. The electromagnetic fraction is the ratio between the energy deposited in the electromagnetic and hadronic calorimeter. Due to the transition between barrel and endcap calorimeter, the region between $1.0 < |\eta| < 1.4$ is known to underestimate electromagnetic deposit. This regime is therefore excluded.

In addition, a type-2 lepton jet must have a small jet width given by

$$W \equiv \frac{\sum_i \Delta R^i \cdot p_T^i}{\Sigma_i p_T^i} < 0.1\,. \tag{135}$$

The sum takes all particles of the calorimeter jet into account. So far type-2 jets can still originate from prompt decays. Therefore, an isolation criterion is applied. It states that the scalar $p_T$ sum of all charged tracks in the inner detector within $\Delta R < 0.5$ around the jet has to be less than 3 GeV. In this procedure only tracks with $p_T > 400$ MeV and impact parameter $|z_0| < 10$ mm and $|d_0| < 10$ mm are considered.

How many lepton jets of the respective type are expected depends enormously on the dark photon decay mode and its lifetime. It is obvious that a type-0 lepton jet requires a decay to muons, but for a type-2 jet, it is not so clear.

A type-2 can be for example created by a decay to a charged pion or kaons inside any of the calorimeters. But a decay to neutral pions, for example, requires to happen inside the hadronic calorimeter in order to be identified to as a type-2 jet. Since $\pi^0$'s decay immediately to photons thus would lead to a large electromagnetic fraction if they would be created inside the electromagnetic calorimeter. For a decay inside the hadronic calorimeter, however, the photons would look like any other hadronic deposit, thus would potentially pass the type-2 selection criteria. The same holds for a $A' \to e^+e^-$ decay.

These arguments become especially interesting when we consider more complicated decay channels like $A' \to \pi^+\pi^-\pi^0$. Here, it depends crucially on how much energy the $\pi^0$ carries, but usually such a decay would be vetoed for a decay in the electromagnetic calorimeter, but accepted if the $A'$ decays in the hadronic calorimeter, just due to the subsequent $\pi^0 \to \gamma\gamma$ process.

The situation is even more complex for the decay $A' \to K_L^0 K_S^0$. The $K_L^0$ is stable on the lengthscale of the LHC, *i.e.* a lifetime longer than $\sim 10^{-10}$ $s$. It does not leave a track in the inner detector as it is charge neutral and does also not leave any deposit in the electromagnetic detector. It is, therefore, the perfect candidate for a type-2 lepton jet, even for very prompt decays within the inner detector. For the latter, however, the $K_S^0$ has to decay slow enough to not leave a track in the inner detector with its decay to $\pi^+\pi^-$ (branching ratio 69%) or a large electromagnetic deposit due to $K_S^0 \to \pi^0\pi^0$ (branching ratio 31%).

We summarise the properties of the most important $A'$ decay channels in tab. 7. A type-1 lepton jet requires at least two $A'$ being emitted from the same $\chi$ particle with one of them decaying to muons and the other to something else. It is accordingly rare.

| Detector | $A' \to e^+e^-$ | $A' \to \mu^+\mu^-$ | $A' \to \pi^+\pi^-/K^+K^-$ | $A' \to \pi^+\pi^-\pi^0$ | $A' \to K_L^0 K_S^0$ |
|---|---|---|---|---|---|
| LJ type | 2 (calorimeter) | 0 (muonic) | 2 (calorimeter) | 2 (calorimeter) | 2 (calorimeter) |
| ID | track | track | track | track | (✓) |
| ECAL | EM fraction | ✓ | ✓ | EM fraction | (✓) |
| HCAL | ✓ | ✓ | ✓ | ✓ | ✓ |

Table 7: Illustration of where in the detector a specific $A'$ decay must happen in order to potentially be reconstructed as a lepton jet. The detector components are *ID* for the inner detector, *ECAL* for the electromagnetic calorimeter, and *HCAL* for the hadronic calorimeter. For decays that will be vetoed, a reason for the veto is given, for example *EM fraction* for a too large electromagnetic fraction of the calorimeter jet. The type of lepton jet as which each decay mode is most likely to be reconstructed is given at the top of the table.

Main background sources are cosmic rays, which just happen to have the right timing and fake an interaction without actually leaving a track in the inner detector. The likelihood for this to occur is incredibly low, but cosmic rays are abundant despite the LHC being underground. Nevertheless, cosmic rays are well studied at the LHC and ATLAS estimates in total about $40 \pm 9$ background events. Most of them contribute to the signal regions involving type-0 lepton jets.

Another source of background events are multijet events faking mainly type-2 lepton jets. ATLAS estimates around $70 \pm 11$ events at 8 TeV.

### 8.4.3 Projected Limits

We recast the prompt and displaced lepton jet search by ATLAS. Tab. 8 shows the results of the prompt search for 7 TeV events with 5/fb integrated luminosity and the expected number of events for $\sqrt{s} = 13$ TeV and 100/fb integrated luminosity. We can clearly see that the number of events for both signal benchmarks is comparable to the background. Benchmark point B performs better than benchmark A due to the shorter dark photon lifetime. Thus more decays are actually prompt. The situation improves drastically at a center-of-mass energy of 13 TeV, where the signal is between a factor of 3 and 10 larger than the background.

The results for our recast of the displaced analysis is shown in tab. 9. We present information about the 8 TeV run with 20.3/fb of integrated luminosity and expected event numbers at 13 TeV with 100/fb of integrated luminosity. Note that we restrict ourselves to the 0–0 signal region at 13 TeV. The reason for this is that the displaced analysis is highly technical and background estimations are non-trivial and data-driven. Thus without having access to 13 TeV data we do not know how large the background will be. The 0–0 category, however, is dominated by cosmic ray back-

| | 7 TeV | 13 TeV |
|---|---|---|
| Benchmark A | 0.8 | 109 |
| Benchmark B | 3.9 | 334 |
| All backgrounds | $0.5 \pm 0.3$ | $30 \pm 18$ |
| data | 3 | |

Table 8: Predicted number of events for the prompt lepton jet analysis for both benchmark points from table 5. We compared this to the background predictions and the observed event rates from ref. [306]. We use 5/fb and 100/fb of integrated luminosity, respectively.

| | Lepton jet type | | | | | | | |
|---|---|---|---|---|---|---|---|---|
| | 0-0 | 0-1 | 0-2 | 1-1 | 1-2 | 2-2 | All | All excl. 2-2 |
| Cosmic ray bkg. | 15 | 0 | 14 | 0 | 0 | 11 | $40 \pm 11 \pm 9$ | $29 \pm 9 \pm 29$ |
| **8 TeV** | | | | | | | | |
| Multi-jet bkg. | | | | | | | $70 \pm 58 \pm 11$ | $12 \pm 9 \pm 2$ |
| Benchmark A | 14 | 3 | 104 | 0 | 14 | 200 | $335 \pm 18 \pm 100$ | $135 \pm 12 \pm 41$ |
| Benchmark B | 2.1 | 0.4 | 3.0 | 0 | 0.3 | 1.2 | $7 \pm 2.1 \pm 2.6$ | $5.8 \pm 1.7 \pm 2.4$ |
| data | 11 | 0 | 11 | 4 | 3 | 90 | 119 | 29 |
| **13 TeV** | | | | | | | | |
| Benchmark A | 169 | | | | | | | |
| Benchmark B | 28 | | | | | | | |

Table 9: Predicted number of events for the displaced lepton jet analysis for both benchmark parameter points from table 5. We compare this to the background predictions and the observed event rates from ref. [307]. In the last two columns, the first error is the statistical uncertainty, while the second one is systematic. Our sensitivity study at $\sqrt{s} = 13$ TeV includes only type 0–0 events because a reliable extrapolation of the multijet background to 13 TeV is difficult.

grounds, which is independent of the center-of-mass energy. As a result our limits obtained at 13 TeV will be very conservative.

Since benchmark point B is probed by the prompt search due to its shorter dark photon lifetime, the displaced search is sensitive to benchmark point A.

We use the $CL_s$ method [149] to obtain limits on $\sigma(pp \to Z')\mathrm{BR}(Z' \to \bar{\chi}\chi)$, where we assume a systematic uncertainty of 30% in the signal rate. Background rates are the respective ATLAS estimations, wherever necessary rescaled to 13 TeV. We present our results for benchmark point A and B in fig. 41 and fig. 42, respectively. In each panel, we vary one of the model parameters while keeping all others fixed.

We obtain in total five different limits. Two are based on the prompt lepton jet search and correspond to 7 TeV data and a 13 TeV extrapolation. The other three use the displaced lepton jet analysis. We show a limit estimate for 13 TeV data using only the 0–0 signal region, as discussed previously. The other two are both based on 8 TeV

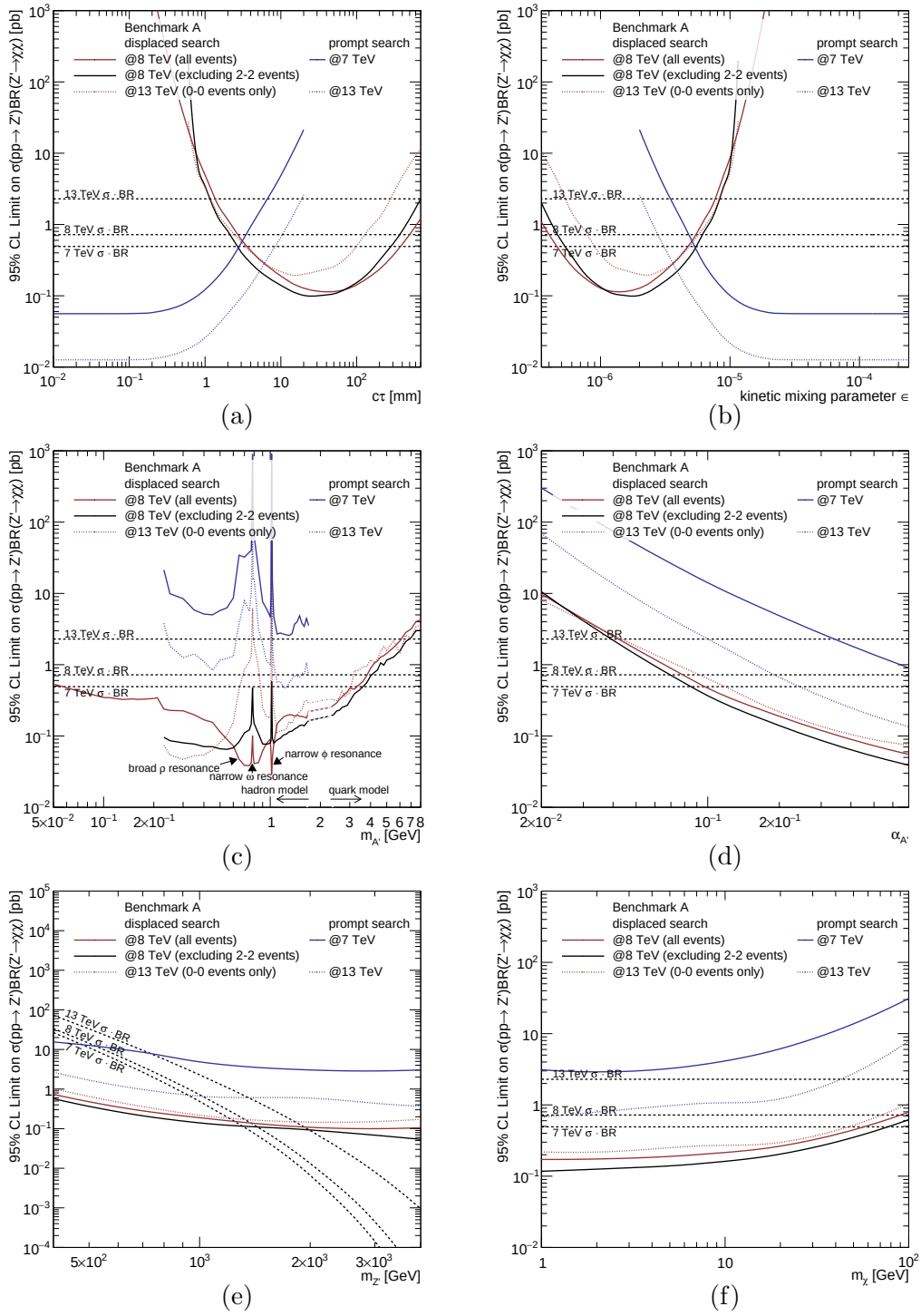


Figure 41: 95% CL upper limits on $\sigma(pp \to Z')\mathrm{BR}(Z' \to \bar{\chi}\chi)$ as a function of the model parameters for benchmark point A from table 5. In each panel, we vary one parameter while keeping the others fixed. Exclusion limits from the 7 TeV ATLAS search for prompt lepton jets [306] (solid blue) and from the 8 TeV ATLAS search for displaced lepton jets [307] are shown. For the latter search, we show results including all lepton jet events (red solid) and excluding the 2–2 category (black solid). The predicted sensitivity at $\sqrt{s} = 13$ TeV is shown as blue/red dotted curves. The black dotted lines in each panel show the predicted production cross sections of our signal model.

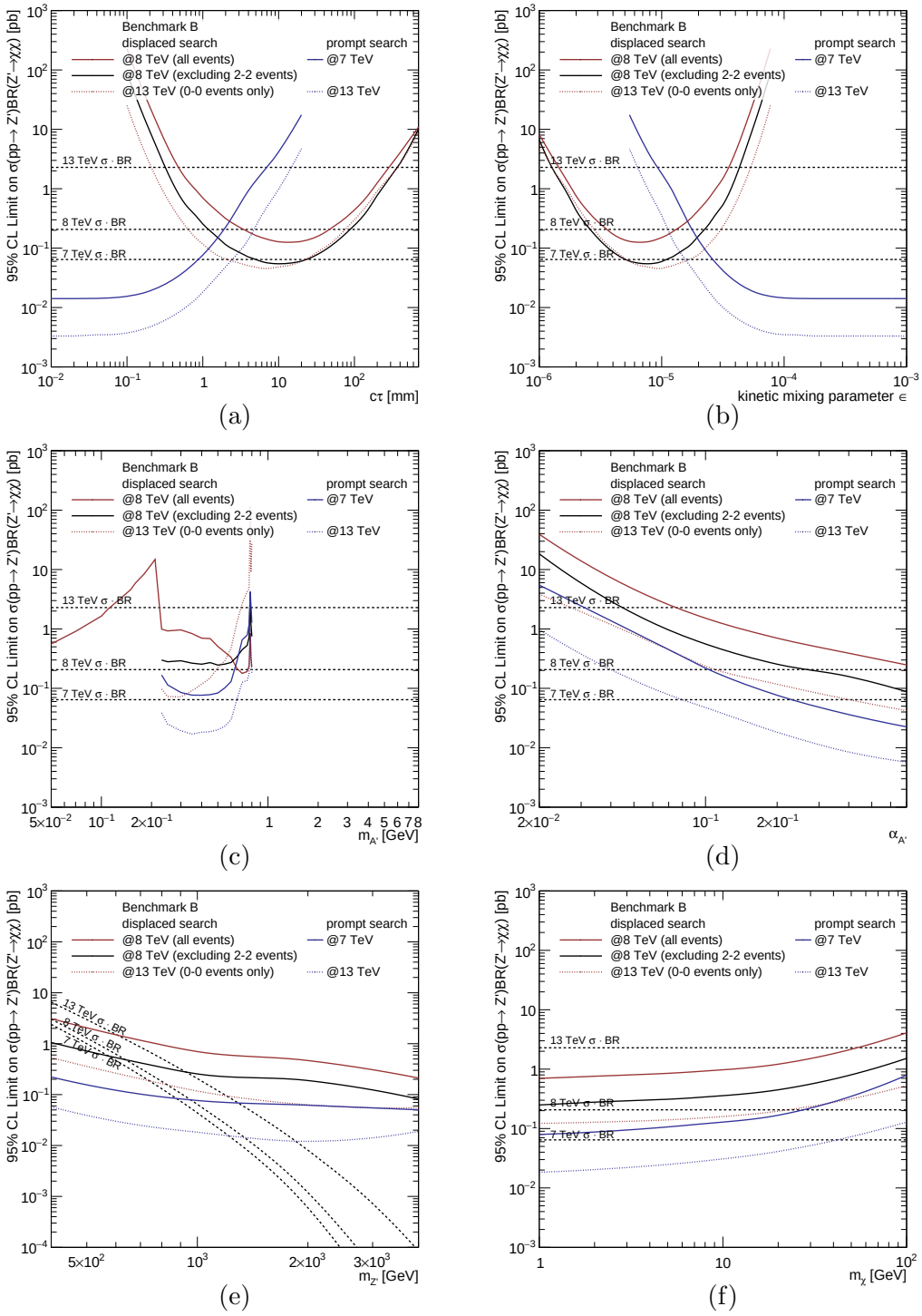


Figure 42: Same as fig. 41, but for benchmark point B from table 5.

data. One uses all six signal regions, whereas the other excludes 2–2 events. The reason for this is that the 2–2 category is dominated by QCD multijet background. In case the dark photon mass is such that it decays dominantly to leptons, our signal would not even significantly contribute to this signal region. Thus by excluding this category, the background can be reduced drastically.

We also show as horizontal lines the predicted values for $\sigma(pp \to Z')\mathrm{BR}(Z' \to \bar{\chi}\chi)$ at different center-of-mass energies.

Let us first focus on the results for benchmark point A in fig. 41. The first panel shows the model dependence on the dark photon lifetime $\tau$, which is equivalent to the second panel using $\epsilon$. We can easily see that the prompt search is very sensitive for low lifetimes with a decay length $c\tau \lesssim 1$ mm ($\epsilon \gtrsim 10^{-5}$). For larger decay lengths the dark photons do not decay in the inner detector anymore. But at this very point, the displaced lepton jet search starts to be constraining, as more decays products are not leaving a track anymore. It reaches peak sensitivity at around $c\tau = 10$–$100$ mm, which corresponds to $\epsilon \simeq \text{few} \times 10^{-6}$. For even larger lifetimes, however, the displaced search looses sensitivity too, as most dark photons are decay completely outside the ATLAS detector.

The lifetime for which the displaced lepton jets search reaches peak sensitivity depends strongly on the exact dark photon mass and underlying kinematics. In this context, note that there is a slight shift between the 8 TeV results including or excluding 2–2 events. This is due to the different detector volumes in which a specific dark photon decay can be identified as a lepton jet, see tab. 7.

A type-0 lepton jet relies on muons and the respective detector part in which a decay must happen is the electromagnetic or hadronic calorimeter. Many of the decay channels leading to type-2 jets are only reconstructed with an $A'$ decay in the hadronic calorimeter. Thus their available detector volume is smaller than for muons, but also further away from the interaction point. Hence, they prefer larger $A'$ lifetimes. As a result, the peak sensitivity moves to somewhat smaller lifetimes when excluding the 2-2 category, as the sensitivity relies more on type-0 jets.

Using similar arguments we can also understand the third panel of fig. 41, where we scan over the dark photon mass. Varying the dark photon mass is equivalent to scanning over various different decay channels, according to fig. 1. Fig. 41 (c) shows a lot of structure with peaks and dips, all of which are related to different decay channels [167].

At very small masses below the muon threshold the only decay channel is to electrons. Thus, only the 2-2 event category will be populated by signal events. Thus there is only a single limit obtained by the displaced 8 TeV search including all event

categories. This changes as soon as a decay to muons is kinematically allowed.

Note that most limits are getting weaker once a mass of $m_{A'} \sim 700$ MeV is reached. Here, the dark photon decays more often to charged pions due to the broad $\rho$ resonance. As most limits rely on a significant branching ratio to muons they are subsequently weaker. An exception is again the displaced 8 TeV search including all event categories, as they can efficiently reconstruct a decay to $\pi^+\pi^-$ as type-2 lepton jets.

At about $m_{A'} \approx$ MeV a sharp peak can be seen. Here, the $\omega$ resonance causes the dark photon to decay mainly to $\pi^+\pi^-\pi^0$. As discussed earlier, the additional neutral pion tends to veto the respective lepton jet, unless the decay happens in the hadronic calorimeter. But since this corresponds to a smaller active detector volume than for instance for $A' \to \pi^+\pi^-, \mu^+\mu^-$, the overall sensitivity decreases.

Another sharp peak can be seen at the narrow $\phi$ resonance with $m_{A'} \sim 1$ GeV. Here, the main decay channel is into $K_L^0 K_S^0$. We have seen earlier that this decay channel is optimal for a type-2 lepton jet, as it potentially allows the dark photon to even decay promptly. Thus the displaced 8 TeV search including all event categories receives a large increase in sensitivity. All other limits, however, decrease due to the much smaller branching fraction to muons.

For even larger $A'$ masses the hadronic decay channels are described via quarks, which subsequently hadronise. Thus the limits tend to be featureless. The overall sensitivity decrease for higher masses, as the number of emitted dark photons decreases simultaneously. Furthermore, the limits of the prompt lepton jet search stops at dark photon masses of 2 GeV, due to the invariant mass cut $m_{\mu\mu} < 2$ GeV.

Note that we left a gap around 2 GeV when calculating the dark photon branching ratios, see fig. 1 and corresponding discussion. We did not simulate this respective regime, but instead linearly interpolated between $m_{A'} = 1.7$ GeV and $m_{A'} = 2.3$ GeV. Fig. 41 (c) shows that this is can be done in a smooth way.

Fig. 41 (d) shows how, unsurprisingly, the limits improve with increasing dark fine structure constant $\alpha_{A'}$. This causes more dark photons to be emitted and hence the analysis efficiencies increase. For very large $\alpha_{A'}$, however, the perturbative treatment of the dark parton shower breaks down.

When increasing the resonance mass $m_{Z'}$ in fig. 41 (e) we see that the sensitivity increases. This is because a larger amount of energy is transferred to the dark matter pair, subsequently emitting more dark photons than before. This effect, however, fights against the on-shell condition for the $Z'$, as the center-of-mass energy is then not high enough.

Increasing the dark matter mass in fig. 41 (f) decreases the overall sensitivity, as for higher $\chi$ masses final state radiation is suppressed.

Comparing both benchmark points between fig. 41 and fig. 42, we see very similar features. Overall, benchmark point B is easier to detect in prompt searches due to its smaller $c\tau$. In fact, most limits are somewhat better, as lower $\chi$ and $A'$ masses mean that there is more final state radiation in general. When scanning over the dark photon mass, however, the limits stop at 800 MeV. Here, the relation $m_{A'} > 2m_\chi$ sets in, causing our dark photons to decay invisibly to dark matter, $A' \to \bar{\chi}\chi$.

In order to put our results in a more global context, we compare our upper bounds with recent limits on the dark photon $\epsilon$–$m_{A'}$ parameter space in fig. 43. These constraints are coming from the electron and muon anomalous magnetic moment [347–349], HADES [350], KLOE 2013 [351] and 2014 [352], the test run results from APEX [353], BaBar 2009 [354] and 2014 [355], beam dump experiments E137, E141, and E774 [356–358], A1 [359], Orsay [360], U70 [361], CHARM [362], LSND [363], as well as from astrophysical observations [364, 365] and $\pi^0$ decays [366]. For the 8 TeV displaced lepton jet search we decide for each parameter point individually whether it is beneficial to exclude 2-2 events or not. The lighter colored region around $m_{A'} = 2$ GeV corresponds to the transition region between the analysis in terms of hadron final states and the analysis in terms of quark final states and is based on linear interpolation.

Most of our bounds cover a complementary parameter space compared to any of the low energy experiments. We have to keep in mind, though, that these experiments test the dark photon in a model independent fashion, whereas we rely on the existence of a light dark matter particle which can be pair produced at the LHC.

Note that for decreasing $A'$ masses the kinetic mixing parameter $\epsilon$ needs to decrease in order to obtain competitive limits. This is due to the fact that $\epsilon$ is related to the dark photon lifetime via the dark photon decay width. And the latter changes when moving to a different $m_{A'}$ mass. Thus, in order to keep the dark photon lifetime constant, $\epsilon$ has to increase when decreasing $m_{A'}$.

Unsurprisingly, also the shape of our exclusion limits in fig. 43 is affected by the hadronic resonance $\rho$, $\omega$, and $\phi$, increasing or decreasing the respective limit as discussed before. Note for example the vertical gaps in the prompt lepton jet search. They are clearly visible at 7 TeV but are expected to be completely closed at 13 TeV due to the large increase in signal rate. Unfortunately, the prompt search is again limited to dark photon masses below 2 TeV.

In addition, we note that benchmark point A is already excluded by ATLAS 8 TeV data using the displaced lepton jet analysis. Benchmark point B is not excluded using 7 TeV and 8 TeV data, but expected to be ruled out using 13 TeV results. We want to point out too that our limits are very conservative, as in case of the prompt lepton jet

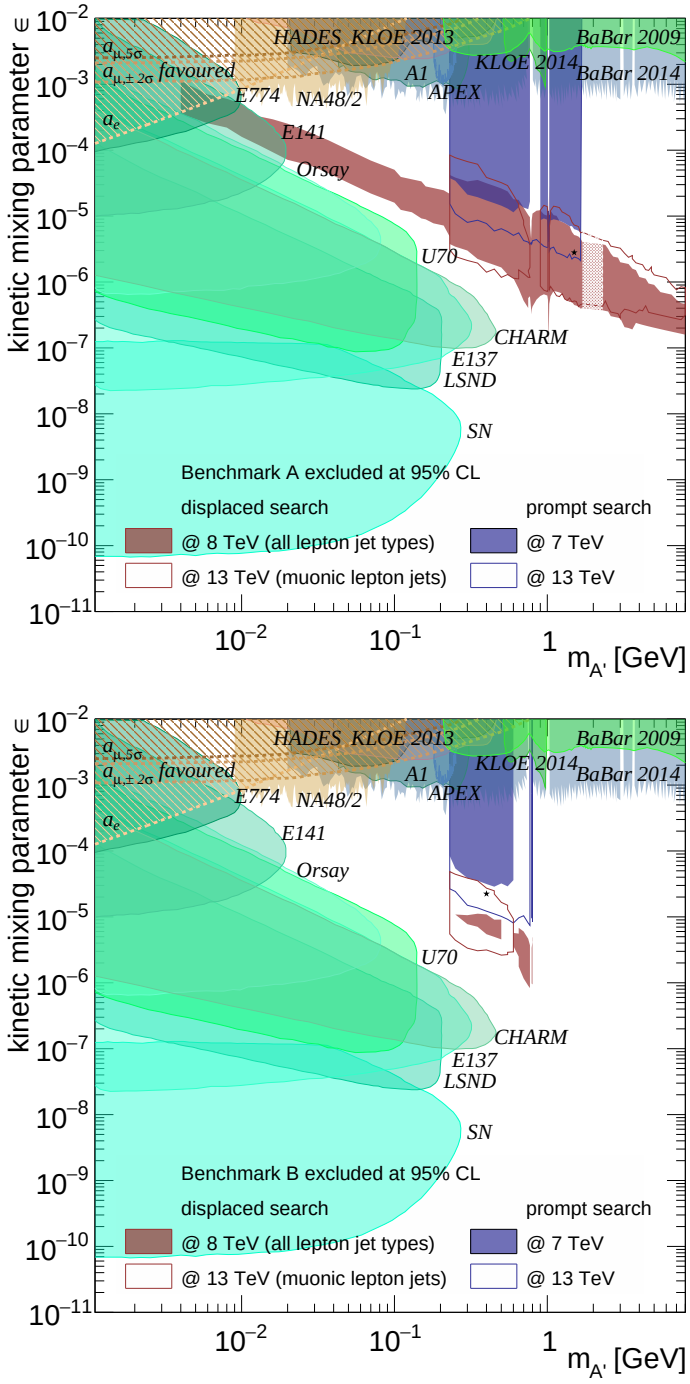


Figure 43: 95% CL constraints on the dark photon parameters $m_{A'}$ and $\epsilon$, with all other model parameters fixed at the benchmark points A (B) from table 5 in the top (bottom) panel. We show exclusion limits from the ATLAS search for prompt lepton jets in 5/fb of 7 TeV data [306] (blue shaded region) and from their displaced lepton jet search in 20.3/fb of 8 TeV data [307] (red shaded region), as well as projected sensitivities for 100/fb of 13 TeV data (blue/red unshaded regions). Black stars correspond to the exact benchmark points A and B, respectively.

search we only consider muonic lepton jets and the displaced 13 TeV results are based only on 0–0 events. The actual limits can be drastically improved when including all categories appropriately.

## 8.5 Lepton Jets at a 100 TeV Collider

A future 100 TeV collider has usually a significant edge over the LHC, as production cross sections from Standard Model extensions are much larger. This will also be true for the production mechanism for our dark matter pair. But the subsequent dark parton shower depends strongly on the kinematics of the process itself, which are also changing.

First of all, the average number of dark photons and their energy spectrum depends mainly on the energy of the dark matter particle. This in turn is given by the partonic energy of the process, *i.e.* the resonance mass in case of $s$-channel production. As much larger masses can be probed at the LHC we expect therefore stronger dark radiation. This is illustrated in fig. 44, where we show the distribution of expected number of dark photons for various different partonic energies. Note that we reduced the dark fine structure constant significantly and still obtain a reasonable number of dark photons.

But in addition, it offers also other possible production mechanisms. Consider for example an off-shell $t$-channel production, where the relevant partonic energy is given by the valence quark PDF. At the LHC this is too small to yield significant dark radiation, but this changes at a 100 TeV collider. Thus, basically all electroweak-scale production channels can be probed.

## 8.6 Discussion

In this chapter, we discussed a resonance decaying to invisible dark matter particles. The only way to detect such a dark matter pair production is with initial or final state radiation. The first one leads to the more common monojet search, but we were focusing on the latter.

Final state radiation requires an interaction in the dark sector, where our choice was a $\chi$-$A'$ interaction, where the mass of $\chi$ and $A'$ are both of order GeV. The emitted dark photons decay back to the Standard Model through their kinetic mixing with the photon. This leads to a unique kind of signature, referred to as lepton jets.

As the dark photon can be long-lived, ATLAS performed two different searches targeting prompt and displaced lepton jets. We recast both searches to obtain limits

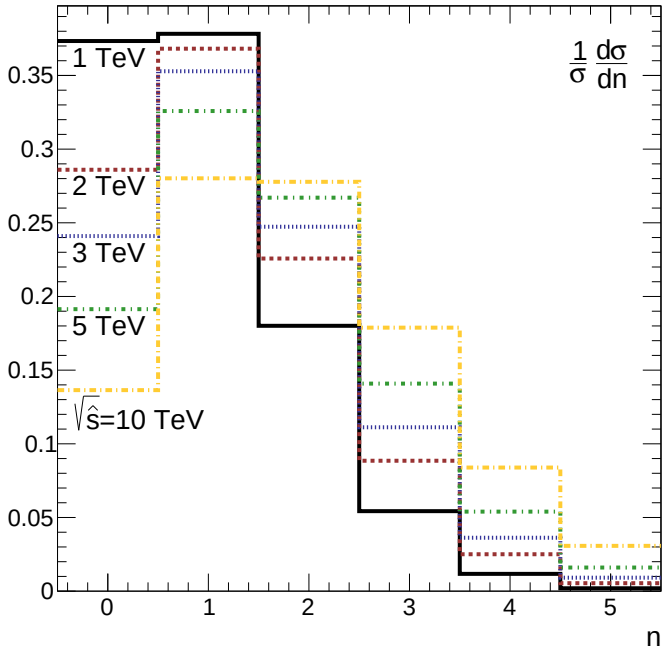


Figure 44: The distribution of the expected number of emitted dark photons in pair production process $pp \to \bar{\chi}\chi$ for several values of the partonic center of mass energy $\sqrt{\hat{s}}$. We have used a dark fine structure constant of $\alpha' = 0.05$, a DM mass of $m_\chi = 4$ GeV, and a dark photon mass $m_{A'} = 1.5$ GeV.

on our radiating dark matter model and estimate for future sensitivity.

We found that the upper bounds on such a process are sometimes non-trivial due to the various different dark photon decay channels and the respective detector response. Overall, the LHC probes a complementary regime in the dark photon parameter space. These bounds are expected to improve drastically when the center-of-mass energy is enhanced from 7 TeV or 8 TeV to 13 TeV, or even to 100 TeV at a future collider.

In addition, we developed a semi-analytic description for the dark parton shower. We paid special interest to the number of photons emitted for different dark matter energies, and also computed the respective energy distribution of the dark matter particle and the emitted dark photons. Such calculations are able to predict the amount of radiation that is above the detection threshold at a collider without having to simulate Monte Carlo events.

# CHAPTER 9

# Summary

In this dissertation we studied various aspects of resonance searches for heavy new particles.

We first worked in a two Higgs doublet model framework with flavour changing couplings of the Higgs to either quarks or leptons. If the Standard Model Higgs exhibits only small flavour changing couplings, the heavy neutral Higgs $H^0$ can still have a very large flavour violating coupling. Thus we motivated a reinterpretation of the CMS $h \to \tau\mu$ resonance search for a $H^0 \to \tau\mu$ process. The results obtained by our recast were translated into bounds on the two Higgs doublet model parameter space. We found them to be stronger than existing limits in certain regimes.

In addition we assumed a quark flavour violating coupling of the type $htu$. A novel search for a $pp \to H^0 t \to thh$ process was presented, where we made extensive use of the intermediate resonance masses of the top, $h$ and $H^0$. This search yields much stronger limits for a large range of parameters than the conventional search for a rare $t \to hu$ decay.

We then moved on to a coloured Standard Model extension. A massive coloured octet vector $X_\mu$ has the curious property that the single production mode $pp \to X$ is highly model-dependent, but the pair production channel $pp \to XX$ is not. This motivates searches for pair produced resonances decaying to quarks. Existing searches consider a four jet or four top final state, but not a mixed final state like $t\bar{t}JJ$.

We designed an analysis for such a mixed final state and showed it yields better limits on the mass of the heavy octet vector than existing searches if the branching ratio $\mathrm{BR}(X \to t\bar{t})$ is neither very large nor very small.

We then focused on post-discovery aspects of resonance searches. Once a resonance is found we have to distinguish between different model hypotheses. An important information is the spin of the resonance, which can be typically inferred from the kinematics of the process. This requires a good measurement of the final state particles, which in case of a boosted hadronic diboson $pp \to X \to VV' \to jjjj$ process is not necessarily given.

We studied the effects of jet substructure on the reconstruction of angular correlations and identified analysis cuts that skew the kinematic observables. These observables were used to determine a projected reach for a discrimination between various different model hypotheses using a $m_X = 2$ TeV case study. The result showed that, despite significant modification of the angular observables by the jet substructure algorithms, a discrimination is still possible at moderated integrated luminosity.

In the last part of this dissertation dark matter pair production via a heavy $Z'$ resonance was discussed. This channel is identified at the LHC as missing energy if significant initial state radiation is present. However, we showed that stronger limits can be obtained if the model includes a dark sector coupling between dark matter and a dark photon. In this case the dark matter pair is accompanied by final state radiation.

We developed a semi-analytic description of such a dark parton shower. Using this formalism we are able to calculate the average number of dark photons radiated in such a process, as well as their respective energy spectrum. This showed that significant radiation can be achieved while still being in agreement with existing constraints.

Lepton jets are the typical signature of a dark parton shower since the dark photons can decay to Standard Model particles through kinetic mixing with the photon. The size of the kinetic mixing parameter determines whether the decay will be prompt or lead to displaced vertices. We extensively discussed the phenomenological effects of such a model. The bounds on the model parameter space were calculated using a recast of an existing prompt and displaced lepton jet search. The limits cover a parameter region different to those covered by other experiments.

CHAPTER 10

# Bibliography


[1] **CMS** Collaboration, S. Chatrchyan et al., *Observation of a new boson at a mass of 125 GeV with the CMS experiment at the LHC*, *Phys. Lett.* **B716** (2013) 30–61, [arXiv:1207.7235].

[2] **ATLAS Collaboration** Collaboration, G. Aad et al., *Observation of a new particle in the search for the Standard Model Higgs boson with the ATLAS detector at the LHC*, *Phys.Lett.* **B716** (2012) 1–29, [arXiv:1207.7214].

[3] M. Buschmann, J. Kopp, J. Liu, and X.-P. Wang, *New Signatures of Flavor Violating Higgs Couplings*, *JHEP* **06** (2016) 149, [arXiv:1601.02616].

[4] M. Buschmann and F. Yu, *Angular observables for spin discrimination in boosted diboson final states*, *JHEP* **09** (2016) 036, [arXiv:1604.06096].

[5] M. Buschmann, J. Kopp, J. Liu, and P. A. N. Machado, *Lepton Jets from Radiating Dark Matter*, *JHEP* **07** (2015) 045, [arXiv:1505.07459].

[6] T. Golling et al., *Physics at a 100 TeV pp collider: beyond the Standard Model phenomena*, *Submitted to: Phys. Rept.* (2016) [arXiv:1606.00947].

[7] F. Zwicky, *On the Masses of Nebulae and of Clusters of Nebulae*, *Astrophys. J.* **86** (1937) 217–246.

[8] F. Zwicky, *Die Rotverschiebung von extragalaktischen Nebeln*, *Helv. Phys. Acta* **6** (1933) 110–127. [Gen. Rel. Grav.41,207(2009)].

[9] E. Corbelli and P. Salucci, *The Extended Rotation Curve and the Dark Matter Halo of M33*, *Mon. Not. Roy. Astron. Soc.* **311** (2000) 441–447, [astro-ph/9909252].

[10] A. N. Taylor, S. Dye, T. J. Broadhurst, N. Benitez, and E. van Kampen, *Gravitational lens magnification and the mass of abell 1689*, *Astrophys. J.* **501** (1998) 539, [astro-ph/9801158].

[11] **WMAP** Collaboration, G. Hinshaw et al., *Five-Year Wilkinson Microwave Anisotropy Probe (WMAP) Observations: Data Processing, Sky Maps, and Basic Results*, *Astrophys. J. Suppl.* **180** (2009) 225–245, [arXiv:0803.0732].

[12] G. Paál, I. Horváth, and B. Lukács, *Inflation and compactification from galaxy redshifts?*, *Astrophysics and Space Science* **191** (1992), no. 1 107–124.

[13] **WMAP** Collaboration, D. N. Spergel et al., *Wilkinson Microwave Anisotropy Probe (WMAP) three year results: implications for cosmology*, *Astrophys. J. Suppl.* **170** (2007) 377, [astro-ph/0603449].

[14] F. Bernardeau, S. Colombi, E. Gaztanaga, and R. Scoccimarro, *Large scale structure of the universe and cosmological perturbation theory*, *Phys. Rept.* **367** (2002) 1–248, [astro-ph/0112551].

[15] R. Davis, D. S. Harmer, and K. C. Hoffman, *Search for neutrinos from the sun*, *Phys. Rev. Lett.* **20** (May, 1968) 1205–1209.

[16] **Particle Data Group** Collaboration, R. M. Barnett et al., *Review of particle physics. Particle Data Group*, *Phys. Rev.* **D54** (1996) 1–720.

[17] **CMS** Collaboration, V. Khachatryan et al., *Search for Lepton-Flavour-Violating Decays of the Higgs Boson*, *Phys. Lett.* **B749** (2015) 337–362, [arXiv:1502.07400].

[18] J. D. Bjorken and S. Weinberg, *A Mechanism for Nonconservation of Muon Number*, *Phys. Rev. Lett.* **38** (1977) 622.

[19] B. McWilliams and L.-F. Li, *Virtual Effects of Higgs Particles*, *Nucl. Phys.* **B179** (1981) 62.

[20] K. S. Babu and S. Nandi, *Natural fermion mass hierarchy and new signals for the Higgs boson*, *Phys. Rev.* **D62** (2000) 033002, [hep-ph/9907213].

[21] J. L. Diaz-Cruz and J. Toscano, *Lepton flavor violating decays of Higgs bosons beyond the standard model*, *Phys.Rev.* **D62** (2000) 116005, [hep-ph/9910233].

[22] T. Han and D. Marfatia, *$h \to \mu\tau$ at hadron colliders*, *Phys. Rev. Lett.* **86** (2001) 1442–1445, [hep-ph/0008141].

[23] G. F. Giudice and O. Lebedev, *Higgs-dependent Yukawa couplings*, *Phys.Lett.* **B665** (2008) 79–85, [arXiv:0804.1753].

[24] J. A. Aguilar-Saavedra, *A Minimal set of top-Higgs anomalous couplings*, *Nucl. Phys.* **B821** (2009) 215–227, [arXiv:0904.2387].

[25] A. Goudelis, O. Lebedev, and J.-h. Park, *Higgs-induced lepton flavor violation*, *Phys. Lett.* **B707** (2012) 369–374, [arXiv:1111.1715].

[26] G. Blankenburg, J. Ellis, and G. Isidori, *Flavour-Changing Decays of a 125 GeV Higgs-like Particle*, *Phys.Lett.* **B712** (2012) 386–390, [arXiv:1202.5704].

[27] S. Kanemura, T. Ota, and K. Tsumura, *Lepton flavor violation in Higgs boson decays under the rare tau decay results*, *Phys. Rev.* **D73** (2006) 016006, [hep-ph/0505191].

[28] S. Davidson and G. J. Grenier, *Lepton flavour violating Higgs and tau to mu gamma*, *Phys. Rev.* **D81** (2010) 095016, [arXiv:1001.0434].

[29] R. Harnik, J. Kopp, and J. Zupan, *Flavor Violating Higgs Decays*, *JHEP* **1303** (2013) 026, [arXiv:1209.1397].

[30] S. Davidson and P. Verdier, *LHC sensitivity to the decay of a Higgs boson to tau mu*, arXiv:1211.1248.

[31] A. Celis, V. Cirigliano, and E. Passemar, *Lepton flavor violation in the Higgs sector and the role of hadronic tau-lepton decays*, arXiv:1309.3564.

[32] M. Gorbahn and U. Haisch, *Searching for $t \to c(u)h$ with dipole moments*, arXiv:1404.4873.

[33] T. D. Lee, *A Theory of Spontaneous T Violation*, *Phys. Rev.* **D8** (1973) 1226–1239.

[34] G. C. Branco, P. M. Ferreira, L. Lavoura, M. N. Rebelo, M. Sher, and J. P. Silva, *Theory and phenomenology of two-Higgs-doublet models*, *Phys. Rept.* **516** (2012) 1–102, [arXiv:1106.0034].

[35] R. A. Diaz, *Phenomenological analysis of the two Higgs doublet model*. PhD thesis, Colombia, U. Natl., 2002. hep-ph/0212237.

[36] A. Celis, V. Ilisie, and A. Pich, *LHC constraints on two-Higgs doublet models*, *JHEP* **07** (2013) 053, [arXiv:1302.4022].

[37] J. Baglio, O. Eberhardt, U. Nierste, and M. Wiebusch, *Benchmarks for Higgs Pair Production and Heavy Higgs boson Searches in the Two-Higgs-Doublet Model of Type II*, *Phys. Rev.* **D90** (2014), no. 1 015008, [arXiv:1403.1264].

[38] J. F. Gunion and H. E. Haber, *The CP conserving two Higgs doublet model: The Approach to the decoupling limit*, *Phys. Rev.* **D67** (2003) 075019, [hep-ph/0207010].

[39] J. Kopp and M. Nardecchia, *Flavor and CP violation in Higgs decays*, *JHEP* **10** (2014) 156, [arXiv:1406.5303].

[40] D. A. Sierra and A. Vicente, *Explaining the CMS Higgs flavor violating decay excess*, arXiv:1409.7690.

[41] A. Crivellin, G. D'Ambrosio, and J. Heeck, *Explaining $h \to \mu^\pm\tau^\mp$, $B \to K^*\mu^+\mu^-$ and $B \to K\mu^+\mu^-/B \to Ke^+e^-$ in a two-Higgs-doublet model with gauged $L_\mu - L_\tau$*, arXiv:1501.00993.

[42] L. de Lima, C. S. Machado, R. D. Matheus, and L. A. F. d. Prado, *Higgs Flavor Violation as a Signal to Discriminate Models*, arXiv:1501.06923.

[43] Y. Omura, E. Senaha, and K. Tobe, *Lepton-flavor-violating Higgs decay $h \to \mu\tau$ and muon anomalous magnetic moment in a general two Higgs doublet model*, *JHEP* **05** (2015) 028, [arXiv:1502.07824].

[44] I. Dorsner, S. Fajfer, A. Greljo, J. F. Kamenik, N. Kosnik, et al., *New Physics Models Facing Lepton Flavor Violating Higgs Decays at the Percent Level*, arXiv:1502.07784.

[45] B. Altunkaynak, W.-S. Hou, C. Kao, M. Kohda, and B. McCoy, *Flavor Changing Heavy Higgs Interactions at the LHC*, arXiv:1506.00651.

[46] A. Crivellin, J. Heeck, and P. Stoffer, *A perturbed lepton-specific two-Higgs-doublet model facing experimental hints for physics beyond the Standard Model*, arXiv:1507.07567.

[47] W. Altmannshofer, S. Gori, A. L. Kagan, L. Silvestrini, and J. Zupan, *Uncovering Mass Generation Through Higgs Flavor Violation*, arXiv:1507.07927.

[48] F. J. Botella, G. C. Branco, M. Nebot, and M. N. Rebelo, *Flavour Changing Higgs Couplings in a Class of Two Higgs Doublet Models*, arXiv:1508.05101.

[49] A. Arhrib, R. Benbrik, C.-H. Chen, M. Gomez-Bock, and S. Semlali, *Two-Higgs-Doublet type-II and -III models and $t \to ch$ at the LHC*, arXiv:1508.06490.

[50] R. Benbrik, C.-H. Chen, and T. Nomura, *$h, Z \to \ell_i \bar{\ell}_j$, $\Delta a_\mu$, $\tau \to (3\mu, \mu\gamma)$ in generic two-Higgs-doublet models*, arXiv:1511.08544.

[51] **UTfit** Collaboration, M. Bona et al., *Model-independent constraints on $\Delta F = 2$ operators and the scale of new physics*, *JHEP* **03** (2008) 049, [arXiv:0707.0636].

[52] R. S. Chivukula, A. Farzinnia, J. Ren, and E. H. Simmons, *Constraints on the Scalar Sector of the Renormalizable Coloron Model*, *Phys. Rev.* **D88** (2013), no. 7 075020, [arXiv:1307.1064]. [Erratum: Phys. Rev.D89,no.5,059905(2014)].

[53] R. S. Chivukula, A. G. Cohen, and E. H. Simmons, *New strong interactions at the Tevatron?*, *Phys. Lett.* **B380** (1996) 92–98, [hep-ph/9603311].

[54] Y. Bai and B. A. Dobrescu, *Heavy octets and Tevatron signals with three or four b jets*, *JHEP* **07** (2011) 100, [arXiv:1012.5814].

[55] C. T. Hill and S. J. Parke, *Top production: Sensitivity to new physics*, *Phys. Rev.* **D49** (1994) 4454–4462, [hep-ph/9312324].

[56] D. A. Dicus, B. Dutta, and S. Nandi, *Top quark signature in extended color theories*, *Phys. Rev.* **D51** (1995) 6085–6091, [hep-ph/9412370].

[57] E. H. Simmons, *Coloron phenomenology*, *Phys. Rev.* **D55** (1997) 1678–1683, [hep-ph/9608269].

[58] P. H. Frampton and S. L. Glashow, *Chiral Color: An Alternative to the Standard Model*, *Phys. Lett.* **B190** (1987) 157–161.

[59] M. V. Martynov and A. D. Smirnov, *Chiral color symmetry and possible G-prime-boson effects at the Tevatron and LHC*, *Mod. Phys. Lett.* **A24** (2009) 1897–1905, [arXiv:0906.4525].

[60] P. H. Frampton, J. Shu, and K. Wang, *Axigluon as Possible Explanation for p anti-p —¿ t anti-t Forward-Backward Asymmetry*, *Phys. Lett.* **B683** (2010) 294–297, [arXiv:0911.2955].

[61] P. H. Frampton and S. L. Glashow, *Unifiable Chiral Color With Natural Gim Mechanism*, *Phys. Rev. Lett.* **58** (1987) 2168.

[62] O. Antunano, J. H. Kuhn, and G. Rodrigo, *Top quarks, axigluons and charge asymmetries at hadron colliders*, *Phys. Rev.* **D77** (2008) 014003, [arXiv:0709.1652].

[63] P. Ferrario and G. Rodrigo, *Constraining heavy colored resonances from top-antitop quark events*, *Phys. Rev.* **D80** (2009) 051701, [arXiv:0906.5541].

[64] G. Rodrigo and P. Ferrario, *Charge asymmetry: A Theory appraisal*, *Nuovo Cim.* **C033** (2010), no. 4 221–228, [arXiv:1007.4328].

[65] R. S. Chivukula, E. H. Simmons, and C. P. Yuan, *Axigluons cannot explain the observed top quark forward-backward asymmetry*, *Phys. Rev.* **D82** (2010) 094009, [arXiv:1007.0260].

[66] G. Marques Tavares and M. Schmaltz, *Explaining the t-tbar asymmetry with a light axigluon*, *Phys. Rev.* **D84** (2011) 054008, [arXiv:1107.0978].

[67] J. Bagger, C. Schmidt, and S. King, *Axigluon Production in Hadronic Collisions*, *Phys. Rev.* **D37** (1988) 1188.

[68] C. T. Hill, *Topcolor: Top quark condensation in a gauge extension of the standard model*, *Phys. Lett.* **B266** (1991) 419–424.

[69] C. T. Hill, *Topcolor assisted technicolor*, *Phys. Lett.* **B345** (1995) 483–489, [hep-ph/9411426].

[70] M. B. Popovic and E. H. Simmons, *A Heavy top quark from flavor universal colorons*, *Phys. Rev.* **D58** (1998) 095007, [hep-ph/9806287].

[71] F. Braam, M. Flossdorf, R. S. Chivukula, S. Di Chiara, and E. H. Simmons, *Hypercharge-Universal Topcolor*, *Phys. Rev.* **D77** (2008) 055005, [arXiv:0711.1127].

[72] K. Agashe, M. Bauer, F. Goertz, S. J. Lee, L. Vecchi, L.-T. Wang, and F. Yu, *Constraining RS Models by Future Flavor and Collider Measurements: A Snowmass Whitepaper*, arXiv:1310.1070.

[73] D. A. Dicus, C. D. McMullen, and S. Nandi, *Collider implications of Kaluza-Klein excitations of the gluons*, *Phys. Rev.* **D65** (2002) 076007, [hep-ph/0012259].

[74] T. Appelquist, H.-C. Cheng, and B. A. Dobrescu, *Bounds on universal extra dimensions*, *Phys. Rev.* **D64** (2001) 035002, [hep-ph/0012100].

[75] L. Randall and R. Sundrum, *A Large mass hierarchy from a small extra dimension*, *Phys. Rev. Lett.* **83** (1999) 3370–3373, [hep-ph/9905221].

[76] L. Randall and R. Sundrum, *An Alternative to compactification*, *Phys. Rev. Lett.* **83** (1999) 4690–4693, [hep-th/9906064].

[77] H. Davoudiasl, J. L. Hewett, and T. G. Rizzo, *Experimental probes of localized gravity: On and off the wall*, *Phys. Rev.* **D63** (2001) 075004, [hep-ph/0006041].

[78] B. Lillie, L. Randall, and L.-T. Wang, *The Bulk RS KK-gluon at the LHC*, *JHEP* **09** (2007) 074, [hep-ph/0701166].

[79] A. Datta, K. Kong, and K. T. Matchev, *Minimal Universal Extra Dimensions in CalcHEP/CompHEP*, *New J. Phys.* **12** (2010) 075017, [arXiv:1002.4624].

[80] S. J. Huber and Q. Shafi, *Fermion masses, mixings and proton decay in a Randall-Sundrum model*, *Phys. Lett.* **B498** (2001) 256–262, [hep-ph/0010195].

[81] T. Kaluza, *On the Problem of Unity in Physics*, *Sitzungsber. Preuss. Akad. Wiss. Berlin (Math. Phys.)* **1921** (1921) 966–972.

[82] O. Klein, *Quantum Theory and Five-Dimensional Theory of Relativity. (In German and English)*, *Z. Phys.* **37** (1926) 895–906. [Surveys High Energ. Phys.5,241(1986)].

[83] R. D. Peccei and H. R. Quinn, *Constraints imposed by* CP *conservation in the presence of pseudoparticles*, *Phys. Rev. D* **16** (Sep, 1977) 1791–1797.

[84] R. D. Peccei and H. R. Quinn, CP, *Phys. Rev. Lett.* **38** (Jun, 1977) 1440–1443.

[85] K. Petraki and R. R. Volkas, *Review of asymmetric dark matter*, *Int. J. Mod. Phys.* **A28** (2013) 1330028, [arXiv:1305.4939].

[86] L. Ackerman, M. R. Buckley, S. M. Carroll, and M. Kamionkowski, *Dark Matter and Dark Radiation*, *Phys. Rev.* **D79** (2009) 023519, [arXiv:0810.5126]. [,277(2008)].

[87] M. R. Whalley, *A compilation of data on hadronic total cross sections in $e^+e^-$ interactions*, *Journal of Physics G: Nuclear and Particle Physics* **29** (2003), no. 12A A1.

[88] "Hepdata on-line data review." *http://hepdata.cedar.ac.uk/review/rsig/*.

[89] S. Catani, Y. L. Dokshitzer, M. H. Seymour, and B. R. Webber, *Longitudinally invariant $K_t$ clustering algorithms for hadron hadron collisions*, *Nucl. Phys.* **B406** (1993) 187–224.

[90] M. Cacciari, G. P. Salam, and G. Soyez, *The Anti-k(t) jet clustering algorithm*, *JHEP* **04** (2008) 063, [arXiv:0802.1189].

[91] Y. L. Dokshitzer, G. D. Leder, S. Moretti, and B. R. Webber, *Better jet clustering algorithms*, *JHEP* **08** (1997) 001, [hep-ph/9707323].

[92] J. M. Butterworth, A. R. Davison, M. Rubin, and G. P. Salam, *Jet substructure as a new Higgs search channel at the LHC*, *Phys. Rev. Lett.* **100** (2008) 242001, [arXiv:0802.2470].

[93] A. Abdesselam et al., *Boosted objects: A Probe of beyond the Standard Model physics*, *Eur. Phys. J.* **C71** (2011) 1661, [arXiv:1012.5412].

[94] A. Altheimer et al., *Jet Substructure at the Tevatron and LHC: New results, new tools, new benchmarks*, *J. Phys.* **G39** (2012) 063001, [arXiv:1201.0008].

[95] A. Altheimer et al., *Boosted objects and jet substructure at the LHC. Report of BOOST2012, held at IFIC Valencia, 23rd-27th of July 2012*, *Eur. Phys. J.* **C74** (2014), no. 3 2792, [arXiv:1311.2708].

[96] D. Adams et al., *Towards an Understanding of the Correlations in Jet Substructure*, *Eur. Phys. J.* **C75** (2015), no. 9 409, [arXiv:1504.00679].

[97] **ATLAS** Collaboration, G. Aad et al., *Jet mass and substructure of inclusive jets in $\sqrt{s} = 7$ TeV pp collisions with the ATLAS experiment*, *JHEP* **05** (2012) 128, [arXiv:1203.4606].

[98] **ATLAS** Collaboration, G. Aad et al., *Performance of jet substructure techniques for large-R jets in proton-proton collisions at $\sqrt{s} = 7$ TeV using the ATLAS detector*, *JHEP* **09** (2013) 076, [arXiv:1306.4945].

[99] S. D. Ellis, C. K. Vermilion, and J. R. Walsh, *Techniques for improved heavy particle searches with jet substructure*, *Phys. Rev.* **D80** (2009) 051501, [arXiv:0903.5081].

[100] S. D. Ellis, C. K. Vermilion, and J. R. Walsh, *Recombination Algorithms and Jet Substructure: Pruning as a Tool for Heavy Particle Searches*, *Phys. Rev.* **D81** (2010) 094023, [arXiv:0912.0033].

[101] D. Krohn, J. Thaler, and L.-T. Wang, *Jet Trimming*, *JHEP* **02** (2010) 084, [arXiv:0912.1342].

[102] J. Thaler and K. Van Tilburg, *Identifying Boosted Objects with N-subjettiness*, *JHEP* **03** (2011) 015, [arXiv:1011.2268].

[103] J. Thaler and K. Van Tilburg, *Maximizing Boosted Top Identification by Minimizing N-subjettiness*, *JHEP* **02** (2012) 093, [arXiv:1108.2701].

[104] A. J. Larkoski, G. P. Salam, and J. Thaler, *Energy Correlation Functions for Jet Substructure*, *JHEP* **06** (2013) 108, [arXiv:1305.0007].

[105] A. J. Larkoski, I. Moult, and D. Neill, *Power Counting to Better Jet Observables*, *JHEP* **12** (2014) 009, [arXiv:1409.6298].

[106] A. J. Larkoski, I. Moult, and D. Neill, *Analytic Boosted Boson Discrimination*, arXiv:1507.03018.

[107] M. Blanke, A. J. Buras, B. Duling, S. Gori, and A. Weiler, $\Delta$ *F=2 Observables and Fine-Tuning in a Warped Extra Dimension with Custodial Protection*, *JHEP* **03** (2009) 001, [arXiv:0809.1073].

[108] S. Casagrande, F. Goertz, U. Haisch, M. Neubert, and T. Pfoh, *Flavor Physics in the Randall-Sundrum Model: I. Theoretical Setup and Electroweak Precision Tests*, *JHEP* **10** (2008) 094, [arXiv:0807.4937].

[109] M. E. Albrecht, M. Blanke, A. J. Buras, B. Duling, and K. Gemmler, *Electroweak and Flavour Structure of a Warped Extra Dimension with Custodial Protection*, *JHEP* **09** (2009) 064, [arXiv:0903.2415].

[110] A. J. Buras, B. Duling, and S. Gori, *The Impact of Kaluza-Klein Fermions on Standard Model Fermion Couplings in a RS Model with Custodial Protection*, *JHEP* **09** (2009) 076, [arXiv:0905.2318].

[111] A. Azatov, M. Toharia, and L. Zhu, *Higgs Mediated FCNC's in Warped Extra Dimensions*, *Phys. Rev.* **D80** (2009) 035016, [arXiv:0906.1990].

[112] A. Arhrib, Y. Cheng, and O. C. W. Kong, *Higgs to mu+tau Decay in Supersymmetry without R-parity*, *Europhys. Lett.* **101** (2013) 31003, [arXiv:1208.4669].

[113] A. Arhrib, Y. Cheng, and O. C. Kong, *A Comprehensive Analysis on Lepton Flavor Violating Higgs to mu + tau Decay in Supersymmetry without R Parity*, arXiv:1210.8241.

[114] D. Aloni, Y. Nir, and E. Stamou, *Large BR($h \to \tau\mu$) in the MSSM*, arXiv:1511.00979.

[115] A. Dery, A. Efrati, Y. Hochberg, and Y. Nir, *What if $BR(h \to \mu\mu)/BR(h \to \tau\tau)$ does not equal $m_\mu^2/m_\tau^2$?*, *JHEP* **1305** (2013) 039, [arXiv:1302.3229].

[116] M. D. Campos, A. E. C. HernÃ¡ndez, H. PÃ¤s, and E. Schumacher, *Higgs $\to \mu\tau$ as an indication for $S_4$ flavor symmetry*, arXiv:1408.1652.

[117] A. Dery, A. Efrati, Y. Nir, Y. Soreq, and V. Susič, *Model building for flavor changing Higgs couplings*, arXiv:1408.1371.

[118] J. Heeck, M. Holthausen, W. Rodejohann, and Y. Shimizu, *Higgs $\to \mu\tau$ in Abelian and Non-Abelian Flavor Symmetry Models*, arXiv:1412.3671.

[119] I. de Medeiros Varzielas, O. Fischer, and V. Maurer, *$\mathbb{A}_4$ symmetry at colliders and in the universe*, *JHEP* **08** (2015) 080, [arXiv:1504.03955].

[120] I. d. M. Varzielas and O. Fischer, *Non-Abelian family symmetries as portals to dark matter*, arXiv:1512.00869.

[121] E. Arganda, A. M. Curiel, M. J. Herrero, and D. Temes, *Lepton flavor violating Higgs boson decays from massive seesaw neutrinos*, *Phys.Rev.* **D71** (2005) 035011, [hep-ph/0407302].

[122] E. Arganda, M. Herrero, X. Marcano, and C. Weiland, *Imprints of Massive ISS Neutrinos in LFV Higgs Decays*, arXiv:1405.4300.

[123] E. Arganda, M. J. Herrero, X. Marcano, and C. Weiland, *Enhancement of the LFV Higgs decay rates from SUSY loops in the Inverse Seesaw Model*, arXiv:1508.04623.

[124] A. Falkowski, D. M. Straub, and A. Vicente, *Vector-like leptons: Higgs decays and collider phenomenology*, *JHEP* **1405** (2014) 092, [arXiv:1312.5329].

[125] K. Cheung, W.-Y. Keung, and P.-Y. Tseng, *Leptoquark induced rare decay amplitudes $h \to \tau^\mp \mu^\pm$ and $\tau \to \mu\gamma$*, arXiv:1508.01897.

[126] S. Baek and K. Nishiwaki, *Leptoquark explanation of $h \to \mu\tau$ and muon $(g-2)$*, arXiv:1509.07410.

[127] S. Baek and Z.-F. Kang, *Naturally Large Radiative Lepton Flavor Violating Higgs Decay Mediated by Lepton-flavored Dark Matter*, arXiv:1510.00100.

[128] K. Agashe and R. Contino, *Composite Higgs-Mediated FCNC*, *Phys. Rev.* **D80** (2009) 075016, [arXiv:0906.1542].

[129] N. Craig, J. A. Evans, R. Gray, M. Park, S. Somalwar, et al., *Searching for $t \to ch$ with Multi-Leptons*, arXiv:1207.6794.

[130] D. Atwood, S. K. Gupta, and A. Soni, *Constraining the flavor changing Higgs couplings to the top-quark at the LHC*, *JHEP* **10** (2014) 57, [arXiv:1305.2427].

[131] K.-F. Chen, W.-S. Hou, C. Kao, and M. Kohda, *When the Higgs meets the Top: Search for $t \to ch^0$ at the LHC*, arXiv:1304.8037.

[132] A. Greljo, J. F. Kamenik, and J. Kopp, *Disentangling Flavor Violation in the Top-Higgs Sector at the LHC*, arXiv:1404.1278.

[133] L. Wu, *Enhancing thj Production from Top-Higgs FCNC Couplings*, arXiv:1407.6113.

[134] A. Crivellin and L. Mercolli, *$B- > X_d\gamma$ and constraints on new physics*, *Phys. Rev.* **D84** (2011) 114005, [arXiv:1106.5499].

[135] A. Crivellin, A. Kokulu, and C. Greub, *Flavor-phenomenology of two-Higgs-doublet models with generic Yukawa structure*, *Phys. Rev.* **D87** (2013), no. 9 094031, [arXiv:1303.5877].

[136] **ATLAS** Collaboration, G. Aad et al., *Search for lepton-flavour-violating $H \to \mu\tau$ decays of the Higgs boson with the ATLAS detector*, arXiv:1508.03372.

[137] D. Eriksson, J. Rathsman, and O. Stal, *2HDMC: Two-Higgs-Doublet Model Calculator Physics and Manual*, *Comput. Phys. Commun.* **181** (2010) 189–205, [arXiv:0902.0851].

[138] **BaBar** Collaboration, B. Aubert et al., *Searches for Lepton Flavor Violation in the Decays $\tau^\pm \to e^\pm\gamma$ and $\tau^\pm \to \mu^\pm\gamma$*, *Phys. Rev. Lett.* **104** (2010) 021802, [arXiv:0908.2381].

[139] D. Chang, W. S. Hou, and W.-Y. Keung, *Two loop contributions of flavor changing neutral Higgs bosons to $\mu \to e\gamma$*, *Phys. Rev.* **D48** (1993) 217–224, [hep-ph/9302267].

[140] **LHC Higgs Cross Section Working Group** Collaboration, S. Dittmaier et al., *Handbook of LHC Higgs Cross Sections: 1. Inclusive Observables*, arXiv:1101.0593.

[141] J. R. Ellis, M. K. Gaillard, and D. V. Nanopoulos, *A Phenomenological Profile of the Higgs Boson*, *Nucl. Phys.* **B106** (1976) 292.

[142] M. A. Shifman, A. I. Vainshtein, M. B. Voloshin, and V. I. Zakharov, *Low-Energy Theorems for Higgs Boson Couplings to Photons*, *Sov. J. Nucl. Phys.* **30** (1979) 711–716. [Yad. Fiz.30,1368(1979)].

[143] B. A. Kniehl and M. Spira, *Low-energy theorems in Higgs physics*, *Z. Phys.* **C69** (1995) 77–88, [hep-ph/9505225].

[144] J. Alwall, R. Frederix, S. Frixione, V. Hirschi, F. Maltoni, O. Mattelaer, H. S. Shao, T. Stelzer, P. Torrielli, and M. Zaro, *The automated computation of tree-level and next-to-leading order differential cross sections, and their matching to parton shower simulations*, *JHEP* **07** (2014) 079, [arXiv:1405.0301].

[145] T. Sjostrand, S. Mrenna, and P. Z. Skands, *PYTHIA 6.4 Physics and Manual*, *JHEP* **05** (2006) 026, [hep-ph/0603175].

[146] **DELPHES 3** Collaboration, J. de Favereau, C. Delaere, P. Demin, A. Giammanco, V. LemaÃ®tre, A. Mertens, and M. Selvaggi, *DELPHES 3, A modular framework for fast simulation of a generic collider experiment*, *JHEP* **02** (2014) 057, [arXiv:1307.6346].

[147] R. K. Ellis, I. Hinchliffe, M. Soldate, and J. J. van der Bij, *Higgs Decay to tau+ tau-: A Possible Signature of Intermediate Mass Higgs Bosons at the SSC*, *Nucl. Phys.* **B297** (1988) 221–243.

[148] C. Collaboration, *Performance of $\tau$-lepton reconstruction and identification in cms*, *Journal of Instrumentation* **7** (2012), no. 01 P01001.

[149] A. L. Read, *Presentation of search results: The CL(s) technique*, *J.Phys.* **G28** (2002) 2693–2704.

[150] **ATLAS** Collaboration, G. Aad et al., *Search for top quark decays $t \to qH$ with $H \to \gamma\gamma$ using the ATLAS detector*, *JHEP* **06** (2014) 008, [arXiv:1403.6293].

[151] **ATLAS** Collaboration, G. Aad et al., *Search for flavour-changing neutral current top quark decays $t \to Hq$ in pp collisions at $\sqrt{s} = 8$ TeV with the ATLAS detector*, arXiv:1509.06047.

[152] C. Zhang and F. Maltoni, *Top-quark decay into Higgs boson and a light quark at next-to-leading order in QCD*, *Phys.Rev.* **D88** (2013) 054005, [arXiv:1305.7386].

[153] **CMS** Collaboration, C. Collaboration, *Combined multilepton and diphoton limit on t to cH*, .

[154] **CMS** Collaboration, V. Khachatryan et al., *Searches for heavy Higgs bosons in two-Higgs-doublet models and for t?ch decay using multilepton and diphoton final states in pp collisions at 8 TeV*, *Phys. Rev.* **D90** (2014) 112013, [arXiv:1410.2751].

[155] **CMS** Collaboration, C. Collaboration, *Search for top quark decays via Higgs-boson-mediated flavor changing neutral currents in pp collisions at $\sqrt{s}$ = 8 TeV*, .

[156] **CMS** Collaboration, S. Chatrchyan et al., *Search for new physics in events with same-sign dileptons and b jets in pp collisions at $\sqrt{s} = 8$ TeV*, *JHEP* **03** (2013) 037, [arXiv:1212.6194]. [Erratum: JHEP07,041(2013)].

[157] R. Goldouzian, *Search for top quark flavor changing neutral currents in same-sign top quark production*, *Phys. Rev.* **D91** (2015), no. 1 014022, [arXiv:1408.0493].

[158] **ATLAS** Collaboration, T. A. collaboration, *Search for anomalous production of events with same-sign dileptons and b jets in 14.3 $fb^{-1}$ of pp collisions at $\sqrt{s} = 8$ TeV with the ATLAS detector*, .

[159] **ATLAS** Collaboration, T. A. collaboration, *Search for a high-mass Higgs boson in the $H \to WW \to l\nu l\nu$ decay channel with the ATLAS detector using 21 $fb^{-1}$ of proton-proton collision data*, in *Proceedings, 2013 European Physical Society Conference on High Energy Physics (EPS-HEP 2013)*, (Geneva), CERN, CERN, 2013.

[160] **ATLAS** Collaboration, G. Aad et al., *Search for an additional, heavy Higgs boson in the $H \to ZZ$ decay channel at $\sqrt{s}$ = 8 TeV in pp collision data with the ATLAS detector*, arXiv:1507.05930.

[161] J. M. No and M. Ramsey-Musolf, *Probing the Higgs Portal at the LHC Through Resonant di-Higgs Production*, *Phys. Rev.* **D89** (2014), no. 9 095031, [arXiv:1310.6035].

[162] **ATLAS** Collaboration, *Measurements of the properties of the Higgs-like boson in the four lepton decay channel with the ATLAS detector using 25 $fb^{-1}$ of proton-proton collision data*, .

[163] **CMS** Collaboration, S. Chatrchyan et al., *Search for a standard-model-like Higgs boson with a mass in the range 145 to 1000 GeV at the LHC*, *Eur. Phys. J.* **C73** (2013) 2469, [arXiv:1304.0213].

[164] **ATLAS** Collaboration, G. Aad et al., *Searches for Higgs boson pair production in the $hh \to bb\tau\tau, \gamma\gamma WW^*, \gamma\gamma bb, bbbb$ channels with the ATLAS detector*, *Phys. Rev.* **D92** (2015) 092004, [arXiv:1509.04670].

[165] M. E. Peskin and T. Takeuchi, *Estimation of oblique electroweak corrections*, *Phys. Rev.* **D46** (1992) 381–409.

[166] **ALEPH Collaboration, DELPHI Collaboration, L3 Collaboration, OPAL Collaboration, SLD Collaboration, LEP Electroweak Working Group, SLD Electroweak Group, SLD Heavy Flavour Group** Collaboration, *Precision electroweak measurements on the Z resonance*, *Phys.Rept.* **427** (2006) 257–454, [hep-ex/0509008].

[167] **Particle Data Group** Collaboration, K. A. Olive et al., *Review of Particle Physics*, *Chin. Phys.* **C38** (2014) 090001.

[168] T. Gleisberg, S. Hoeche, F. Krauss, M. Schonherr, S. Schumann, F. Siegert, and J. Winter, *Event generation with SHERPA 1.1*, *JHEP* **02** (2009) 007, [arXiv:0811.4622].

[169] F. Krauss, R. Kuhn, and G. Soff, *AMEGIC++ 1.0: A Matrix element generator in C++*, *JHEP* **02** (2002) 044, [hep-ph/0109036].

[170] F. Cascioli, P. Maierhofer, and S. Pozzorini, *Scattering Amplitudes with Open Loops*, *Phys. Rev. Lett.* **108** (2012) 111601, [arXiv:1111.5206].

[171] A. Denner, S. Dittmaier, and L. Hofer, *COLLIER - A fortran-library for one-loop integrals*, *PoS* **LL2014** (2014) 071, [arXiv:1407.0087].

[172] C. F. Berger, Z. Bern, L. J. Dixon, F. Febres Cordero, D. Forde, H. Ita, D. A. Kosower, and D. Maitre, *An Automated Implementation of On-Shell Methods for One-Loop Amplitudes*, *Phys. Rev.* **D78** (2008) 036003, [arXiv:0803.4180].

[173] **CMS** Collaboration, S. Chatrchyan et al., *Identification of b-quark jets with the CMS experiment*, *JINST* **8** (2013) P04013, [arXiv:1211.4462].

[174] **CMS** Collaboration, C. Diez Pardos, *Object definition and performance at CMS*, *J. Phys. Conf. Ser.* **452** (2013), no. 1 012015.

[175] **CMS** Collaboration, *Combination of standard model Higgs boson searches and measurements of the properties of the new boson with a mass near 125 GeV*, .

[176] B. A. Dobrescu, K. Kong, and R. Mahbubani, *Massive color-octet bosons and pairs of resonances at hadron colliders*, *Physics Letters B* **670** (2008), no. 2 119 – 123.

[177] **ATLAS** Collaboration, M. Aaboud et al., *Search for new phenomena in dijet events using 37 $fb^{-1}$ of pp collision data collected at $\sqrt{s}$ =13 TeV with the ATLAS detector*, arXiv:1703.09127.

[178] **CMS** Collaboration, C. Collaboration, *Searches for dijet resonances in pp collisions at $\sqrt{s} = 13$ TeV using data collected in 2016.*, .

[179] **ATLAS** Collaboration, G. Aad et al., *A search for $t\bar{t}$ resonances using lepton-plus-jets events in proton-proton collisions at $\sqrt{s} = 8$ TeV with the ATLAS detector*, *JHEP* **08** (2015) 148, [arXiv:1505.07018].

[180] **CMS** Collaboration, V. Khachatryan et al., *Search for resonant $t\bar{t}$ production in proton-proton collisions at $\sqrt{s}$ = 8??TeV*, *Phys. Rev.* **D93** (2016), no. 1 012001, [arXiv:1506.03062].

[181] **CMS** Collaboration, *Search for Heavy Resonances Decaying into bb and bg Final States in pp Collisions at sqrt(s) = 8 TeV*, .

[182] **ATLAS** Collaboration, T. A. collaboration, *Search for four-top-quark production in final states with one charged lepton and multiple jets using 3.2 $fb^{-1}$ of proton-proton collisions at $\sqrt{s}$ = 13 TeV with the ATLAS detector at the LHC*, .

[183] **CMS** Collaboration, V. Khachatryan et al., *Search for Standard Model Production of Four Top Quarks in the Lepton + Jets Channel in pp Collisions at $\sqrt{s}$ = 8 TeV*, *JHEP* **11** (2014) 154, [arXiv:1409.7339].

[184] **ATLAS** Collaboration, T. A. collaboration, *A search for pair produced resonances in four jets final states in proton-proton collisions at $\sqrt{s}$=13 TeV with the ATLAS experiment*, .

[185] **CMS** Collaboration, V. Khachatryan et al., *Search for pair-produced resonances decaying to jet pairs in proton?proton collisions at $\sqrt{s}$ = 8 TeV*, *Phys. Lett.* **B747** (2015) 98–119, [arXiv:1412.7706].

[186] R. Sekhar Chivukula, P. Ittisamai, and E. H. Simmons, *Distinguishing flavor nonuniversal colorons from Z? bosons at the LHC*, *Phys. Rev.* **D91** (2015), no. 5 055021, [arXiv:1406.2003].

[187] T. Sjostrand, S. Mrenna, and P. Z. Skands, *A Brief Introduction to PYTHIA 8.1*, *Comput. Phys. Commun.* **178** (2008) 852–867, [arXiv:0710.3820].

[188] N. Cabibbo and A. Maksymowicz, *Angular Correlations in Ke-4 Decays and Determination of Low-Energy pi-pi Phase Shifts*, *Phys. Rev.* **137** (1965) B438–B443. [Erratum: Phys. Rev.168,1926(1968)].

[189] J. R. Dell'Aquila and C. A. Nelson, *P or CP Determination by Sequential Decays: V1 V2 Modes With Decays Into $\bar{\ell}$epton (A) $\ell(B)$ And/or $\bar{q}$ (A) $q(B)$*, *Phys. Rev.* **D33** (1986) 80.

[190] J. R. Dell'Aquila and C. A. Nelson, *Distinguishing a Spin 0 Technipion and an Elementary Higgs Boson: V1 V2 Modes With Decays Into $\bar{\ell}$epton (A) $\ell(B)$ And/or $\bar{q}$ (A) $q(B)$*, *Phys. Rev.* **D33** (1986) 93.

[191] C. A. Nelson, *Correlation Between Decay Planes in Higgs Boson Decays Into W Pair (Into Z Pair)*, *Phys. Rev.* **D37** (1988) 1220.

[192] Y. Gao, A. V. Gritsan, Z. Guo, K. Melnikov, M. Schulze, and N. V. Tran, *Spin determination of single-produced resonances at hadron colliders*, *Phys. Rev.* **D81** (2010) 075022, [arXiv:1001.3396].

[193] S. Bolognesi, Y. Gao, A. V. Gritsan, K. Melnikov, M. Schulze, N. V. Tran, and A. Whitbeck, *On the spin and parity of a single-produced resonance at the LHC*, *Phys. Rev.* **D86** (2012) 095031, [arXiv:1208.4018].

[194] **ATLAS** Collaboration, G. Aad et al., *Study of the spin and parity of the Higgs boson in diboson decays with the ATLAS detector*, *Eur. Phys. J.* **C75** (2015), no. 10 476, [arXiv:1506.05669].

[195] **ATLAS** Collaboration, G. Aad et al., *Measurements of the Higgs boson production and decay rates and coupling strengths using pp collision data at $\sqrt{s} = 7$ and 8 TeV in the ATLAS experiment*, *Eur. Phys. J.* **C76** (2016), no. 1 6, [arXiv:1507.04548].

[196] **CMS** Collaboration, V. Khachatryan et al., *Constraints on the spin-parity and anomalous HVV couplings of the Higgs boson in proton collisions at 7 and 8 TeV*, *Phys. Rev.* **D92** (2015), no. 1 012004, [arXiv:1411.3441].

[197] **CMS** Collaboration, V. Khachatryan et al., *Precise determination of the mass of the Higgs boson and tests of compatibility of its couplings with the standard model predictions using proton collisions at 7 and 8 TeV*, *Eur. Phys. J.* **C75** (2015), no. 5 212, [arXiv:1412.8662].

[198] **ATLAS** Collaboration, G. Aad et al., *Search for high-mass diboson resonances with boson-tagged jets in proton-proton collisions at $\sqrt{s} = 8$ TeV with the ATLAS detector*, arXiv:1506.00962.

[199] **CMS** Collaboration, V. Khachatryan et al., *Search for massive resonances in dijet systems containing jets tagged as W or Z boson decays in pp collisions at $\sqrt{s} = 8$ TeV*, *JHEP* **08** (2014) 173, [arXiv:1405.1994].

[200] C.-H. Chen and T. Nomura, *Diboson excess in the Higgs singlet and vector-like quark models*, arXiv:1509.02039.

[201] C.-H. Chen and T. Nomura, *2 TeV Higgs boson and diboson excess at the LHC*, *Phys. Lett.* **B749** (2015) 464–468, [arXiv:1507.04431].

[202] Y. Omura, K. Tobe, and K. Tsumura, *Survey of Higgs interpretations of the diboson excesses*, *Phys. Rev.* **D92** (2015), no. 5 055015, [arXiv:1507.05028].

[203] W. Chao, *ATLAS Diboson Excesses from the Stealth Doublet Model*, arXiv:1507.05310.

[204] D. Aristizabal Sierra, J. Herrero-Garcia, D. Restrepo, and A. Vicente, *Diboson anomaly: heavy Higgs resonance and QCD vector-like exotics*, arXiv:1510.03437.

[205] C. Petersson and R. Torre, *ATLAS diboson excess from low scale supersymmetry breaking*, arXiv:1508.05632.

[206] B. C. Allanach, P. S. B. Dev, and K. Sakurai, *The ATLAS Di-boson Excess Could Be an R-parity Violating Di-stau Excess*, arXiv:1511.01483.

[207] C.-W. Chiang, H. Fukuda, K. Harigaya, M. Ibe, and T. T. Yanagida, *Diboson Resonance as a Portal to Hidden Strong Dynamics*, *JHEP* **11** (2015) 015, [arXiv:1507.02483].

[208] G. Cacciapaglia, A. Deandrea, and M. Hashimoto, *Scalar Hint from the Diboson Excess?*, *Phys. Rev. Lett.* **115** (2015), no. 17 171802, [arXiv:1507.03098].

[209] H. S. Fukano, M. Kurachi, S. Matsuzaki, K. Terashi, and K. Yamawaki, *2 TeV Walking Technirho at LHC?*, *Phys. Lett.* **B750** (2015) 259–265, [arXiv:1506.03751].

[210] D. B. Franzosi, M. T. Frandsen, and F. Sannino, *Diboson Signals via Fermi Scale Spin-One States*, arXiv:1506.04392.

[211] A. Thamm, R. Torre, and A. Wulzer, *Composite Heavy Vector Triplet in the ATLAS Diboson Excess*, *Phys. Rev. Lett.* **115** (2015), no. 22 221802, [arXiv:1506.08688].

[212] L. Bian, D. Liu, and J. Shu, *Low Scale Composite Higgs Model and 1.8 $\sim$ 2 TeV Diboson Excess*, arXiv:1507.06018.

[213] H. Fritzsch, *Composite Weak Bosons at the LHC*, arXiv:1507.06499.

[214] K. Lane and L. Prichett, *Heavy Vector Partners of the Light Composite Higgs*, arXiv:1507.07102.

[215] M. Low, A. Tesi, and L.-T. Wang, *Composite spin-1 resonances at the LHC*, *Phys. Rev.* **D92** (2015), no. 8 085019, [arXiv:1507.07557].

[216] H. S. Fukano, S. Matsuzaki, K. Terashi, and K. Yamawaki, *Conformal Barrier and Hidden Local Symmetry Constraints: Walking Technirhos in LHC Diboson Channels*, arXiv:1510.08184.

[217] G. Cacciapaglia and M. T. Frandsen, *Unitarity implications of a diboson resonance in the TeV region for Higgs physics*, *Phys. Rev.* **D92** (2015) 055035, [arXiv:1507.00900].

[218] B. C. Allanach, B. Gripaios, and D. Sutherland, *Anatomy of the ATLAS diboson anomaly*, *Phys. Rev.* **D92** (2015), no. 5 055003, [arXiv:1507.01638].

[219] L. Bian, D. Liu, J. Shu, and Y. Zhang, *Interference Effect on Resonance Studies and the Diboson Excess*, arXiv:1509.02787.

[220] B. Bhattacherjee, P. Byakti, C. K. Khosa, J. Lahiri, and G. Mendiratta, *Alternative search strategies for a BSM resonance fitting ATLAS diboson excess*, arXiv:1511.02797.

[221] S.-S. Xue, *Vector-like $W^{\pm}$-boson coupling at TeV and fermion-mass hierarchy (two boson-tagged jets vs four quark jets)*, arXiv:1506.05994.

[222] B. A. Dobrescu and Z. Liu, *$W'$ Boson near 2 TeV: Predictions for Run 2 of the LHC*, *Phys. Rev. Lett.* **115** (2015), no. 21 211802, [arXiv:1506.06736].

[223] B. A. Dobrescu and Z. Liu, *Heavy Higgs bosons and the 2 TeV $W'$ boson*, *JHEP* **10** (2015) 118, [arXiv:1507.01923].

[224] Y. Gao, T. Ghosh, K. Sinha, and J.-H. Yu, *SU(2)xSU(2)xU(1) interpretations of the diboson and Wh excesses*, *Phys. Rev.* **D92** (2015), no. 5 055030, [arXiv:1506.07511].

[225] J. Brehmer, J. Hewett, J. Kopp, T. Rizzo, and J. Tattersall, *Symmetry Restored in Dibosons at the LHC?*, *JHEP* **10** (2015) 182, [arXiv:1507.00013].

[226] J. Heeck and S. Patra, *Minimal Left-Right Symmetric Dark Matter*, *Phys. Rev. Lett.* **115** (2015), no. 12 121804, [arXiv:1507.01584].

[227] P. S. Bhupal Dev and R. N. Mohapatra, *Unified explanation of the eejj, diboson and dijet resonances at the LHC*, *Phys. Rev. Lett.* **115** (2015), no. 18 181803, [arXiv:1508.02277].

[228] F. F. Deppisch, L. Graf, S. Kulkarni, S. Patra, W. Rodejohann, N. Sahu, and U. Sarkar, *Reconciling the 2 TeV Excesses at the LHC in a Linear Seesaw Left-Right Model*, arXiv:1508.05940.

[229] U. Aydemir, D. Minic, C. Sun, and T. Takeuchi, *Pati-Salam Unification from Non-commutative Geometry and the TeV-scale $W_R$ boson*, arXiv:1509.01606.

[230] R. L. Awasthi, P. S. B. Dev, and M. Mitra, *Implications of the Diboson Excess for Neutrinoless Double Beta Decay and Lepton Flavor Violation in TeV Scale Left Right Symmetric Model*, arXiv:1509.05387.

[231] P. Ko and T. Nomura, *$SU(2)_L \times SU(2)_R$ minimal dark matter with 2 TeV $W'$*, arXiv:1510.07872.

[232] J. H. Collins and W. H. Ng, *A 2 TeV $W_R$, Supersymmetry, and the Higgs Mass*, arXiv:1510.08083.

[233] B. A. Dobrescu and P. J. Fox, *Signals of a 2 TeV $W'$ boson and a heavier $Z'$ boson*, arXiv:1511.02148.

[234] J. A. Aguilar-Saavedra and F. R. Joaquim, *Multiboson production in W' decays*, arXiv:1512.00396.

[235] U. Aydemir, *SO(10) grand unification in light of recent LHC searches and colored scalars at the TeV-scale*, *Int. J. Mod. Phys.* **A31** (2016) 1650034, [arXiv:1512.00568].

[236] J. L. Evans, N. Nagata, K. A. Olive, and J. Zheng, *The ATLAS Diboson Resonance in Non-Supersymmetric SO(10)*, arXiv:1512.02184.

[237] A. Das, N. Nagata, and N. Okada, *Testing the 2-TeV Resonance with Trileptons*, *JHEP* **03** (2016) 049, [arXiv:1601.05079].

[238] J. Hisano, N. Nagata, and Y. Omura, *Interpretations of the ATLAS Diboson Resonances*, *Phys. Rev.* **D92** (2015), no. 5 055001, [arXiv:1506.03931].

[239] A. Alves, A. Berlin, S. Profumo, and F. S. Queiroz, *Dirac-fermionic dark matter in $U(1)_X$ models*, *JHEP* **10** (2015) 076, [arXiv:1506.06767].

[240] L. A. Anchordoqui, I. Antoniadis, H. Goldberg, X. Huang, D. Lust, and T. R. Taylor, *Stringy origin of diboson and dijet excesses at the LHC*, *Phys. Lett.* **B749** (2015) 484–488, [arXiv:1507.05299].

[241] A. E. Faraggi and M. Guzzi, *Extra $Z'$ s and $W'$ s in heterotic-string derived models*, *Eur. Phys. J.* **C75** (2015), no. 11 537, [arXiv:1507.07406].

[242] T. Li, J. A. Maxin, V. E. Mayes, and D. V. Nanopoulos, *The Diboson Excesses in Leptophobic $U(1)_{\rm LP}$ Models from String Theories*, arXiv:1509.06821.

[243] Z.-W. Wang, F. S. Sage, T. G. Steele, and R. B. Mann, *Can an Asymptotically-Safe Conformal $U(1)'$ Model Address the LHC Diboson Excess?*, arXiv:1511.02531.

[244] B. Allanach, F. S. Queiroz, A. Strumia, and S. Sun, *Z' models for the LHCb and g-2 muon anomalies*, arXiv:1511.07447.

[245] W.-Z. Feng, Z. Liu, and P. Nath, *ATLAS Diboson Excess from Stueckelberg Mechanism*, arXiv:1511.08921.

[246] K. Cheung, W.-Y. Keung, P.-Y. Tseng, and T.-C. Yuan, *Interpretations of the ATLAS Diboson Anomaly*, *Phys. Lett.* **B751** (2015) 188–194, [arXiv:1506.06064].

[247] Q.-H. Cao, B. Yan, and D.-M. Zhang, *Simple non-Abelian extensions of the standard model gauge group and the diboson excesses at the LHC*, *Phys. Rev.* **D92** (2015), no. 9 095025, [arXiv:1507.00268].

[248] T. Abe, R. Nagai, S. Okawa, and M. Tanabashi, *Unitarity sum rules, three-site moose model, and the ATLAS 2 TeV diboson anomalies*, *Phys. Rev.* **D92** (2015), no. 5 055016, [arXiv:1507.01185].

[249] T. Abe, T. Kitahara, and M. M. Nojiri, *Prospects for Spin-1 Resonance Search at 13 TeV LHC and the ATLAS Diboson Excess*, arXiv:1507.01681.

[250] H. S. Fukano, S. Matsuzaki, and K. Yamawaki, *Conformal Barrier for New Vector Bosons Decay to the Higgs*, arXiv:1507.03428.

[251] T. Appelquist, Y. Bai, J. Ingoldby, and M. Piai, *Spectrum-doubled Heavy Vector Bosons at the LHC*, arXiv:1511.05473.

[252] K. Das, T. Li, S. Nandi, and S. K. Rai, *The Diboson Excesses in an Anomaly Free Leptophobic Left-Right Model*, arXiv:1512.00190.

[253] V. Sanz, *On the compatibility of the diboson excess with a gg-initiated composite sector*, arXiv:1507.03553.

[254] H. Terazawa and M. Yasue, *Excited Gauge and Higgs Bosons in the Unified Composite Model*, arXiv:1508.00172.

[255] J. A. Aguilar-Saavedra, *Triboson interpretations of the ATLAS diboson excess*, *JHEP* **10** (2015) 099, [arXiv:1506.06739].

[256] D. Kim, K. Kong, H. M. Lee, and S. C. Park, *Diboson Excesses Demystified in Effective Field Theory Approach*, arXiv:1507.06312.

[257] S. P. Liew and S. Shirai, *Testing ATLAS Diboson Excess with Dark Matter Searches at LHC*, *JHEP* **11** (2015) 191, [arXiv:1507.08273].

[258] P. Arnan, D. Espriu, and F. Mescia, *Interpreting a 2 TeV resonance in WW scattering*, arXiv:1508.00174.

[259] S. Fichet and G. von Gersdorff, *Effective theory for neutral resonances and a statistical dissection of the ATLAS diboson excess*, arXiv:1508.04814.

[260] A. Sajjad, *Understanding diboson anomalies*, arXiv:1511.02244.

[261] *Search for resonances with boson-tagged jets in 3.2/fb of p p collisions at $\sqrt{s}$ = 13 TeV collected with the ATLAS detector*, Tech. Rep. ATLAS-CONF-2015-073, CERN, Geneva, Dec, 2015.

[262] **CMS Collaboration** Collaboration, *Search for massive resonances decaying into pairs of boosted W and Z bosons at $\sqrt{s}$ = 13 TeV*, Tech. Rep. CMS-PAS-EXO-15-002, CERN, Geneva, 2015.

[263] **ATLAS** Collaboration, G. Aad et al., *Search for resonant diboson production in the $\ell\ell q\bar{q}$ final state in pp collisions at $\sqrt{s} = 8$ TeV with the ATLAS detector*, *Eur. Phys. J.* **C75** (2015) 69, [arXiv:1409.6190].

[264] **ATLAS** Collaboration, G. Aad et al., *Search for production of $WW/WZ$ resonances decaying to a lepton, neutrino and jets in pp collisions at $\sqrt{s} = 8$ TeV with the ATLAS detector*, *Eur. Phys. J.* **C75** (2015), no. 5 209, [arXiv:1503.04677]. [Erratum: Eur. Phys. J.C75,370(2015)].

[265] **CMS** Collaboration, V. Khachatryan et al., *Search for massive resonances decaying into pairs of boosted bosons in semi-leptonic final states at $\sqrt{s} = 8$ TeV*, *JHEP* **08** (2014) 174, [arXiv:1405.3447].

[266] **ATLAS** Collaboration, G. Aad et al., *Search for $WZ$ resonances in the fully leptonic channel using pp collisions at $\sqrt{s} = 8$ TeV with the ATLAS detector*, *Phys. Lett.* **B737** (2014) 223–243, [arXiv:1406.4456].

[267] **CMS** Collaboration, V. Khachatryan et al., *Search for new resonances decaying via WZ to leptons in proton-proton collisions at $\sqrt{s} = 8$ TeV*, *Phys. Lett.* **B740** (2015) 83–104, [arXiv:1407.3476].

[268] **ATLAS** Collaboration, G. Aad et al., *Combination of searches for $WW$, $WZ$, and $ZZ$ resonances in pp collisions at $\sqrt{s} = 8$ TeV with the ATLAS detector*, arXiv:1512.05099.

[269] J. Brehmer et al., *The Diboson Excess: Experimental Situation and Classification of Explanations; A Les Houches Pre-Proceeding*, arXiv:1512.04357.

[270] **ATLAS** Collaboration, G. Aad et al., *Search for new phenomena in the dijet mass distribution using $p-p$ collision data at $\sqrt{s} = 8$ TeV with the ATLAS detector*, *Phys. Rev.* **D91** (2015), no. 5 052007, [arXiv:1407.1376].

[271] **ATLAS** Collaboration, G. Aad et al., *Search for new phenomena in dijet mass and angular distributions from pp collisions at $\sqrt{s} = 13$ TeV with the ATLAS detector*, *Phys. Lett.* **B754** (2016) 302–322, [arXiv:1512.01530]. [Phys. Lett.B754,302(2016)].

[272] **ATLAS** Collaboration, G. Aad et al., *Search for a new resonance decaying to a $W$ or $Z$ boson and a Higgs boson in the $\ell\ell/\ell\nu/\nu\nu + b\bar{b}$ final states with the ATLAS detector*, *Eur. Phys. J.* **C75** (2015), no. 6 263, [arXiv:1503.08089].

[273] *Search for new resonances decaying to a $W$ or $Z$ boson and a Higgs boson in the $\ell\ell b\bar{b}$, $\ell\nu b\bar{b}$, and $\nu\nu b\bar{b}$ channels in pp collisions at $\sqrt{s} = 13$ TeV with the ATLAS detector*, Tech. Rep. ATLAS-CONF-2015-074, CERN, Geneva, Dec, 2015.

[274] **CMS** Collaboration, V. Khachatryan et al., *Search for resonances and quantum black holes using dijet mass spectra in proton-proton collisions at $\sqrt{s} = 8$ TeV*, *Phys.Rev.* **D91** (2015), no. 5 052009, [arXiv:1501.04198].

[275] **CMS** Collaboration, V. Khachatryan et al., *Search for narrow resonances decaying to dijets in proton-proton collisions at sqrt(s) = 13 TeV*, arXiv:1512.01224.

[276] **CMS** Collaboration, V. Khachatryan et al., *Search for Narrow High-Mass Resonances in Proton-Proton Collisions at $\sqrt{s} = 8$ TeV Decaying to a Z and a Higgs Boson*, *Phys. Lett.* **B748** (2015) 255–277, [arXiv:1502.04994].

[277] **CMS** Collaboration, V. Khachatryan et al., *Search for A Massive Resonance Decaying into a Higgs Boson and a W or Z Boson in Hadronic Final States in Proton-Proton Collisions at $\sqrt{s} = 8$ TeV*, arXiv:1506.01443.

[278] **CMS** Collaboration, V. Khachatryan et al., *Search for massive WH resonances decaying into the l nu b anti-b final state at sqrt(s)=8 TeV*, arXiv:1601.06431.

[279] Y. Chen, N. Tran, and R. Vega-Morales, *Scrutinizing the Higgs Signal and Background in the $2e2\mu$ Golden Channel*, *JHEP* **01** (2013) 182, [arXiv:1211.1959].

[280] Y. Chen, E. Di Marco, J. Lykken, M. Spiropulu, R. Vega-Morales, and S. Xie, *8D likelihood effective Higgs couplings extraction framework in $h \to 4\ell$*, *JHEP* **01** (2015) 125, [arXiv:1401.2077].

[281] Y. Chen, E. Di Marco, J. Lykken, M. Spiropulu, R. Vega-Morales, and S. Xie, *Technical Note for 8D Likelihood Effective Higgs Couplings Extraction Framework in the Golden Channel*, arXiv:1410.4817.

[282] *Search for diboson resonances in the llqq final state in pp collisions at $\sqrt{s}$ = 13 TeV with the ATLAS detector*, Tech. Rep. ATLAS-CONF-2015-071, CERN, Geneva, Dec, 2015.

[283] *Search for $WW/WZ$ resonance production in the $\ell\nu qq$ final state at $\sqrt{s} = 13$ TeV with the ATLAS detector at the LHC*, Tech. Rep. ATLAS-CONF-2015-075, CERN, Geneva, Dec, 2015.

[284] A. Alloul, N. D. Christensen, C. Degrande, C. Duhr, and B. Fuks, *FeynRules 2.0 - A complete toolbox for tree-level phenomenology*, *Comput. Phys. Commun.* **185** (2014) 2250–2300, [arXiv:1310.1921].

[285] J. Alwall, M. Herquet, F. Maltoni, O. Mattelaer, and T. Stelzer, *MadGraph 5 : Going Beyond*, *JHEP* **06** (2011) 128, [arXiv:1106.0522].

[286] D. Pappadopulo, A. Thamm, R. Torre, and A. Wulzer, *Heavy Vector Triplets: Bridging Theory and Data*, *JHEP* **09** (2014) 060, [arXiv:1402.4431].

[287] K. Hagiwara, J. Kanzaki, Q. Li, and K. Mawatari, *HELAS and MadGraph/MadEvent with spin-2 particles*, *Eur. Phys. J.* **C56** (2008) 435–447, [arXiv:0805.2554].

[288] T. Sjostrand, S. Ask, J. R. Christiansen, R. Corke, N. Desai, et al., *An Introduction to PYTHIA 8.2*, arXiv:1410.3012.

[289] M. Cacciari, G. P. Salam, and G. Soyez, *FastJet User Manual*, *Eur.Phys.J.* **C72** (2012) 1896, [arXiv:1111.6097].

[290] **CMS** Collaboration, V. Khachatryan et al., *Identification techniques for highly boosted W bosons that decay into hadrons*, *JHEP* **12** (2014) 017, [arXiv:1410.4227].

[291] C. Hackstein and M. Spannowsky, *Boosting Higgs discovery: The Forgotten channel*, *Phys. Rev.* **D82** (2010) 113012, [arXiv:1008.2202].

[292] C. Englert, C. Hackstein, and M. Spannowsky, *Measuring spin and CP from semi-hadronic ZZ decays using jet substructure*, *Phys. Rev.* **D82** (2010) 114024, [arXiv:1010.0676].

[293] D. N. Spergel and P. J. Steinhardt, *Observational evidence for selfinteracting cold dark matter*, *Phys.Rev.Lett.* **84** (2000) 3760–3763, [astro-ph/9909386].

[294] S. Tulin, H.-B. Yu, and K. M. Zurek, *Beyond Collisionless Dark Matter: Particle Physics Dynamics for Dark Matter Halo Structure*, *Phys.Rev.* **D87** (2013), no. 11 115007, [arXiv:1302.3898].

[295] J. Hisano, S. Matsumoto, and M. M. Nojiri, *Explosive dark matter annihilation*, *Phys.Rev.Lett.* **92** (2004) 031303, [hep-ph/0307216].

[296] M. Cirelli, M. Kadastik, M. Raidal, and A. Strumia, *Model-independent implications of the $e^{\pm}$, $\bar{p}$ cosmic ray spectra on properties of Dark Matter*, *Nucl.Phys.* **B813** (2009) 1–21, [arXiv:0809.2409].

[297] N. Arkani-Hamed, D. P. Finkbeiner, T. R. Slatyer, and N. Weiner, *A Theory of Dark Matter*, *Phys.Rev.* **D79** (2009) 015014, [arXiv:0810.0713].

[298] W. Shepherd, T. M. P. Tait, and G. Zaharijas, *Bound states of weakly interacting dark matter*, *Phys. Rev.* **D79** (2009) 055022, [arXiv:0901.2125].

[299] W. Altmannshofer, P. J. Fox, R. Harnik, G. D. Kribs, and N. Raj, *Dark Matter Signals in Dilepton Production at Hadron Colliders*, *Phys. Rev.* **D91** (2015), no. 11 115006, [arXiv:1411.6743].

[300] M. Vogelsberger, S. Genel, V. Springel, P. Torrey, D. Sijacki, et al., *Properties of galaxies reproduced by a hydrodynamic simulation*, *Nature* **509** (2014) 177–182, [arXiv:1405.1418].

[301] T. Sawala, C. S. Frenk, A. Fattahi, J. F. Navarro, R. G. Bower, et al., *Local Group galaxies emerge from the dark*, arXiv:1412.2748.

[302] R. Massey, L. Williams, R. Smit, M. Swinbank, T. D. Kitching, et al., *The behaviour of dark matter associated with 4 bright cluster galaxies in the 10kpc*

*core of Abell 3827*, *Mon.Not.Roy.Astron.Soc.* **449** (2015) 3393, [arXiv:1504.03388].

[303] F. Kahlhoefer, K. Schmidt-Hoberg, J. Kummer, and S. Sarkar, *On the interpretation of dark matter self-interactions in Abell 3827*, arXiv:1504.06576.

[304] B. Holdom, *Two U(1)'s and Epsilon Charge Shifts*, *Phys.Lett.* **B166** (1986) 196.

[305] J. Jaeckel and A. Ringwald, *The Low-Energy Frontier of Particle Physics*, *Ann.Rev.Nucl.Part.Sci.* **60** (2010) 405–437, [arXiv:1002.0329].

[306] **ATLAS** Collaboration, G. Aad et al., *A search for prompt lepton-jets in pp collisions at $\sqrt{s} = 7$ TeV with the ATLAS detector*, *Phys.Lett.* **B719** (2013) 299–317, [arXiv:1212.5409].

[307] **ATLAS** Collaboration, G. Aad et al., *Search for long-lived neutral particles decaying into lepton jets in proton-proton collisions at $\sqrt{s} = 8$ TeV with the ATLAS detector*, *JHEP* **1411** (2014) 088, [arXiv:1409.0746].

[308] N. Arkani-Hamed and N. Weiner, *LHC Signals for a SuperUnified Theory of Dark Matter*, *JHEP* **0812** (2008) 104, [arXiv:0810.0714].

[309] C. Cheung, J. T. Ruderman, L.-T. Wang, and I. Yavin, *Lepton Jets in (Supersymmetric) Electroweak Processes*, *JHEP* **1004** (2010) 116, [arXiv:0909.0290].

[310] A. Katz and R. Sundrum, *Breaking the Dark Force*, *JHEP* **0906** (2009) 003, [arXiv:0902.3271].

[311] Y. Bai and Z. Han, *Measuring the Dark Force at the LHC*, *Phys.Rev.Lett.* **103** (2009) 051801, [arXiv:0902.0006].

[312] M. Baumgart, C. Cheung, J. T. Ruderman, L.-T. Wang, and I. Yavin, *Non-Abelian Dark Sectors and Their Collider Signatures*, *JHEP* **0904** (2009) 014, [arXiv:0901.0283].

[313] Y. F. Chan, M. Low, D. E. Morrissey, and A. P. Spray, *LHC Signatures of a Minimal Supersymmetric Hidden Valley*, *JHEP* **1205** (2012) 155, [arXiv:1112.2705].

[314] A. Falkowski, J. T. Ruderman, T. Volansky, and J. Zupan, *Discovering Higgs Decays to Lepton Jets at Hadron Colliders*, *Phys.Rev.Lett.* **105** (2010) 241801, [arXiv:1007.3496].

[315] D. Curtin, R. Essig, S. Gori, P. Jaiswal, A. Katz, et al., *Exotic Decays of the 125 GeV Higgs Boson*, arXiv:1312.4992.

[316] A. Gupta, R. Primulando, and P. Saraswat, *A New Probe of Dark Sector Dynamics at the LHC*, *JHEP* **09** (2015) 079, [arXiv:1504.01385].

[317] M. Autran, K. Bauer, T. Lin, and D. Whiteson, *Searches for dark matter in events with a resonance and missing transverse energy*, *Phys. Rev.* **D92** (2015), no. 3 035007, [arXiv:1504.01386].

[318] Y. Bai, J. Bourbeau, and T. Lin, *Dark matter searches with a mono-$Z'$ jet*, *JHEP* **06** (2015) 205, [arXiv:1504.01395].

[319] B. Batell, M. Pospelov, and A. Ritz, *Probing a Secluded U(1) at B-factories*, *Phys.Rev.* **D79** (2009) 115008, [arXiv:0903.0363].

[320] R. Essig, P. Schuster, and N. Toro, *Probing Dark Forces and Light Hidden Sectors at Low-Energy $e^+e^-$ Colliders*, *Phys.Rev.* **D80** (2009) 015003, [arXiv:0903.3941].

[321] P. Schwaller, D. Stolarski, and A. Weiler, *Emerging Jets*, arXiv:1502.05409.

[322] T. Cohen, M. Lisanti, and H. K. Lou, *Semi-visible Jets: Dark Matter Undercover at the LHC*, arXiv:1503.00009.

[323] Y. Bai and A. Rajaraman, *Dark Matter Jets at the LHC*, arXiv:1109.6009.

[324] **ATLAS** Collaboration, G. Aad et al., *Search for long-lived, weakly interacting particles that decay to displaced hadronic jets in proton-proton collisions at $\sqrt{s} = 8$ TeV with the ATLAS detector*, arXiv:1504.03634.

[325] J. Liu, N. Weiner, and W. Xue, *Signals of a Light Dark Force in the Galactic Center*, arXiv:1412.1485.

[326] J.-M. Zheng, Z.-H. Yu, J.-W. Shao, X.-J. Bi, Z. Li, et al., *Constraining the interaction strength between dark matter and visible matter: I. fermionic dark matter*, *Nucl.Phys.* **B854** (2012) 350–374, [arXiv:1012.2022].

[327] H. Dreiner, M. Huck, M. Kramer, D. Schmeier, and J. Tattersall, *Illuminating Dark Matter at the ILC*, arXiv:1211.2254.

[328] R. T. D'Agnolo and J. T. Ruderman, *Forbidden Dark Matter*, arXiv:1505.07107.

[329] K. Petraki, L. Pearce, and A. Kusenko, *Self-interacting asymmetric dark matter coupled to a light massive dark photon*, *JCAP* **1407** (2014) 039, [arXiv:1403.1077].

[330] **SuperCDMS** Collaboration, R. Agnese et al., *Search for Low-Mass Weakly Interacting Massive Particles Using Voltage-Assisted Calorimetric Ionization Detection in the SuperCDMS Experiment*, *Phys.Rev.Lett.* **112** (2014), no. 4 041302, [arXiv:1309.3259].

[331] **CDF** Collaboration, T. Aaltonen et al., *Search for new particles decaying into dijets in proton-antiproton collisions at s**(1/2) = 1.96-TeV*, *Phys. Rev.* **D79** (2009) 112002, [arXiv:0812.4036].

[332] **ATLAS** Collaboration, G. Aad et al., *Search for new phenomena in final states with an energetic jet and large missing transverse momentum in pp collisions at $\sqrt{s}$ =8 TeV with the ATLAS detector*, *Eur. Phys. J.* **C75** (2015), no. 7 299, [arXiv:1502.01518]. [Erratum: Eur. Phys. J.C75,no.9,408(2015)].

[333] **CMS** Collaboration, V. Khachatryan et al., *Search for dark matter, extra dimensions, and unparticles in monojet events in proton-proton collisions at $\sqrt{s} = 8$ TeV*, *Eur. Phys. J.* **C75** (2015), no. 5 235, [arXiv:1408.3583].

[334] S. W. Randall, M. Markevitch, D. Clowe, A. H. Gonzalez, and M. Bradac, *Constraints on the Self-Interaction Cross-Section of Dark Matter from Numerical Simulations of the Merging Galaxy Cluster 1E 0657-56*, *Astrophys.J.* **679** (2008) 1173–1180, [arXiv:0704.0261].

[335] A. H. Peter, M. Rocha, J. S. Bullock, and M. Kaplinghat, *Cosmological Simulations with Self-Interacting Dark Matter II: Halo Shapes vs. Observations*, *Mon.Not.Roy.Astron.Soc.* **430** (2013) 105, [arXiv:1208.3026].

[336] T. Plehn, *Lectures on LHC Physics*, *Lect.Notes Phys.* **844** (2012) 1–193, [arXiv:0910.4182].

[337] P. Ciafaloni, D. Comelli, A. Riotto, F. Sala, A. Strumia, et al., *Weak Corrections are Relevant for Dark Matter Indirect Detection*, *JCAP* **1103** (2011) 019, [arXiv:1009.0224].

[338] J. C. Collins, D. E. Soper, and G. F. Sterman, *Factorization of Hard Processes in QCD*, *Adv.Ser.Direct.High Energy Phys.* **5** (1988) 1–91, [hep-ph/0409313].

[339] S. Catani, S. Dittmaier, M. H. Seymour, and Z. Trocsanyi, *The Dipole formalism for next-to-leading order QCD calculations with massive partons*, *Nucl.Phys.* **B627** (2002) 189–265, [hep-ph/0201036].

[340] A. Arbuzov, *Nonsinglet splitting functions in QED*, *Phys.Lett.* **B470** (1999) 252–258, [hep-ph/9908361].

[341] G. Arfken and H. Weber, *Mathematical methods for physicists*. Elsevier Acad. Press, 2008.

[342] J. W. Cooley and J. W. Tukey, *An algorithm for the machine calculation of complex fourier series*, *Math. Comput.* **19** (1965) 297–301.

[343] L. Carloni and T. Sjostrand, *Visible Effects of Invisible Hidden Valley Radiation*, *JHEP* **1009** (2010) 105, [arXiv:1006.2911].

[344] L. Carloni, J. Rathsman, and T. Sjostrand, *Discerning Secluded Sector gauge structures*, *JHEP* **1104** (2011) 091, [arXiv:1102.3795].

[345] A. Belyaev, N. D. Christensen, and A. Pukhov, *CalcHEP 3.4 for collider physics within and beyond the Standard Model*, *Comput. Phys. Commun.* **184** (2013) 1729–1769, [arXiv:1207.6082].

[346] J. M. Campbell, R. K. Ellis, and W. T. Giele, *A Multi-Threaded Version of MCFM*, arXiv:1503.06182. see in particular the plots on the MCFM website at *http://mcfm.fnal.gov/*.

[347] M. Pospelov, *Secluded U(1) below the weak scale*, *Phys.Rev.* **D80** (2009) 095002, [arXiv:0811.1030].

[348] H. Davoudiasl, H.-S. Lee, and W. J. Marciano, *Dark Side of Higgs Diphoton Decays and Muon g-2*, *Phys.Rev.* **D86** (2012) 095009, [arXiv:1208.2973].

[349] M. Endo, K. Hamaguchi, and G. Mishima, *Constraints on Hidden Photon Models from Electron g-2 and Hydrogen Spectroscopy*, *Phys.Rev.* **D86** (2012) 095029, [arXiv:1209.2558].

[350] **HADES** Collaboration, G. Agakishiev et al., *Searching a Dark Photon with HADES*, *Phys.Lett.* **B731** (2014) 265–271, [arXiv:1311.0216].

[351] **KLOE-2** Collaboration, D. Babusci et al., *Limit on the production of a light vector gauge boson in phi meson decays with the KLOE detector*, *Phys.Lett.* **B720** (2013) 111–115, [arXiv:1210.3927].

[352] **KLOE-2** Collaboration, D. Babusci et al., *Search for light vector boson production in $e^+e^- \to \mu^+\mu^-\gamma$ interactions with the KLOE experiment*, *Phys.Lett.* **B736** (2014) 459–464, [arXiv:1404.7772].

[353] **APEX** Collaboration, S. Abrahamyan et al., *Search for a New Gauge Boson in Electron-Nucleus Fixed-Target Scattering by the APEX Experiment*, *Phys.Rev.Lett.* **107** (2011) 191804, [arXiv:1108.2750].

[354] **BaBar** Collaboration, B. Aubert et al., *Search for Dimuon Decays of a Light Scalar Boson in Radiative Transitions* $\Upsilon \to \gamma A^0$, *Phys.Rev.Lett.* **103** (2009) 081803, [arXiv:0905.4539].

[355] **BaBar** Collaboration, J. Lees et al., *Search for a Dark Photon in* $e^+e^-$ *Collisions at BaBar*, *Phys.Rev.Lett.* **113** (2014), no. 20 201801, [arXiv:1406.2980].

[356] J. Blümlein and J. Brunner, *New Exclusion Limits for Dark Gauge Forces from Beam-Dump Data*, *Phys.Lett.* **B701** (2011) 155–159, [arXiv:1104.2747].

[357] J. D. Bjorken, R. Essig, P. Schuster, and N. Toro, *New Fixed-Target Experiments to Search for Dark Gauge Forces*, *Phys.Rev.* **D80** (2009) 075018, [arXiv:0906.0580].

[358] A. Bross, M. Crisler, S. H. Pordes, J. Volk, S. Errede, et al., *A Search for Shortlived Particles Produced in an Electron Beam Dump*, *Phys.Rev.Lett.* **67** (1991) 2942–2945.

[359] **A1** Collaboration, H. Merkel et al., *Search for Light Gauge Bosons of the Dark Sector at the Mainz Microtron*, *Phys.Rev.Lett.* **106** (2011) 251802, [arXiv:1101.4091].

[360] M. Davier and H. Nguyen Ngoc, *An Unambiguous Search for a Light Higgs Boson*, *Phys.Lett.* **B229** (1989) 150.

[361] J. Blümlein and J. Brunner, *New Exclusion Limits on Dark Gauge Forces from Proton Bremsstrahlung in Beam-Dump Data*, *Phys.Lett.* **B731** (2014) 320–326, [arXiv:1311.3870].

[362] S. Gninenko, *Constraints on sub-GeV hidden sector gauge bosons from a search for heavy neutrino decays*, *Phys.Lett.* **B713** (2012) 244–248, [arXiv:1204.3583].

[363] R. Essig, R. Harnik, J. Kaplan, and N. Toro, *Discovering New Light States at Neutrino Experiments*, *Phys.Rev.* **D82** (2010) 113008, [arXiv:1008.0636].

[364] J. B. Dent, F. Ferrer, and L. M. Krauss, *Constraints on Light Hidden Sector Gauge Bosons from Supernova Cooling*, arXiv:1201.2683.

[365] H. K. Dreiner, J.-F. Fortin, C. Hanhart, and L. Ubaldi, *Supernova constraints on MeV dark sectors from $e^+e^-$ annihilations*, *Phys.Rev.* **D89** (2014), no. 10 105015, [arXiv:1310.3826].

[366] **CERN NA48/2** Collaboration, *Search for the dark photon in $\pi^0$ decays*, arXiv:1504.00607.

## 10.1 List of Figures

## 10.2 List of Tables